E687

STUDY OF D AND D_s MESONS DECAYING INTO $K\bar{K}\pi$ FINAL STATE IN A HIGH ENERGY PHOTOPRODUCTION EXPERIMENT

A Dissertation

Submitted to the Graduate School
of the University of Notre Dame
in Partial Fulfillment of the Requirements
for the Degree of

Doctor of Philosophy

by

Manuel Eugenio Zanabria, B.S.

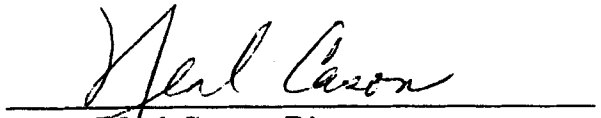

Neal Cason, Director

Department of Physics
Notre Dame, Indiana

October, 1992

TABLE OF CONTENTS

LIST OF FIGURES

LIST OF TABLES

ACKNOWLEDGEMENTS

I would like to express my gratitude to my advisor, Neal Cason, for his guidance, assistance, and support during the years I spent at Notre Dame. I wish to thank Professor Bill Shephard for his guidance and advice specially in the data analysis. A special thanks to Jerome Busenitz for all his assistance and advice in the construction of "C2", in the run of the experiment, and in the data analysis. Thanks for being patient, while I was a beginner in the field. I wish to thank Randy Ruchti, Jim Bishop as well as all the faculty, and staff of the Notre Dame High Energy Group for their assistance during all these years. Also I want to thank each of my fellow graduate students for all the help received before, during, and after the run of the experiment. The discussions we had in order to do the data analysis were very helpful.

The Fermilab E687 experiment is a collaboration of more than 60 Physicists. The success of the experiment is due to the contribution of all the members of the collaboration. I want to express to each of you my gratitude.

Finally, it would be a long list to mention each person that encouraged me to finish this thesis. I would like to thank all of my friends and family for their support.

CHAPTER 1

INTRODUCTION

There are three pseudoscalar charmed mesons, the D^0 ($c\bar{u}$), D^+ ($c\bar{d}$), and the $D_s(c\bar{s})$. All are combinations of light and charmed quarks; all have weak decays [1].

The D^0 and D^+ masses are well established:

$$M_{D^0} = 1864.5 \pm 0.5 MeV \tag{1.1}$$

$$M_{D^+} = 1869.3 \pm 0.5 MeV$$

Measurements of the D_s mass average for various experiments gives a value of 1969.5 ± 0.7 (See Table 1.1 [1]).

The weak decays of quarks are governed by the charged current

$$J_\mu = (\overline{uct})\gamma_\mu(1-\gamma_5)U \begin{pmatrix} d \\ s \\ b \end{pmatrix} \tag{1.2}$$

where the upper and lower members of the quark families are coupled by the Kobayashi-Maskawa (K-M) matrix " U " given by ([2]):

$$U = \begin{pmatrix} V_{ud} & V_{us} & V_{ub} \\ V_{cd} & V_{cs} & V_{cb} \\ V_{td} & V_{ts} & V_{tb} \end{pmatrix} \tag{1.3}$$

and $\gamma_\mu(1-\gamma_5)$ is the weak vertex factor (γ_μ are the Dirac matrices). The charm decays are controlled by the K-M elements V_{cd} and V_{cs} (See Fig. 1.1), which are very

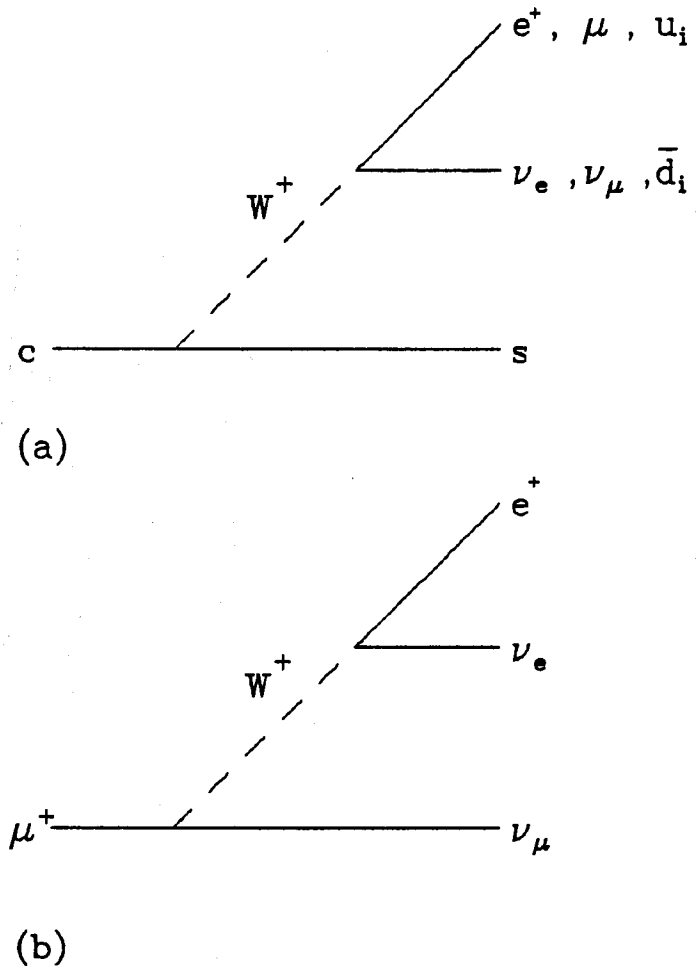

Figure 1.1: Weak decays diagram for: a) Charm Quark showing the 5 decay possibilities; two semileptonic, and the hadronic decay, the index "i" standing for the 3 possible color options. b) Muon decay to $\rightarrow \overline{\nu_\mu} e^+ \nu_e$

TABLE 1.1
MEASUREMENTS OF THE D_s MASS

Experiment	Mode	Mass (MeV)
CLEO	$\phi\pi^+$	1970 ± 5
TASSO	$\phi\pi^+$	1975 ± 9
ARGUS	$\phi\pi^+$	1970.4 ± 2.3
NA-11	$KK\pi$	1972.8 ± 2.1
NA-32	$KK\pi$	1969.1 ± 1.2
MARK III	$\phi\pi^+$	1973 ± 4
E691	$\phi\pi$	1968.1 ± 0.8

nearly equal to $\sin\theta_c$ and $\cos\theta_c$, respectively, where θ_c is the Cabibbo angle. The value $\sin\theta_c$ is known to be 0.221 $\pm$0.002 so that charmed quark decays to strange quarks are favored over decays to down quarks by a factor of $\left|\frac{cos(\theta_c)}{sin(\theta_c)}\right|^2 \simeq 20$. Charm decays are therefore dominated by "Cabibbo-favored" decays to strange quarks. This was an essential indication that the particles now known as D mesons carried the charm quantum number [3].

1.1 Weak decays of Charmed Mesons

There are three classes of charmed meson decay: leptonic, semileptonic, and hadronic. For the pseudoscalar D-mesons the purely leptonic decay is suppressed due to helicity conservation. The expected branching fractions are about 10^{-4} for $D^+ \rightarrow \mu^+\nu_\mu$ and 10^{-3} for $D_s^+ \rightarrow \mu^+\nu_\mu$. The purely leptonic decay (See Fig. 1.2.a). has not yet been observed [3].

The semileptonic decays of charmed mesons occur through the beta decay of the charmed quark [3] (See Fig. 1.2.b). The inclusive rate can be calculated approxi-

mately using the same formula as for muon decay:

$$\Gamma(D \rightarrow \ell^+ x) = \Gamma_0 \equiv \frac{G^2}{192\pi^3} m_c^5 f(\frac{m_s}{m_c}) \tag{1.4}$$

where f is a function that takes into account the finite mass of the strange quark. It has been estimated that the semileptonic decay rates for the D^0, D^+, and D_s are equal to a good approximation, and any differences in the total decay rates are due to the hadronic decays [3].

Ignoring strong interactions, there are three basic diagrams at the valence quark level for hadronic charms decays, shown in Fig. 1.3: (a) spectator decay, (b) W exchange and (c) W annihilation. The dominant process is spectator decay, in which the non-charm quark is not involved at the weak vertex. Since the D's have spin zero the W exchange and W annihilation diagrams are suppressed by helicity conservation at the light quark vertex. The valence quark model is very naive, but provides a starting point for discussing the basics issues in charm decay. According to the spectator model, the heavy quark decays weakly, and the light quark does not participate in the decay. Using this model, the decay of the charm quark: c $\rightarrow$ s($e\nu_e$ or $\mu\nu_\mu$ or $u\bar{d}$) is similar to the decay of the muon: $\mu^+ \rightarrow \overline{\nu_\mu} e^+ \nu_e$ ([4]). Thus one can estimate the charm lifetime (and hence the D lifetime) ignoring all QCD corrections [5] in terms of the muon lifetime.

The muon decay rate $\Gamma(\mu^+ \rightarrow e^+ \nu_e \overline{\nu_\mu})$, neglecting photon radiative corrections and the mass of the electron, can be calculated and is found to be:

$$\Gamma(\mu^+ \rightarrow e^+ \nu_e \overline{\nu_\mu}) = \frac{G_F^2 m_\mu^5}{192\pi^3}$$

where G_F is the Fermi coupling constant and m_μ is the muon mass [6]. The muon lifetime τ_μ is:

$$\tau_\mu = \Gamma^{-1}(\mu^+ \rightarrow e^+ \nu_e \overline{\nu_\mu})$$

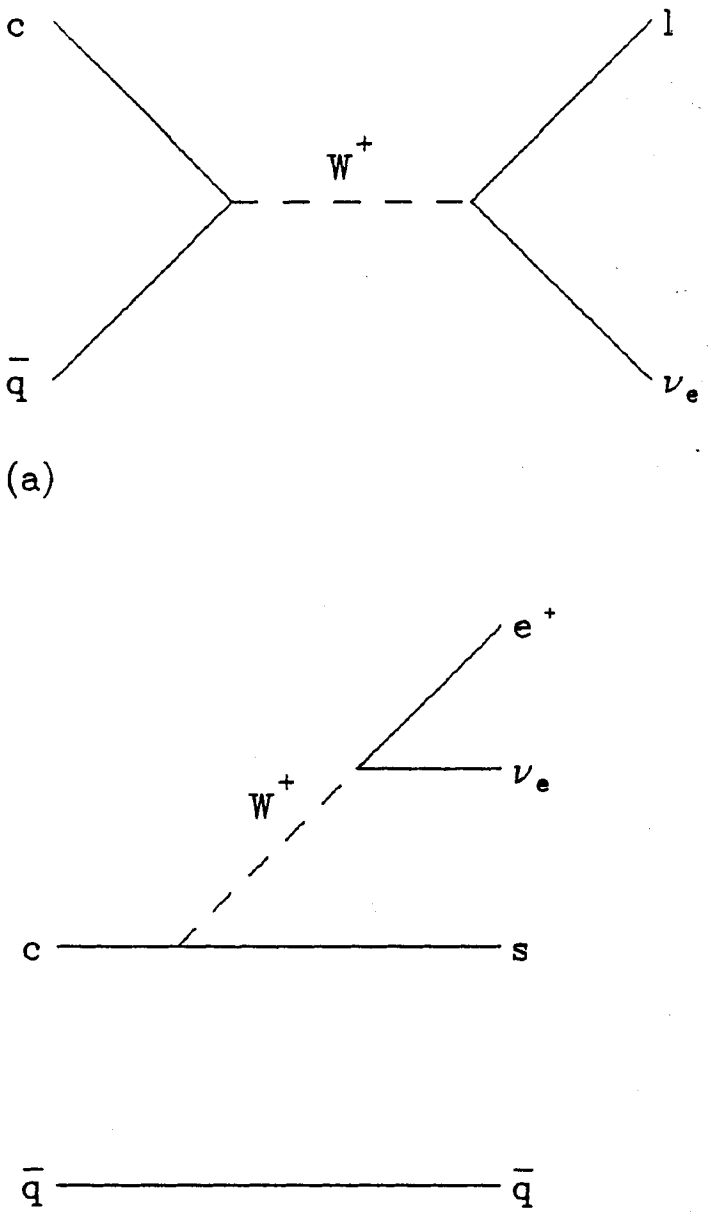

Figure 1.2: Quark level diagrams for: a) purely leptonic charm decays, b) semileptonic charm decays

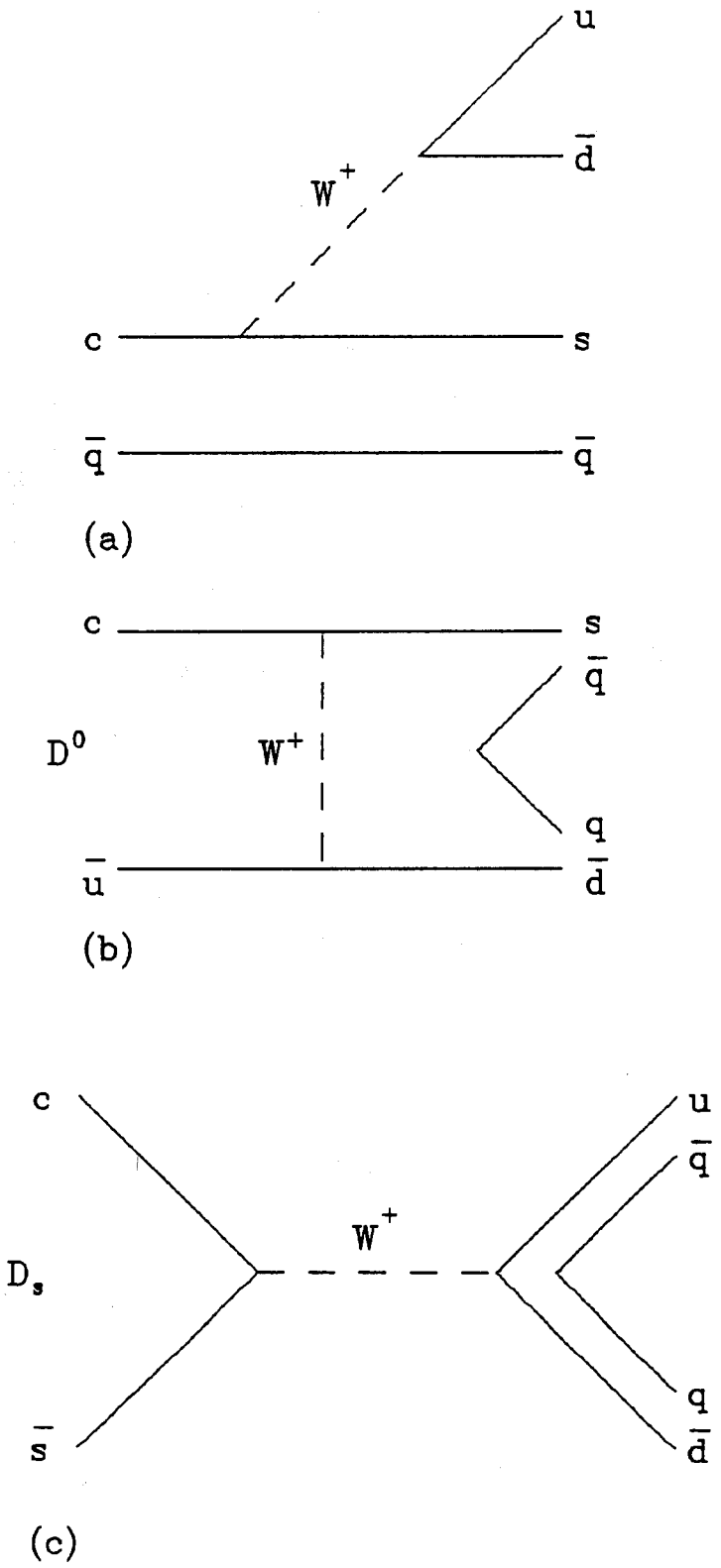

Figure 1.3: Quark level diagrams for hadronic charm decays: a) spectator decay, b) W exchange, and c) W annihilation

TABLE 1.2
CHARMED MESON LIFETIME SUMMARY

	Lifetime (ps)
D^0	0.42 ± 0.08
D^+	1.06 ± 0.23
D_s	0.45 ± 0.30

Scaling the muon rate, one can estimate the charm quark lifetime:

$$\tau(charm) = \tau(\mu)\frac{1}{5}(\frac{m_\mu}{m_c})^5 \simeq 0.6psec.$$

Thus the c quark lifetime is predicted to be on the order of 10^{-13} seconds. Some of the predictions of the naive spectator model are: 1) equal lifetimes for the D^0, D^+, and D_s; and 2) equal semileptonic branching ratios for the D^0 and D^+.

The experimental data collected do not agree with the predictions of the spectator model. There are large differences in lifetimes for the D^0, D^+ and D_s, with $\tau(D^0) \simeq \tau(D_s)$ and $\tau(D^+) \simeq 2\tau(D^0)$ (see Table 1.2 [7]). With respect to the semileptonic branching ratio, the experimental data indicate an average branching ratio lower than 20%. These discrepancies lead to a more detailed model of the spectator decay. Beginning with the inclusion of strong interactions and QCD effects the original Hamiltonian is modified with a new term that is an effective neutral current induced by hard gluon exchange [3]. QCD corrections lead to a number of predictions: 1) there is a nonleptonic enhancement that would lower the semileptonic branching ratio from 20 % to 14 %; and 2) there is an effective neutral current interaction that populates certain "color-suppressed" final states. (See Fig. 1.4.b.)

From the experimental data available (especially from MARK III), there is no indication that the lifetime difference is due to semileptonic decays. Therefore the explanation is expected to be in the hadronic decays. As mentioned earlier, of the

diagrams that contribute to the hadronic decay of D mesons (see Fig. 1.3) the annihilation and W exchange modes are suppressed by helicity conservation. The decay rates expected from these diagrams are much smaller than for spectator decays; $\Gamma_{an} \ll \Gamma_{sp}$. [5].

D_s decays to $\phi\pi$ which lead to $s\bar{s}$ final states are expected to take place via the spectator diagram. If decays should take place via annihilation, the final states will be $\pi\pi\pi$, $\rho\pi$, $\omega\pi$, etc. Experimental measurements show that the contribution of these decays is small [8]. The smallness of the annihilation contribution to D_s decays suggests that the associated W exchange process is also small. Therefore W annihilation and W exchange processes are not the primary cause of the D_s and D^+ lifetime different.

The addition of QCD corrections separates the interaction into effective charged and neutral current operators. In Fig. 1.4.a is shown the spectator diagram for the spectator color-unmixed decay and in Fig. 1.4.b the diagram for the spectator color-suppressed decay. In Fig. 1.5 are shown similar diagrams for the D^0 and D_s. From these diagrams one observes that only in the case of the D^+ the two diagrams produce the same final-state quark, and therefore interfere. There is a large destructive interference which lengthens the D^+ lifetime. [3] More detailed investigation using many exclusive final states [9], [10] leads to the conclusion that it is possible to explain the lifetime difference with such interference effects. On the other hand, there are several works [11], [5] that find that final state interactions can explain the lifetime difference.

The spectator model with QCD corrections is still not good enough to explain branching ratios that involve color suppressed decays, such as $\frac{D^0 \to \bar{K}^0 \pi^0}{D^0 \to K^- \pi^+}$. Stech et al. [9] pointed out that color-suppressed diagrams do not seem to contribute to D decays. Comparison of several decay modes of the D^0 makes it clear that final state

interactions play an important role. Evidence that supports the importance of final state interactions comes from the isospin analysis made by Chau and Cheng [12], as well from Bauer, Stech and Wirbel [9] using the decays $D^0 \to K^-\pi^+$, $D^0 \to \overline{K}^0\pi^0$, and $D^+ \to \overline{K}^0\pi^+$.

In summary, the present theory of hadronic D-decays is based on simple valence quark diagrams, hard gluon QCD corrections, form factors for the final state mesons, and final state interactions [3], [5].

1.1.1 $K\overline{K}\pi$ final state diagrams

This final state is a good testing ground for the models outlined above because of the variety of diagrams which can contribute [13]. In Fig. 1.6 and Fig. 1.7 are shown the diagrams for the D_s Cabibbo-allowed and for the D^+ Cabibbo suppressed decays (the strangeness-changing process $s \to u + W^-$ carries a factor of $\sin\theta_c$ and is weaker than the strangeness-conserving process $d \to u + W^-$ that carries a factor of $\cos\theta_c$. Thus decays that involve the $s \to u + W^-$ vertex are called Cabibbo-suppressed [2]).

In Fig. 1.6 are shown the diagrams contributing to the $D_s^+ \to K^-K^+\pi^+$. Fig. 1.6.a shows the color-unmixed spectator diagram, Fig. 1.6.b the color-mixed or color suppressed spectator decay and Fig. 1.6.c the annihilation decay.

In Fig. 1.7 are shown the diagrams contributing to the $D^+ \to K^-K^+\pi^+$. Fig. 1.7.a shown the color-unmixed spectator decay, Fig. 1.7.b the color-mixed or color suppressed spectator diagram and Fig. 1.7.c the annihilation decay.

From these diagrams one can observe that ([13]):

- $D_s^+ \to \phi\pi^+$ is a pure color-unmixed spectator decay with no annihilation contribution.

- The ratio $\overline{K}^{*0}K^+/\phi\pi^+$ might be expected to be small for the D_s^+ and large for

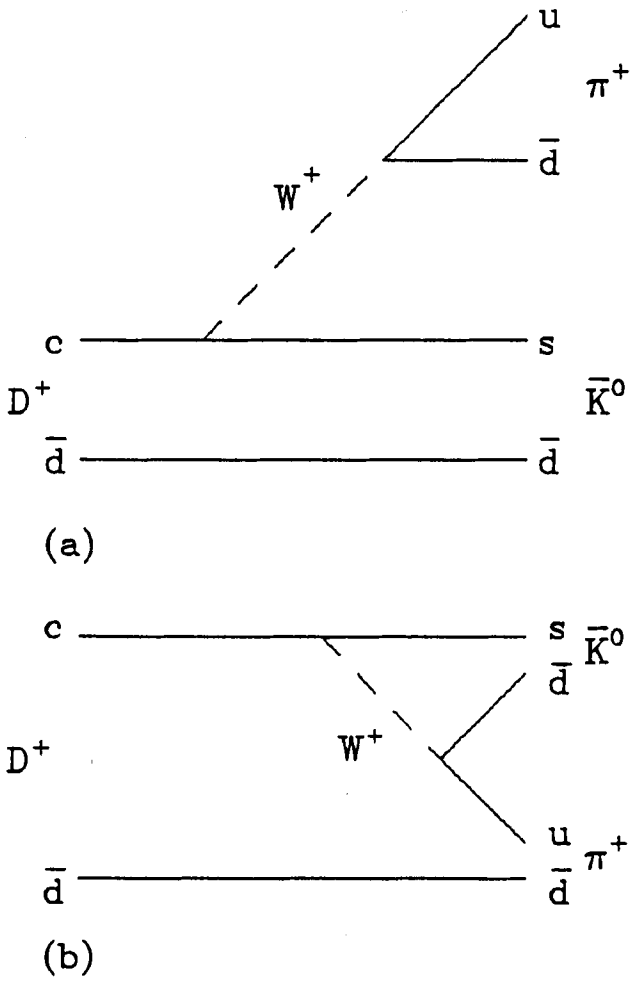

Figure 1.4: Quark level diagrams for hadronic D^+ decays: a) charge current or spectator color allowed decay, b) neutral current or spectator color suppressed decay

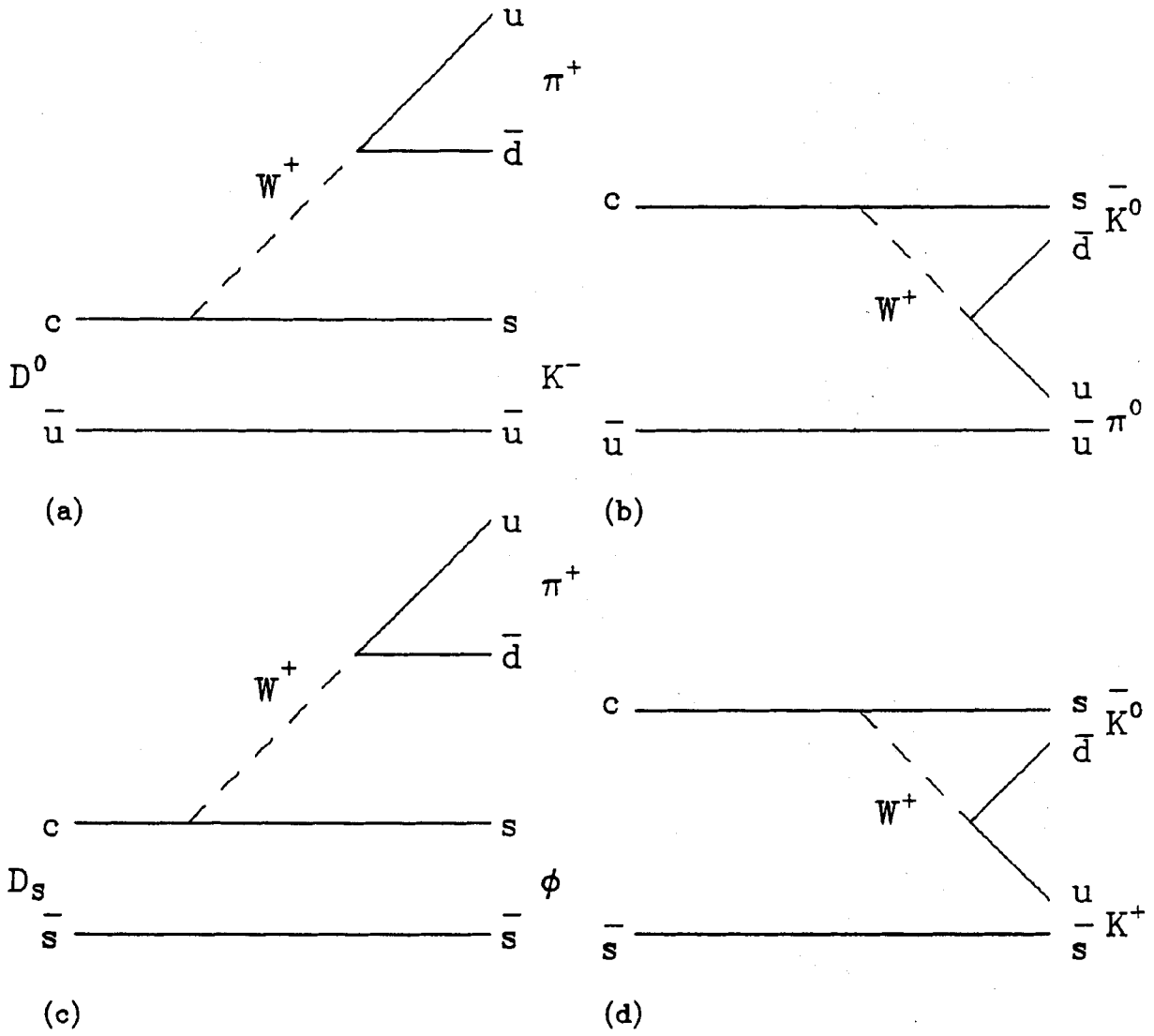

Figure 1.5: Quark level diagrams for hadronic charm decays for the D'': a) color unmixed, b) color suppressed, and for the D_s: c) color unmixed, d) color suppressed

the D^+ since color suppression affects the two modes differently: $\phi\pi$ is allowed for the D_s and suppressed for the D^+ while $\overline{K}^{*0}K^+$ is suppressed for the D_s but allowed for the D^+.

The observed importance of the decay channel $D_s \rightarrow \overline{K}^{*0}K$ is due to the contribution from the spectator color-suppressed diagram and the annihilation diagram. As mentioned above, the amplitude for the color-suppressed decay is (naively) suppressed by a color factor of 1/3 with respect to the spectator color-unmixed decay. The weak annihilation diagram (See Fig. 1.3) describes the process $c\bar{s} \rightarrow u\bar{d}(q\bar{q})$, and will only rarely produce a final state with an $s\bar{s}$ pair [3].

1.2 Motivation

The goal of this thesis is to provide a further study of the color suppression mechanism and the contribution of the spectator and non-spectator diagrams to the $K\overline{K}\pi$ final state. For that purpose an amplitude analysis of the $K^+K^-\pi^+$ decays of the D_s and D^+ mesons is done. The contributions of the resonances to the $K\overline{K}\pi$ final state are found by a fit to the respective D^+ and D_s Dalitz plots. Several previous experiments have reported measurements of $K\overline{K}\pi$ final state branching ratios but, with the exception of E691 [14], none of them has performed an amplitude analyses by a fit to the Dalitz plot.

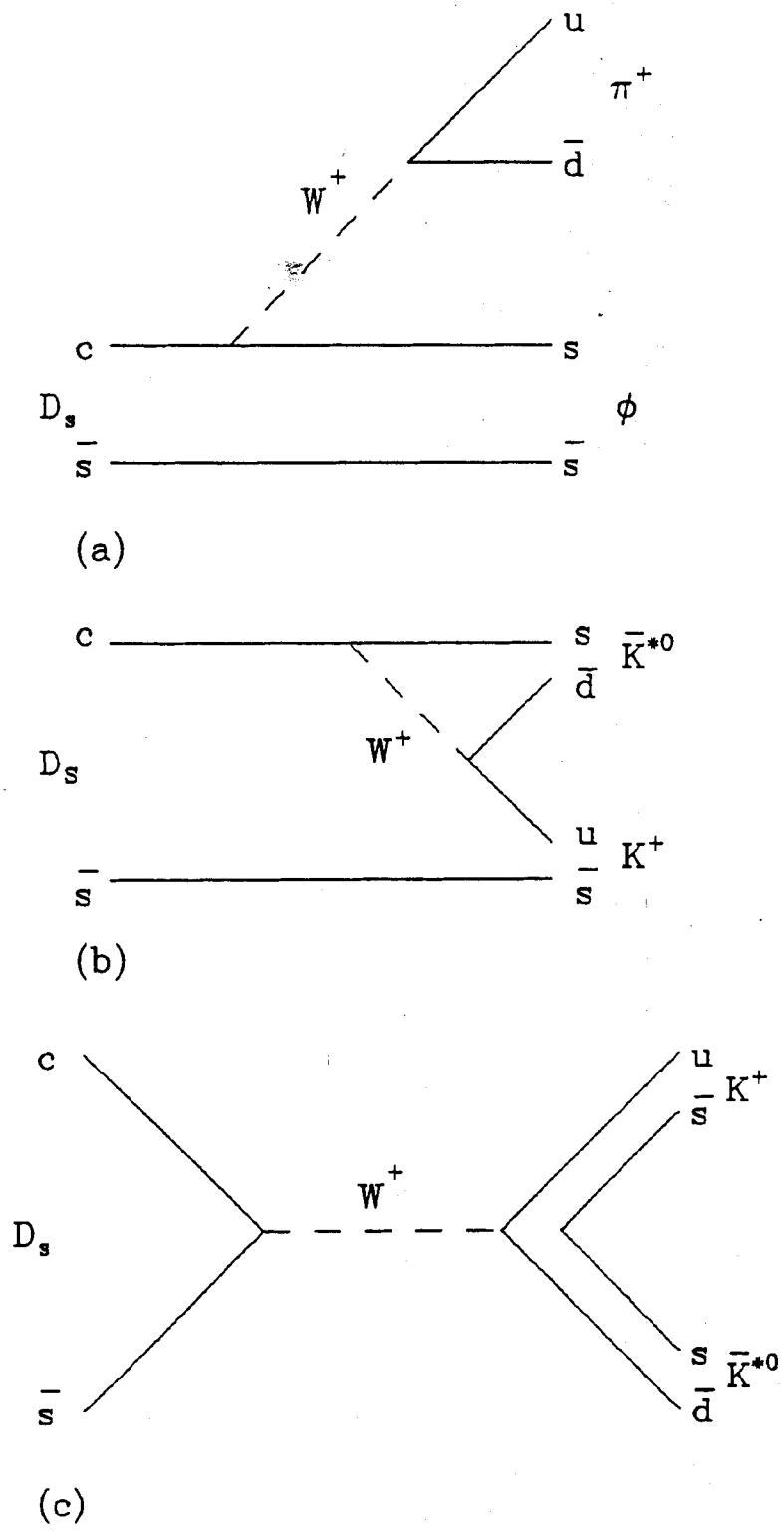

Figure 1.6: Quark level diagrams for hadronic D_s decays: a) charge current or spectator color-unmixed decay, b) neutral current or spectator color suppressed decay, c) annihilation

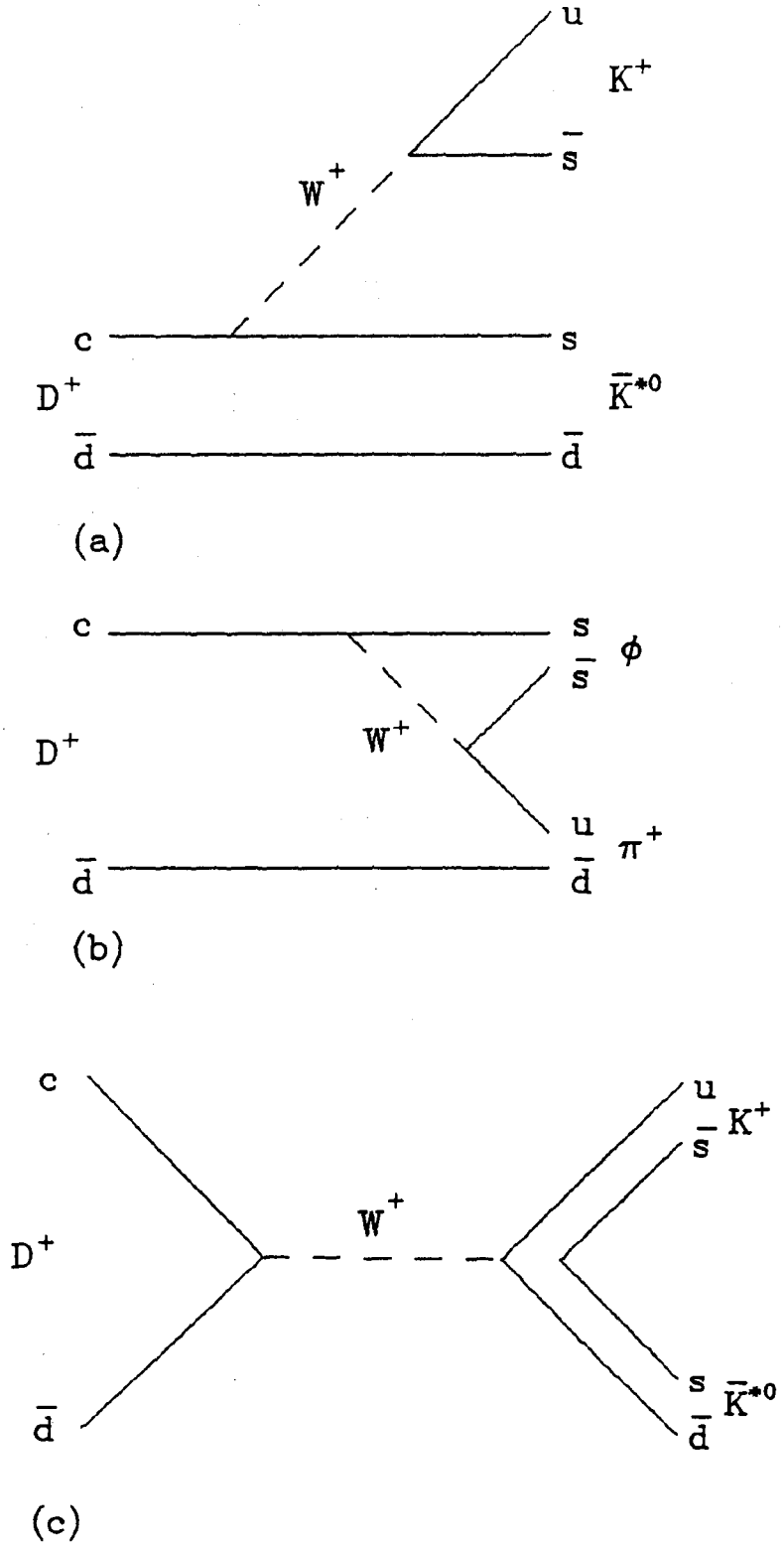

Figure 1.7: Quark level diagrams for hadronic charm decays for the D^+: a) color unmixed, b) color suppressed, c) annihilation

CHAPTER 2

THE E687 DETECTOR

2.1 Introduction

The E687 experiment [15] is a fixed target experiment performed at the wide band hall located in the proton East beam line at Fermi National Accelerator Laboratory. The experiment is a photoproduction experiment whose main purpose is to study particles containing heavy quarks. The identification of these particles depends on the particular properties of their decays. For that purpose E687 is a multiparticle spectrometer for the detection, tracking and identification of the decay particles. The beam consists of photons of 221 GeV average energy incident on a beryllium target. The spectrometer consists of: a Silicon microstrip vertex detector; two analyzing magnets; multiwire proportional chambers which provide high resolution tracking information; a set of three multicell threshold Cerenkov counters for charged particle identification; an electromagnetic calorimeter for photon-electron identification; a hadron calorimeter for hadron identification; and a muon identifier (See Fig. 2.1).

The experiment started calibration runs in June 1987 and began to take data in September of the same year. On October 3 a fire destroyed one of the electromagnetic calorimeters and did damage to some others detectors. After cleanup and rebuilding, the data taking resumed on December 1 and ran until February 15, 1988.

The data used in this thesis come from the period known as the post-fire data

taking period, during which the photons were produced by electrons with 350 GeV mean energy. During this period of time 60 million triggers were recorded. What follows is a description of the beam and the spectrometer [16]. Some of the detectors were crucial for the analysis in this thesis (like the Cerenkov counters), and others were not used at all (e.g. the muon counters).

2.2 The Beam

E687 used the most energetic photon beam in the world with an average energy of 350 GeV/c. The photon beam is produced by the conventional "bremsstrahlung method" (See Fig. 2.2) [17]. The main ring accelerator provides a beam of protons with an energy of 800 GeV/c. The protons hit a beryllium target 18 inches long, called the "primary production target" and, as a consequence of the hadronic interaction, neutral pions are created as are other neutral and charged particles. Photons are created from the decay of neutral pions, and emerge near zero degrees. Downstream of the target there are sweeping magnets that bend the charged particles away, leaving the neutral particles and the photons coming from π^0 decay to travel through the beam line to the next interaction zone. The photons produce electron-positron pairs in a lead foil called the "converter", which is composed of 50% of a radiation length of lead. The electrons are bent away from zero degrees by a system of dipole and quadrupole magnets. Residual neutral particles and unconverted photons travel directly to a neutral dump where they are absorbed. The electron beam is transported around the dump and hits a lead foil called the "radiator", consisting of 20% of a radiation length of lead. Photons are then produced by bremsstrahlung. Downstream of the radiator there are dipole magnets that bend the electrons into a dump while the photons travel to the experimental target.

The photon beam produced in this way has the advantage of having very little

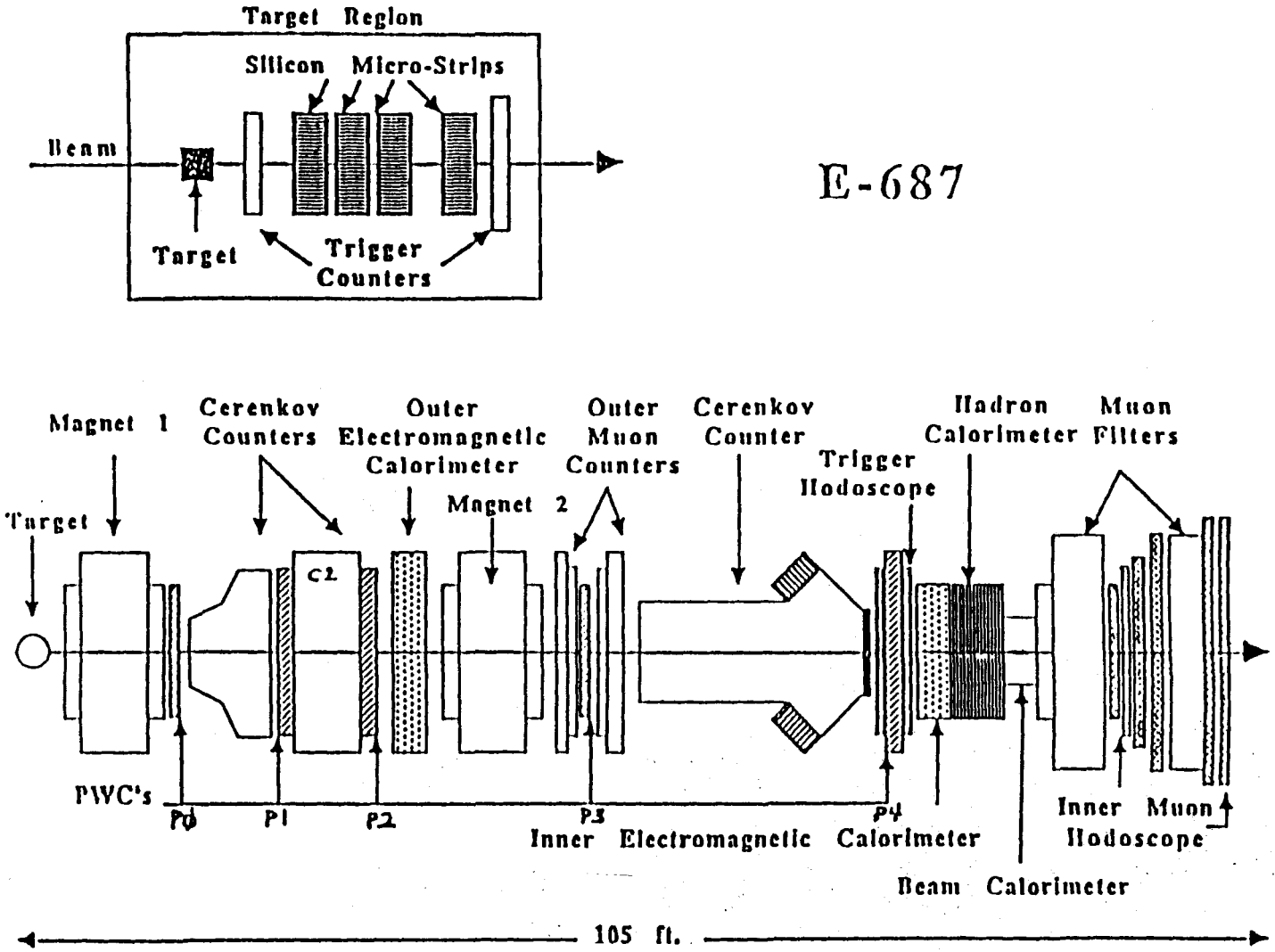

Figure 2.1: Layout for the E687 Spectrometer

hadron contamination. The resultant background of neutral hadrons at the experimental target is, both from Monte Carlo calculation and from measurement, about 10^{-5} neutrons per photon.

The number of incident protons at the primary target during the 20 second duration of the spill (one spill each minute) is about 2.0 X 10^{12}, and the number of photons exceeding 50 GeV at the experimental target was approximately 2 X 10^{7} per spill.

2.3 The Tagging system

The purpose of the Beam Tagging System is to determine the energy of the interacting photon on an event-by-event basis. It also serves as a part of the second-level trigger. (See Fig. 2.3. for a diagram of the system). The incident momentum-selected electron strikes a lead radiator, producing photons by bremsstrahlung. The electron, after this interaction, is momentum analysed in a magnetic spectrometer with the Recoil Electron Shower Hodoscope (RESH). Electrons are identified by a large energy deposition in this RESH hodoscope. Multiple bremsstrahlung may occur in the radiator. Typically, only one photon interacts in the experimental target. The energy of any non-interacting photon is measured in a zero-degree shower counter, the Beam Gamma Monitor (BGM), located towards the end of the spectrometer. The photon energy is calculated, on an event-by-event basis, from the following formula:

$$E_\gamma = E_e - E_{RESH} - E_{BGM} \tag{2.1}$$

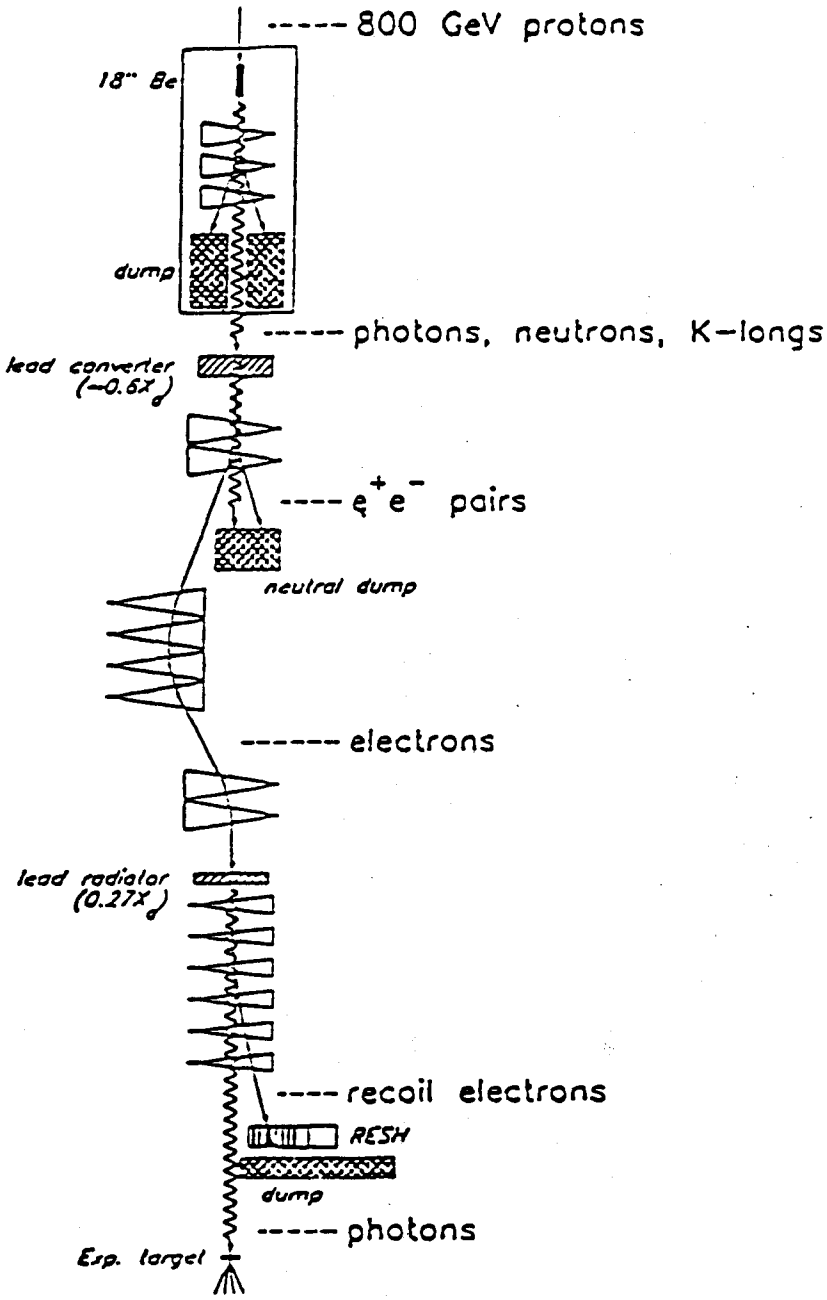

Figure 2.2: Layout for the E687 wide band photon beam line

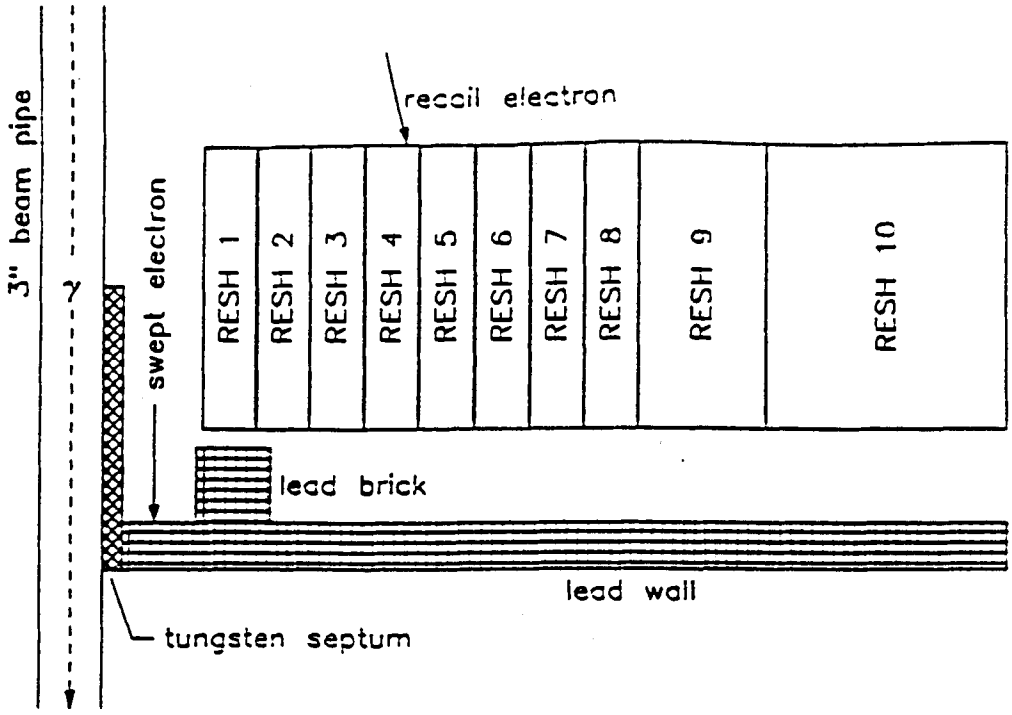

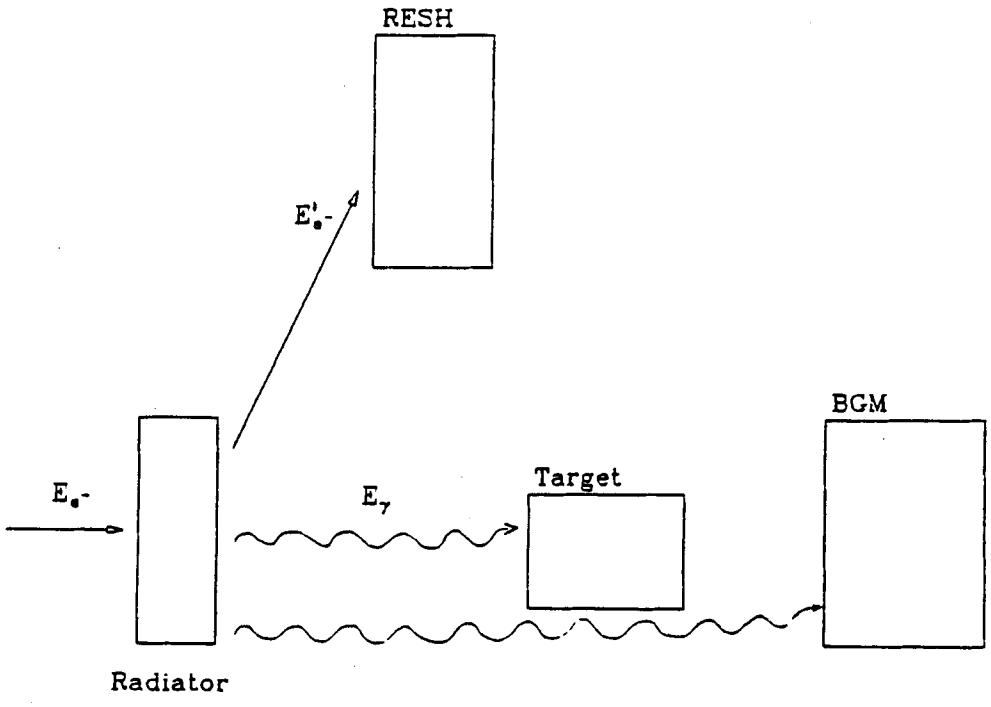

Figure 2.3: The E687 RESH shower counter

2.4 The Target

The targets used in the experiment were of two kinds. One was a beryllium target and the other a silicon active target. The beryllium target was used approximately 90% of the time. There were two beryllium targets used. One consisted of 5 blocks ("5-Be") and the other one of 4 blocks ("4-Be").

The 5-Be target consisted of 5 blocks, with a thickness of 4 mm each, separated by thin air gaps (See Fig. 2.4). The upstream portion was designed to match the beam spot, while the diamond shape of the downstream 3 blocks was designed to match the high resolution region of the first station of the microstrip detectors. The total length was $\sim$ 4.5 cm corresponding to approximately 11.5% of a radiation length and 10% of an interaction length. The silicon active target consisted of 50 silicon wafers.

2.5 The Microstrip Detector

The aim of the E687 experiment is to investigate events involving heavy flavors and to measure the lifetimes of charmed secondaries. The microvertex detector [18] has been designed to reconstruct the complex topology of such events with high efficiency and to identify the decay vertices. The microvertex detector is shown in Fig. 2.5. It consists of twelve Si microstrip planes grouped in four assemblies of X,Y and U oriented detectors. The active area of each detector is divided into a high resolution central region and two outer regions with a lower resolution. All geometrical parameters have been optimized by means of a simulation and pattern recognition program. The central region has been designed with higher resolution in order to disentangle the forward high momentum tracks that are clustered but relatively unaffected by multiple scattering. On the other hand, the lower resolution outer regions are crossed by tracks with a larger spatial separation that, because of their smaller energy, are more affected

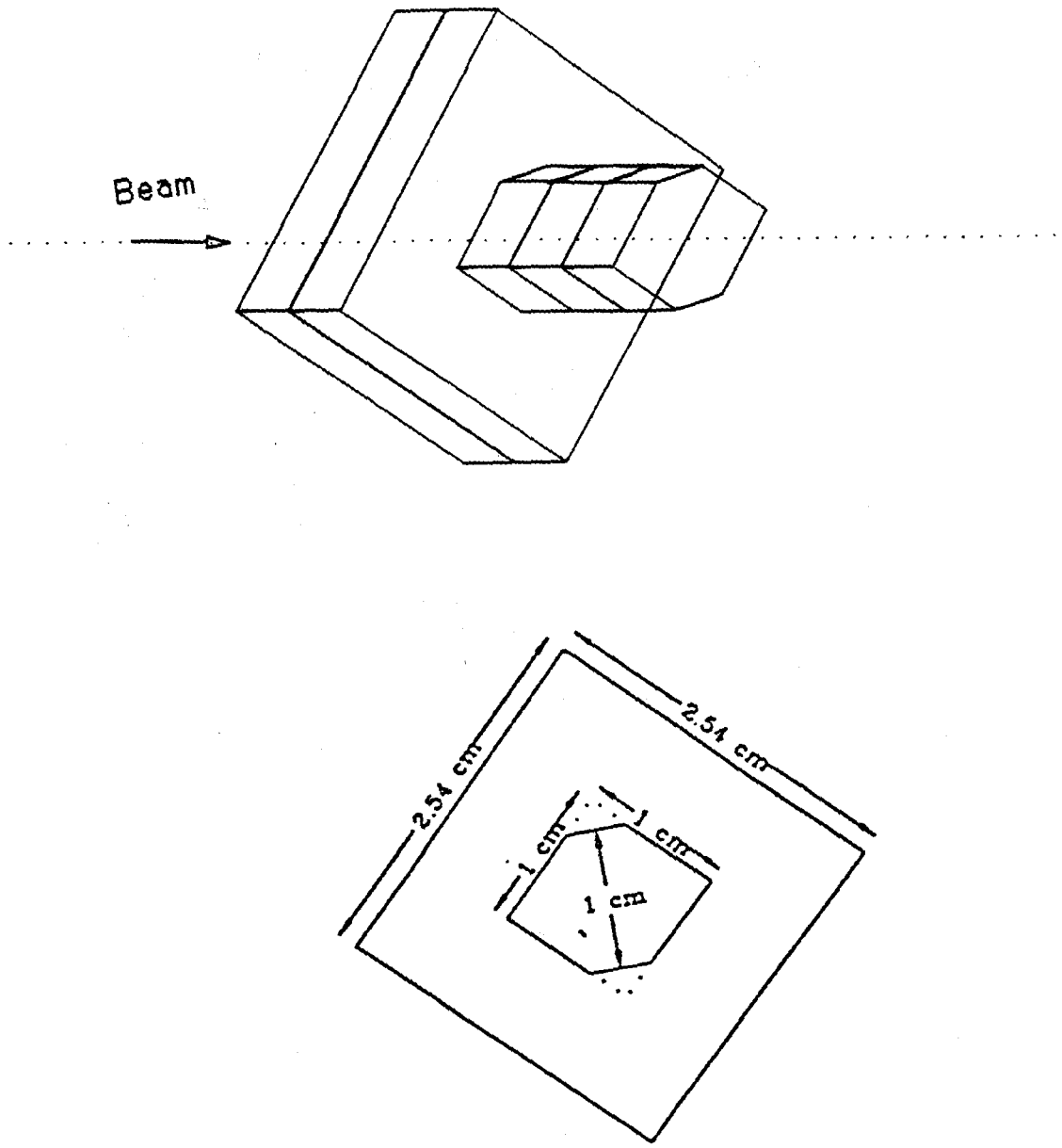

Figure 2.4: The Beryllium target

by the multiple scattering. The angular acceptance of the system is determined by the third detector assembly and matches the spectrometer acceptance. The fourth assembly is displaced downstream for greater track separation in the extreme forward cone.

The silicon wafers employed in the microvertex detector are 300 μm thick and 5x5 cm^2 wide. The characteristics of the microstrip detectors are summarized in Table 2.1.

TABLE 2.1
PROPERTIES OF THE MICROVERTEX DETECTOR

	Station I	Station II	Station III	Station IV
z position:				
1st plane	-.5 cm	5.5 cm	11.5 cm	23.5 cm
2nd plane	0.0 cm	6.0 cm	12.0 cm	24.0 cm
3rd plane	0.5 cm	6.5 cm	12.5 cm	24.5 cm
active area	2.5 x 3.5 cm^2	5 x 5 cm^2	5 x 5cm^2	5 x 5cm^2
high res. area	1 x 3.5 cm^2	2 x 5 cm^2	2 x 5cm^2	2 x 5cm^2
strip pitch	25.50 μm	50.10 μm	50.10 μm	50.10 μm

In each assembly the first, second and third plane measure the X, Y, and U coordinate respectively (The X, Y, and U coordinates are at -45°, -135°, and -90° with respect to the horizontal). The total number of strips is 8400.

2.6 The PWC system

The multiwire proportional chamber (PWC) system for E687 consisted of 20 signal planes grouped into 5 stations with 4 planes per station. These stations were labeled P0, P1, P2, P3, and P4, from upstream to downstream. Stations P0, P1 and P2 were located between the two analysis magnets with P0 just downstream of M1. P3 was located just downstream of M2 and P4 was just downstream of the last Cerenkov

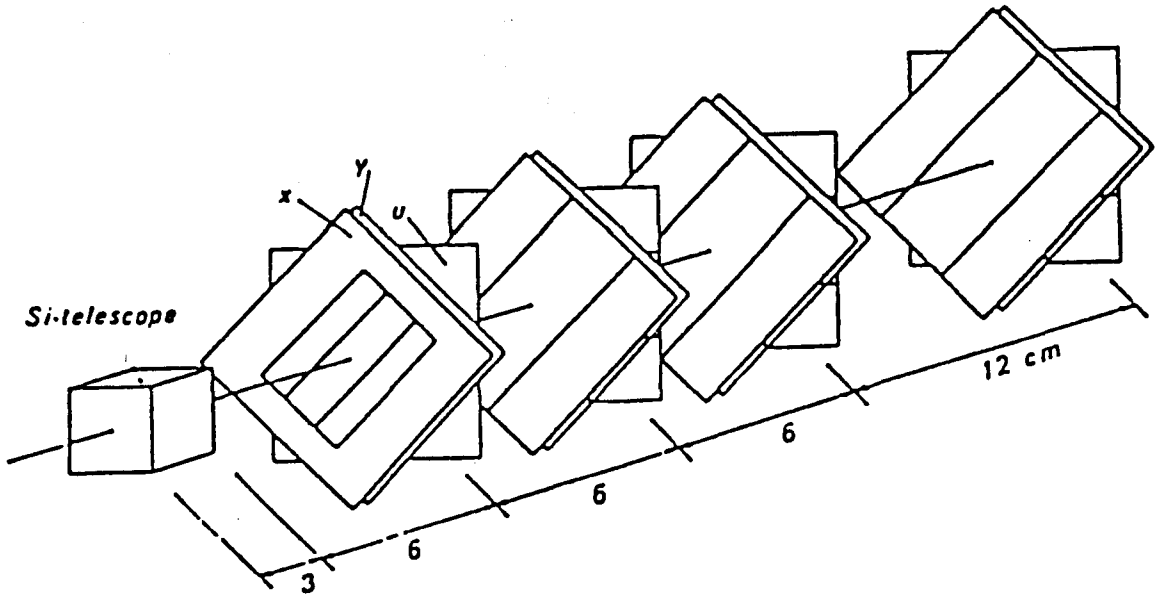

Figure 2.5: The Microvertex detector

counter C3. [16].

Each station had four views (except P4 with three views). The X view wires ran vertically and measured horizontal position. The stereo angle for the U and V views was +/- 11.3 degrees from the Y view. The parameters of the PWCs are listed in Table 2.2.

TABLE 2.2
E687 MWPC SPECIFICATIONS

Station	Aperture (inches)	Plane	N. of Wires	Wire spacing (mm)
P0	30 X 50	X	376	0.2028
		V	640	0.2032
		U	640	0.2031
		Y	624	0.2030
P1	60 X 90	X	512	0.3047
		V	832	0.3047
		U	832	0.3047
		Y	752	0.3049
P2	60 X 90	X	512	0.3049
		V	800	0.3051
		U	832	0.3049
		Y	760	0.3049
P3	30 X 50	X	352	0.2031
		V	640	0.2032
		U	608	0.2033
		Y	624	0.2031
P4	40 X 60	X	336	0.3007
		V	768	0.2001
		U	768	0.1999

2.7 Cerenkov System

The E687 Cerenkov detectors have a very important role in this analysis. It is known that D meson decays contain kaons and pions, so the study of D mesons depends

on the identification of kaons and pions. Separation of kaons and pions is done by the system of three Cerenkov counters. All three are multicell threshold Cerenkov counters and are called C1, C2, and C3 respectively. The counters are all run at atmospheric pressure in the threshold mode. These counters have different threshold momenta, the counter with the highest pion threshold essentially establishing the upper momentum range of conventional particle identification. (See Table 2.3 for counter characteristics.) In Fig. 2.6 is shown the predicted efficiency for a parti-

TABLE 2.3
E687 CERENKOV COUNTERS SPECIFICATIONS

Counter	Gas	Threshold (GeV/c)			Number of Cells
		Pion	kaon	Proton	
C1	He-N_2	6.7	23.3	44.3	90
C2	N_2O	4.5	16.2	30.9	110
C3	He	17.0	61.0	116.2	100

cle (pion) to turn a counter on as a function of momentum for the three Cerenkov counters. This predicted efficiency is related to the momentum by the relation:

$$\epsilon(p) = 1 - e^{-\alpha f(p)}$$

where:

$$f(p) = \frac{sin^2(\theta)}{sin^2(\theta_m)}$$

and α is the average number of photoelectrons for a typical cell. This relation was used for each counter where we have used an average value of α of 3 for C1, and a value of 10 for C2 and C3

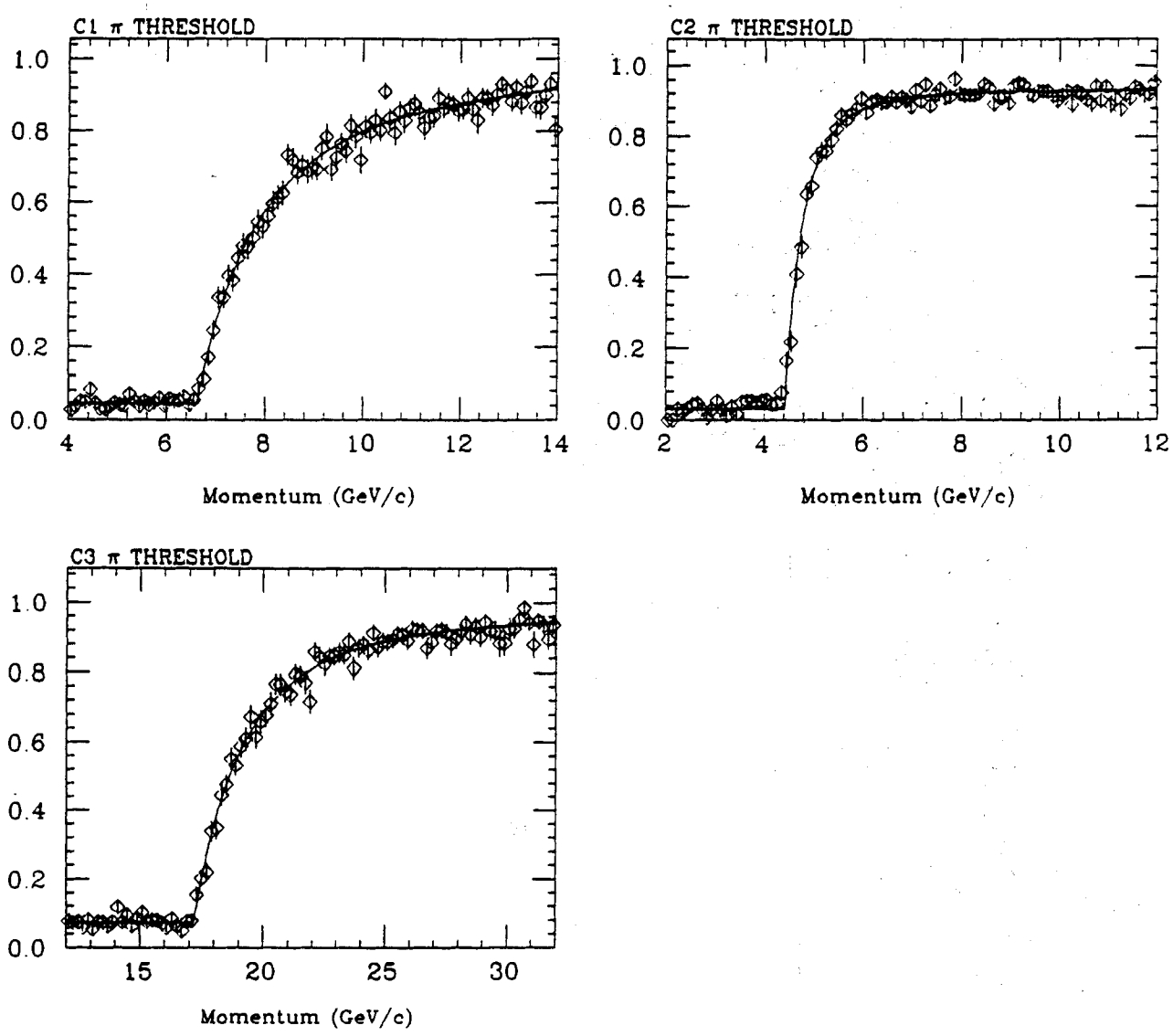

Figure 2.6: Efficiency of a particle (pion) to turn the counter on as a function of momentum for the three Cerenkov counters

2.7.1 C1

The Cerenkov counter C1 is located between P0 and P1. It has an aperture of 50 in. x 80 in. and a length in the beam direction of 71 in. The radiator gas was a helium-nitrogen mixture, giving a pion threshold of 6.7 GeV. This counter used two mirror sets. One is a planar mirror that reflects the Cerenkov photons onto light collection cones which focuses the photons onto photomultiplier tubes. The other set consists of conventional focusing mirrors that focus the photons onto individual phototubes located upstream of the mirror. The overall number of cells for C1 is 90. The average number of photoelectrons detected in a particular cell is 3.

2.7.2 C2

The dimensions for the counter are shown in Fig. 2.7. C2 is located between P1 and P2. The material for the windows of the counter is made of kapton. These windows are almost transparent to the passage of particles through the counter.

The radiator used is N_2O at atmospheric pressure which gives a pion threshold of 4.5 GeV/c. The index of refraction of N_2O is 1.0004646 at 25° C, and it has radiation length of 20,300 cm. N_2O was chosen as a radiator instead of N_2 and CO_2 after a test done at Brookhaven with a test Cerenkov counter which found that the amount of scintillation light observed in N_2O is neglible.

There are two low-mass planar mirror sections for the reflection of Cerenkov photons. The transverse coverage is 63" x 92" . The mirrors make an angle of 90 degrees between them and 45 degrees with the direction of the beam. Each section is made of 32 smaller mirrors with dimensions 11.0" x 11.5" x 0.0394". The mirrors are made of float glass 1mm thick overcoated with a 50 nm layer of MgF_2.

In order to reduce the material in the path of e^+e^- pairs and non-interacting

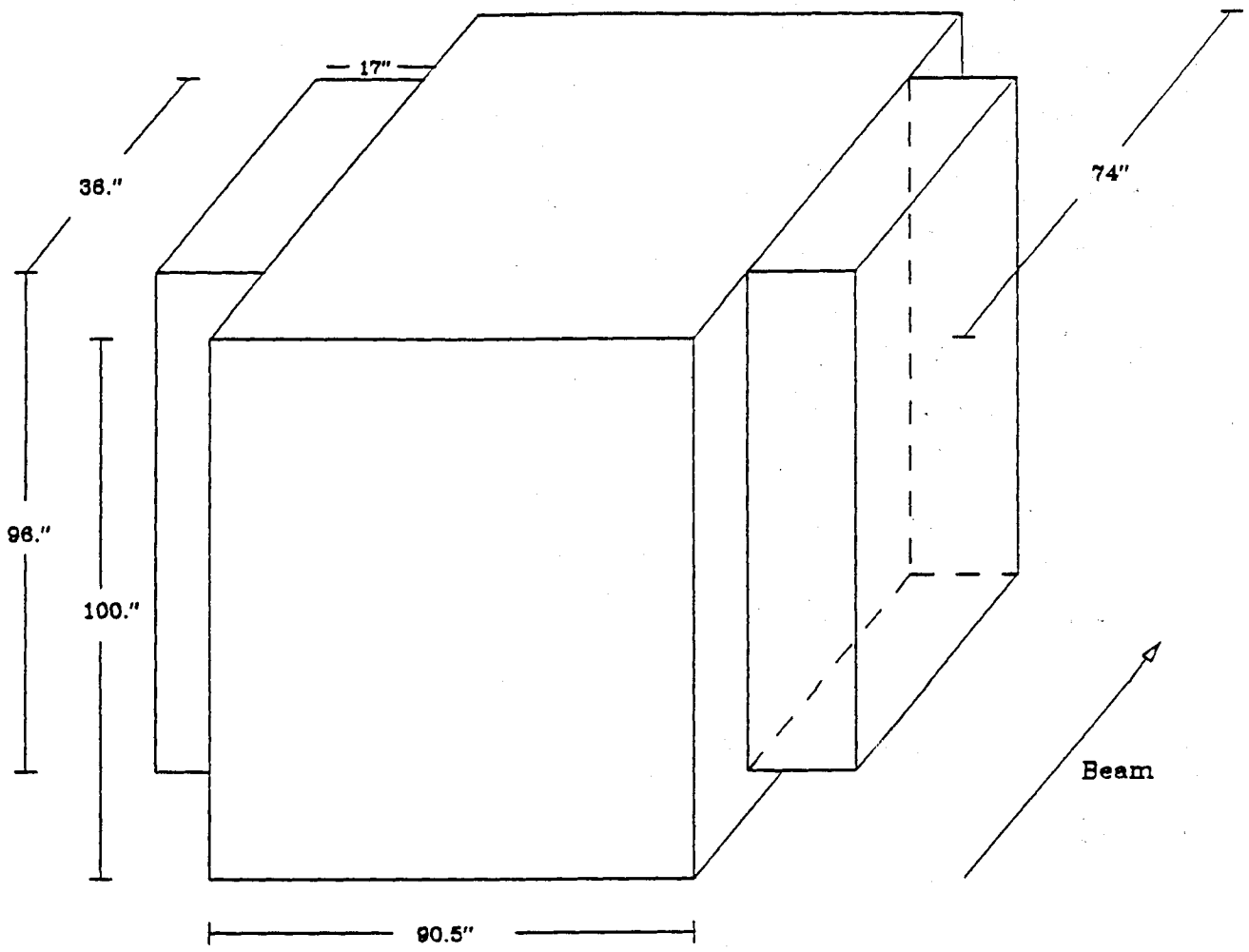

Figure 2.7: Layout for counter C2 (not a scale).

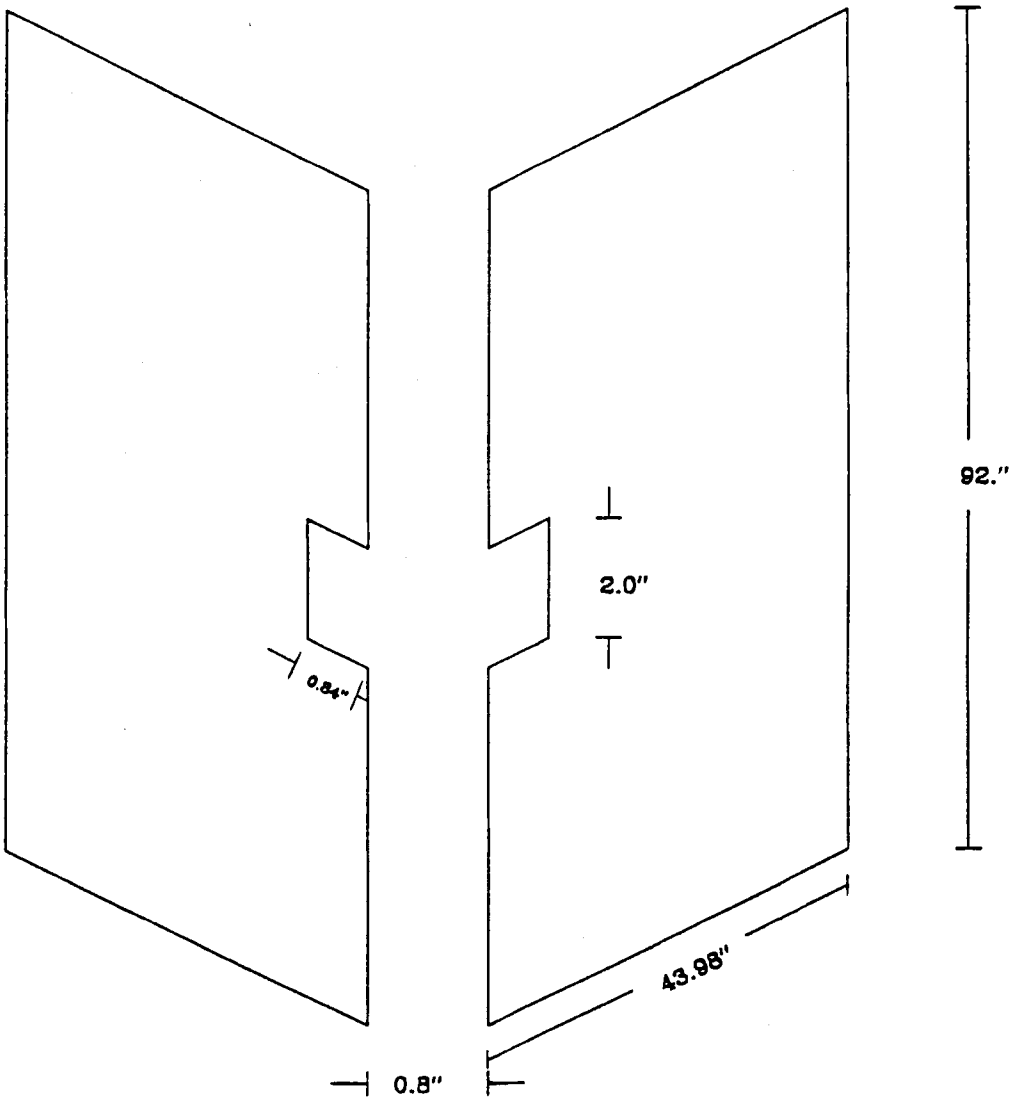

Figure 2.8: Sketch of C2 planar mirrors (not a scale).

photons that come from the target, the design of the mirrors is such that there is a small horizontal separation between them at the center as shown in Fig. 2.8.

The mirrors are supported by a lattice made of Rohacell with a radiation length of 220 cm. The mirrors have 88% reflectivity at a wavelength of 400nm and maintain a reflectivity of greater than 80% down to 220nm, below which practically all the light is absorbed by the radiator before reaching the phototubes. The mirrors reflect the Cerenkov photons toward the light collection cone arrays which are mounted on the side of the structure and which focus the photons onto the faces of the photomultiplier tubes.

There are 110 light collection cones, 55 on each side of the counter. They are arranged as much as possible in a close-packed structure to avoid any separation between them where the light would be undetected. The base material of these cones is of specular quality Coilzak, realuminized and overcoated with a 25 nm thick layer of magnesium fluoride MgF_2. It is well known that the bulk of the Cerenkov radiation is in the ultra-violet range and that photomultiplier tubes are more efficient for detecting light at higher wave lengths. Thus in order to collect as much Cerenkov light as possible, the faces of the photomultipier tubes are coated with a wavelength shifter (p-terphenyl).

The photomultiplier tubes were of two sizes. The inner cells used 2" EMI 9939A tubes, and the outer cells used 5" RCA 8854 tubes. The photomultiplier tubes were shielded from magnetic fields by wrapping them alternately with 9 pieces of mylar and 8 pieces of transformer steel.

C2 Calibration

The counter was calibrated with special runs of muons and electrons. The muons mainly illuminated the inner 2" cells, while the electrons tended to illuminate the

outer 5" cells, especially the ones located at the top and bottom. The goals for the Cerenkov calibration scheme for E687 were [21]:

- Determine the number of photoelectrons for the various Cerenkov cells.
- Determine the positions of the cells boundaries with high precision (say 0.1 inch) relative to the spectrometer coordinate system.
- Determine the pion threshold of the counter.

In order to find the cell boundaries a Joint Probability Distribution (J.P.D.) method was used. The joint probability distribution gives the probability that two adjacent cells are both "on" as a function of distance to the cell boundary for electron or muon tracks with fully contained light in the transverse direction [22]. Fits to the joint probability distribution provides simultaneous information on the following important Cerenkov parameters:

- The number of photoelectrons collected in each cell can be determined from the fit, primarily from the maximum value for the J.P.D. near the adjacent cell boundary. Poisson statistics provides a rough estimate of the mean number of photoelectrons (p.e.) collected in the two cell system:

$$N_{pe} = -2\ln(1 - \sqrt{\epsilon_{max}})$$

  The fit to the J.P.D. can provide an individual p.e. estimate for each of the cells.

- The width of the J.P.D. measures the radius of the Cerenkov cone.
- The position where the J.P.D. reaches a maximum is essentially the mirror boundary between adjacent cells.

The J.P.D. is based on Poisson statistics. The probability of observing n photoelectrons given μ (the average number of photoelectrons found if the light for a given track is fully contained in the cell), and α (the fraction of overlap) is given by the following relation

$$P(n,\mu,\alpha) = \frac{1}{n!}(\alpha\mu)^n e^{-\alpha\mu}$$

Thus the probability of observing zero photoelectrons is given by:

$$P(0,\mu,\alpha) = e^{-\alpha\mu}$$

and the probability that any given cell is on is given by:

$$P(on) = 1 - P(off)$$

$$P(on) = 1 - e^{-\alpha\mu}$$

Thus the probability that two adjacent cells are both on as a function of distance to cell boundary is given by:

$$P = (1 - e^{-\alpha_1\mu_1})(1 - e^{-\alpha_2\mu_2})$$

where μ_i is the average number of photoelectrons cell i would collect if it were to collect all the light emitted by the track, and α_i is the fraction of Cerenkov light intercepted by cell i.

In Fig. 2.9 are shown the fits to several cells using the J.P.D. method. It is interesting to note that the maximum of the distribution corresponds to the geometric boundary between adjacent cells. In Fig. 2.10 is shown the final geometry of C2 obtained by the J.P.D. The geometry obtained by the J.P.D. method was compared with a photographic survey of the counter and they were in overall good agreement.

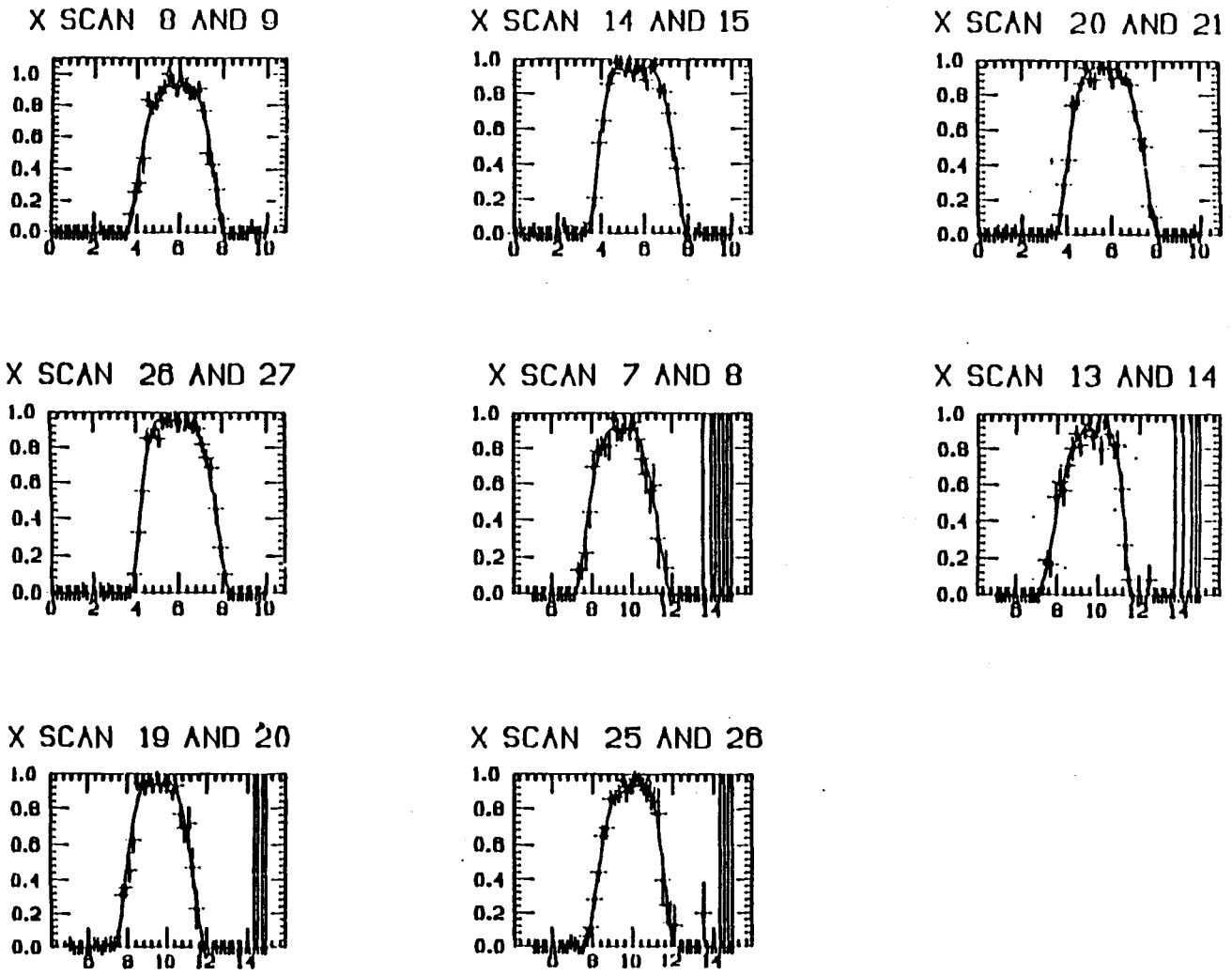

Figure 2.9: Joint Probability Distributions for several cells from C2

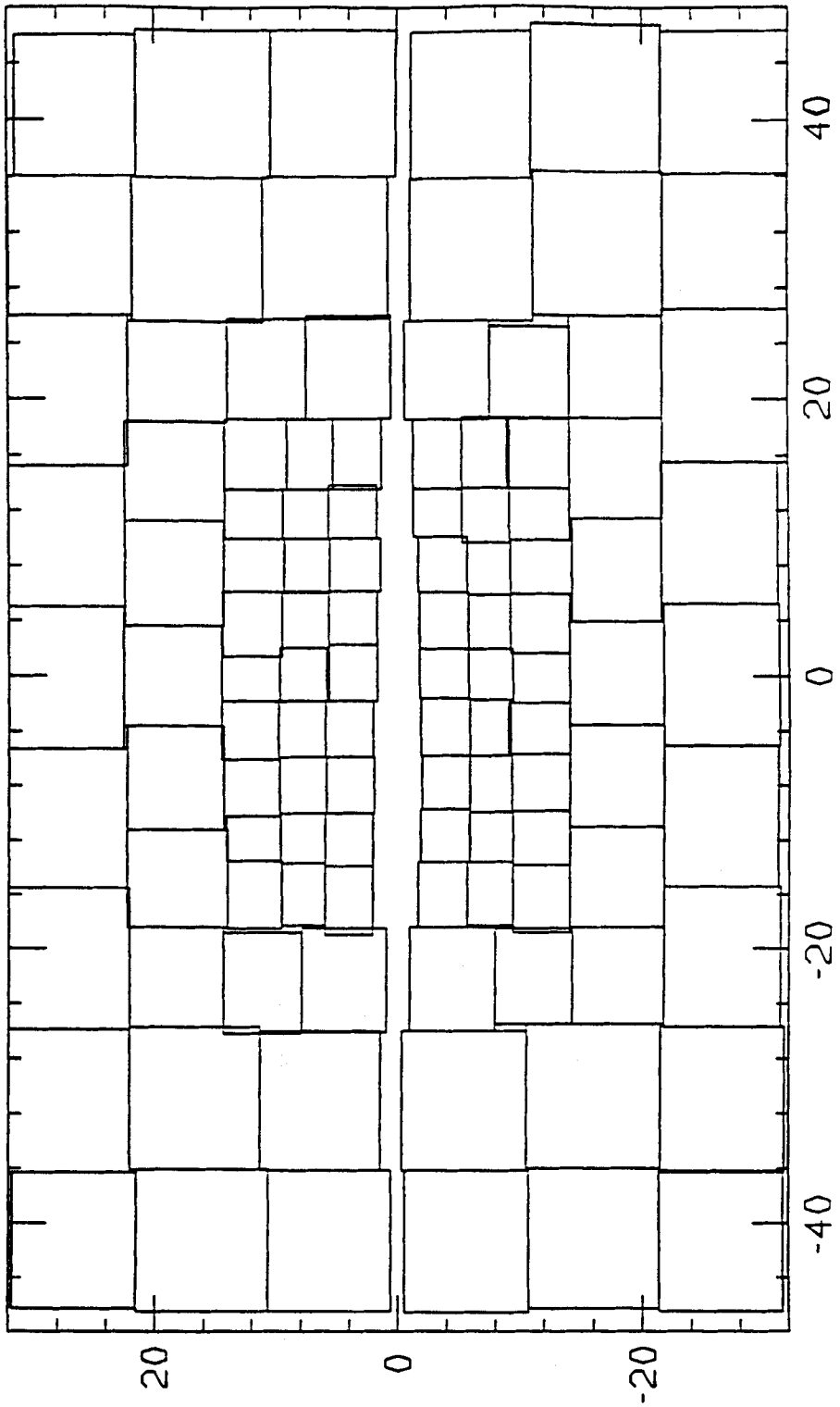

Figure 2.10: C2 Final geometry obtained with the J.P.D. method

The results of the phographic survey were used mainly for the outer cells, where you can not apply the J.P.D. because of low calibration statistics.

The photoelectron yield for the 2-inch cells ranged from 8 to 16 with an average value of 11 photoelectrons. For the 5-inch cells, the yield varied from 5 to 13 photoelectrons with an average value of 8 photoelectrons.

A second procedure was implemented in order to estimate the number of photoelectrons for the cells. This procedure consisted of studying the ADC distributions for the 110 cells. For any given cell the raw pulse height was obtained. Then the raw pulse height was divided by a term (less than 1) that measured the amount of overlap between the light cone and the cell. Thus the average pulse height if the light cone were fully contained in the cell is equal to the average raw pulse height divided by the fraction of overlap (α). The average pulse height $< PH >$ corrected for overlap is given by:

$$< PH >= \frac{< PH_{raw} >}{\alpha}$$

(For all the events there was a condition that the pulse height had to be above pedestal). In order to obtain the average pulse height for events due to one single photoelectron ($< PH_1 >$) the fraction of overlap α was estimated. For this case α has to be very small (0.03)

The average photoelectron $< n_{pe} >$ yield for a given cell is obtained from the following relation:

$$< n_{pe} >= \frac{< PH >}{< PH_1 >}$$

The results for finding the photoelectron yield by this method and the J.P.D. method were compared. The ratio for the photoelectron yield obtained by these two methods is shown in Fig. 2.11. One concludes that the agreement between the two methods was fairly good.

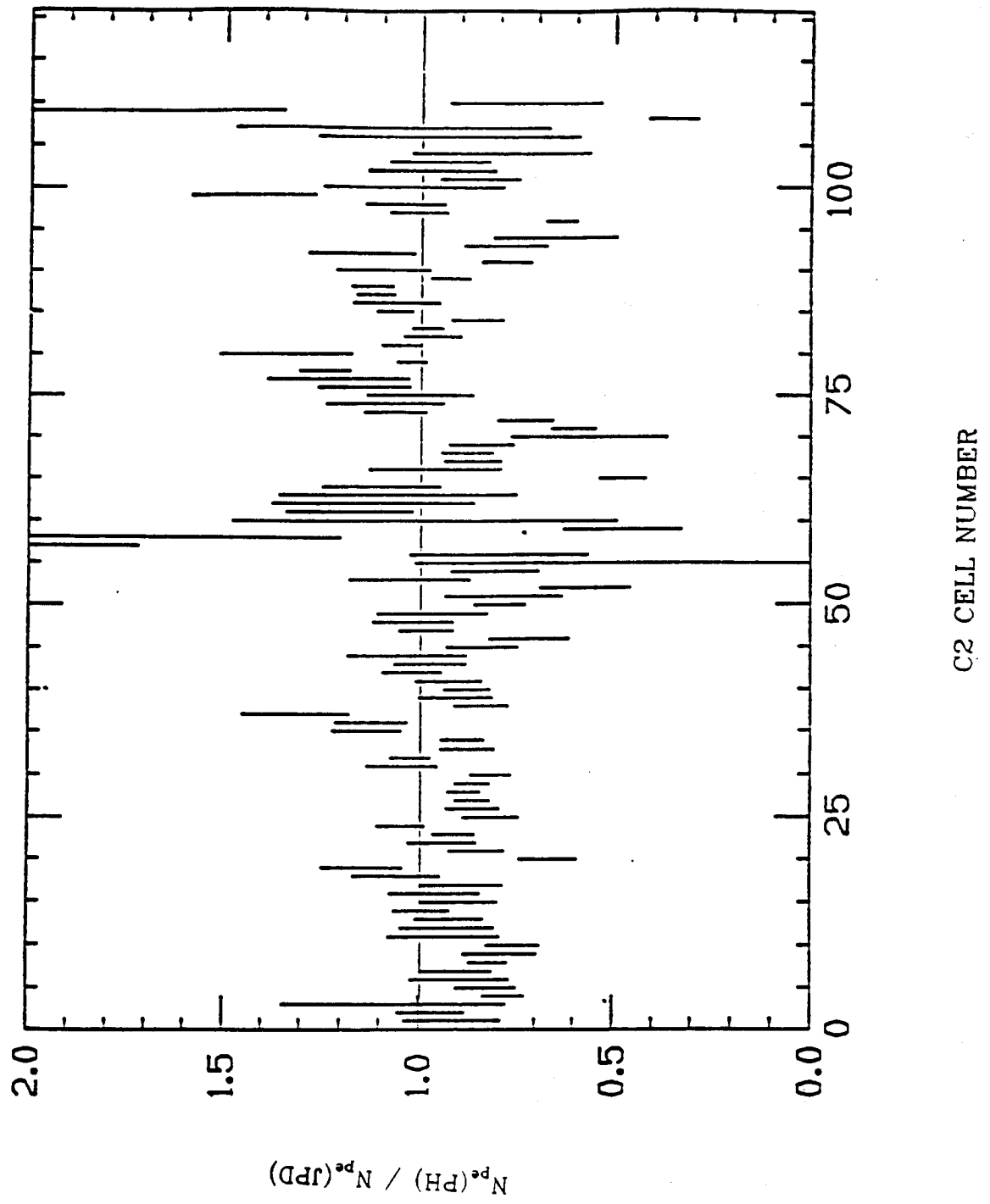

Figure 2.11: Ratio for the photoelectron yield obtained by the pulse height analysis to the photoelectron yield obtained by the J.P.D. versus the cell number for C2 (110 cells)

2.7.3 C3

This counter is located between the MWPCs P3 and P4. C3 is a helium threshold counter with a pion threshold of 17 GeV. The length along the beam direction is 277 in. with an aperture of 60 in. x 93.25 in. C3 operated with 100 spherical glass focusing mirrors. The photoelectron yield for all the cells ranged from 3 to 17 with an average of 9.

2.8 Muon System

There were two sets of muon counters [19]. Each set was an array of vertical and horizontal gas proportional and scintillator tubes. One set was designed for detecting muons produced at wide angles (up to 125 mr) and was located downstream of M2. The other set was designed to detect muons produced at less than 40 mr and was located downstream of the muon filter steel. The muon system is not used in this analysis. These counters are shown in Fig. 2.12.

2.9 Calorimetry

The photon-electron identification for E687 is provided by two electromagnetic calorimeters. Both are lead-scintillator calorimeters: the "Inner Electromagnetic" or IE calorimeter covering the small-angle region; and the "Outer Electromagnetic" or OE calorimeter covering the wide-angle region up to about 150 mrad.

The neutral hadron identification, and lepton-hadron separation is done by the Hadron Calorimeter (HC), which is also used for triggering purposes. The hadron calorimetry covers only the inner region. This region is covered by two separate devices. The HC, located downstream of the inner electromagnetic calorimeter, is an iron gas sampling calorimeter (8 interaction lengths) which covers the region from

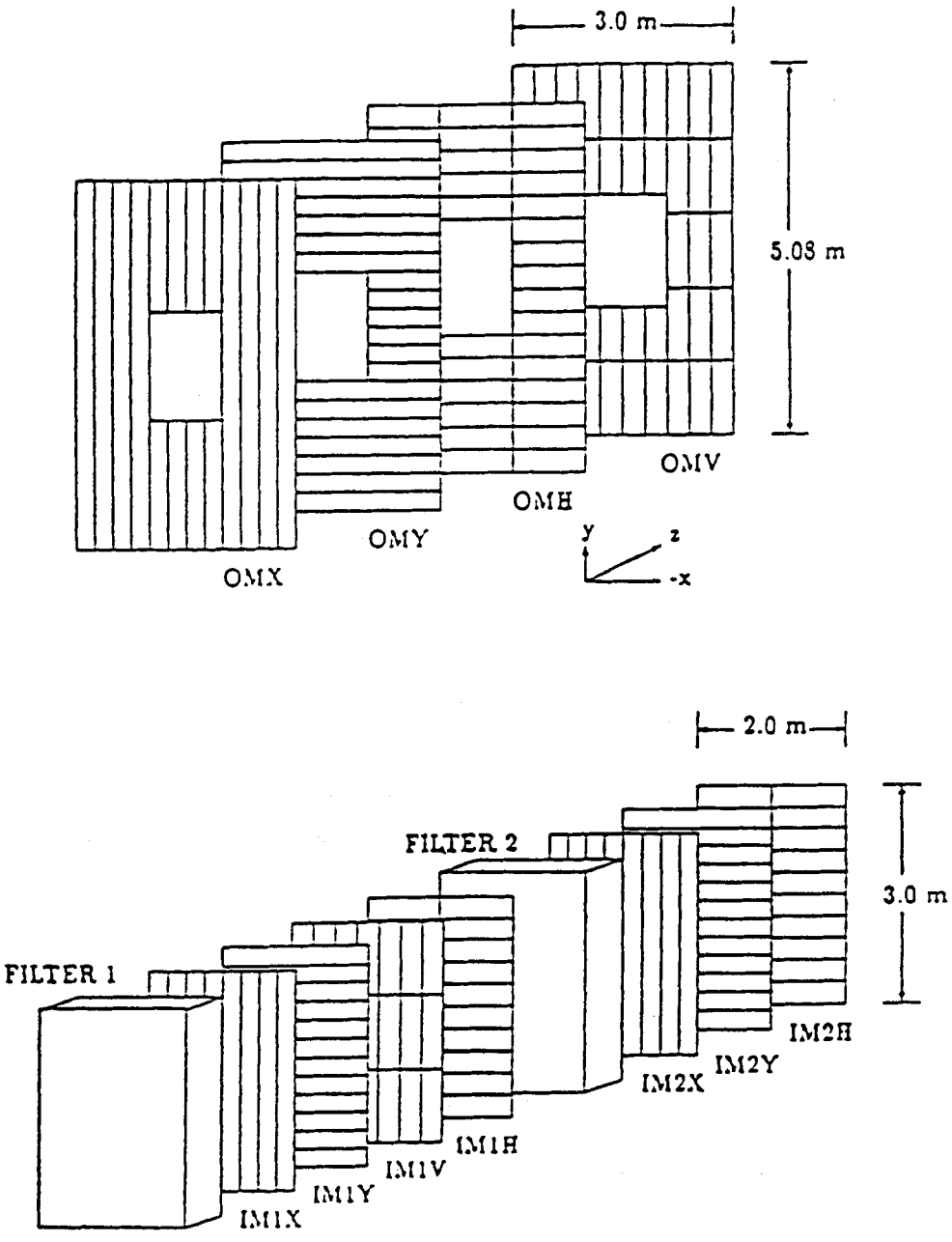

Figure 2.12: The E687 Muon system

5 mrad to approximately 30 mrad. The "Central Hadron Calorimeter" (CHC) is a uranium-scintillator calorimeter (6.4 interaction lengths) that covers the forward +/- 5 mrad beam hole through the HC. [20].

2.10 Trigger System

The trigger was designed to include almost all the hadronic events, and to reject pair production and low energy photon events. The trigger is organized into two levels. The first level trigger or Master Gate is a simple interaction trigger. The required logic can be written as

$$MG = (TR1 \cdot TR2) \cdot \{(H \times V)_{2body} + OH \cdot (H \times V)_{1body}\} \cdot \overline{(A0 + TM1 + TM2)}$$

where the logical names represent hits in the corresponding counters. (See Fig. 2.13.) The requirement of the coincidence of TR1 and TR2 insured the presence of at least one charged particle downstream of the target. Two arrays of scintillator counters, HxV located behind P4, and OH located just in front of OE, provided the logic for the requirement of at least 2 charged particles in the spectrometer. The OH logic signal was the simple OR of all the OH counter signals. The signals from the HxV counters formed 2 logic signals $(HxV)_1$ indicating hits of HxV by at least one charged particle and $(HxV)_2$ by at least two charged particles. The trigger also included veto counters to reject events contaminated by incident charged particles and muons. Signals from the A0 counter, upstream of the target, indicated the presence of charged particles in the photon beam. The signal (TM1 + TM2) indicated halo muons. A typical rate of the master gate trigger was 4×10^5 per spill with 1.5×10^8 photons (with energy greater than 133GeV) per spill in the target.

The second level trigger selected events to be written to magnetic tape. The triggers were derived from logical combinations of the signals from various detectors. The

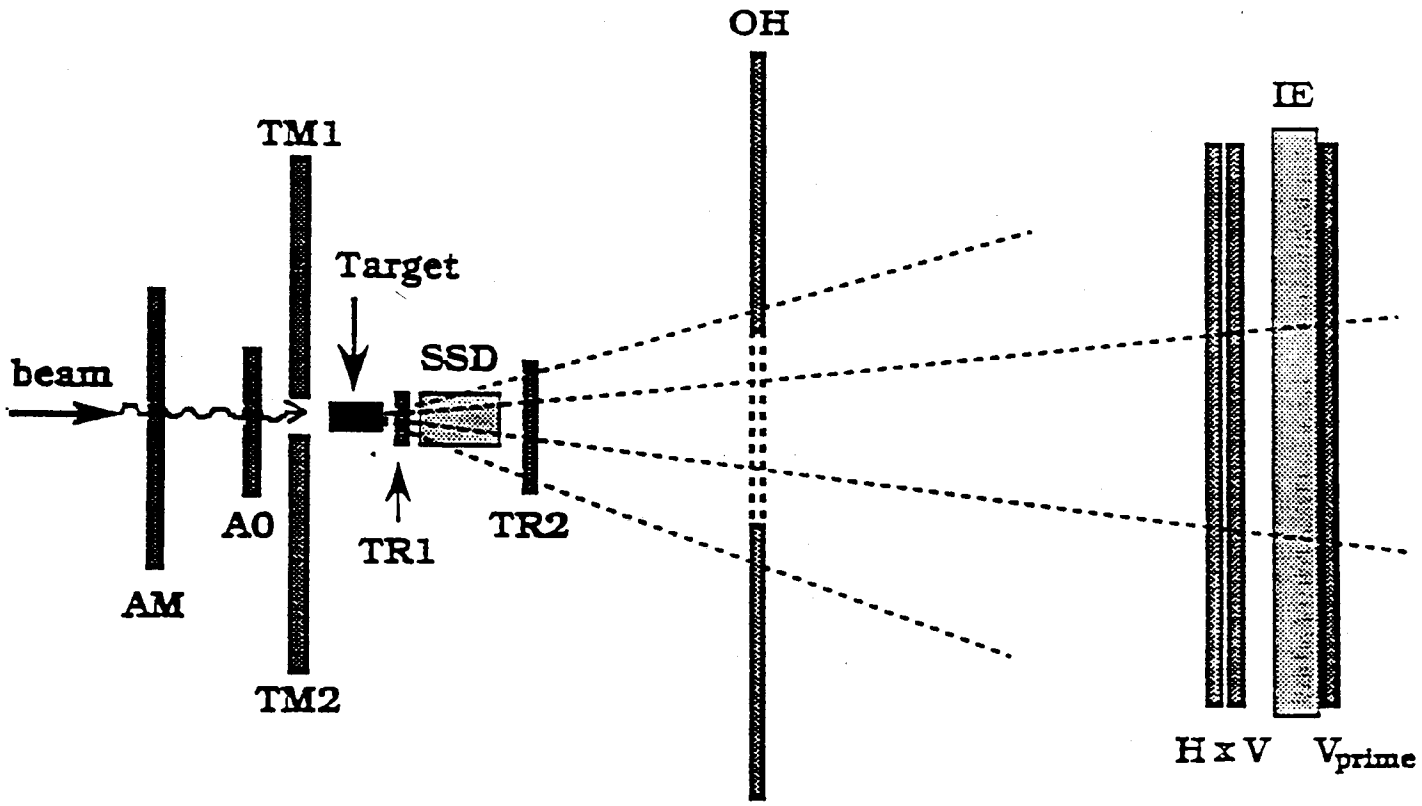

Figure 2.13: Target region detectors (Courtesy of Byung Gu).

logic modules were strobed by a master gate signal, and a logical decision was made within 1μs after the master gate. The main trigger for the 1987-1988 run which typically selected 80% of the data was called the "energy trigger" . This trigger required that the following three logical signals (called buslines) be set: EHADM(busline 18) which was set when the total energy detected by the hadron calorimeters (HC and CHC) was greater than a threshold, typically 35 GeV; RESHL (busline 3) which was set when the total energy of photons measured by RESH was greater than the minimum measurable energy, 138 GeV; and busline 23 which was a logic requirement of hits outside the center region (pair region) of P0 to ensure that at least one charged particle which was not a pair particle passed through the PWC system. Typically, 1500 events per spill satisfied the second level trigger and were written to magnetic tape.

2.11 Data Acquisition

After the interaction of the photon beam with the target, the signals from the different detectors were read out. The TDC's recorded signals from the PWC's, the Fastbus ADC's recorded signals from the calorimeters and Cerenkov counters, and the MIDA ADC's recorded the pulse heights from the SSD strips. The latches recorded hits from the trigger counters, muon counters, and the logic signals of buslines. (See Fig. 2.14.) If an event satisfied the first level trigger, a master gate signal was generated to start the digitization of the signals. The generation of this master gate occurred about 300 ns after the photons interacted with the target. Generation of the next master gate was inhibited for about 1μs. If during this 1 μs a second level trigger was not generated, then the electronics were cleared. If a second level trigger was generated, then the digitized signals were read out and stored in LeCroy 1892 Fastbus Multiple Record Buffer Memory. A PDP 11/45 computer read the Fastbus memories and

wrote the data to 9 track magnetic tapes. A VAX 11/780 controlled the PDP 11/45 through a DR11W link and controlled the read-out electronics through a MicroVax II computer which communicates with the CAMAC branch where most of the readout electronics reside.

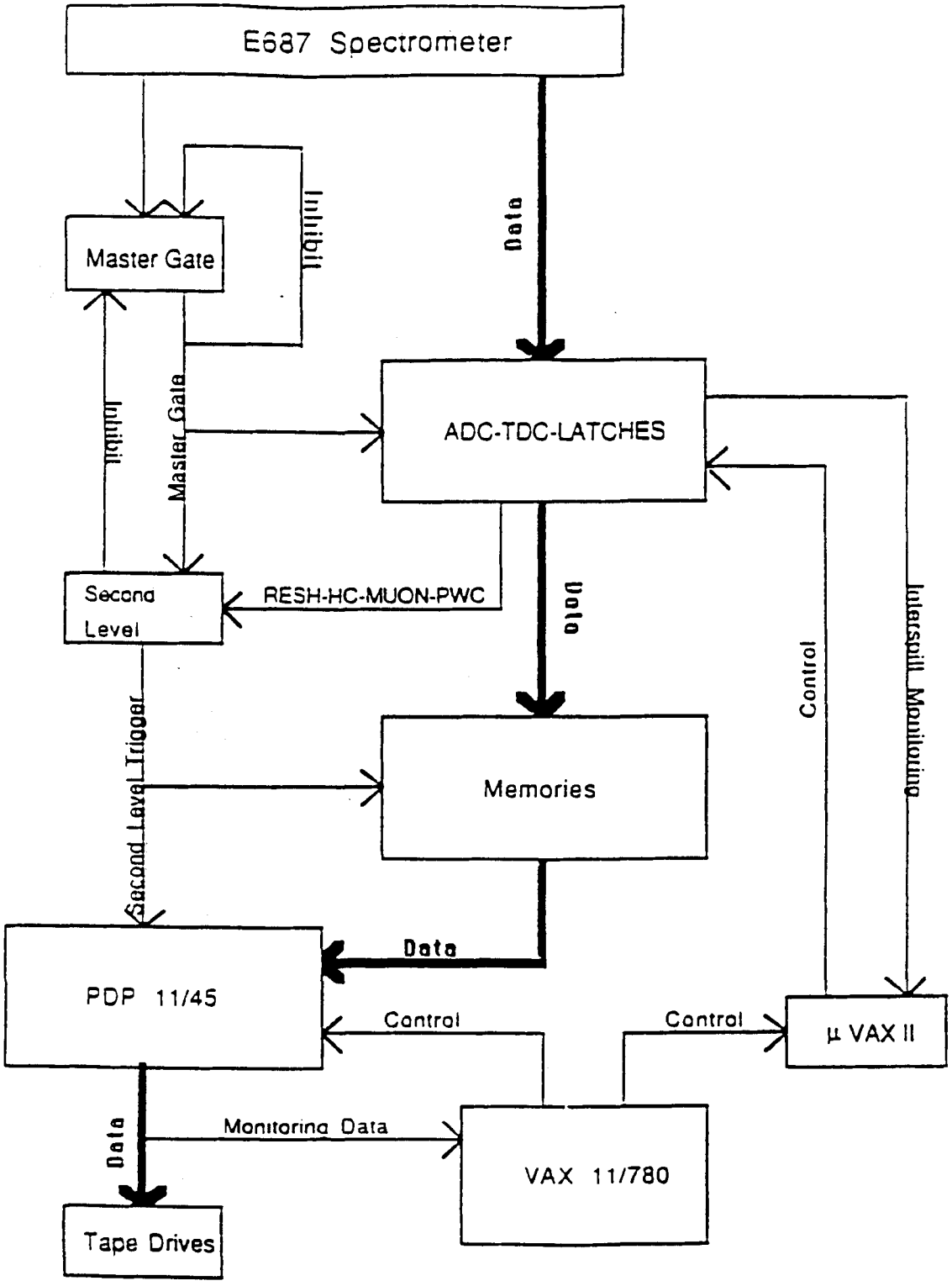

Figure 2.14: Data acquisition system for E687 (Courtesy of Eric Mannel).

CHAPTER 3

DATA RECONSTRUCTION

3.1 Introduction

In E-687 the analysis of the raw data was done by a set of reconstruction programs called "PASS1". The analysis included: SSD track reconstruction; PWC track reconstruction; vertex reconstruction; linking of PWC and SSD tracks; particle identification by the Čerenkov and muon analysis; Vee analysis; and calorimetry . All the "post-fire" raw data tapes were analyzed by PASS1. The program ran on the ACP (advance computer program) machines at Fermilab from April of 1989 to October of the same year. About 80 percent of all the events analyzed were successfully reconstructed. In this chapter a brief description of the reconstruction analysis needed for the $K\overline{K}\pi$ studies is given. The muon, Vee, and calorimeter analyses were not used in this thesis, but references can be found in ref. [16]

3.2 SSD Reconstruction

The microstrip tracking algorithm is based on projection-finding in the three separate views. The first step in the SSD reconstruction is the analysis of hits in the microstrip planes. Projection-finding is then performed, respecting a hierarchy in projection finding, namely: hits on the 3rd and 4th stacks already used to reconstruct a projection track with 4 hits cannot be used for a projection track with less hits. For

all other configurations, sharing of hits among several tracks is fully permitted.

The projections are formed into tracks if they match in space and have a global χ^2 value per degree of freedom lower than 8. Among all the tracks which share the same i projection, the best is selected on the basis of the χ^2 value. The same selection is performed among the tracks which share the same j projection.

The hits not associated with any reconstructed space track are used to search for wide angle tracks and highly multiple-Coulomb scattered tracks. The resolution for a given track with all hits in the high resolution strips of the SSD detector extrapolated to the center of the target is found to be:

$$\sigma_x = 11\mu m \sqrt{1 + \left(\frac{17.5 GeV/c}{P}\right)^2} \tag{3.1}$$

$$\sigma_y = 7.7\mu m \sqrt{1 + \left(\frac{25.0 GeV/c}{P}\right)^2} \tag{3.2}$$

where the second term in the square root is the contribution due to multiple scattering. [23], [24].

3.3 PWC Reconstruction

The PWC tracking algorithm is used to reconstruct tracks with hits in 3, 4, or 5 chambers. In each case a track is required to have hits in the first chamber, P0. A detailed description of the algorithm can be found in [16].

Initially projections are formed from hits in all four views. In the U, V, and Y(bend) views, projections are made using information from the PWC system alone. In the X(non-bend) view, hits are first formed from a seed from the SSD by searching for PWC hits which match the SSD tracks extensions. Tracks are formed by matching all four projections.

After all tracks containing an SSD-extended projection are found, then X-projections are constructed solely from the PWC hits which have not been used already. These X-projections are then matched with unused U,V, and Y projections to form additional tracks.

A least squares fit is performed on all candidate tracks. The fit parameters are the intercepts and slopes of the track in both the X and Y views at the M2 bend plane, and in the case of five chamber tracks, the change in slope in the Y view (bend angle) between the track segments upstream and downstream of M2. A χ^2/d.o.f cut is applied to each track to pass the fit. Tracks were not permitted to have more than 4 missing hits among all the chambers, nor more than 2 missing hits in any one chamber. A particle that passed through 5 PWC's is called a TRACK, while a particle that passed through 3 PWC's (P0, P1, and P2) is called STUB.

3.4 Linking and Momentum Analysis

Linking of SSD tracks and MWPC tracks is done by matching extrapolations at the center of M1. The parameters that are matched are the x, y positions and the slope in x. A least squares fit was performed over the matching tracks using microstrip and MWPC hits. The links were selected after they pass a global χ^2/d.o.f cut. [25]

The momentum of a track is found from the bending angle though the magnets. For a five chamber track the momentum is calculated by the bend-angle in M2. For tracks passing only through M1, the bend-angle was found using the track vertex information and the MWPC track parameters for the region downstream of M1.

The momentum resolution for a five chamber track, including corrections due to multiple scattering (the second term in the square root) is given by the following

relation:

$$\frac{\sigma}{P} = 1.4\% \left(\frac{P}{100GeV}\right) \sqrt{1 + \left(\frac{23GeV}{P}\right)^2}; \tag{3.3}$$

and for a three chamber track:

$$\frac{\sigma}{P} = 3.4\% \left(\frac{P}{100GeV}\right) \sqrt{1 + \left(\frac{17GeV}{P}\right)^2}. \tag{3.4}$$

3.5 Vertex Reconstruction

E687 had two independent vertex reconstruction algorithms. VERTIC, a stand-alone algorithm, uses microstrip tracks in an attempt to find a well defined vertex with the highest multiplicity and an acceptable χ^2. VERTIC was not used at all in this analysis (for information about this algorithm see reference [26]). DVERT, a candidate driven algorithm, was used for the whole $K\overline{K}\pi$ analysis. DVERT searches for charm decays into specified decay modes and was of vital importance in obtaining the $K\overline{K}\pi$ signal and in reducing the level of photoproduced background events. This algorithm finds the position of the primary vertex, the secondary vertex, the decay length and their respective errors. In the next subsection are given details about DVERT. [27]

3.5.1 Candidate Driven Vertex Algorithm

Candidate tracks used by the algorithm include tracks selected by criteria such as particle identification or invariant mass in a chosen region. Then with the full covariance matrix of each track, the decay vertex is found. If the confidence level of the decay vertex fit is less than 0.02 the candidate tracks are rejected. Otherwise the algorithm finds the track momentum vector for the "charm candidate particle", and uses this as a seed with other tracks in the event to find the primary vertex. The algorithm fits to the hypothesis of a common vertex the "charm candidate particle" and these other

tracks selecting one track at a time. The tracks that give a confidence level greater than 0.02 are kept in a list. The next step is to fit the charm candidate track with pairs of tracks from the above list, and the pair that gives the best confidence level is kept as the primary vertex. Then with the remaining tracks the algorithm adds one track at a time to the primary vertex and refits, keeping the track with the best confidence level as being part of the primary vertex. This procedure is done until the best confidence level found for a given track is less than 0.02. In order to find the distance L between the primary and secondary vertex, an impact parameter fit is done. DVERT also finds σ_L, the uncertainty associated with L, which is a measure of the precision with which the distance between the vertices is calculated. The distance L divided by its respective error σ_L is a normalized measure for the significance of separation between the two vertices. L/σ_L is used as a tool to reduce the background due to non-charm events. The variable L/σ_L is called ELSIG, and is used through whole $K\overline{K}\pi$ analysis. Non-charm background is also reduced by making cuts on the χ^2 /d.o.f for the decay vertex.

3.6 Particle Identification

The charged particle identification for E687 was carried out using the Čerenkov counters. A given track could be identified by the Čerenkov system as being consistent with an electron, pion, kaon, or proton hypothesis. Muons were identified by the muon system and the HC. Electrons were also identified by the outer and inner electromagnetic calorimeter. In this analysis only the Čerenkov algorithm was used in order to identify charged particles. A detailed explanation of the Čerenkov algorithm can be founded in [28] Following is a brief description of the algorithm.

First the algorithm establishes if the cells in a given Čerenkov counter are "on" or "off". This is done by checking the pulse height from the ADC's. If the pulse

height is above some threshold (beyond the pedestal) then the cell is called "on" Otherwise the cell is called "off". Next the "on-off" code for a given track in a given counter is determined. This is done by computing the amount of light expected in the intercepted cell and the adjacent ones, assuming the track is a pion. If the cells are "on" and the amount of light deposited in the cells is greater that some assigned value, then the track is flagged as "on". If the cells are "off" and some light was expected then the track is flagged as "off". When the track can not be flagged as "on" or "off", then it is flagged as "confused" (See Table 3.2 where the ITYP variable gives the "on", "off", and "confused" codes for the track). With the known pion, kaon, and proton threshold momenta for each counter, seven momentum regions, were defined in such a way that a given track with a given momentum fell in only one of these seven momentum regions. (See Table 3.1). Here pth, ptk, and

TABLE 3.1
ČERENKOV MOMENTUM REGIONS

Momentum region	Track off	Track on	track confused
p < pth	1110	0001	1111
pth<p< 1.08pth	1110	0011	1111
1.08pth<p< ptk	1100	0011	1111
ptk<p< 1.08ptk	1100	0111	1111
1.08ptk<p< ptp	1000	0111	1111
ptp<p< 1.08ptp	1000	1111	1111
ptp<p	0000	1111	1111

ptp are the threshold momenta for the pion, kaon and proton respectively. Note that

TABLE 3.2
ITYP CODE

ITYP	
1	off
2	on
3	confused
4	out of fiducial volume
5	do not know
15	confused

there is a region defined between the real threshold and the real threshold times 1.08. This is done because a track does not emit a detectable amount of light when it is exactly at the Čerenkov threshold, and very little light is expected when it is not far above the Čerenkov threshold.

The factor of 1.08 is determined from Monte Carlo studies and defines the effective threshold of a Čerenkov counter. These seven momentum regions are defined in order to avoid misidentification near the threshold region, and also to decrease the number of tracks to which the Čerenkov algorithm assigns inconsistent information.

Once the on-off code for a track is determined and compared with the track's momentum region, then a 4-bit status word is set that gives the particle identification as follows:

No bits on : indeterminate

Bit 1 is on : Consistent with being an electron.

Bit 2 is on : Consistent with being a pion.

TABLE 3.3
ČERENKOV PARTICLE IDENTIFICATION CODES

ISTATP	Identification
0	Inconsistent
1	e definite
2	π definite
3	e,π ambiguous
4	K definite
6	π,K ambiguous
7	e,π, K ambiguous
8	p definite
12	K,p ambiguous
14	π,K,p ambiguous
15	confused

Bit 3 is on : Consistent with being a kaon.

Bit 4 is on : Consistent with being an proton.

In order to obtain the final particle identification, the logical AND of the Čerenkov status words for the three detectors is taken, and the result is given by the status word called ISTATP. In Table 3.3. are shown the ISTATP values with the respective particle identification, and in Table 3.4 is shown the array IND. IND is the particle

TABLE 3.4
THE VALUES OF IND(IPR,ITYP)

Momentum region IPR	ITYP				
	1	2	3	4	5
1 (p < pth)	14	1	15	15	15
2 (pth<p< 1.08pth)	14	3	15	15	15
3 (1.08pth<p< ptk)	12	3	15	15	15
4 (ptk<p< 1.08ptk)	12	7	15	15	15
5 (1.08ptk<p< ptp)	8	7	15	15	15
6 (ptp<p< 1.08ptp)	8	15	15	15	15
7 (ptp<p)	0	15	15	15	15

identification of a track for a given counter (ISTATP is determined from the values of IND for all three counters). IND(IPR,ITYP) has two indices. IPR specifies the momentum region in which the track momentum falls, and ITYP gives the on-off code for a track. The performance of the Čerenkov algorithm was evaluated using data and Monte Carlo. In order to evaluate the identification of pions and protons a sample of photoproduced $\Lambda_c D^0$ events was generated using the E687 ROGUE Monte Carlo program (see ref [29], [30]). The Λ_c was made to decay into $\Lambda_0\pi$ and then the Λ_0 decays to $p\pi$. The D^0 decays to ϕK^0_s followed by ϕ to K^+K^- and K^0_s to $\pi^+\pi^-$. All decays were generated according to the PDG lifetimes [7]. The sample was passed through the full reconstruction program. In Table 3.5 are shown the results for the comparison of pions from K^0_s decay in data and in Monte Carlo. The label "H" stands for heavy. This means that the track was identified as a kaon or/and proton. The pion-consistent category is when the second bit of ISTATP is set. In Table 3.6 are shown the results for the comparison of protons from Λ^0 decay in data with Monte Carlo events. The efficiency in the identification of kaons was measured on data. Using the decays $\phi \rightarrow K^+K^-$ and $D^{\pm} \rightarrow K^{\mp}\pi^{\pm}\pi^{\pm}$, the overall identification efficiency

TABLE 3.5
ČERENKOV ID OF PIONS FROM K^0_s decay

Topology	ID	Data	Monte Carlo
tracks	fraction of π consistent	0.90	0.90
tracks	fraction below C3 threshold with e ID	0.06	0.01
tracks	fraction above C2 threshold with H ID	0.03	0.04
stubs	fraction of π consistent	0.94	0.95
stubs	fraction below C1 threshold with e ID	0.03	0.002
stubs	fraction above C2 threshold with H ID	0.04	0.04

TABLE 3.6
ČERENKOV ID OF PROTONS FROM Λ^0 DECAY: FRACTION IDENTIFIED AS PROTON DEFINITE OR KAON/PROTON AMBIGUOUS

proton momentum(GeV)	Data	Monte Carlo
all	0.87	0.93
4.6-16.2	0.84	0.92
16.2-30.5	0.85	0.98
30.5-44.5	0.85	0.95
44.5-62.0	0.94	0.90

for a kaon coming from a ϕ was found to be approximately 80% and for a kaon coming from a D to be approximately 70%.

3.7 Data Reduction

The data collected during the 1987-88 run consisted of approximately 60 million triggers which were written onto 1200 9-track magnetic tapes. The data were reconstructed using the ACP system at Fermilab. About 45 million events were reconstructed by "PASS1".

In order to reduce this data sample to a more manageable level, and with several physics objectives in mind, a "SKIM" process (called SKIM 2) was done in which the

reconstructed data were reduced in the Fermilab AMDAHL machine. SKIM 2 ran from February 1990 through April 1990. The $K\overline{K}\pi$ data come from a "stream" of SKIM 2 called SKIMADEE (see ref. [31]).

The SKIMADEE algorithm searches for a variety of decay modes of the D^+, D_s, D^* and D^0, whose products include $K^\pm$, K_s and π. An event is selected if a D meson candidate can be formed with an invariant mass in a given range and, except in the case of the D^*, if it has good primary and secondary vertex separation as determined by DVERT.

The SKIMADEE substream wrote out approximately 400 tapes. It was necessary to reduce the data sample further for a more special analysis. A subskim was implemented selecting events with two kaons and a pion in the final state. The two kaons were required to have an ISTATP of 4,12 or 7($p > 60$ GeV), and the pion was required not to be a "heavy" (an ISTATP of 2,3,7,14,or 15). The subskim also required $L/\sigma_L > 1$ and that the χ^2/d.o.f for the decay vertex be less than 3.

With these sub-skim criteria 40 tapes were written out, with a total of 554,347 events. In order to speed the time of mounting tapes these 40 tapes were reduced to 5 tapes using a DST (data summary tape) format where only the necessary information for the analysis was written to tape.

CHAPTER 4

$K\overline{K}\pi$ DATA ANALYSIS

The analysis of D and D_s mesons decaying to the final state $K\overline{K}\pi$ is the subject of this chapter. Besides the requirements mentioned in section 3.7 regarding the $K\overline{K}\pi$ event selection criteria, more requirements are added. A detailed analysis of the data sample is described where the vertex and Cerenkov analyses play very important roles. Dalitz plot analyses for the D and D_s are presented and methods used to remove unwanted sources of backgrounds from the data are described. The efficiency and background studies are also presented. Finally the contamination due to $K\overline{K}\pi$ events is studied.

4.1 Introduction

In a charm production experiment it is of vital importance to be able to resolve the primary and decay vertices. It is a well separated decay vertex that allows one to distinguish real charm events from background events.

As discussed in section 3.5, the vertexing routine used in this analysis is the candidate driven vertex algorithm, DVERT. The first requirement in vertexing was to require that DVERT succeeded. The routine fails if: there were no good tracks; there were not enough good tracks; the tracks were not consistent with forming a primary vertex; or a D candidate track was not good. DVERT also requires that the

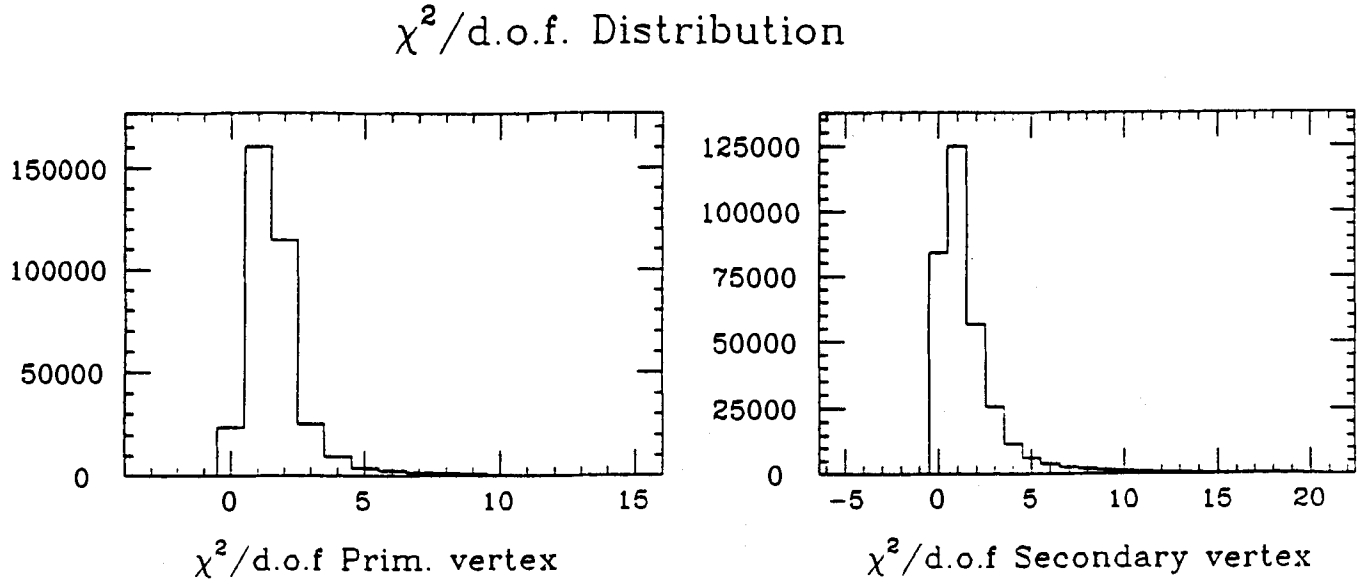

Figure 4.1: χ^2/d.o.f Distribution for the primary and the secondary vertex

D candidate tracks are linked.

Some of the variables returned by DVERT are plotted in Fig. 4.1. These variables will be used as tools for reducing the combinatorial background and to obtain signals for further study. In Fig. 4.1 is shown the χ^2/d.o.f for the primary and secondary vertices. These distributions peak near one as expected, and the tail observed is due primarily to background events. From studies done on the data, it was determined that a cut on the χ^2/d.o.f for the secondary vertex is much more powerful than one for the primary vertex in reducing background.

After DVERT succeeds in determining a primary and secondary vertex, the separation between the two vertices was studied. As mentioned in section 3.5, in order to reduce background and keep signal events, a cut on the L/σ_L ratio was applied. Typically, higher values for the L/σ_L cut reduced background, but at the expense of some signal events. In Fig. 4.2 is shown the distribution for L, the error σ_L and the

ratio L/σ_L. In order to assure that the primary vertex is located in the target region, the z coordinate of the primary vertex was required to be less than zero. Similarly the secondary vertex has to be inside the target region. In Fig. 4.3 are shown the distributions for the x, y, and z coordinates for the decay vertex. It is interested to note that the z coordinate distribution for the secondary vertex peaks below zero, but has a certain number of events above zero. Those events are due to secondary interactions that occur in the scintillator counter TR1 (See Fig. 2.13). Also shown in Fig. 4.3 is the primary vertex track multiplicity determined from the microstrip detector. The track multiplicity peaks around 8 tracks per event.

4.2 Rogue Monte Carlo

The Monte Carlo program used in this analysis was the E687 Monte Carlo package called "ROGUE". The package was developed at the University of Illinois and consisted of two parts; one for the event generator and another one for the spectrometer simulation. The part of the Monte Carlo program that did the event generation is called "GENERIC". The charm particles were produced according to the Photon-Gluon-Fusion model. GENERIC also created background events including electron pairs. Once the selection for the final state was made and the detector response was selected, ROGUE produced a Monte Carlo data tape that was similar to a real data tape. In this way Monte Carlo data could be analyzed by the same routines as the real data [32].

4.3 The $K\overline{K}\pi$ Signal

As mentioned earlier the vertex and Cerenkov analyses were the main tools used in order to obtain the $K\overline{K}\pi$ signal. In order to reduce the amount of data to analyze, the invariant mass for $K^{\pm}K^{\mp}\pi^{\pm}$ decay channel was required to be within $\pm$ 200 MeV/c^2

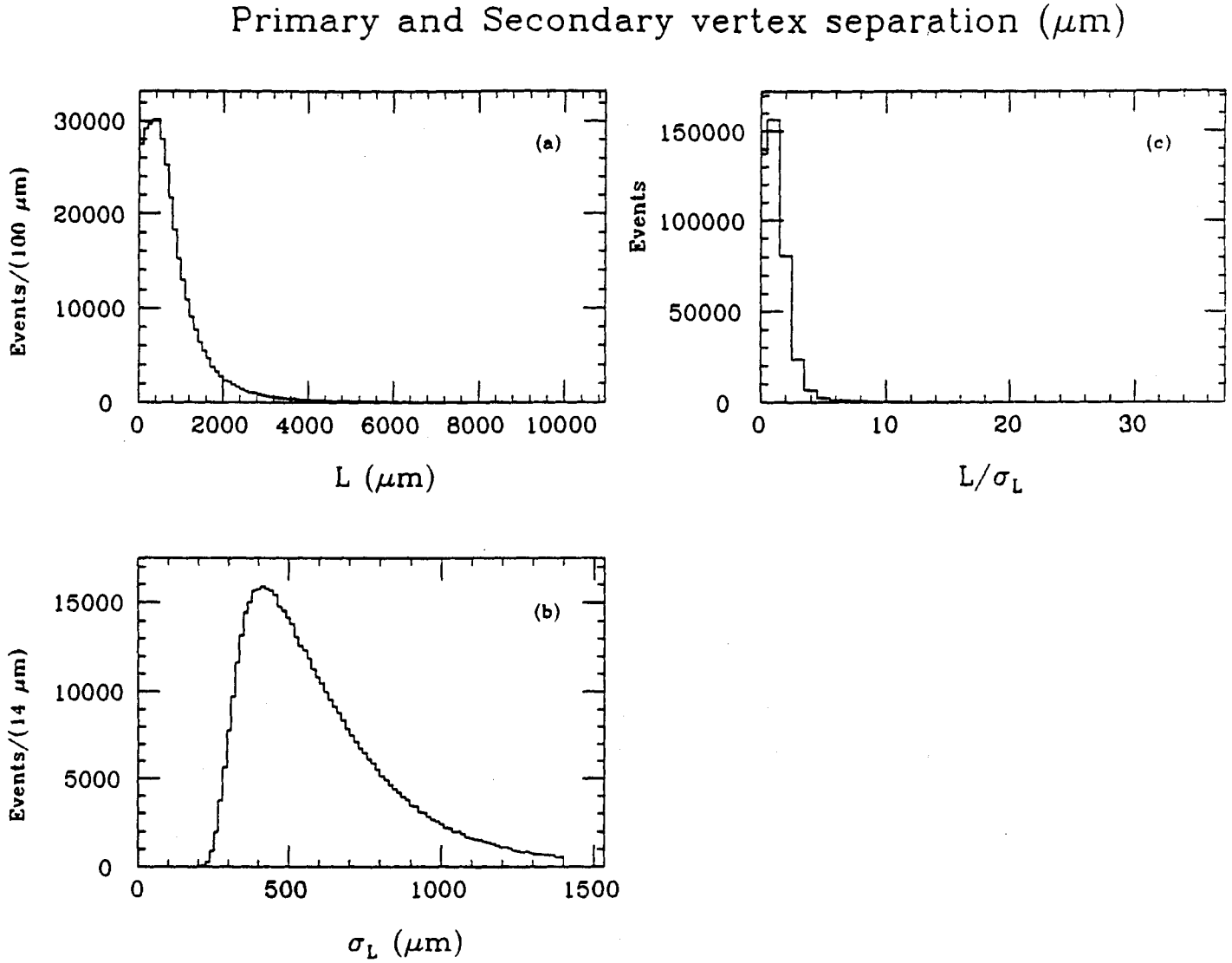

Figure 4.2: Separation between the primary and secondary vertex: a) the separation L, b) the error in L, c) the ratio of L and σ_L

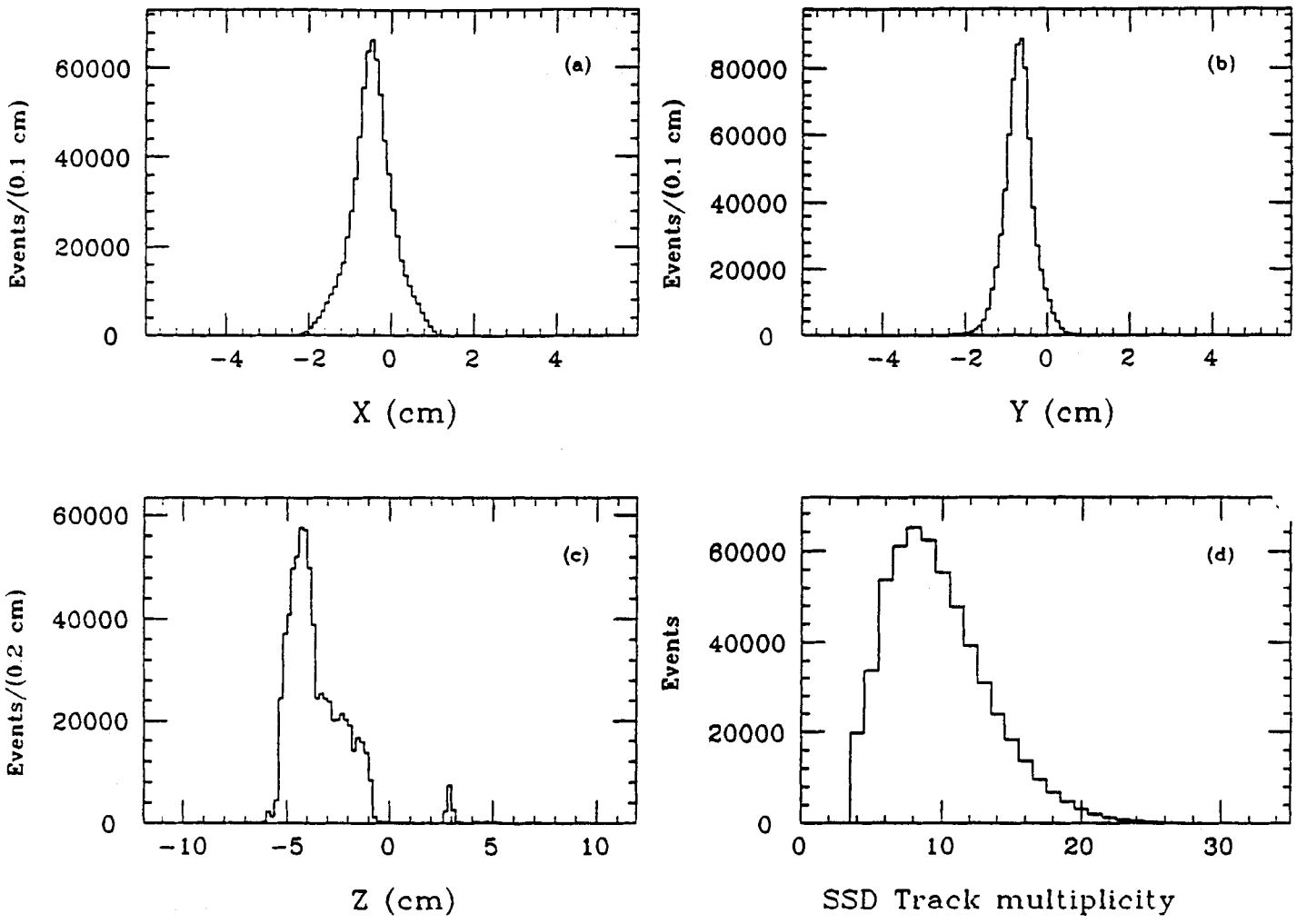

Figure 4.3: Distributions for the decay vertex coordinates: a) X, b) Y, c) Z. Distribution for the SSD track multiplicity: d)

of the nominal $D^{\pm}$ mass.

The D candidate was required to consist of three tracks with two kaon-consistent tracks and one pion-consistent track. "kaon-consistent" means that the track identified by the Cerenkov analysis could be a definite kaon, a kaon/proton ambiguous track, or a kaon/pion/electron ambiguous track with a momentum greater than 60 GeV. The corresponding ISTATP categories for the kaon-consistent definition is 4,12, or 7 (momentum greater than 60 GeV). There is also the charge balance requirement on the kaons: one kaon must have a positive charge and the other one a negative charge.

The pion-consistent definition assigned to a track means that the track identified by the Cerenkov analysis can be a definite pion, a pion/electron ambiguous track, a pion/electron/kaon ambiguous track; or a pion/kaon/proton ambiguous track. Actually the pion-consistent definition for a track is everything but a "Heavy" or an electron, where the label "Heavy" is reserved for tracks being identified as definite kaons, definite protons or kaon/proton ambiguous tracks. The corresponding ISTATP category for the pion-consistent definition are 2,3,7,14,15. (See Table 3.2 for particle identification (id) codes). With these various requirements, the $K\overline{K}\pi$ signal was studied for several values of the decay vertex cut and several values of L/σ_L.

4.3.1 Selection of the Decay Vertex Cut

From studies done, it was found that the χ^2/d.o.f. cut for the decay vertex fit was much more powerful in reducing the background than the χ^2/d.o.f cut for the primary vertex.

The value chosen for the decay vertex cut was selected after a study done on the D and D_s signals. The aim was to select a value for the χ^2/d.o.f. cut for the decay vertex such that the background was reduced and there was an improvement in the

signal to noise ratio.

In Fig. 4.4 is shown the $K\overline{K}\pi$ signal when the χ^2/d.o.f. cut for the decay vertex fit is less than 3 and less than 2. In order to obtain the yield for the D and D_s the $K\overline{K}\pi$ signal was fitted with a Gaussian and the background with a second order polynomial. The signal region of integration was chosen from 1.850 GeV to 1.890 GeV for the D, and from 1.950 GeV to 1.990 GeV for the D_s The results of the fits for several χ^2/d.o.f. cuts and an L/σ_L cut greater than 7 are given in Table 4.1. In Fig. 4.5 are shown the results of the fits for the D and D_s as a function of the L/σ_L cut. It is interested to note that the yield for the D_s decreases faster than for the D. This is due to the fact that the D_s lifetime is shorter than the D lifetime. The yield for both signals decreases for higher values of L/σ_L. The yield for the D_s is more sensitive to the decay vertex cut, decreasing for lower values of this cut, while the yield for the D also decreases but not as significantly as for the D_s.

The background under the signal region for the D and D_s is also reduced when the value for the decay vertex χ^2/d.o.f. cut decreases. It is interested to note that the background under the D signal decreases faster than the Ds background for increasing values of L/σ_L. From the signal to background ratio plots for the D and D_s it is obvious that requiring the decay vertex cut to be < 2.0 considerably reduces the background, without losing much signal, and yields a better signal to background ratio.

4.3.2 Selection of the Kaon Particle Identification Definition

The selection of Cerenkov particle id. for the kaons was carefully studied. One of the sources of background to the $K\overline{K}\pi$ signal comes from the $D^{\pm}$ decaying to $K^{\mp}\pi^{\pm}\pi^{\pm}$, when one of the pions is misidentified as a kaon.

The selection of the kaon particle id. should be restrictive enough to avoid the

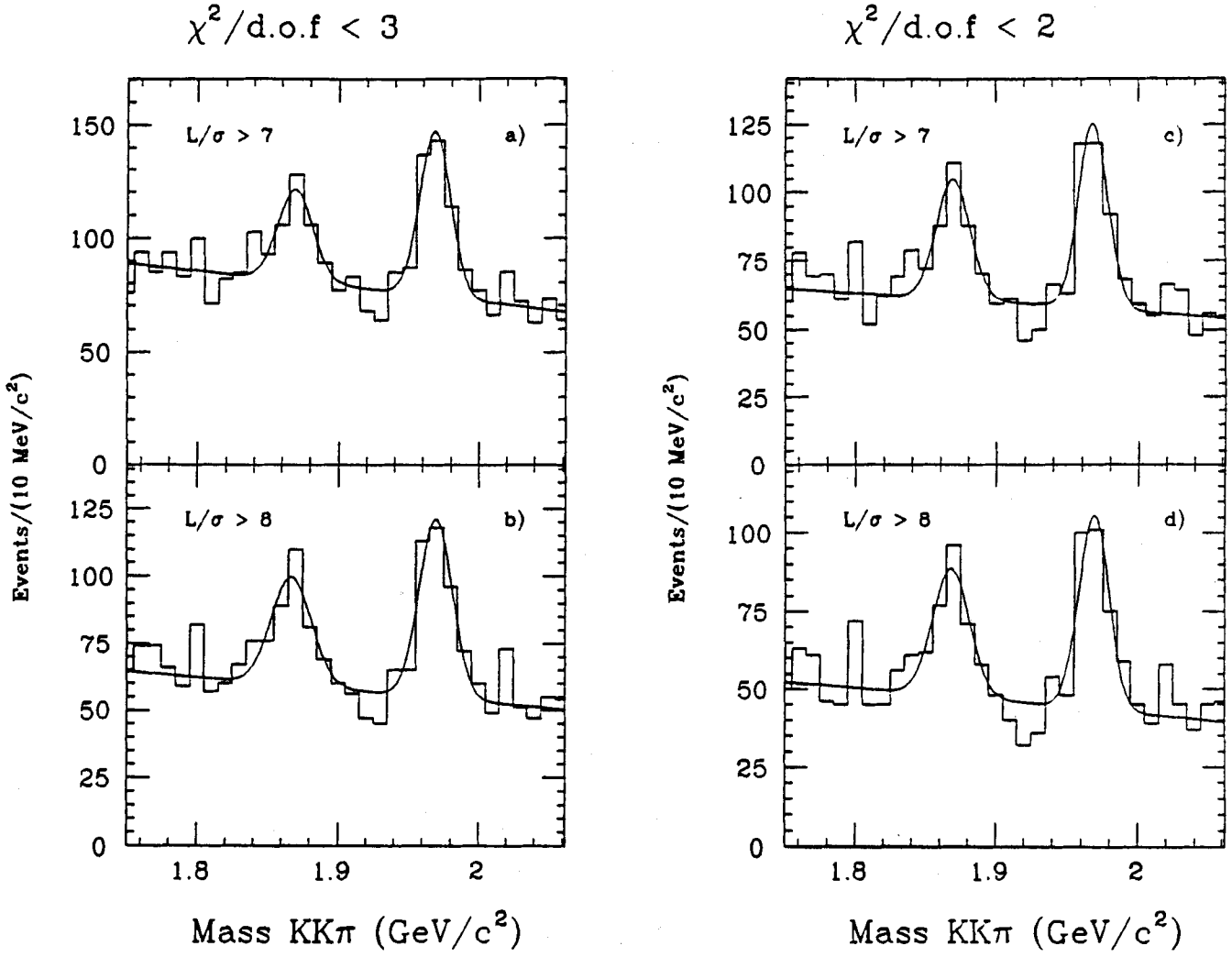

Figure 4.4: $K\overline{K}\pi$ invariant mass distribution for two different values of the decay vertex cut: a) χ^2/d.o.f < 3 and $L/\sigma_L > 7$, b) χ^2/d.o.f < 3 and $L/\sigma_L > 8$, c) χ^2/d.o.f < 2 and $L/\sigma_L > 7$, d) χ^2/d.o.f < 2 and $L/\sigma_L > 8$.

DECAY VERTEX CUT < 3.0: ⊹

DECAY VERTEX CUT < 2.5: ✦

DECAY VERTEX CUT < 2.0: ◇

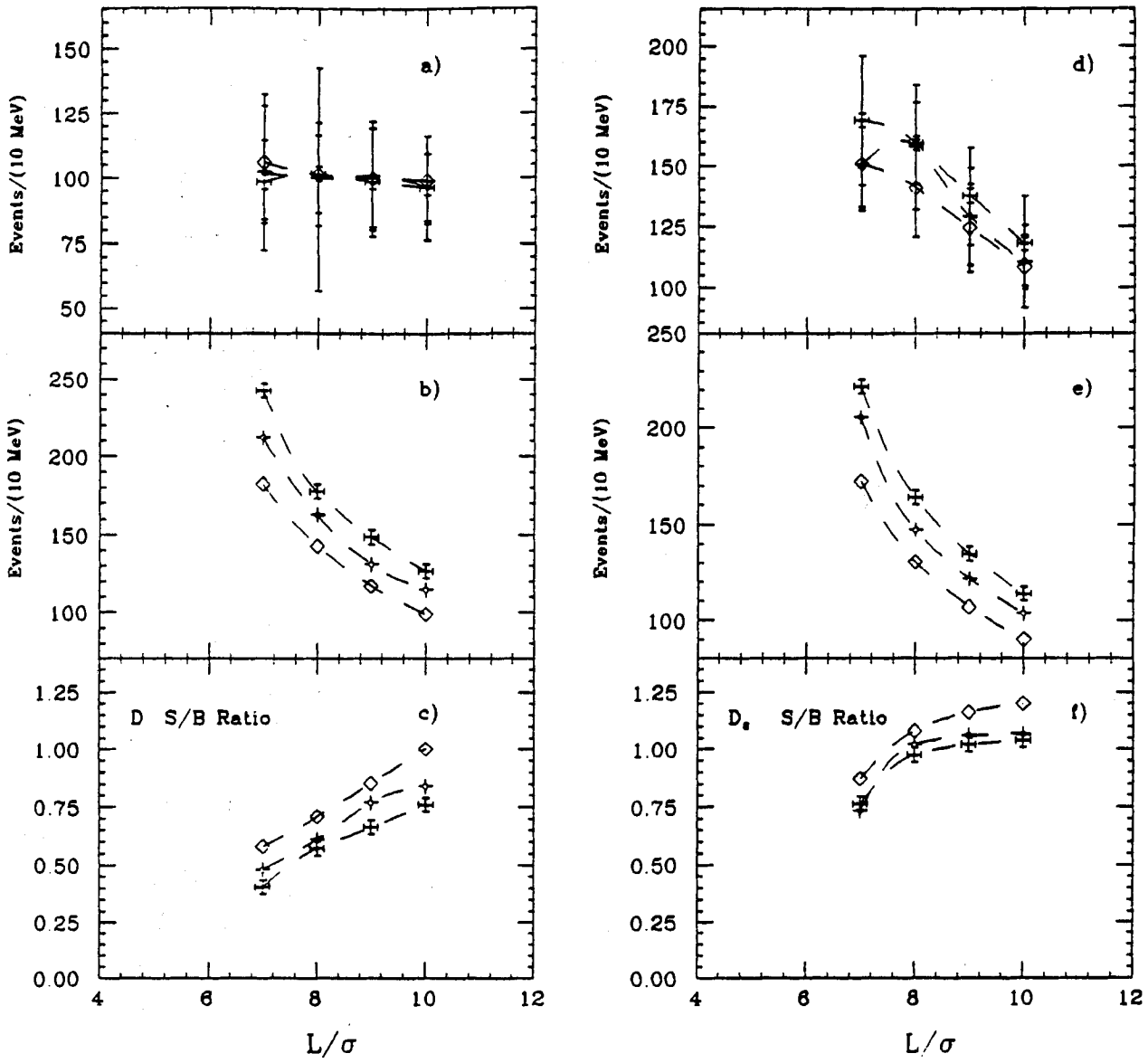

Figure 4.5: Results of the decay vertex studies: a) signal, b) background, and c) signal/background ratio for the D, d) signal, e) background, and f) signal/background ratio for the D_s

TABLE 4.1
FIT RESULTS TO THE $K\bar{K}\pi$ INVARIANT MASS DISTRIBUTION FOR SEVERAL CUTS TO THE χ^2/d.o.f FOR THE DECAY VERTEX AND $L/\sigma_L > 7$

	Mass (MeV)	Width (MeV)	Yield	s/b	χ^2/d.o.f
D	1869 ± 2	12.0 ± 3	99 ± 16	0.40	< 3.0
D	1869 ± 3	11.2 ± 5	102 ± 30	0.48	< 2.5
D	1869 ± 2	11.5 ± 3	105 ± 28	0.70	< 2.0
D_s	1968 ± 1	10.6 ± 1	170 ± 27	0.76	< 3.0
D_s	1968 ± 1	9.4 ± 1	150 ± 19	0.73	< 2.5
D_s	1968 ± 1	9.7 ± 1	150 ± 17	0.87	< 2.0

misidentification problem and at the same time to avoid as much as possible a decrease in the signal.

In Fig. 4.6 are shown the $K\bar{K}\pi$ invariant mass distributions for the three following kaon particle id. definitions used:

- case a) Both kaons must be kaon-consistent. The ISTATP assignment is 4,12 or 7(momentum greater than 60 GeV) for both kaons.
- case b) The kaon with the same sign as the pion must be a kaon-definite. The ISTATP assignment is 4 or 12. The other kaon can be kaon-consistent, with an ISTATP of 4,12, or 7 (momentum greater than 60 GeV)
- case c) Both kaons must be kaon-definite. The ISTATP assignment is 4 or 12.

As was the case in selecting the best value for the χ^2/d.o.f. for the secondary vertex cut, the signal was fitted with a Gaussian and the background with a second order polynomial using the same interval of integration for the D and D_s. In Fig. 4.7 is plotted the yield, the background and the signal to background ratio for the D and D_s signals. It is important to note the difference in the yields for the D_s for cases a) ,b), and c). The large difference in the signal is mainly due to the pions from the

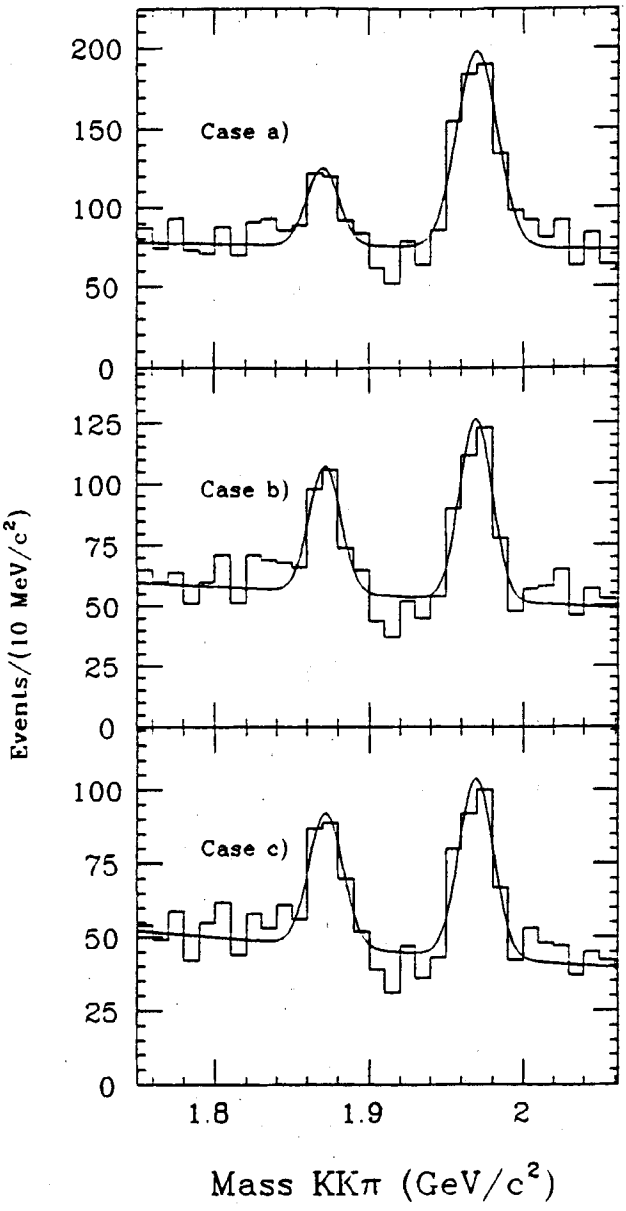

Figure 4.6: $K\bar{K}\pi$ invariant mass distributions for an $L/\sigma_L > 7$ for the following cases: a) both kaons are kaon-consistent, b) the kaon with the same sign of the pion is kaon-definitive, and the other kaon is kaon-consistent, c) both kaons are kaon-definitive.

BOTH KAONS ARE KAON−CONSISTENT: ⧺

THE KAON WITH THE SAME SIGN OF THE PION IS KAON−DEFINITE: ✦

BOTH KAONS ARE KAON−DEFINITE: ◇

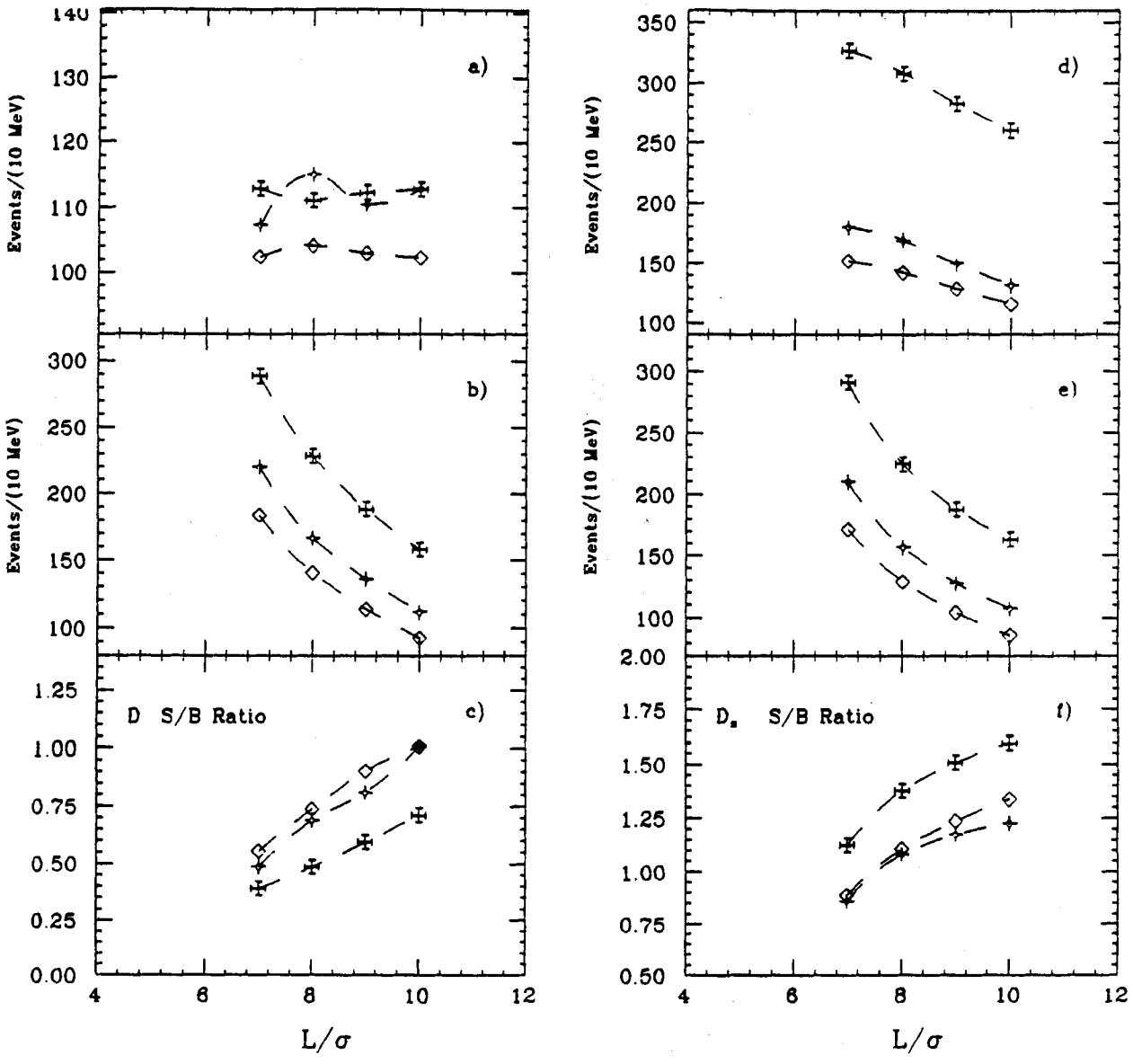

Figure 4.7: Results of the kaon ID studies: a) signal, background, and s/b ratio for the D, b) signal, background, and s/b ratio for the D_s

$K\pi\pi$ decay channel being falsely identified by the Cerenkov analysis as kaons. It is important to note also that the signal to background ratio is almost the same for case b) and c). The yield for the D does not change dramatically as in the case of the D_s. This means the misidentification problem mainly affects the D_s signal.

The D and D_s backgrounds decrease considerably as we tighten the kaon definition. From the signal to background ratio plots, case c) for the D has a slightly better signal to background ratio, but for the D_s there is not much difference between case b) and case c). It was concluded was that selecting case b) considerably reduced the background without losing much signal, and maintained a good signal to background ratio compared with the other cases.

It is also obvious from these studies that there is a problem presented by the contamination of pions from the $K\pi\pi$ decay channel to the $K\overline{K}\pi$ decay channel. Restricting the kaon definition as in case b) or c) reduces this problem but does not eliminate it completely. (The $K\pi\pi$ contamination is the subject of study in another section).

The selection cuts used for the $K\overline{K}\pi$ signal are summarize below:

- Select three-track combinations with one kaon-consistent track, one kaon-definite track and one pion-consistent track.
- kaons must have opposite sign.
- Vertexing routine must succeed.
- The z coordinate of the primary vertex must be located inside the target.
- The χ^2 per d.o.f. for the decay vertex must be less than 2.
- The χ^2 per d.o.f. for the primary vertex must be less than 3.

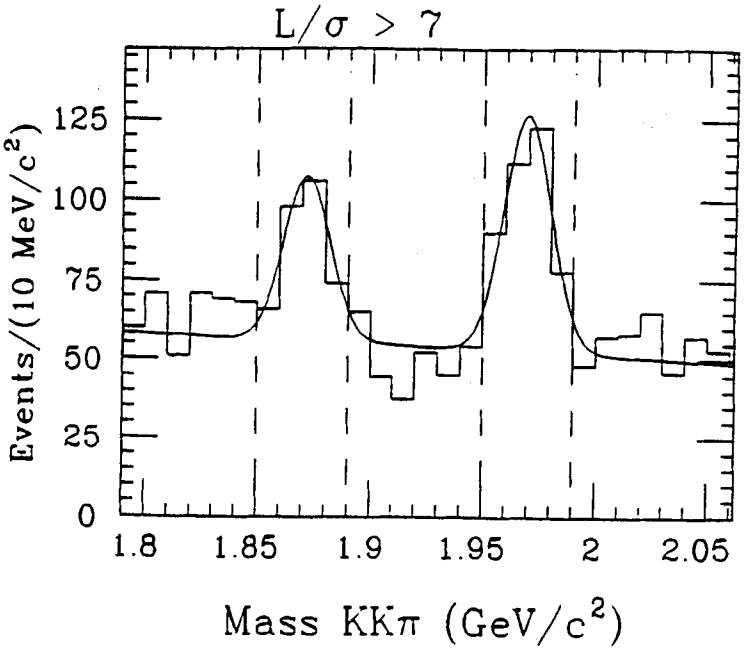

Figure 4.8: $K\overline{K}\pi$ invariant mass distribution. The region between the dashed lines are the D and D_s signals used for the study of the respective Dalitz plot

- Significance of detachment (L/σ_L).

4.4 D and D_s Dalitz Plots

In a three body final state such as $K^+K^-\pi^+$ there are two possible combinations for neutral two body systems, the K^+K^-, and the $K^-\pi^+$. A Dalitz plot is a scatter plot of the square of the effective mass of these two combinations [33].

In Fig. 4.8 is shown the invariant mass distribution for the $K\overline{K}\pi$ sample for L/σ_L > 7. The signal regions for the D and D_s appear between the dashed lines. In this case the D signal region is from 1.850 GeV to 1.890 GeV, and the D_s signal region is from 1.950 GeV to 1.990 GeV.

In Fig. 4.9 the Dalitz plot for the events in the D signal region is shown. There are resonant bands in the plot corresponding to the ϕ and $\overline{K}^{*0}$. The projection on the M^2_{kk} axis is shown in Fig. 4.9b. The peak observed around 1.050 GeV^2 corresponds to the ϕ signal. The projection on the $M^2_{k\pi}$ axis is shown in Fig. 4.9c. In this case

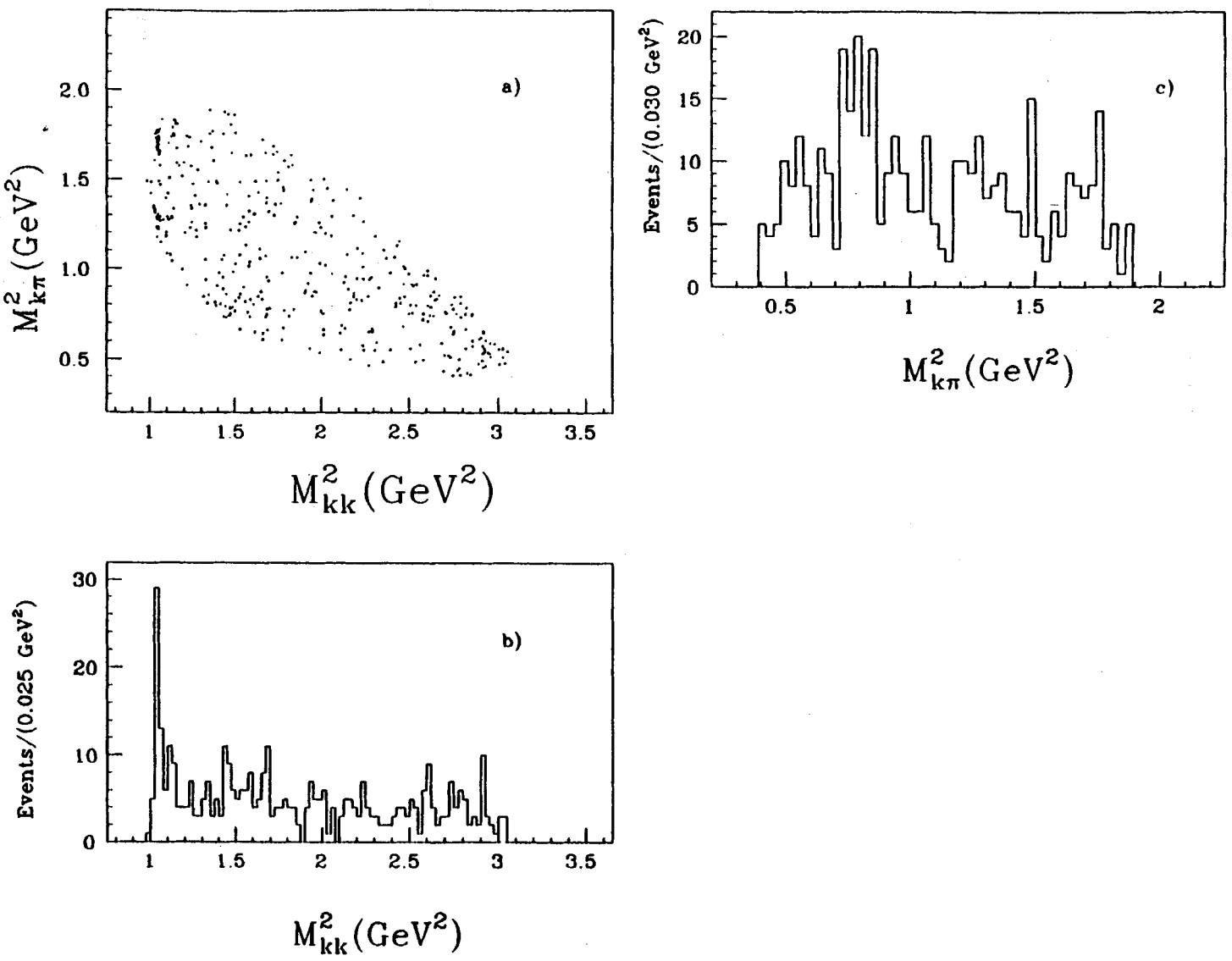

Figure 4.9: Dalitz plot for events under the D signal region, with the respective projections: b) the M^2_{kk} axis, c) the $M^2_{k\pi}$ axis

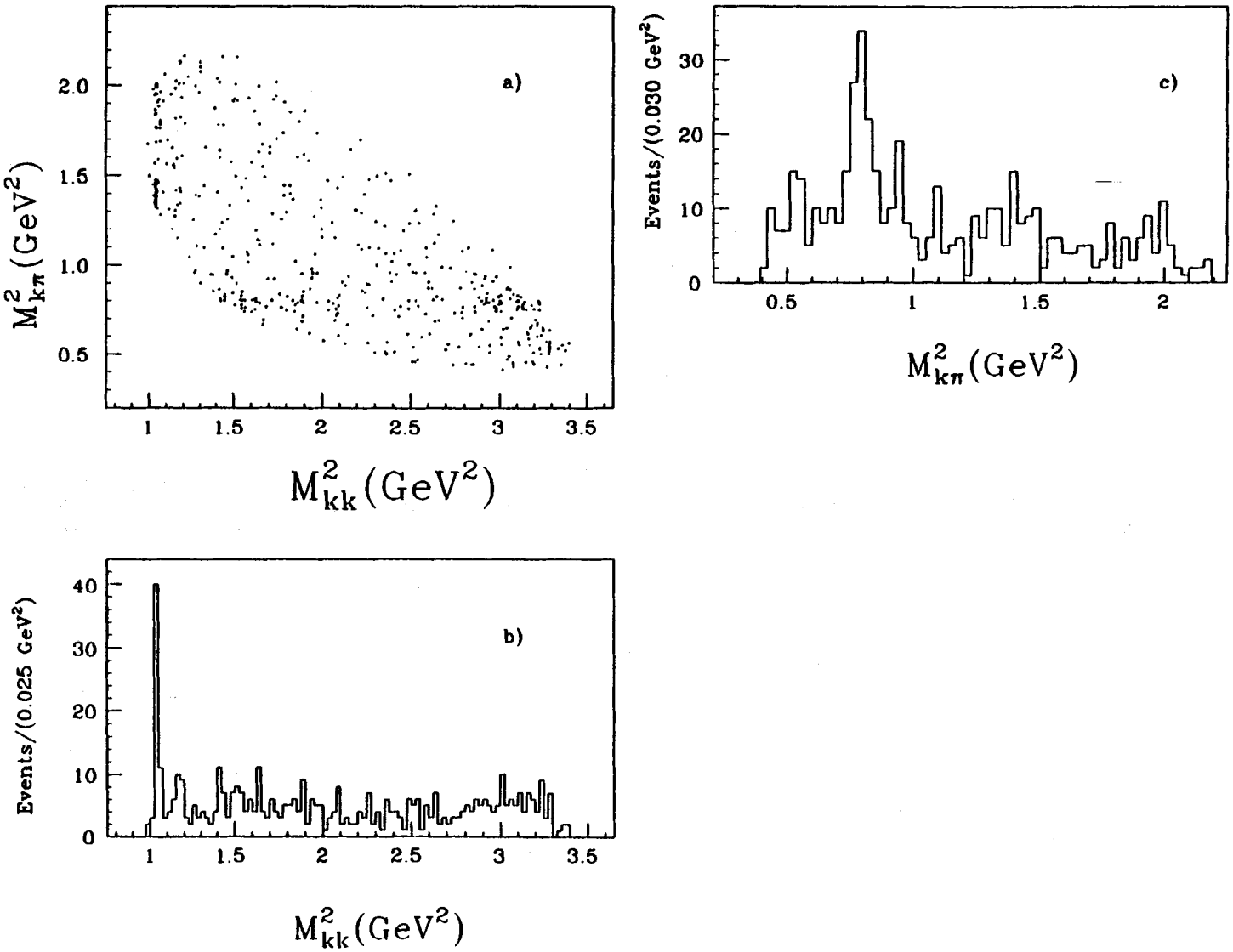

Figure 4.10: Dalitz plot for events under the D_s signal region, with the respective projections: b) the M^2_{kk} axis, c) the $M^2_{k\pi}$ axis

the $\overline{K}^{*0}$ signal appears around 0.8 GeV^2. Note the narrow width of the ϕ component as compared with the $\overline{K}^{*0}$ component.

The ϕ and $\overline{K}^{*0}$ signals observed in the projections are part of a sequence of decays. These are the pseudoscalar-vector (PV) Cabibbo suppressed decays:

- $D \longrightarrow \phi\pi$, $\phi \longrightarrow K^+K^-$
- $D \longrightarrow \overline{K}^{*0}K$, $\overline{K}^{*0} \longrightarrow \overline{K}\pi$

In Fig. 4.10 is shown the Dalitz plot for the events in the D_s signal region, with the projections onto both axes. As in the case of the D Dalitz plot, the ϕ and $\overline{K}^{*0}$ components for the D_s are part of the following pseudoscalar-vector (PV) decay sequence:

- $D_s \longrightarrow \phi\pi$, $\phi \longrightarrow K^+K^-$
- $D_s \longrightarrow \overline{K}^{*0}K$, $\overline{K}^{*0} \rightarrow \overline{K}\pi$

The evidence for ϕ and $\overline{K}^{*0}$ vector meson production can also be observed when the $K\overline{K}$ and $K\pi$ masses of the $K\overline{K}\pi$ events are histogramed. In order to histogram the $K\overline{K}$ and $K\pi$ events two mass ranges were selected: one for the D signal region from 1.85 GeV to 1.89 GeV; and one for the D_s from 1.95 GeV to 1.99 GeV. The histograms are shown in Fig. 4.11 for $L/\sigma_L > 7$. Fig. 4.11a and Fig. 4.11b show the ϕ signal for the D and D_s respectively. Fig. 4.11c and Fig. 4.11d show the $\overline{K}^{*0}$ signal for the D and D_s respectively. From these histograms the evidence for the $\phi\pi$ and $\overline{K}^{*0}K$ decay channels is clear. The ϕ signal appears relatively free of background.

Background events are also present in the Dalitz plot. Non-D and D_s ϕ and $\overline{K}^{*0}$ events are part of the background that appear in both Dalitz plots. Other sources of background such as the contamination from $K\pi\pi$ events are also present. A fit to

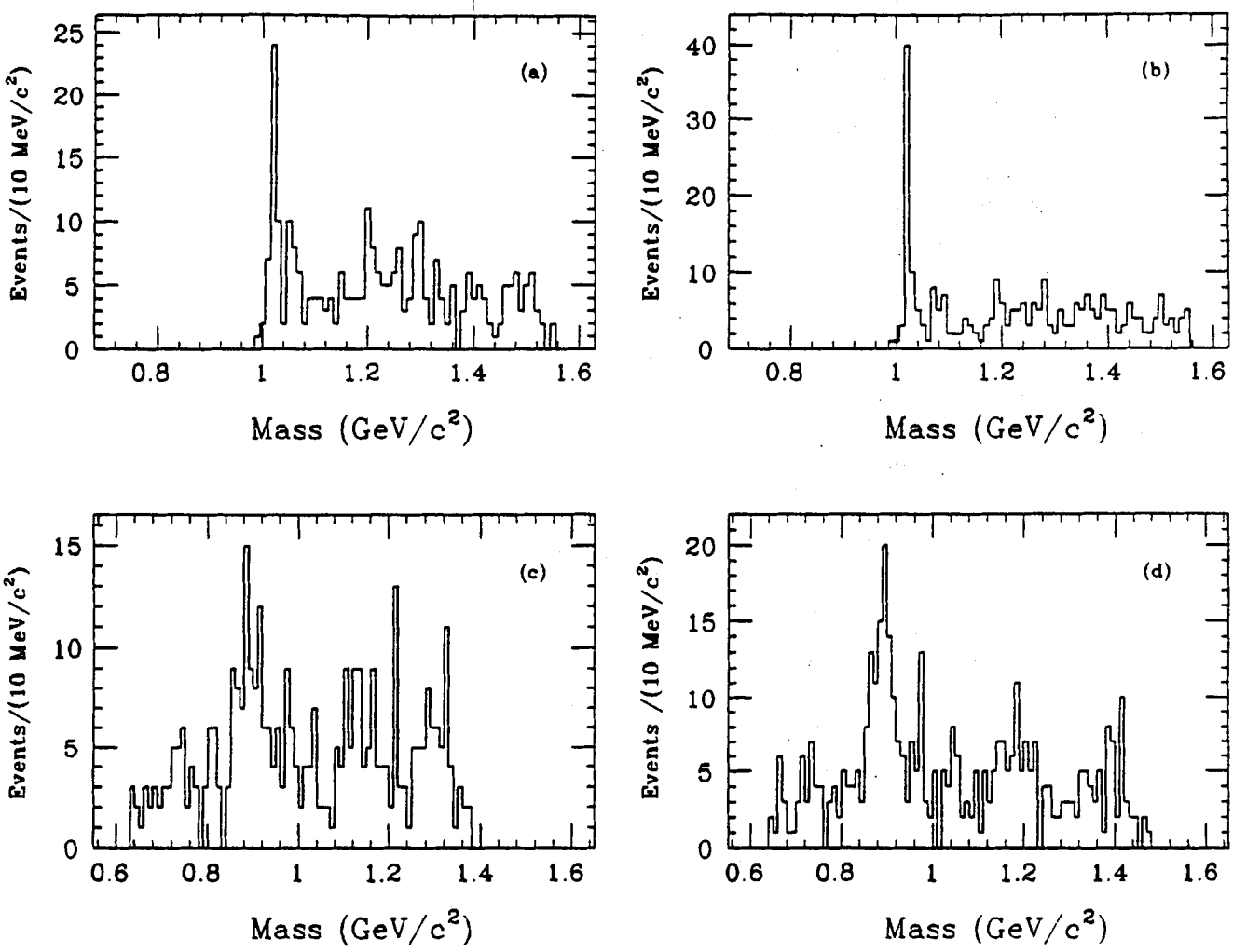

Figure 4.11: ϕ and $\overline{K}^{*0}$ components from the $K\overline{K}\pi$ signal for $L/\sigma_L > 7$: a) ϕ content of the D, b) ϕ content of the D_s, c) $\overline{K}^{*0}$ content of the D, d) $\overline{K}^{*0}$ of the D_s

the projections of the Dalitz plot would only give an estimate of the $\phi\pi$ and $\overline{K}^{*0}K$ decay channels for the D and D_s due to the fact that this procedure would ignore the background contributions and any possible interference between the resonances. The fit of the Dalitz plot is the subject of study of chapter 5.

4.5 Study of the $K\overline{K}\pi$ Dalitz Plots

Clusters of background events with high $K\overline{K}$ mass and low $K\pi$ mass can be seen in the Dalitz plots. These background events are located very close to the K^* band.

In Fig. 4.12 are shown the Dalitz plots for an $L/\sigma_L > 7$ for several background regions and for the signal regions for the D and D_s. In Fig. 4.12.d for the background region that goes from 2.0 GeV^2 to 2.07 GeV^2 a cluster of background events at large M^2_{kk} and small $M^2_{k\pi}$ is clearly seen. In Fig. 4.12.f (the D_s signal region), a similar cluster of events below the K^* band is present. In the $M^2_{k\pi}$ projection the peak around 0.48 GeV^2 is due to this background.

Several studies were carried out to understand the source of these clusters of background events. The distributions of the separation L between the primary and decay vertex and the error σ_L for all the events in the Dalitz plot were studied. The aim was to see if these events have a special L or σ_L. From these L and σ_L distributions there was no indication that cuts on these variables could be used as a tool to eliminate the background.

Next the momentum distributions were studied. For all the events in the Dalitz plot the kaon, pion and $K\overline{K}\pi$ momentum distributions were plotted. In addition, the same distributions for a subset of events, namely the ones that form the cluster below the K^* band, were studied.

The results are shown for an $L/\sigma_L > 7$ in Fig. 4.13. In Fig. 4.13.a , Fig. 4.13.c, and Fig. 4.13.e, are shown the momentum distributions for the kaon, pion and $K\overline{K}\pi$ when

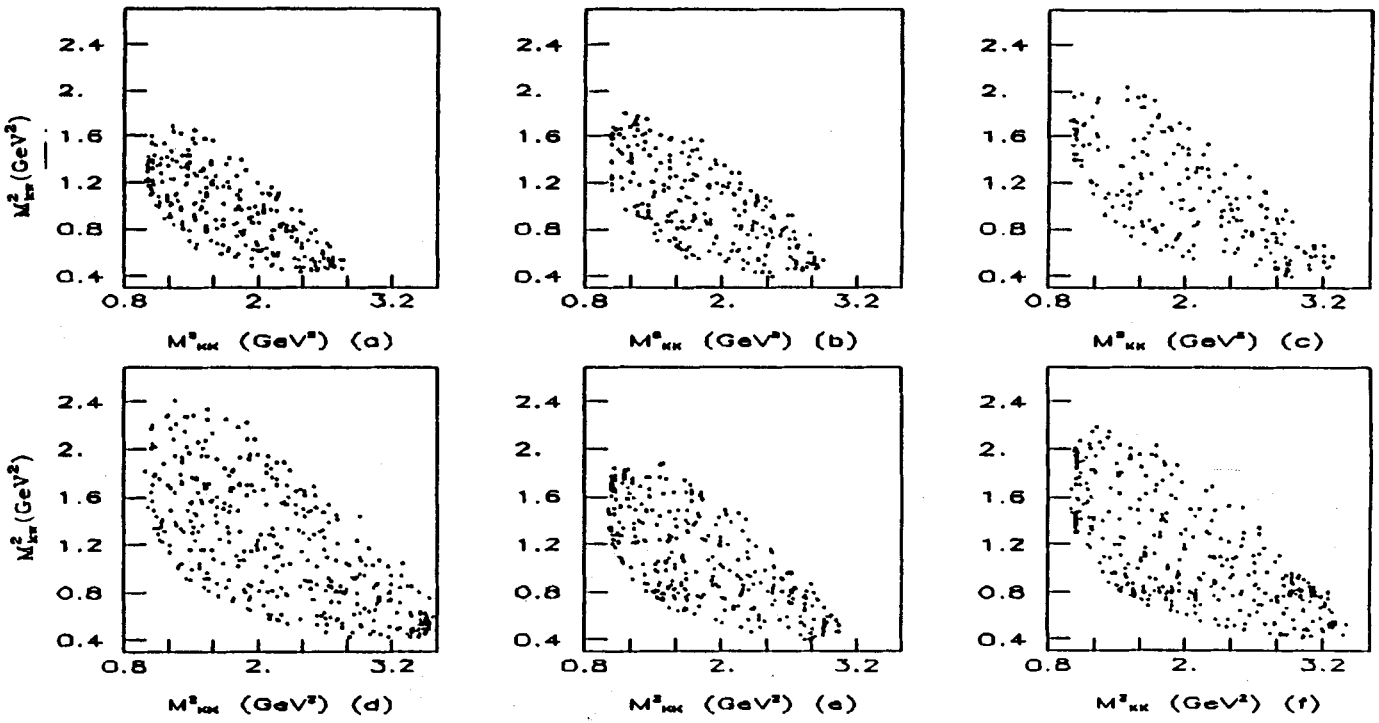

Figure 4.12: Dalitz plots for the following $K\bar{K}\pi$ mass intervals: a) 1.77 GeV to 1.81 GeV, b) 1.81 GeV to 1.85 GeV, c) 1.91 GeV to 1.95 GeV, d) 2.0 GeV to 2.07 GeV, e) 1.855 GeV to 1.885 GeV, f) 1.955 GeV to 1.985 GeV.

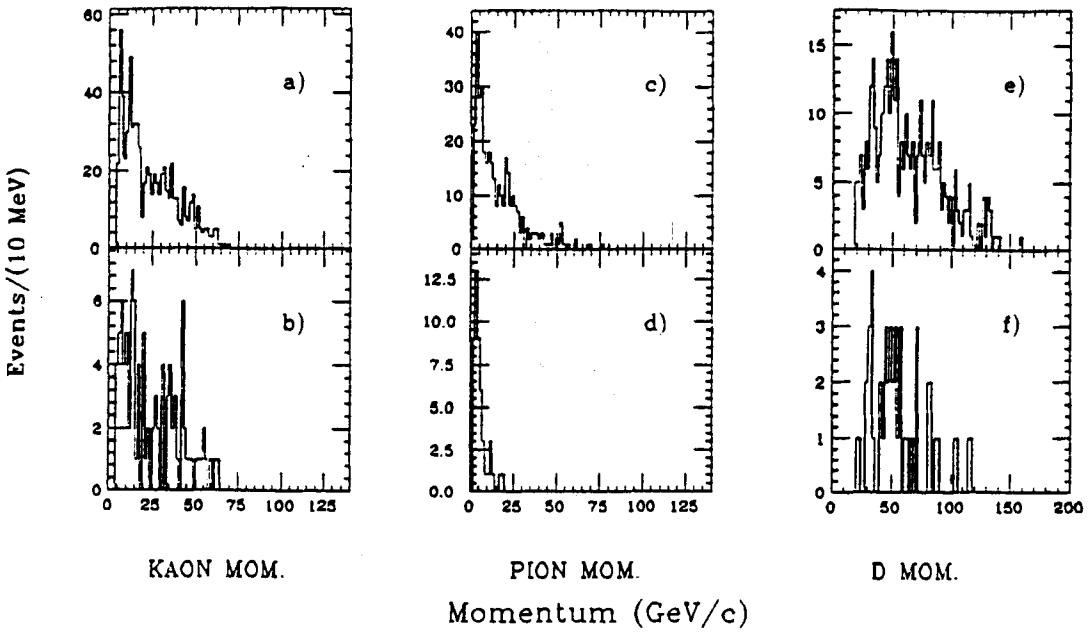

Figure 4.13: Momentum distribution for kaons,pion,and D when the $K\overline{K}\pi$ mass is between 1.850 GeV and 1.890 GeV. b), d), f) are a subset of a), c), and e) because there is a requirement that M^2_{kk} be > 2.6 GeV^2 and $M^2_{k\pi}$ be < 0.55 GeV ^{2}

the $K\overline{K}\pi$ mass is between 1.850 GeV and 1.890 GeV (D signal region). Fig. 4.13.b, Fig. 4.13.d, Fig. 4.13.f are a subset of Fig. 4.13.a, c,and e for the events with M^2_{kk} greater than 2.6 GeV^2 and $M^2_{k\pi}$ less than 0.55 GeV^2.

In Fig. 4.14.a, Fig. 4.14.c, Fig. 4.14.e are shown the momentum distributions for the kaon, pion and $K\overline{K}\pi$ for the D_s signal region (1.95 to 1.990 GeV). In this case the subset of events with M^2_{kk} greater than 2.85 GeV^2 and $M^2_{k\pi}$ less than 0.55 GeV^2 is shown in Fig. 4.14.b, Fig. 4.14.d, Fig. 4.14.f.

Finally, in Fig. 4.15.a, Fig. 4.15.c and Fig. 4.15.e are shown the momentum distributions for the events in the background region from 2.0 GeV to 2.07 GeV. The subset of events are shown in Fig. 4.15.b, Fig. 4.15.d, and Fig. 4.15.f. These events are selected when the M^2_{kk} are greater than 3.2 GeV^2 and $M^2_{k\pi}$ less than 0.65 GeV^2.

From the momentum distributions, it is obvious that the cluster of background

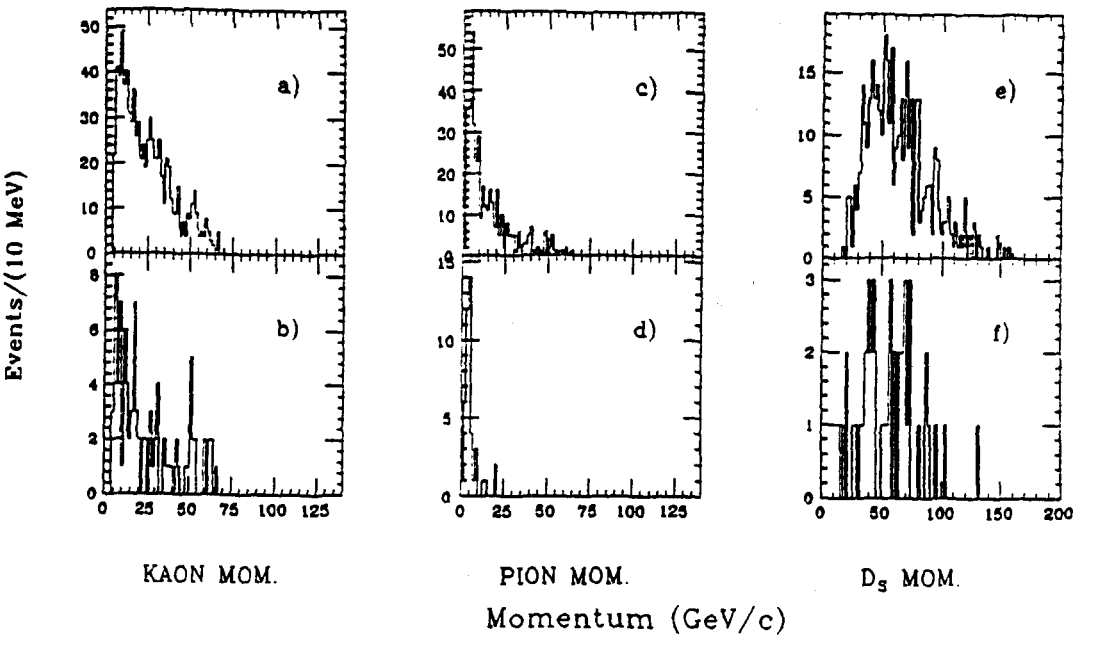

Figure 4.14: Momentum distribution for kaons, pion, and D_s when the $K\overline{K}\pi$ mass is between 1.950 GeV and 1.990 GeV. b), d), f) are a subset of a), c), and e) because there is a requirement that M^2_{kk} be > 2.85 GeV^2 and $M^2_{k\pi}$ be < 0.55 GeV ^{2}

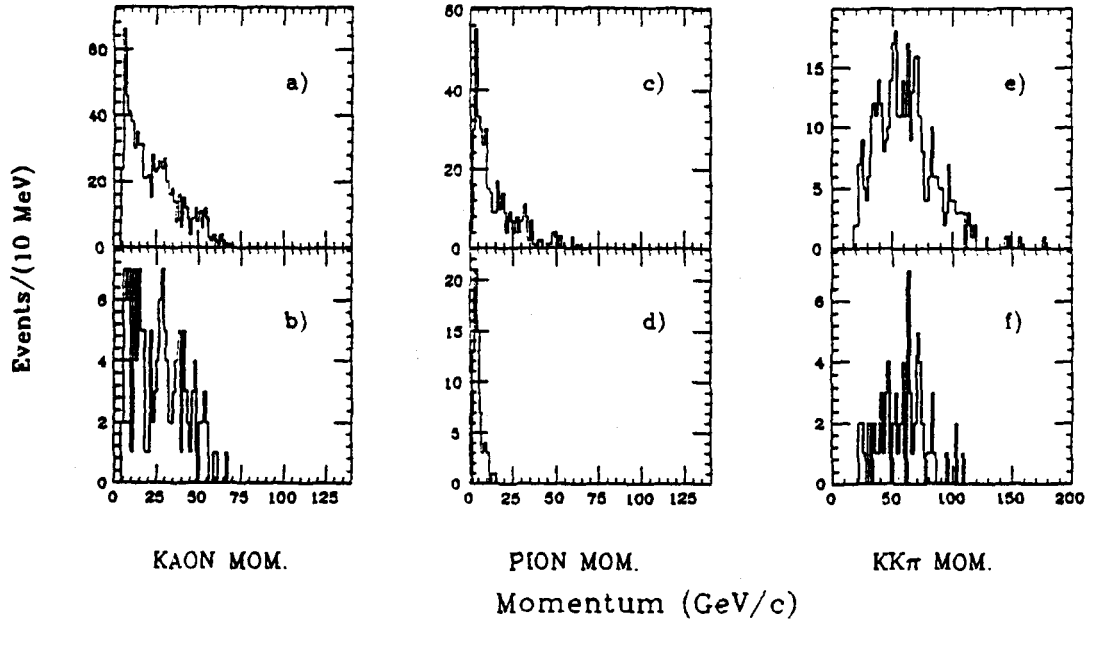

Figure 4.15: Momentum distribution for kaons, pion, and D_s when the $K\overline{K}\pi$ mass is between 1.950 GeV and 1.990 GeV. b), d), f) are a subset of a), c), and e) because there is a requirement that M^2_{kk} be > 3.2 GeV^2 and $M^2_{k\pi}$ be < 0.65 GeV ^{2}

events is made up of events with a low momentum pion. The question is whether these low momentum pions are real pions or if they are low momentum electrons below the C2 pion threshold, which do not fire C2 and are flagged as pions by the Cerenkov analysis. (For tracks with a momentum below the C2 threshold, the Cerenkov analysis will assign an ISTATP of 14 if C2 does not fire).

In the analysis so far, a pion has been defined to be everything but a heavy (K or K/p ambiguous) or electron. At this point a new pion definition was adopted; an ISTATP of 14 is rejected, and the new pion ISTATP can be only 2,3,7,15.

With this new pion Cerenkov ID, the $K\overline{K}\pi$ sample was again studied. For the new pion definition and $L/\sigma_L > 7$, the Dalitz plots for the several background and signal regions are shown in Fig. 4.16. It is interesting to compare these plots with the ones shown in Fig. 4.12. The momentum distributions for the events rejected by the new pion definition (events where the pion has an ISTATP of 14), were also studied and it was found that, as expected, the new pion definition rejects mainly low momentum tracks below the C2 pion threshold (4.6 GeV).

In order to study the effect of the new pion definition on the signal, the background, and the signal to background ratio (S/B), the invariant mass distributions for the $K\overline{K}\pi$ final state were fitted. The signal terms were discribed with a Gaussian and the background with a second order polynomial. The regions of integration used to obtain the yield for the signal and background were: from 1.850 to 1.890 GeV for the D, and from 1.950 to 1.990 GeV for the D_s. In Table 4.2 are shown the results of the fit for an $L/\sigma_L > 8$ and in Fig. 4.17 is plotted the signal, background and signal to background ratio as a function of the Elsig cut. From Fig. 4.17, it can be seen that the yield for the D and D_s signals decreases with the new pion id. but since the background is reduced there is improvement in the signal to background ratio.

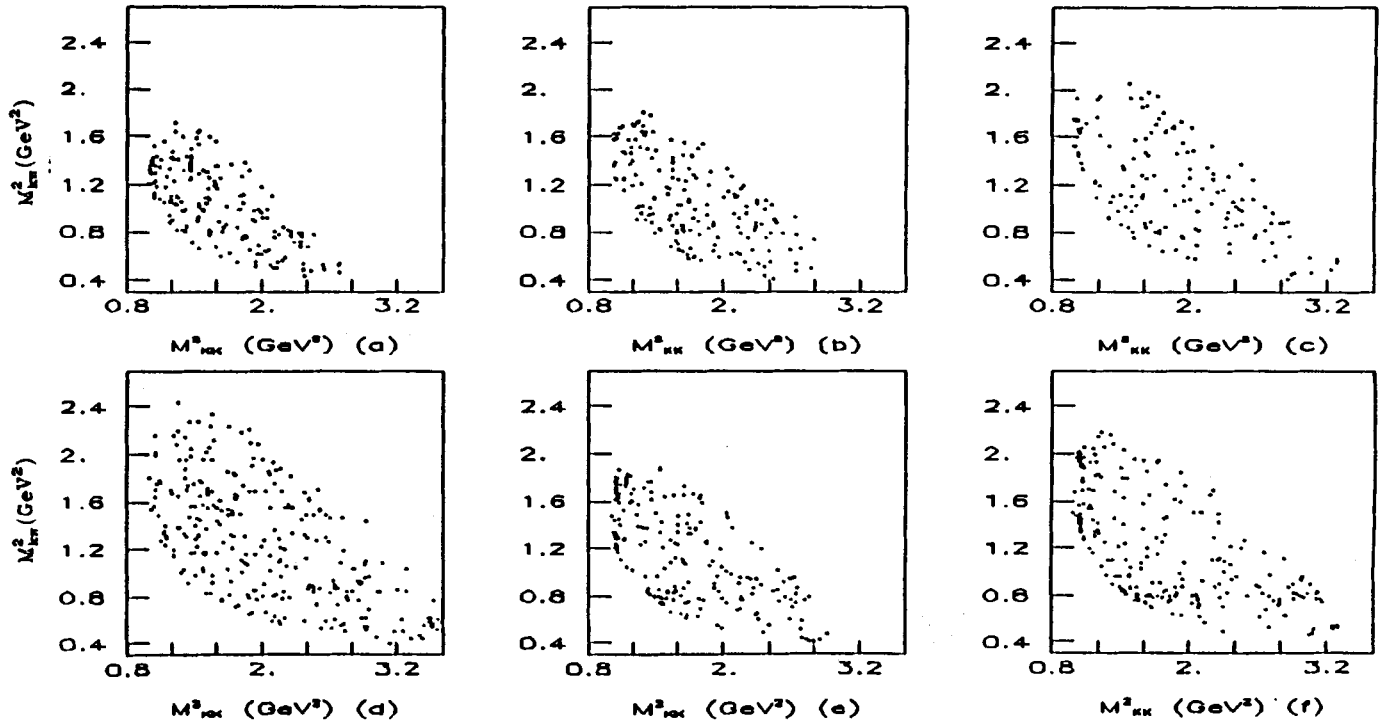

Figure 4.16: Dalitz plots with pion cerenkov ISTATP required to be 2,3,7, or 15 for the following $K\bar{K}\pi$ mass regions: a) 1.77 GeV to 1.81 GeV, b) 1.81 GeV to 1.85 GeV, c) 1.91 GeV to 1.95 GeV, d) 2.0 GeV to 2.07 GeV, e) 1.855 GeV to 1.885 GeV, f) 1.955 GeV to 1.985 GeV.

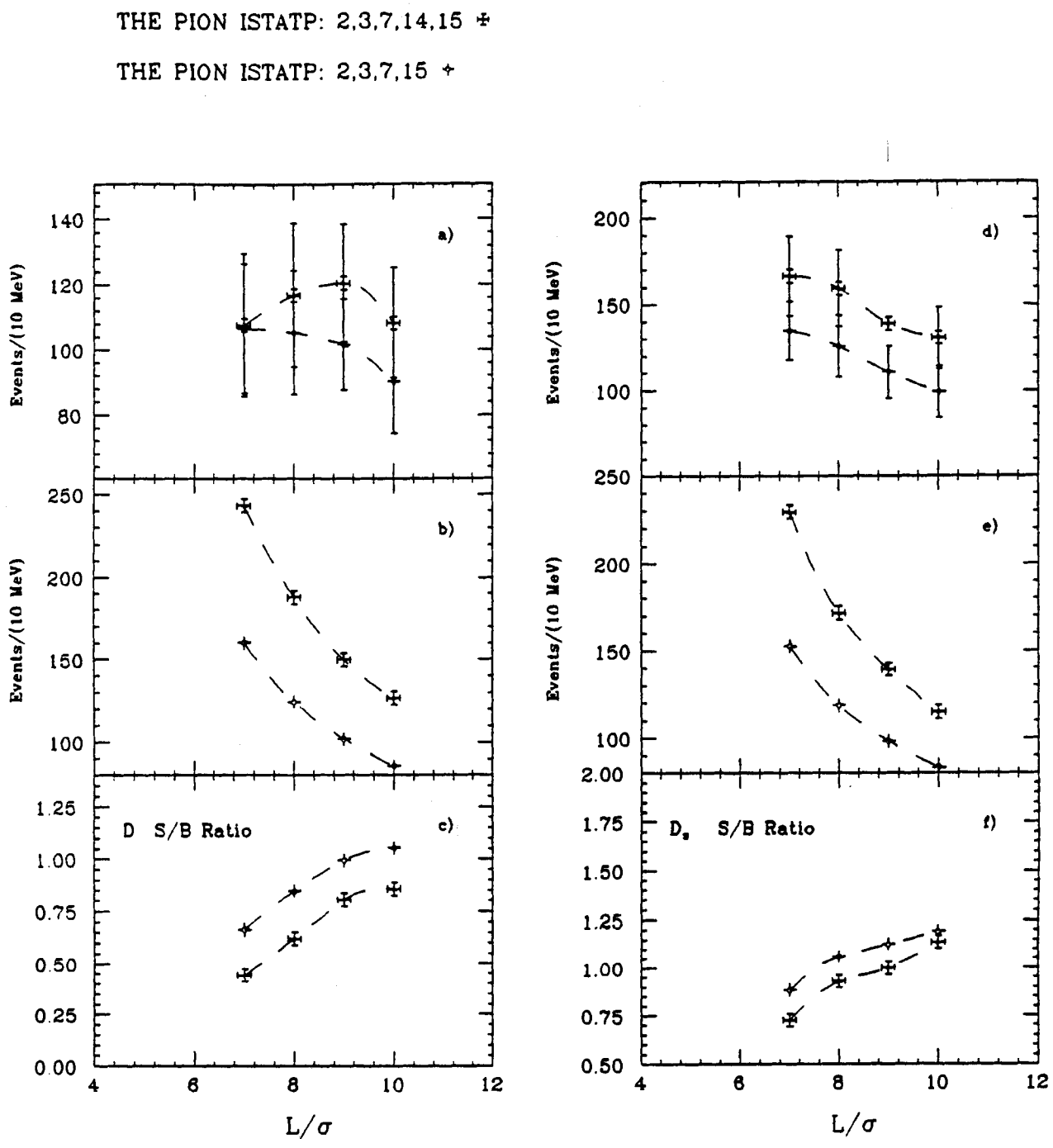

Figure 4.17: Results for two different pion id. requirements: a) signal, b) background, and c) s/b ratio for the D, d) signal, e) background, and f) s/b ratio for the D_s.

TABLE 4.2
RESULTS OF THE FITS TO THE $K\overline{K}\pi$ INVARIANT MASS DISTRIBUTIONS FOR TWO DIFFERENT π DEFINITIONS FOR AN $L/\sigma_L > 8$.

	Mass (MeV)	Width (MeV)	Yield	S/B	π ISTATP
D	1872 ± 2	11 ± 2	117 ± 22	0.6	2,3,7,14,15
D	1869 ± 2	11 ± 2	105 ± 19	0.8	2,3,7,15
D_s	1970 ± 1	11 ± 1	159 ± 22	0.9	2,3,7,14,15
D_s	1970 ± 1	10 ± 1	126 ± 18	1.05	2,3,7,15

4.5.1 Decrease of the Signal Region Size for the D and D_s

In order to increase the signal-to-noise ratio for the D and D_s in the Dalitz plot, the size of the signal region has been reduced. For the D, the range was reduced from 1.850 - 1.890 GeV to 1.855 - 1.885 GeV. For the D_s, the range was reduced from 1.950 - 1.990 GeV to 1.955 - 1.985 GeV. The results shown in the remainder of this chapter are for the 30 MeV regions.

4.6 Efficiency Studies

In order to obtain the contributions from the different resonances, a Dalitz plot fit has been made for the D and D_s. This procedure requires that the variation in acceptance and reconstruction efficiency at every point in the Dalitz plot must be known. Preliminary Monte Carlo studies showed that the efficiency across the Dalitz plot was not constant. This was the case for both the D and D_s. The efficiency across the Dalitz plot was obtained by determining a function of the form

$$\epsilon = \epsilon(M^2_{kk}, M^2_{k\pi}).$$

In order to find ϵ, ROGUE Monte Carlo samples of 220,000 events and 260,000 events were created for the D and for the D_s, respectively. In each case the final state

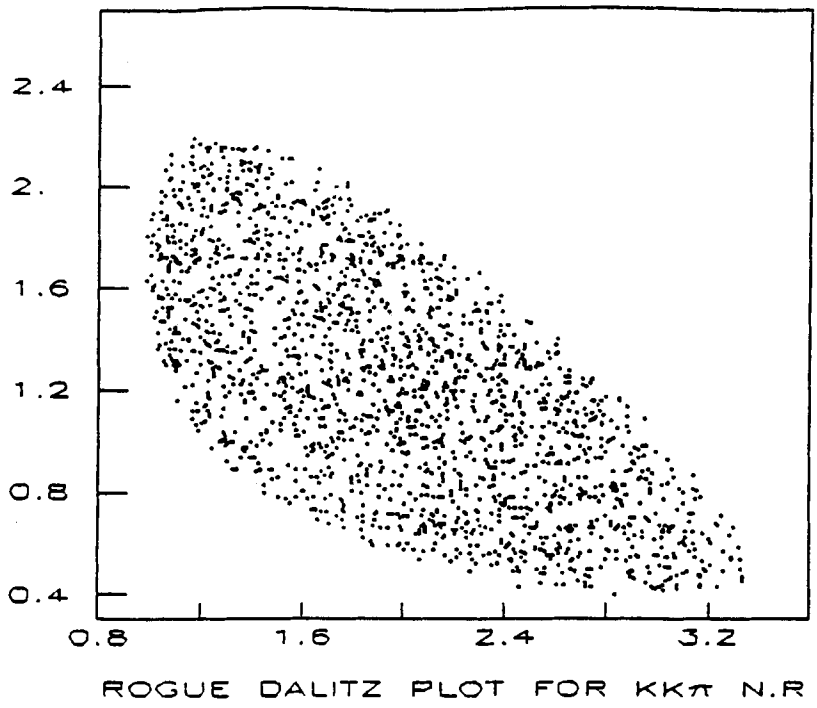

Figure 4.18: Dalitz plot for Rogue Monte Carlo events, when the final state is the D_s decaying to $K\overline{K}\pi$ non-resonant

was the non-resonant $K\overline{K}\pi$ channel for which the generated events evenly populate the Dalitz plot (See Fig. 4.18). The goal was to find for a given point on the plot the ratio of reconstructed to generated events. The reconstructed events were found using the same cuts as those that were applied to the data.

The Dalitz plot was divided into rectangular bins, each bin having a dimension of 0.1 GeV^2 in M^2_{kk} by 0.12 GeV^2 in $M^2_{k\pi}$. With this bin size, the Dalitz plot is entirely covered by 170 bins and 230 bins for the D and D_s regions respectively.

In Fig. 4.19 are shown the results for the D. For each bin is shown the number of reconstructed events and the number of generated events. In Fig. 4.20 are shown the results for the D_s.

The Dalitz plot was divided into rows and columns. The following procedure was then used to obtain smooth functions that give the value of the efficiency for any given bin in a row or column. For a given row, a histogram of the number of events

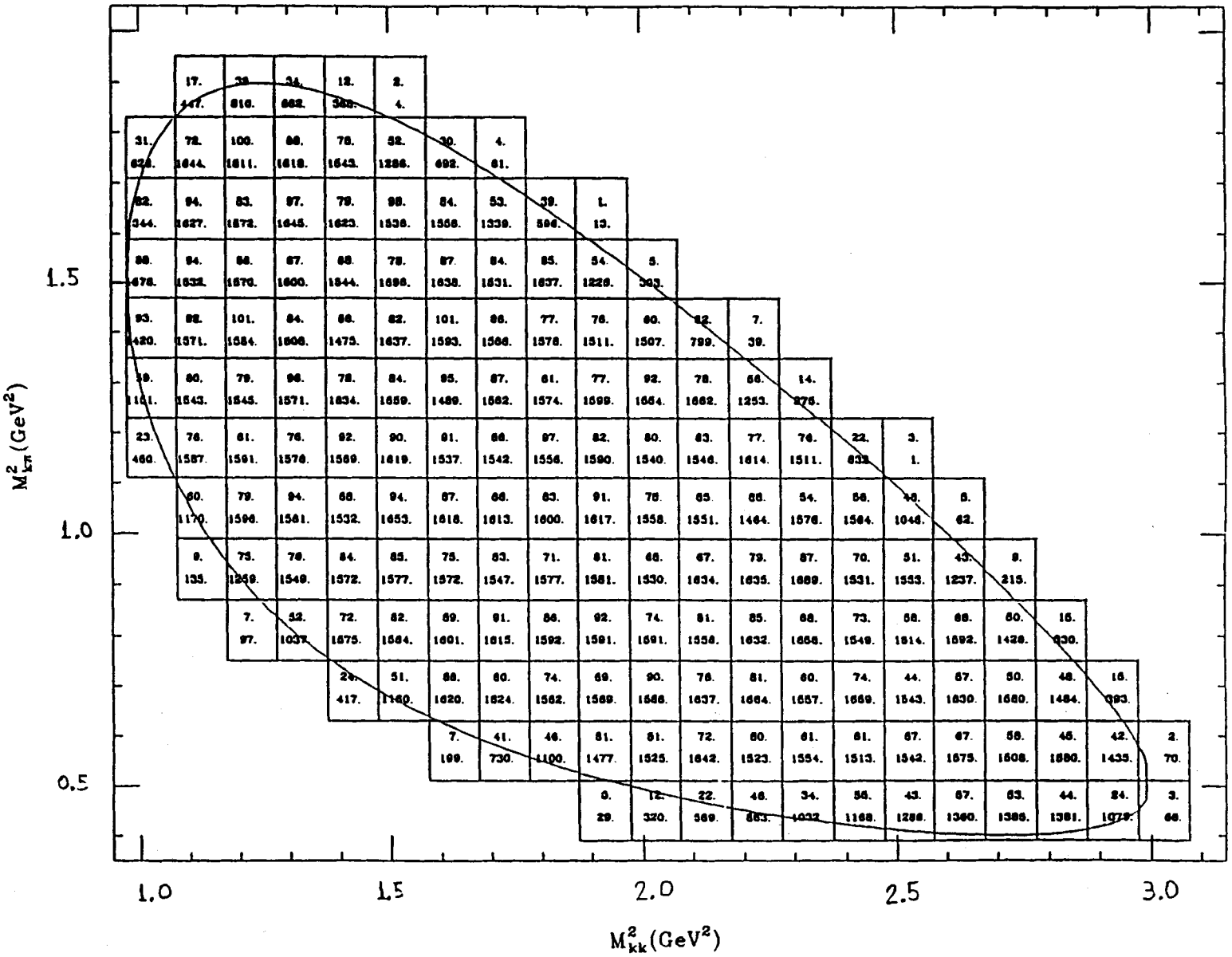

Figure 4.19: Dalitz plot showing the raw number of generated and reconstructed events in each bin for 220000 Rogue Monte Carlo events for the D

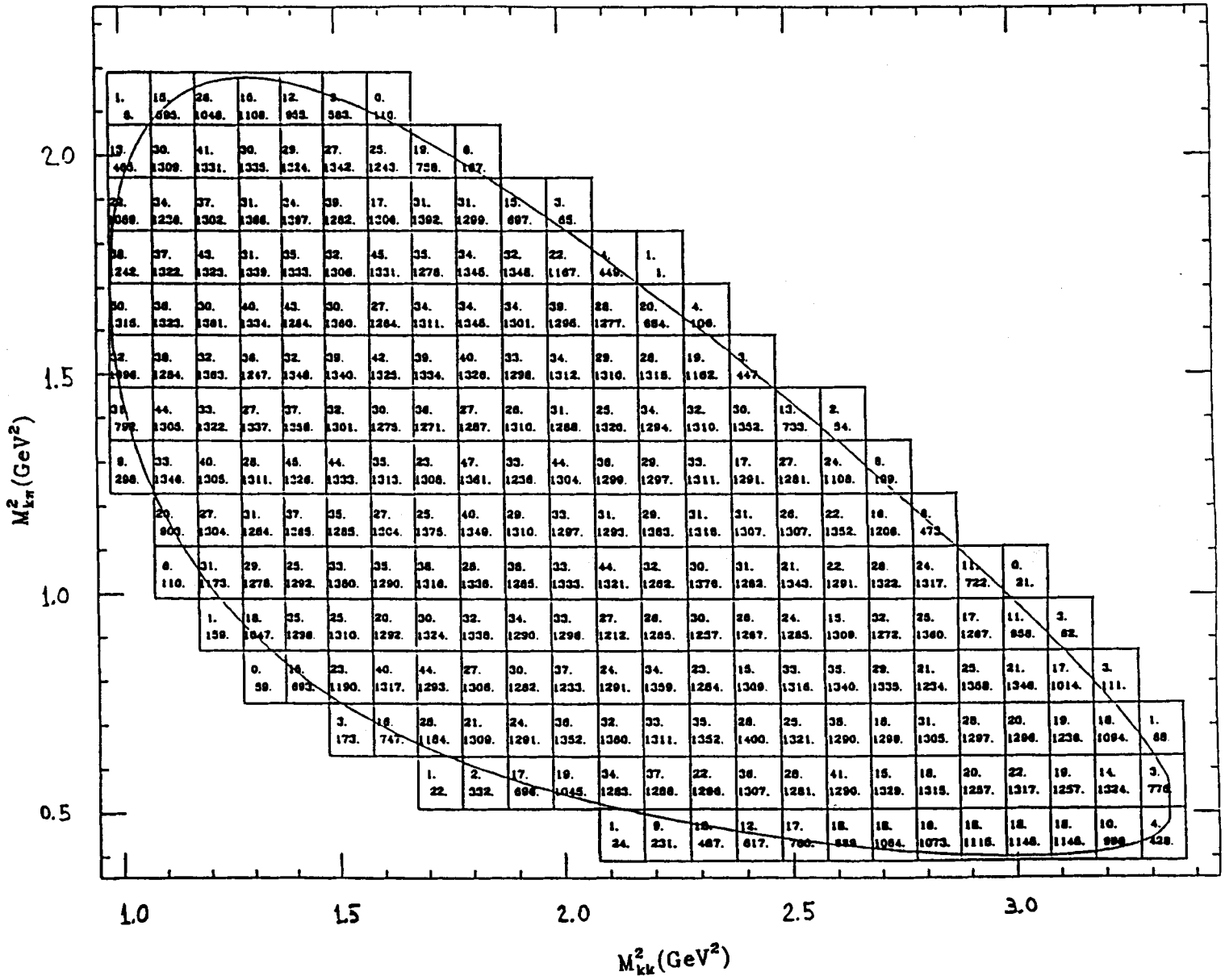

Figure 4.20: Dalitz plot showing the raw number of generated and reconstructed events in each bin for 260000 Rogue Monte Carlo events for the D_s

in each bin versus M^2_{kk} is created. This is done for the generated and reconstructed events; and the errors in the histogram were taken to be the statistical errors. The ratio of reconstructed to generated events in a given row or column was found and the histogram of this ratio was produced (error bar included). In Fig. 4.21 are shown examples of the histograms created in the case of the D_s. In Fig. 4.21.a are shown the distributions for the number of generated events vs the M^2_{kk} for several rows in the D_s Dalitz plot (Fig. 4.20). (The label "one", is assigned to the row with the lowest $M^2_{k\pi}$ value.) In Fig. 4.21.b are shown the distributions for the number of reconstructed events vs M^2_{kk}, for the same rows as in Fig. 4.21a. Finally in Fig. 4.21.c are shown the ratios of the reconstructed to generated distributions, for the same rows mentioned above. In Fig. 4.23 are shown the results for several columns (similar results as in Fig. 4.21). The next step was to fit the distribution for each of the rows and columns with a smooth curve. Using a polynomial of degree n where n could be 0,1,2,3,4,5 as needed, the distributions were fitted in order to obtain a smooth curve that represents the efficiency for that given row (or column). In Fig. 4.22 is shown the results of the fit for several rows.

The result of this fitting procedure was two values of efficiency for each Dalitz plot bin. The ideal situation would be to find that the efficiency for a given bin found using the row does not differ much from the efficiency found using the column.

The efficiency used in any given bin in the Dalitz plot, was taken to be the average of the efficiencies found using the rows and columns. The efficiency across the Dalitz plot was calculated for several values of the L/σ_L cut. The integrated efficiency for an L/σ_L cut > 7 was found to be 0.048 and 0.024 for the D and D_s respectively.

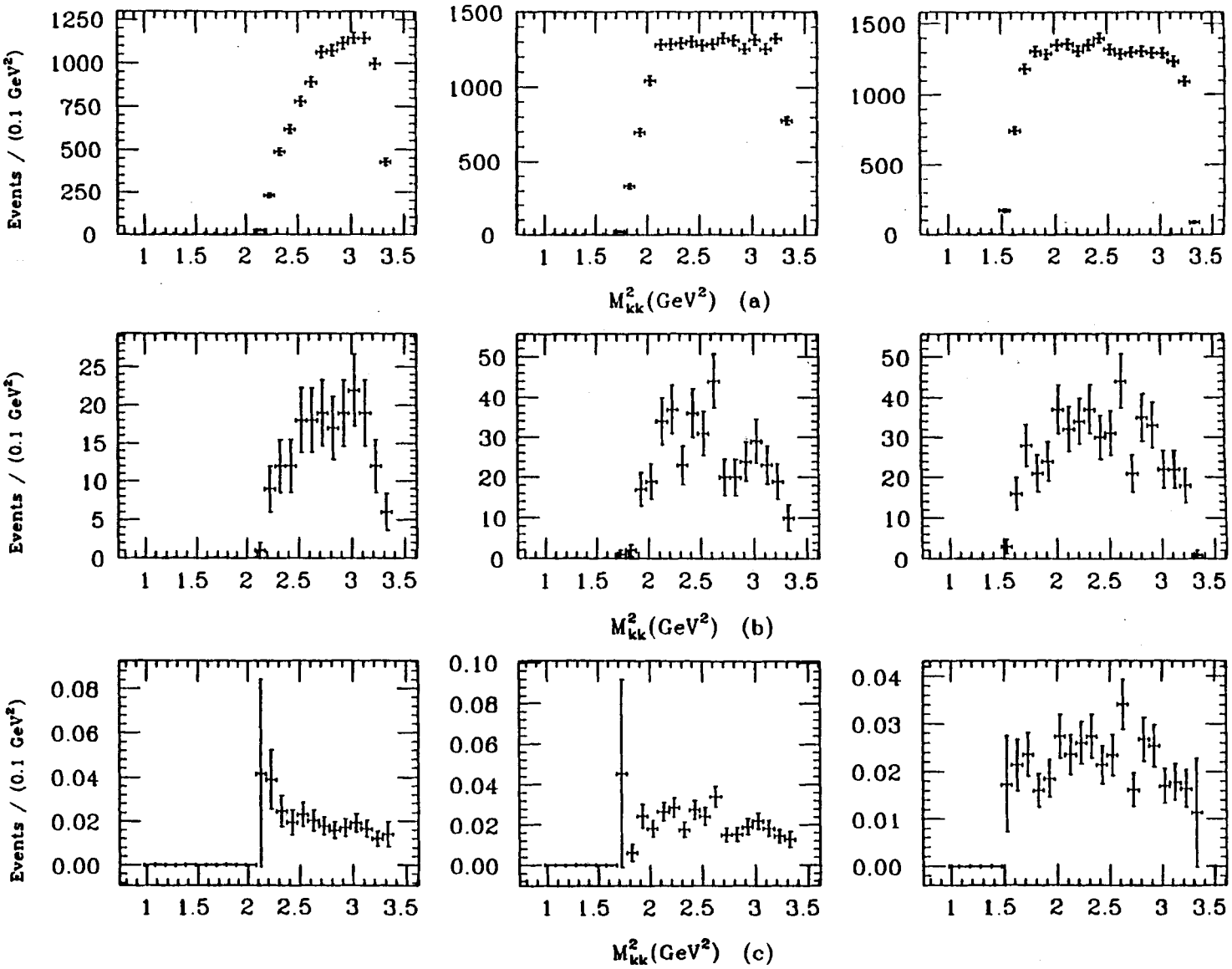

Figure 4.21: Histograms for rows 1,2,3 for an L/σ_L cut > 7: a) D_s generated events, b) D_s reconstructed events, c)the ratio of gen ed to reconstructed events.

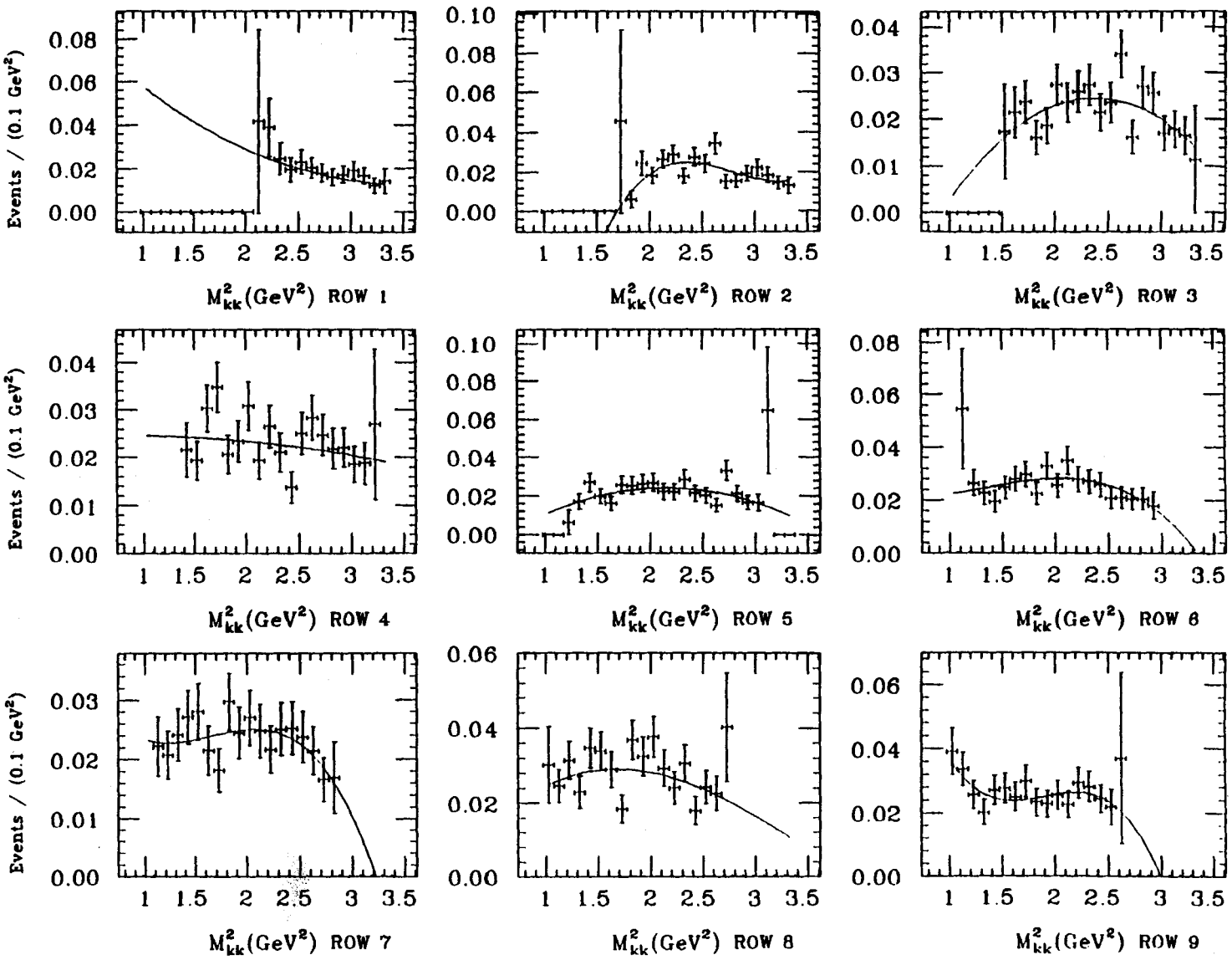

Figure 4.22: Fit to the ratio of generated to reconstructed events for several rows for an Elsig cut > 7. for the D,

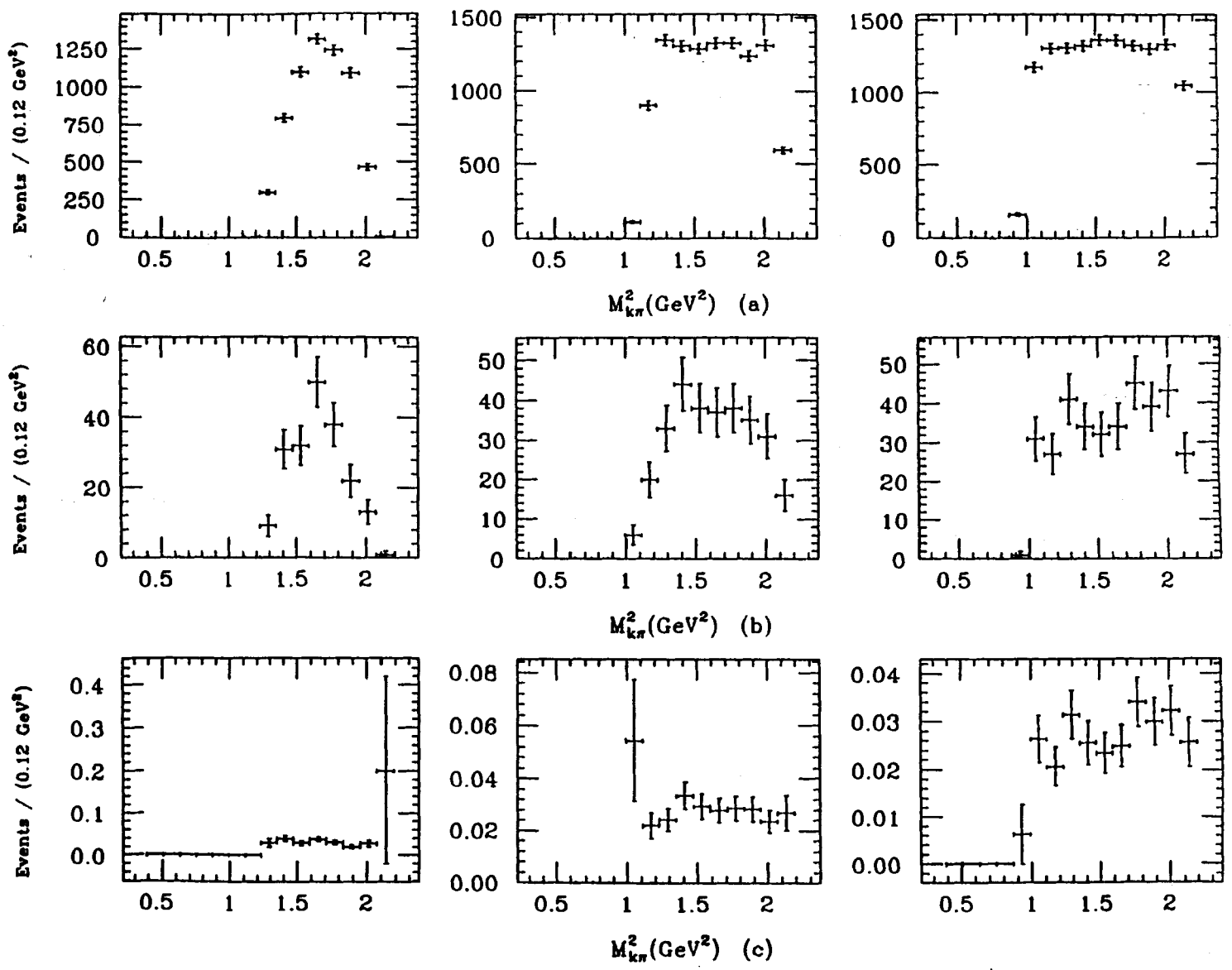

Figure 4.23: Histograms for columns 1,2,3 for an L/σ_L cut > 7: a) D, generated events, b) D, reconstructed events, c)the ratio of generated to reconstructed events.

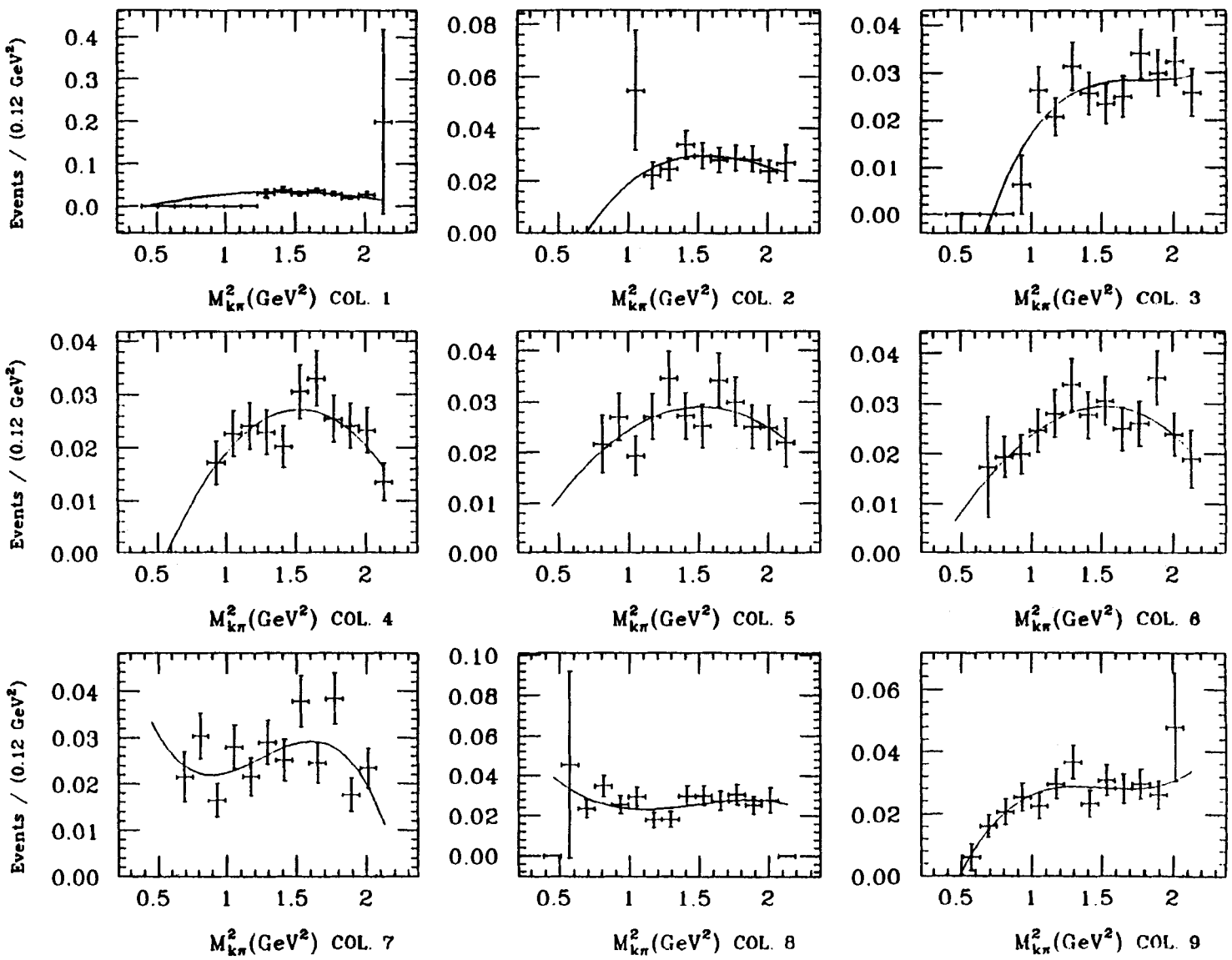

Figure 4.24: Fit to the ratio of generated to reconstructed events for several columns for an Elsig cut > 7. for the D,

4.7 Background Studies

Evidence for ϕ and $\overline{K}^{*0}$ production in D and D_s decay was presented in section 4.4. There can be ϕ and $\overline{K}^{*0}$ events produced that are not part of the D or D_s signal; these are a source of background that has to be evaluated. In addition, there are non-resonant background events which uniformly populate the Dalitz plot.

Another source of background is contamination of $K\pi\pi$ events classified as $K\overline{K}\pi$. These events might be expecteded to populate the Dalitz uniformly. Combinatorial background events that pass all the selection cuts are also expected to randomly populate the Dalitz plot. It is not necessary to find the individual contributions from each of the different sources of background; one may estimate the total amount of $\overline{K}^{*0}$, ϕ, and $K\overline{K}\pi$ non-resonant background in the D and D_s signal regions, and use this information in the fit to the Dalitz plots. This is one of the aims of the background studies.

For that purpose four mass regions were chosen for the study of the background (see Fig. 4.25). The mass regions were chosen at masses below the D, between the D and D_s, and above the D_s; the sizes of the regions were chosen to provide enough statistics for the analyses. The regions are the following:

- 1.70 GeV to 1.77 GeV
- 1.77 GeV to 1.84 GeV
- 1.91 GeV to 1.94 GeV
- 2.00 GeV to 2.07 GeV

In Fig. 4.26 are shown the Dalitz plots for events in the four mass regions with $L/\sigma_L > 7$. In order to study the content of ϕ and $\overline{K}^{*0}$ for each of the Dalitz plots,

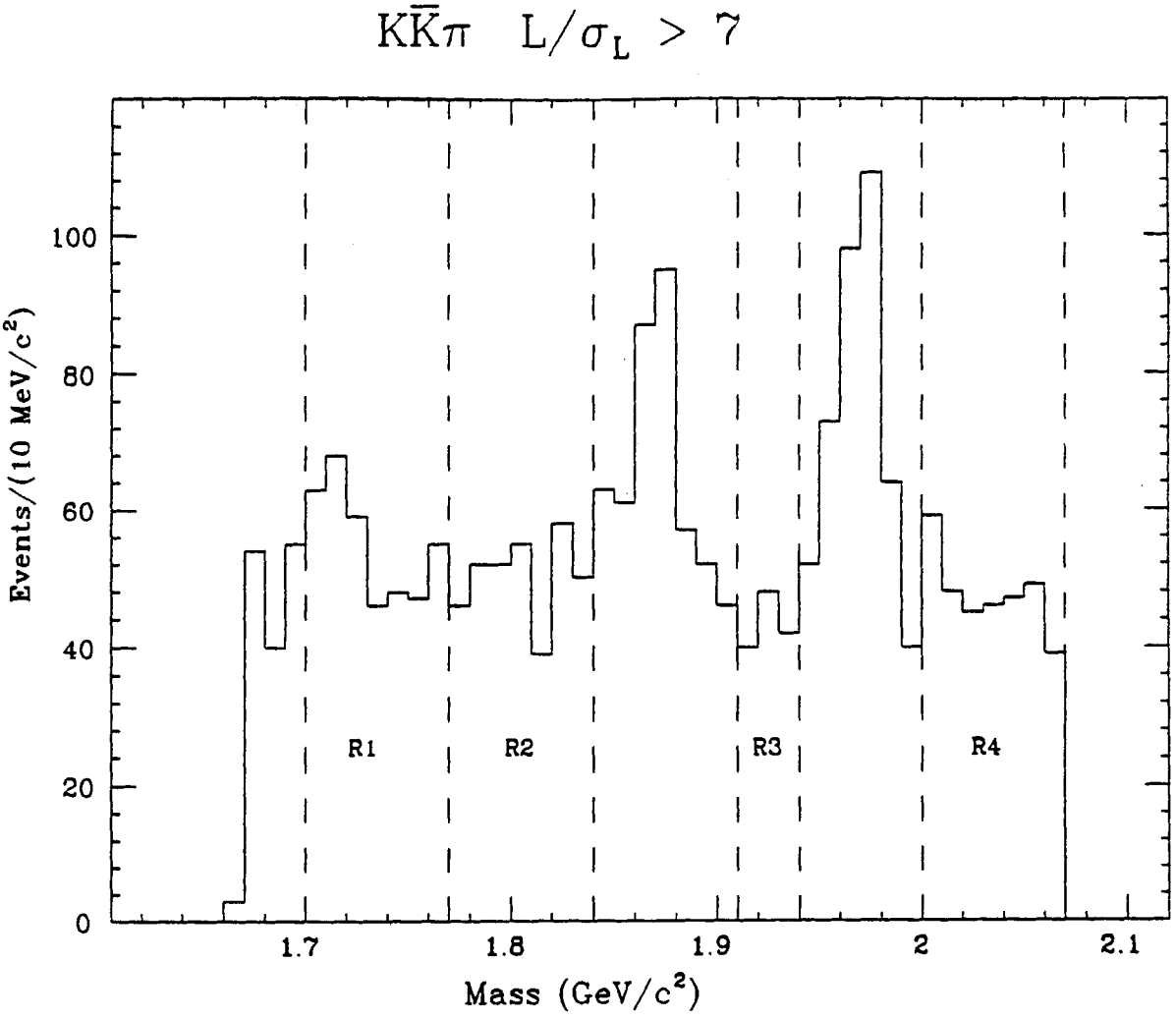

Figure 4.25: $K\bar{K}\pi$ invariant mass distribution showing the four background regions: R1 from 1.70 GeV to 1.77 GeV, R2 from 1.77 GeV to 1.84 GeV, R3 from 1.905 GeV to 1.940 GeV, and R4 from 2.0 GeV to 2.07 GeV.

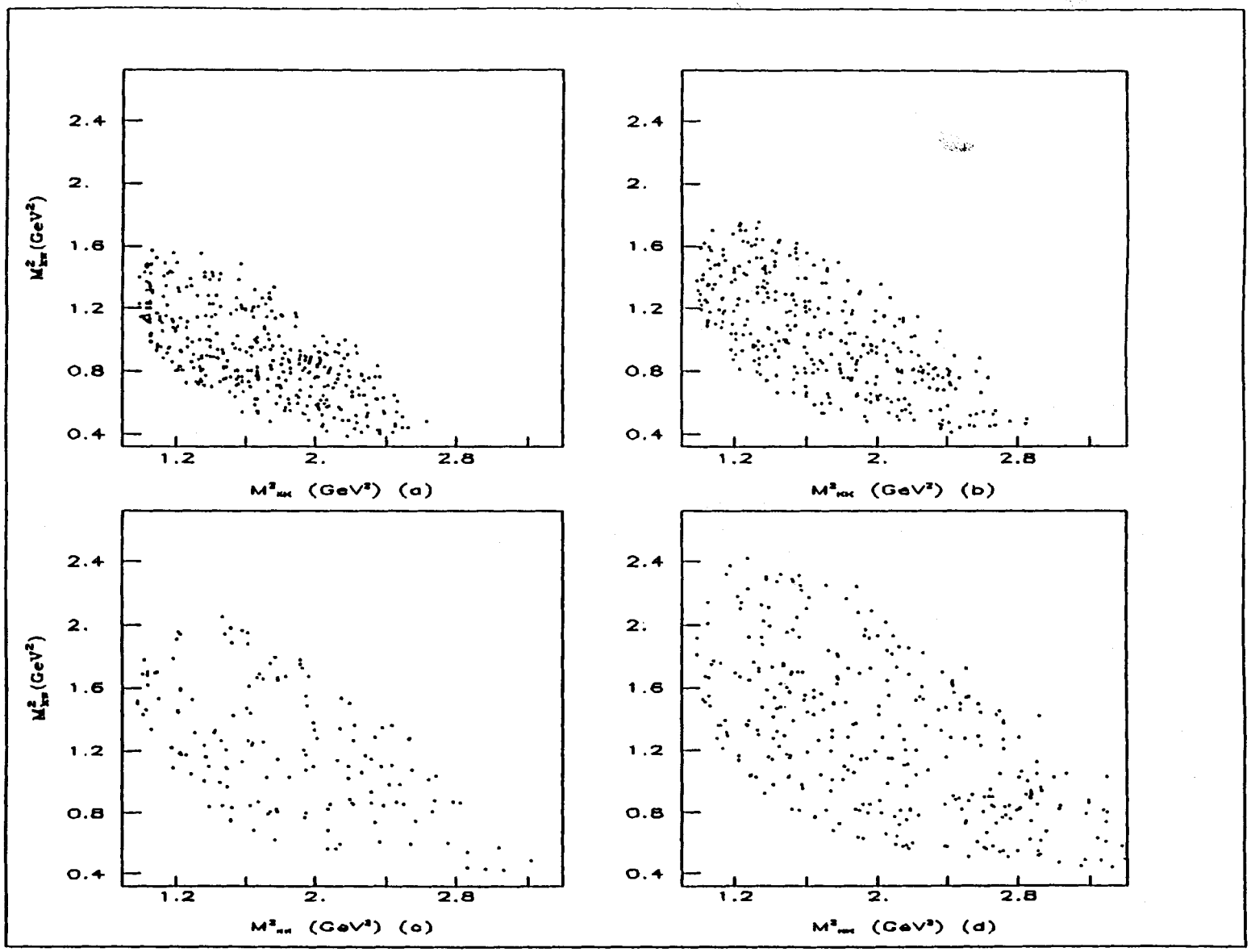

Figure 4.26: Dalitz plots for several background regions for $L/\sigma_L > 7$: a) 1.70 GeV to 1.77 GeV, b) 1.77 GeV to 1.84 GeV, c) 1.905 GeV to 1.940 GeV, d) 2.0 GeV to 2.07 GeV.

the M^2_{kk} projection and $M^2_{k\pi}$ projection were first examined. Then $K\overline{K}$ and $K\pi$ mass histograms were used to determine the ϕ and $\overline{K}^{*0}$ signals.

The $K\overline{K}$ and $K\pi$ mass distributions for $L/\sigma_L > 7$ for the four mass regions are shown in Fig. 4.27 and Fig. 4.28. The ϕ signal at about 1.02 GeV is seen to decrease as the $K\overline{K}\pi$ mass increases; the $\overline{K}^{*0}$ signal near 0.9 GeV appears to remain constant. Since the statistics are limited, the ϕ and $\overline{K}^{*0}$ signals were estimated by counting the numbers of events in the bins corresponding to the signal region minus the estimated background events in the same bins. The signal region for the ϕ was defined as 1.0125 GeV to 1.0250 GeV and for the K^* was defined as 0.860 GeV to 0.920 GeV.

The numbers of $\overline{K}^{*0}$ and ϕ thus obtained were scaled to correspond with size of the D and D_s signal region (30 MeV). In Fig. 4.29 and Fig. 4.30 are shown the estimated numbers of $\overline{K}^{*0}$ and ϕ events per 30 MeV respectively for several L/σ_L cuts.

In order to find the amount of $K\overline{K}\pi$ non-resonant background in the D and D_s signal regions, the following approach was used: from the fit to the $K\overline{K}\pi$ invariant mass distribution one obtains the total number of background events(B) in the D and D_s signal regions. The assumption is that the background under either signal is composed of the ϕ, $\overline{K}^{*0}$, and $K\overline{K}\pi$ non-resonant background. With the values for the ϕ and $\overline{K}^{*0}$ background events obtained from the plots of Fig. 4.29 and Fig. 4.30, and with B from the fit to the mass distribution, one obtains an estimate of the number of $K\overline{K}\pi$ non-resonant background events.

A second method was also employed to estimate the numbers of background $\overline{K}^{*0}$, ϕ and $K\overline{K}\pi$ non-resonant events under the D and D_s signals. This method used fits to the Dalitz plot for the same background mass regions described above. The results of the Dalitz plot fits to the background regions agree within the statistical error with the results presented in this section. (The fit to the Dalitz plot is described in the next chapter and the results of the fits to the background region will be given in

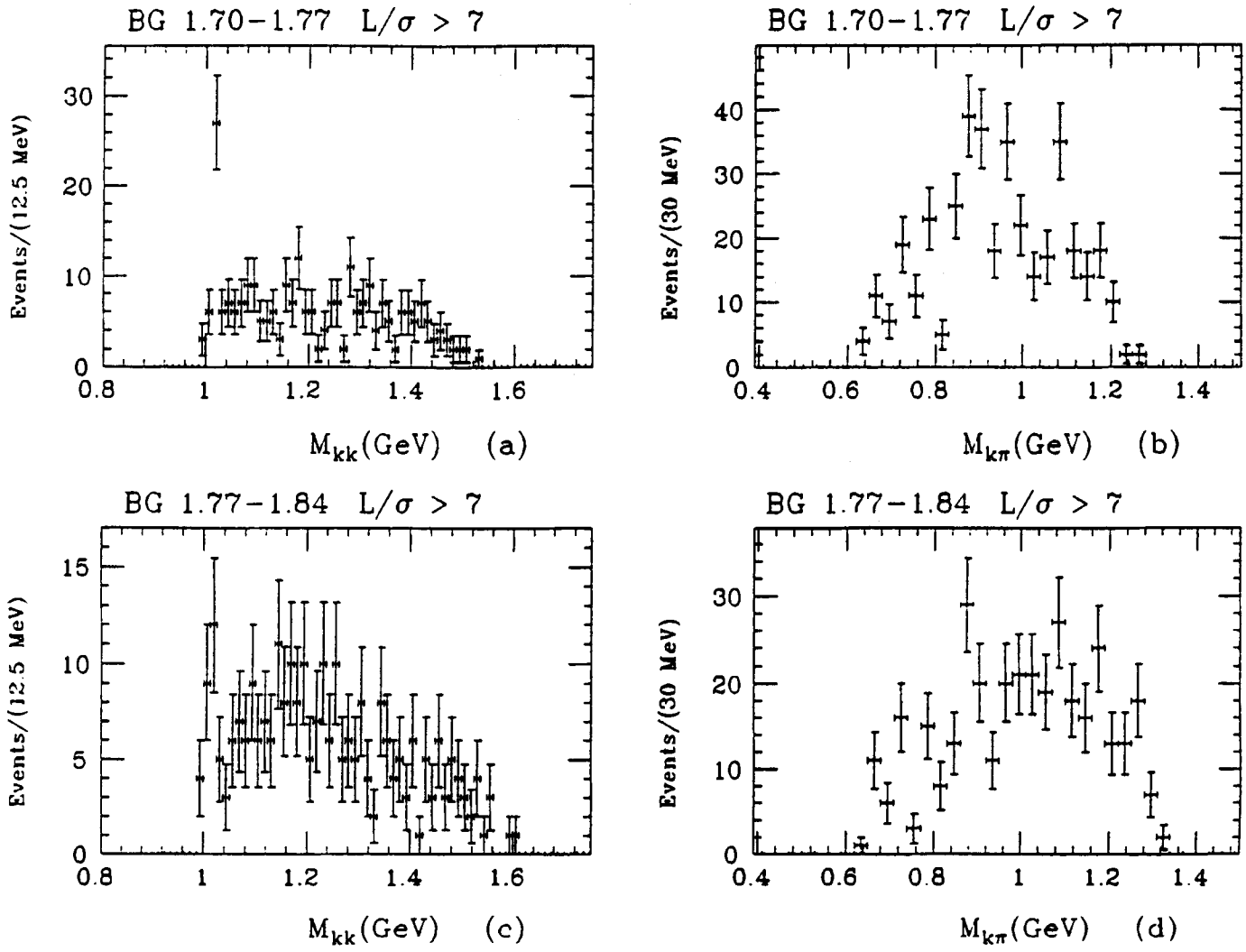

Figure 4.27: M_{kk} and $M_{k\pi}$ distributions for the background regions 1.70 GeV to 1.77 GeV and 1.77 GeV to 1.84 GeV.

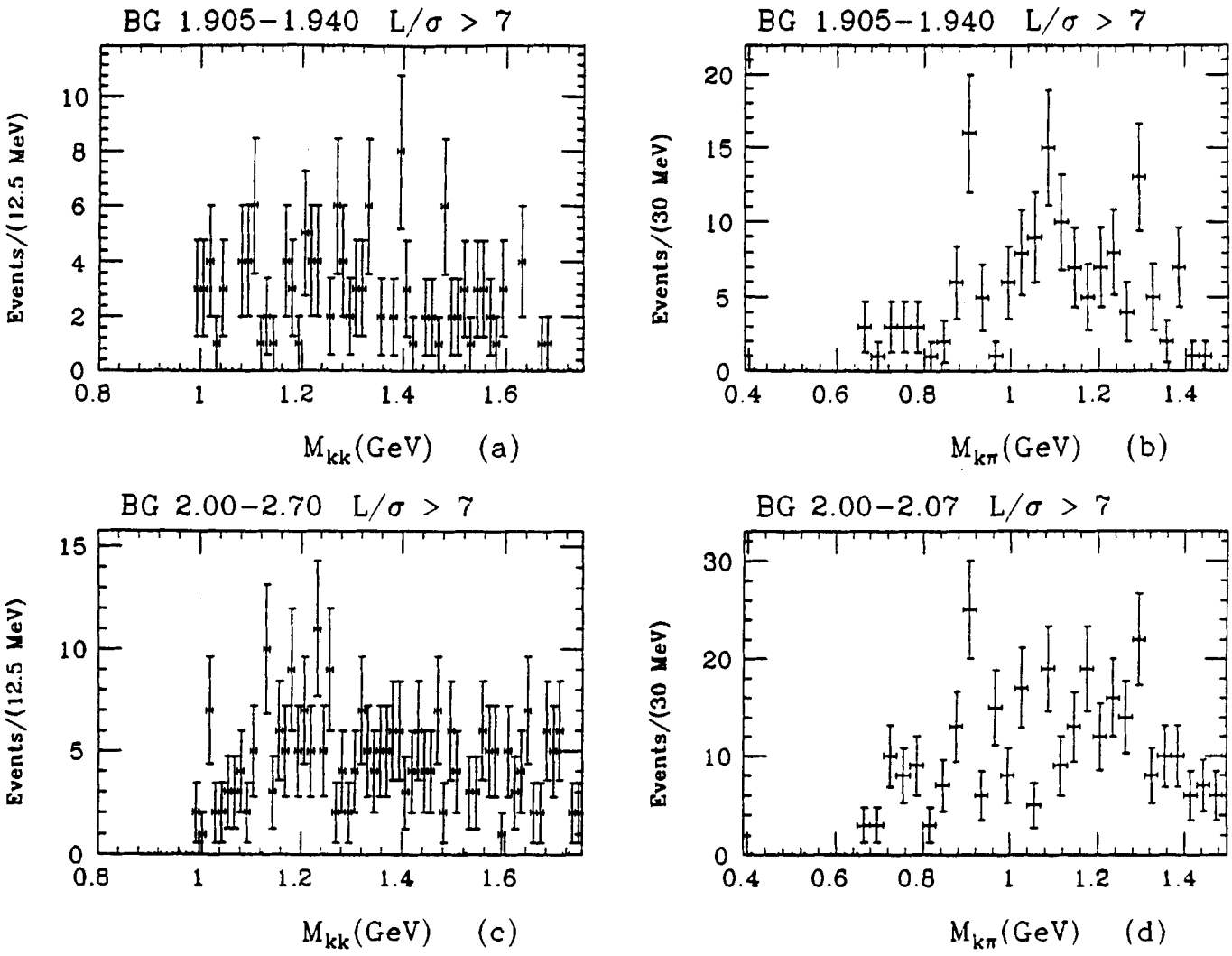

Figure 4.28: M_{kk} and $M_{k\pi}$ distributions for the background regions 1.905 GeV to 1.940 GeV and 2.0 GeV to 2.07 GeV

chapter 6).

4.8 $K\pi\pi$ Contamination

As mentioned earlier in this chapter, this contamination problem arises when one of the pions from the D decaying to the $K\pi\pi$ channel is misidentified by the Cerenkov analysis as a kaon. There is a "reflection peak" in the D_s region due to the misidentified events. From Monte Carlo studies it was found that the reflection peak has a non-Gaussian shape with a threshold at low mass, peaking around 2 GeV/c^2, and decreasing exponentially toward high mass above 2 GeV/c^2.

The amount of $K\pi\pi$ contamination can be significantly reduced (up to a certain level) by using a more restrictive kaon definition.

In order to observe the misidentification, the pion mass is assigned to the kaon with the same sign as the pion in events classified as $K\overline{K}\pi$ events. The $K\pi\pi$ invariant mass is then histogrammed to see if there is peak around the D mass. This analysis has been done for three different definitions for kaons:

- First definition: Both kaons can have an ISTATP of 4,12,or 7(momentum greater than 60 GeV).
- Second definition: the kaon with the same sign as the pion must have an ISTATP of 4 or 12.
- Third definition: both kaons must have an ISTATP of 4 or 12.

The histograms are shown for an L/σ_L cut of 7, and for the pion ISTATP definition of 2,3,7,14,15.

The results using the first kaon definition are shown in Fig. 4.31.a. In Fig. 4.31.b, are shown results from a similar analysis when the second kaon definition is used, and in Fig. 4.31.c when the third kaon definition is used.

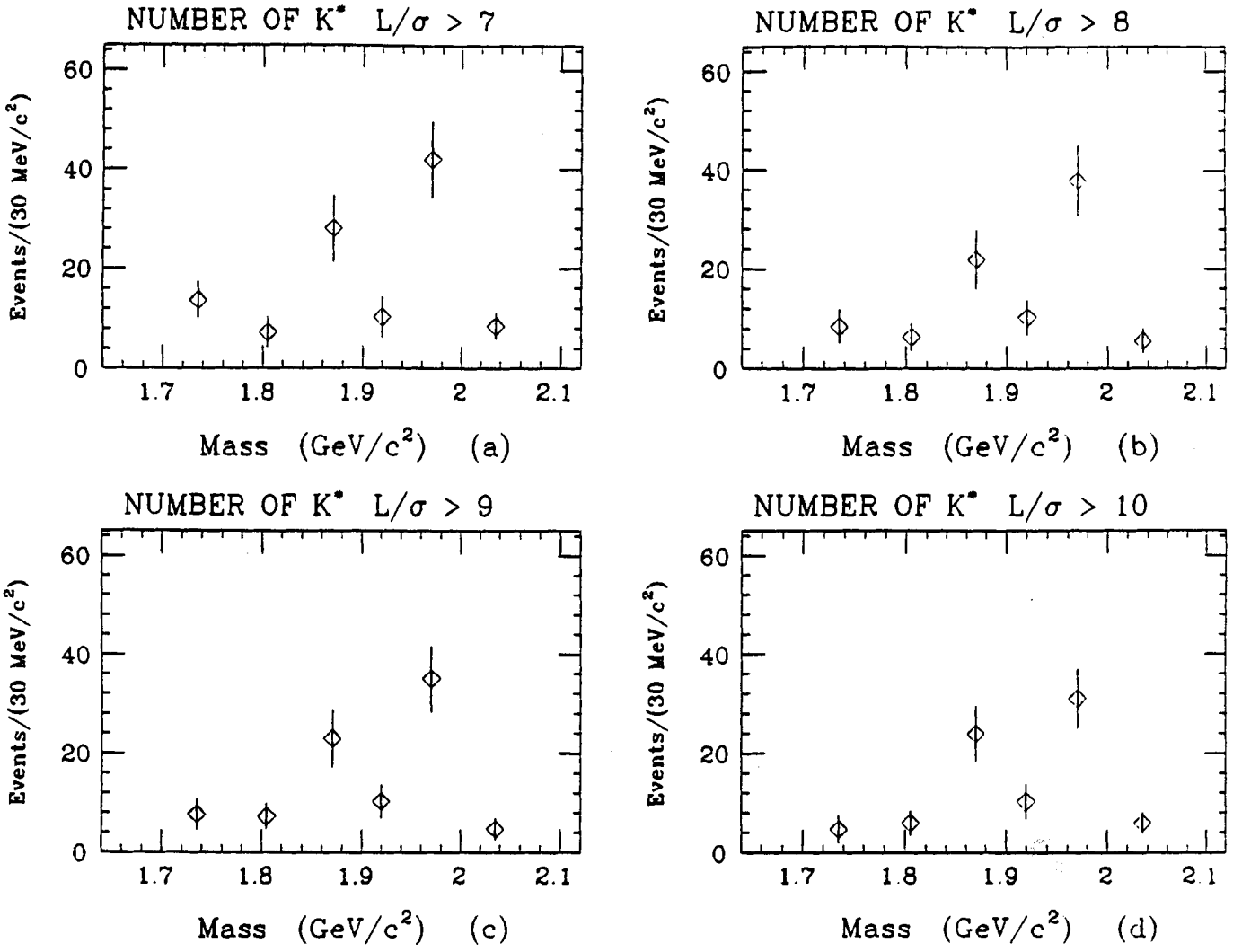

Figure 4.29: Number of $\overline{K}^{*0}$ per 30 MeV/c^2 for several values of the L/σ_L cut.

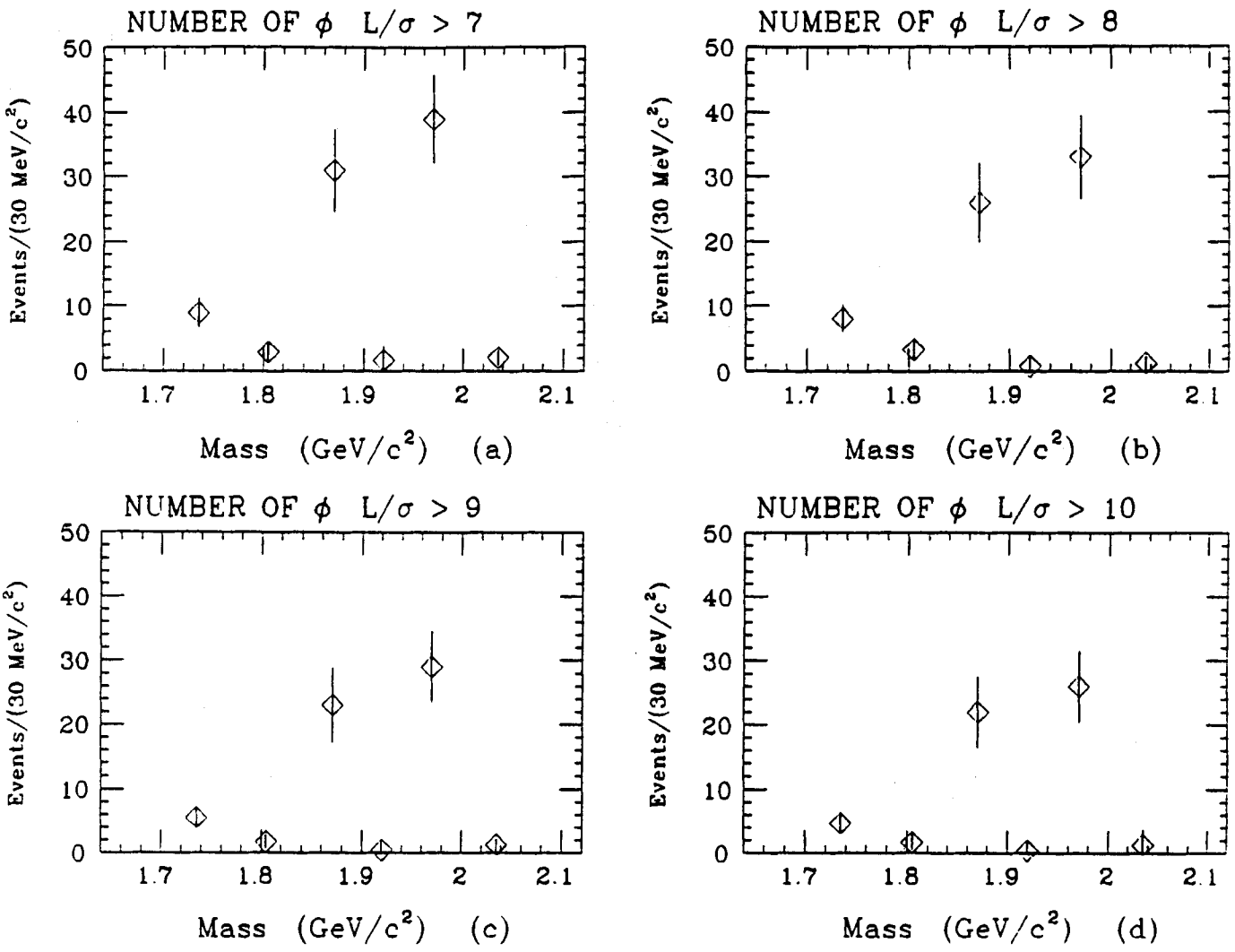

Figure 4.30: Number of ϕ per per 30 MeV/c^2 for several values of the L/σ_L cut.

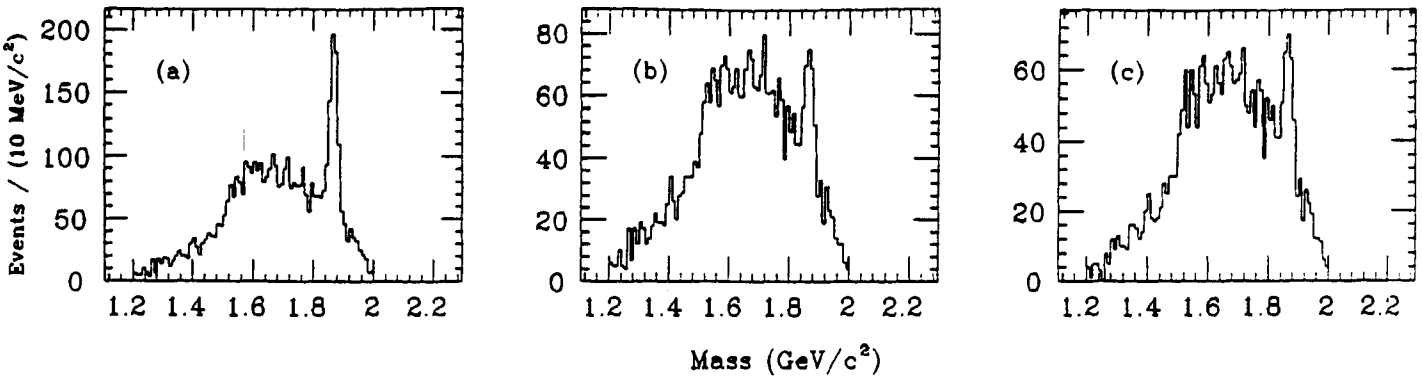

Figure 4.31: Invariant mass distribution for an L/σ_L cut $> 7.$ after the kaon with the same sign of the pion has been assigned the pion mass for the following kaon definitions a) first definition, b) second definition, c) third definition.

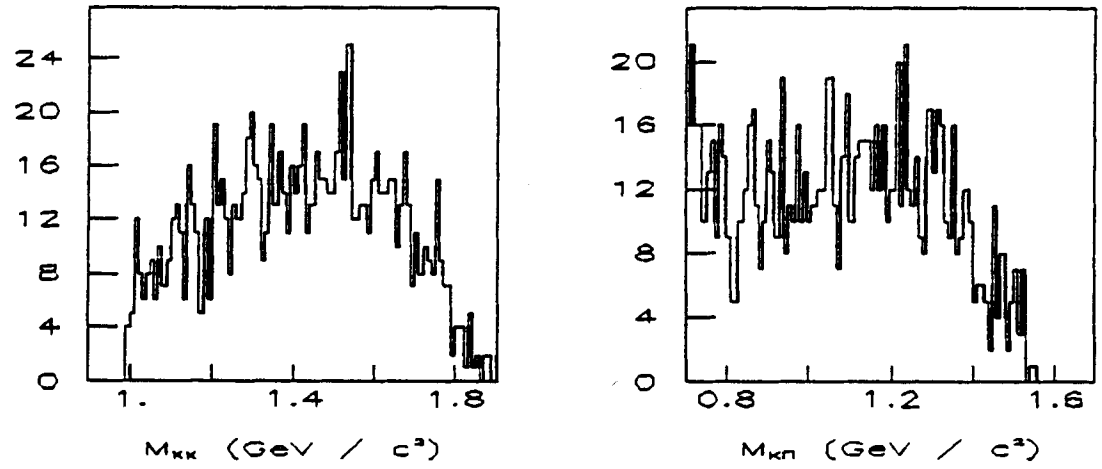

Figure 4.32: Monte Carlo Invariant mass distribution for: a) combinations of $K\overline{K}$, b) combinations of $K\pi$.

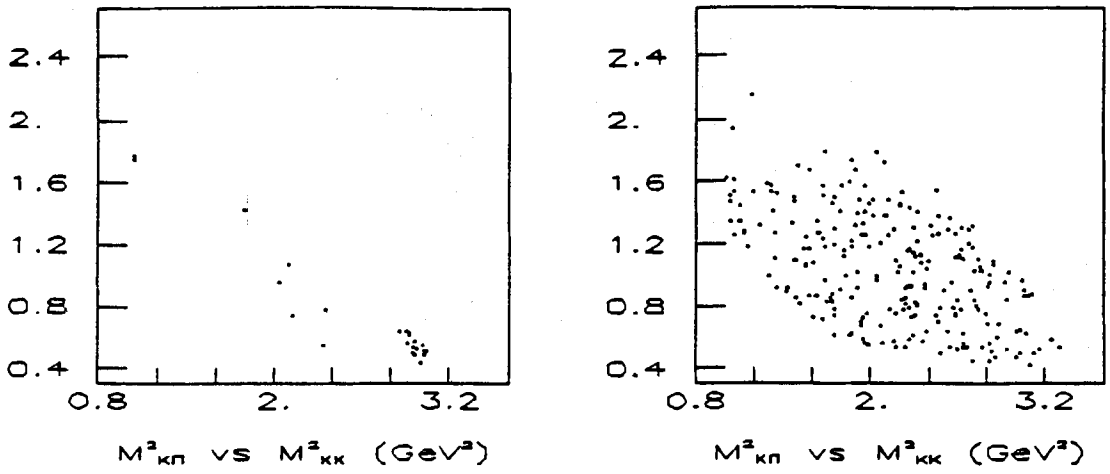

Figure 4.33: Monte Carlo Dalitz plots for misidentified events: a) under the D signal and b) events under the D_s signal.

A similar analysis is also done for the $K\overline{K}\pi$ events that are in the mass range from 1.950 GeV to 1.990 GeV. It is clear that the amount of $K\pi\pi$ contamination decreases when the Cerenkov id. for at least one kaon is defined to be only kaon definite or kaon/proton ambiguous (ISTATP = 4 or 12).

In order to estimate the number of $K\pi\pi$ events that are falsely flagged as $K\overline{K}\pi$ a sample of 270000 Rogue Monte Carlo events was generated, where the final state was the charmed D meson decaying to $K\pi\pi$. The strategy was to assign kaon mass to one of the pions of the $K\pi\pi$ system and study the effect of the misidentification. The first attempt was to see if the $K\pi\pi$ events that are misidentified have a structure in the D or D_s Dalitz plot. For that purpose the $K\overline{K}$ and $K\pi$ mass distributions were plotted for several L/σ_L cuts (See Fig. 4.32).

In the $K\overline{K}$ and $K\pi$ invariant mass plots of Fig. 4.32 there is no indication of a ϕ or K^* signal. The location of the $K\pi\pi$ misidentified events in the D and D_s Dalitz plots

is shown in Fig. 4.33. As expected we can ignore the effect of the $K\pi\pi$ contamination on the D signal.

In the D_s Dalitz plot of Fig. 4.33 there is no indication of a ϕ or K^* band. With respect to the structure of the $K\pi\pi$ misidentified events, an absence of points for the region that correspond to low mass for the m^2_{kk} and high mass for the $m^2_{k\pi}$ is observed.

A discussion can be made also about the location in the Dalitz plot of the background events. This location depends on which of the pions of the D^+ is misidentified. This is important when the $\overline{K}^{*0}$ contributes to the $K\pi\pi$ final state. From Monte Carlo studies it was found that if the pion that does not form the $\overline{K}^{*0}$ is the one misidentified, the location of the background event in the D_s Dalitz plot tends to be in the $\overline{K}^{*0}$ band. If the pion that forms the $\overline{K}^{*0}$ is the one which is misidentified, then the event location in the D_s Dalitz plot tends to be in the lower part of the ϕ band. In any case, if the number of misidentified events under the D_s signal is small, then the structure due to misidentified events can be ignored.

Several procedures were used in order to estimate the number of misidentified $K\pi\pi$ events in the $K\overline{K}\pi$ data samples. First, by studying the yield of misidentified Monte Carlo $K\pi\pi$ events, one can estimate the number of misidentified events under the D_s signal region. This yield is divided by the total number of events generated, multiplied by the ratio of the branching ratios of D^+ decaying to $K\pi\pi$ and D_s decaying to $K\overline{K}\pi$ and then multiplied by the number of data events in the $D \rightarrow K\pi\pi$ signal region. From this procedure the number of misidentified events among the 282 events in the D_s signal region for an $L/\sigma_L > 7$ was estimated to be only 15 events.

A second procedure parameterized the reflection peak due to the misidentification. This distribution is asymmetric and decreases slowly at high $K\overline{K}\pi$ mass. The asymmetric signal was fitted with the following function (x = $K\overline{K}\pi$ mass):

TABLE 4.3
ESTIMATE FOR THE NUMBER OF MISIDENTIFIED EVENTS

Mass interval (GeV/c^2)	Number of Misid. events	L/σ_L
1.955 - 1.985	5	7
1.955 - 2.07	22.	7
1.955 - 1.985	7	8
1.955 - 2.07	31.	8
1.955 - 1.985	5	9
1.955 - 2.07	21.	9

$$f(x) = \begin{cases} Ae^{\frac{-(x-x_0)^2}{2\sigma}} & \text{if } x < x_0 \\ Ae^{\frac{-(x-x_0)^2}{2\sigma}} + Bxe^{\frac{x-x_0}{-\lambda}} & \text{if } x \geq x_0 \end{cases}$$

The above formula represents a Gaussian distribution (with center at x_0) with an exponential tail (see Fig. 4.34). From the fit the following values for the parameters were obtained:

- $x_0 = 1.990$ GeV
- $\sigma = 0.026$ GeV
- $\lambda = 1.990$
- A/B = 0.25

The above parameterization was included in fits to the data for the $K\overline{K}\pi$ signal. Integrating the number of events under the curve of this parameterization then gives an estimate for the number of misidentified events. In Table 4.3. is shown the numbers of events in the $K\overline{K}\pi$ sample as determined by this procedure.

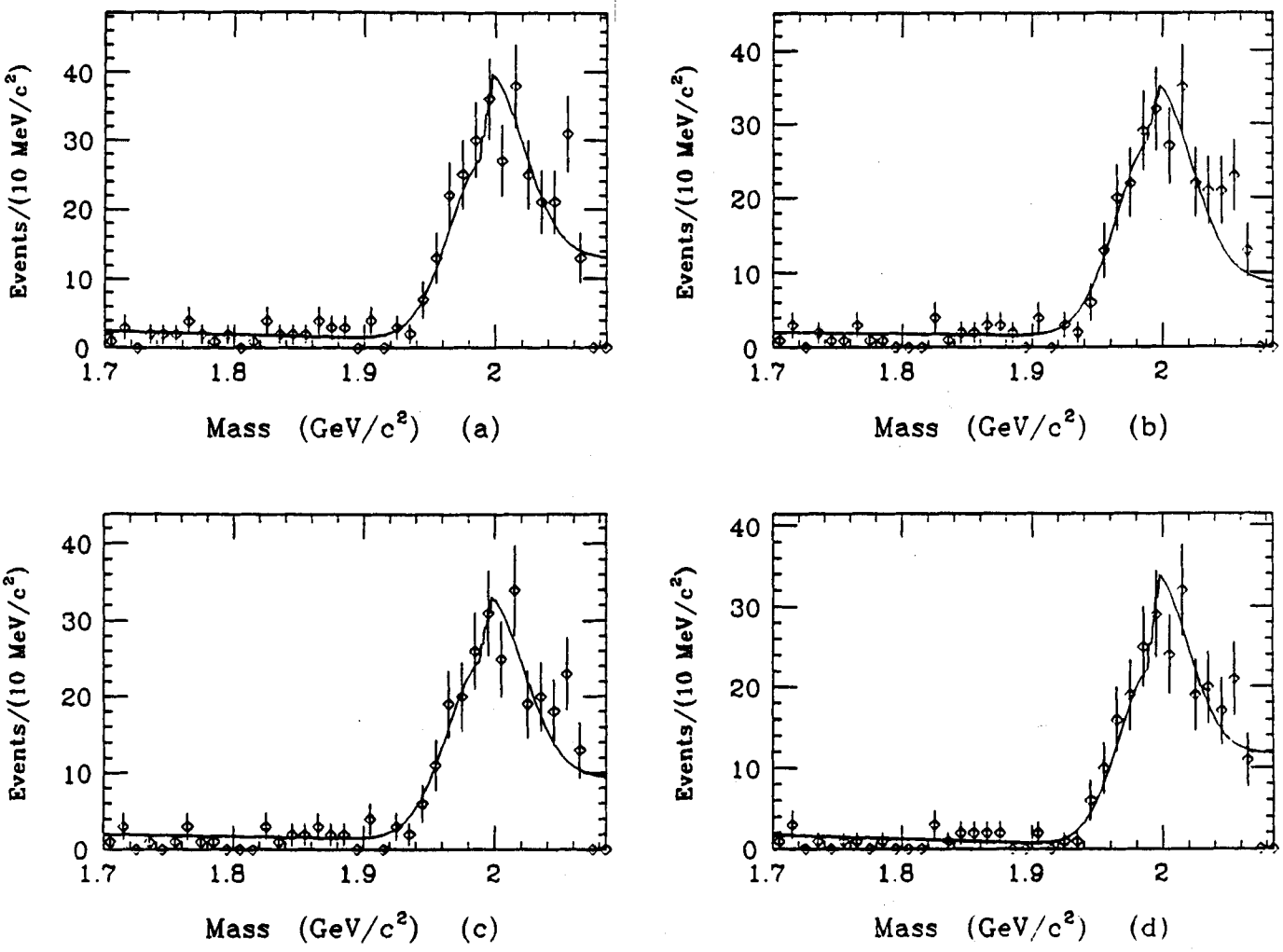

Figure 4.34: Fit to the Monte Carlo signal showing the reflection peak for the following values of L/σ_L: a) $L/\sigma_L > 7$, b) $L/\sigma_L > 8$, c) $L/\sigma_L > 9$, and d) $L/\sigma_L > 10$.

From the two procedures used to estimate the number of misidentified $K\pi\pi$ events, one can conclude that the contamination problem is small enough so that the contribution to structure of the Dalitz plot from these events is not significant. Nevertheless, due to the uncertainty in the background estimate from these two methods, the effect on the data were studied. For all $K\overline{K}\pi$ events in the D_s signal region (1.955 GeV - 1.985 GeV), the pion mass was assigned to the kaon with the same sign as the pion. Then the value of the $K\pi\pi$ invariant mass was calculated and if this value was in the D signal region (1.855 Gev - 1.885 GeV) then that event was rejected. From Monte Carlo studies it was found that this cut did not introduce a significant bias in the structure seen in the D_s Dalitz plot.

The branching ratios for the D_s decaying to $\overline{K}^{*0}K$ and $K\overline{K}\pi$ non-resonant with respect to the $\phi\pi$ decay channel were calculated with the above cut. The results changed less than one standard deviation from the results when the above cut was not used. (See chapter 6 for branching ratio results).

CHAPTER 5

DALITZ PLOT FITTING PROCEDURE

In order to obtain the contributions to the $K\overline{K}\pi$ signal from the three decay channels $K\overline{K}\pi$, $\overline{K}^{*0}K$ and $\phi\pi$ and to calculate branching ratios, a standard amplitude analysis was carried out. For that purpose a maximum likelihood fit to the Dalitz plot was performed. The Dalitz plot fitting procedure has several advantages over other techniques in determining branching ratios. The momentum of the final state particles and the spin of the two-body resonances are taken into account. In addition the likelihood function is built in such a way that interference among the different decay channels is included. Included in the analysis is also the background contribution from different sources to the different channels. The efficiency as a function of the variables in the Dalitz plot is used.

The method used to describe the population density of a Dalitz plot for a three body system final state was developed by C. Zemach [34]. In this method the amplitudes are built using all the parameters available in the decay. The original paper by Zemach was in reference to the decay K_L to 3π. The same procedure has been adapted to study many three-body system. For example it was adapted by M. Rath [33] for the $K^0_sK^0_s\pi^0$ system, and by R. Gardner [35] for the $K^0_s\pi\pi$ final state. In this analysis the amplitudes for the $K\overline{K}\pi$ final state system were built following these two procedures.

The CERN minimizing routine MINUIT has been used to determine the parameters of the likelihood function as well as the error for each parameter. An error analysis is presented.

5.1 Maximum Likelihood Function

In order to perform a maximum likelihood fit on an event-by-event basis, the total likelihood is defined as the product of the likelihood for each event:

$$L = \prod_{i=1}^{n} L_i \tag{5.1}$$

where for each event i the likelihood L_i is defined as:

$$L_i = f_s L_{is} + f_b L_{ib}. \tag{5.2}$$

The L_i consist of two terms; one for the signal L_{is} (could be either the D or D_s signal) and another for the background L_{ib}, and each term is multiplied by a constant that weights the amount of signal and background contributions to the Dalitz plot. The factor f_s is determined from the fit to the $K\overline{K}\pi$ invariant mass distributions, and is defined as:

$$f_s = \frac{s}{s+b} \tag{5.3}$$

where the term s is the number of signal events for the D or D_s signal region and the term b is the number of background events in the same signal region. Once f_s is calculated, the factor f_b is defined in such a way that the sum of both factors must be one

$$f_s + f_b = 1 \tag{5.4}$$

The two factors are fixed in the fit.

In order for L_i to be a probability density function (p.d.f), the integral of L_i over all available phase space must be unity

$$\int L_i d\Omega = 1 \tag{5.5}$$

where $d\Omega$ is the term corresponding to a differential of phase space. In terms of the variables of the Dalitz plot the differential of phase space is written as:

$$d\Omega = d_{m^2_{kk}} d_{m^2_{k\pi}} \tag{5.6}$$

5.1.1 Likelihood for the Signal

The term in the likelihood that describes the signal is a coherent sum of complex amplitudes that overlap and interfere. There are three such amplitudes, one for each decay channel making up the $K\overline{K}\pi$ signal. These are the $K\overline{K}\pi$ non-resonant, $\phi\pi$ and $\overline{K}^{*o}K$ signals. The likelihood for the signal is defined as:

$$L'_{is} = \epsilon \left| \sqrt{c_{nr}} e^{i\theta_{nr}} S_{nr} + \sqrt{c_{k^*k}} e^{i\theta_{k^*k}} S_{k^*k} + \sqrt{c_{\phi\pi}} e^{i\theta_{\phi\pi}} S_{\phi\pi} \right|^2 \tag{5.7}$$

where for a given decay channel j:

- c_j are fit coefficients;
- θ_j are the phase angles;
- S_j are the amplitudes; and
- ϵ is the efficiency, and is a function of m^2_{kk} and $m^2_{k\pi}$.

The prime superscript on L_{is} indicates an unnormalized likelihood. The amplitudes are weighted by the coefficients (c_j) that determine the contribution of each decay channel; the phase angles modulate the respective interference among the decay channels; and the efficiency, as mentioned in chapter 4, varies over the available phase space as a function of the variables m^2_{kk} and $m^2_{k\pi}$.

The individual amplitudes S_j for the decay channel are properly normalized over the available phase space. For example, for a given decay channel j the normalized amplitude is defined as:

$$S_j = \frac{S'_j}{\sqrt{\int \left|S'_j\right|^2 d\Omega}}. \tag{5.8}$$

In the above formula the integration is done numerically. Each individual amplitude is a complex quantity, and can be written as:

$$S_j = re^{i\alpha_j} \tag{5.9}$$

where r is the modulus and α is the intrinsic phase angle of the amplitude j. This quantity depends on the mass of the decay products, with the phase angle coming from the complex Breit-Wigner amplitude involved.

The likelihood L'_{is} has to be normalized:

$$L_{is} = \frac{L'_{is}}{\int L'_{is} d\Omega}. \tag{5.10}$$

The integral of L'_{is} is carried out numerically. The fit coefficients and phase angles do not depend on the phase space variables, so they can be factored out of the integral. The integration is done before the fitting and the values obtained are stored in a file to be read later on in the fitting procedure.

Once the likelihood for the signal events is properly normalized, one can define the fit fraction for each decay channel as the fit coefficient for the respective channel divided by the normalization constant N_c. (This is defined as: $N_c = \int L_{is} d\Omega$. For the purpose of evaluating the fit fractions, the efficiency is not included.) Due to the interference among the decay channels the sum of the fit fractions is not necessarily one.

The model that describes the three-body decay process can assume that the resonances interfere (the coherent case) or that there is no interference (the incoherent

case). In the latter case the sum of the fit fractions is one. (In the present analysis both possibilities have been considered.)

5.1.2 The Amplitudes

As mentioned before the amplitudes are complex and overlap and can interfere. The amplitude for the $K\overline{K}\pi$ non-resonant decay channel is taken to be a constant over the entire phase space. With the normalization condition this amplitude is given by: $\frac{1}{\sqrt{\int d\Omega}}$.

The amplitudes for the resonance decay channels (namely the $\phi\pi$ and $\overline{K}^{*0}K$ modes) are constructed in such a way that they model the strong decay of the ϕ and K^* and also take into account the conservation of angular momentum for the decay of a pseudoscalar (the D or D_s meson) into a vector(the ϕ or the K^*) and another pseudoscalar (the pion or kaon). Each amplitude is built using the cross product of the covariant spin vector of the two body resonance with the four momentum of the recoiling third particle evaluated in the rest frame of the three body decay system. (See Fig. 5.1) H

To illustrate the method, the amplitude for the K^*K decay channel is worked out as an example (the $\phi\pi$ decay channel is completely analogous). The spin of the K^* is represented by the four-momentum vector: $(0,\vec{p}'_k - \vec{p}'_\pi)$, where the three-momentum vector part is evaluated in the K^* rest frame. In order to represent the spin of the K^* in the three-body rest frame, the three-momentum vectors for the K and the π are represented as four-momentum vectors in a covariant form given by Zemach :

$$\vec{p}'_k \rightarrow p_k - \frac{(p_k + p_\pi)}{m^2_{k\pi}}(p_k \cdot (p_k + p_\pi))$$

$$\vec{p}'_\pi \rightarrow p_\pi - \frac{(p_k + p_\pi)}{m^2_{k\pi}}(p_\pi \cdot (p_k + p_\pi))$$

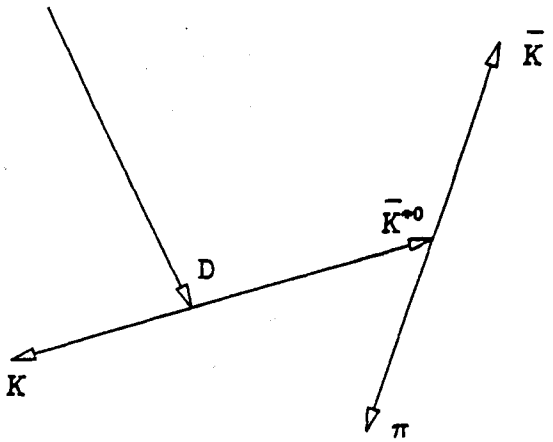

Figure 5.1: Sketch of the three-body rest system for the $K\overline{K}\pi$ final state. The sequence of decays is: $D \rightarrow \overline{K}^{*0}K$ followed by the decay of the $\overline{K}^{*0} \rightarrow \overline{K}\pi$.

where p_k and p_π are the respective four momenta of the kaon and pion respectively, and $m^2_{k\pi}$ is the effective mass of the $k\pi$ system. In this way the spin of the K^* in the three-body rest system is represented by the following expression:

$$(p_k - p_\pi) + \frac{q_{k\pi}}{m^2_{k\pi}}(m^2_\pi - m^2_k) \tag{5.11}$$

where the term $q_{k\pi}$ is defined as $p_k + p_\pi$. The scalar product of the covariant spin vector of the K^* and the four momentum of the recoiling kaon in the $K\overline{K}\pi$ rest system is given by:

$$((p_k - p_\pi) + \frac{q_{k\pi}}{m^2_{k\pi}}(m^2_\pi - m^2_k)) \cdot p_k \tag{5.12}$$

The above equation can be written in terms of the variables of the Dalitz plot, m^2_{kk} and $m^2_{k\pi}$. For that purpose the following relations are used:

$$m^2_{k\pi} = (p_k + p_\pi)^2 \tag{5.13}$$

and

$$M^2 = (p_k + p_{\overline{k}} + p_\pi)^2 \tag{5.14}$$

Where $m^2_{k\pi}$ is the effective mass for the decay products of the K^* and M is the rest mass of the parent particle (it could be either the D or D_s). With the above relations the scalar product between the covariant spin vector of the K^* and the four momentum of the recoiling kaon is calculated and is entirely a function of the variables available in the decay process. So, for simplicity, one can define the scalar product by a function $g(m^2_{kk}, m^2_{k\pi})$:

$$g(m^2_{kk}, m^2_{k\pi}) = ((p_k - p_\pi) + \frac{q_{k\pi}}{m^2_{k\pi}}(m^2_\pi - m^2_k)) \cdot p_k. \tag{5.15}$$

Explicitly g is given by the following relation:

$$g(m^2_{kk}, m^2_{k\pi}) = \frac{1}{2}\left(m^2_{kk} - m^2_k - m^2_k\right)\left(1 - \frac{m^2_k - m^2_\pi}{m^2_{k\pi}}\right) \tag{5.16}$$

$$-\frac{1}{2}\left(M^2 + m^2_k - m^2_{kk} - m^2_{k\pi}\right)\left(1 + \frac{m^2_k - m^2_\pi}{m^2_{k\pi}}\right)$$

For the $\phi\pi$ decay channel the function $g(m^2_{kk}, m^2_{k\pi})$ is given by:

$$g(m^2_{kk}, m^2_{k\pi}) = \frac{1}{2}\left(M^2 - m^2_{kk} + m^2_\pi\right) + m^2_k - m^2_{k\pi}$$

In the above equations m_k and m_π are the respective rest masses of the kaon and pion and taken from the Particle Data Group (P.D.G.) [7].

Finally the amplitude needs a term that parameterizes the strong decay either for the ϕ or K^*. The common Breit-Wigner resonance function is used. This function is defined as follows: (again with the K^*K decay channel as an example)

$$BW(k^*) = \frac{\sqrt{m_{k^*}\Gamma_0}}{m^2_{k^*} - m^2_{k\pi} - im_{k^*}\Gamma(m_{k\pi})} \tag{5.17}$$

where:

- m_{k^*} is the nominal mass for the K^* (0.892 GeV/c^2);
- $m_{k\pi}$ is the effective mass combination for the decay products of the K^*;
- Γ_0 is the natural width for the K^* (found from Monte Carlo (50 MeV/c^2) ; and
- $\Gamma(m_{k\pi}) = \Gamma_0(\frac{p_{k\pi}}{p_{k^*}})^3$

  The term $p_{k\pi}$ is the two body breakup momentum of the $K\overline{K}\pi$ system. The term p_{k^*} is the breakup momentum at the nominal K^* mass. This value is a constant and taken from the P.D.G.

Finally, the amplitude for the $\phi\pi$ or $\overline{K}^{*0}K$ decay channel can be written as:

$$S_j^{'} = g_j(m_{kk}^2, m_{k\pi}^2)BW_j \tag{5.18}$$

where j represent a given decay channel, and the prime stands for the unnormalized amplitude.

5.1.3 Likelihood for the Background

The likelihood for the background term is made up of an incoherent sum of complex amplitudes. The complex amplitudes for the background do not include the Zemach factors. Each amplitude is weighted by a different coefficient (b_j) that has already been predetermined, from the measured background contribution for the three different decay channels. These coefficients are not allowed to varied in the fit. (See in chapter 4 the section on background studies). Explicitly the likelihood for the background is written as:

$$L_{ib}^{'} = b_{nr}\,|B_{nr}|^2 + b_{k^*k}\,|B_{k^*k}|^2 + b_{\phi\pi}\,|B_{\phi\pi}|^2 \tag{5.19}$$

The amplitudes for each of the decay channel backgrounds are also properly normalized

$$B_j = \frac{B_j'}{\sqrt{\int \left|B_j'\right|^2 d\Omega}} \tag{5.20}$$

and the likelihood for the background is normalized in the following way:

$$L_{ib} = \frac{b_{nr}\left|B_{nr}\right|^2 + b_{k^*k}\left|B_{k^*k}\right|^2 + b_{\phi\pi}\left|B_{\phi\pi}\right|^2}{b_{nr} + b_{k^*k} + b_{\phi\pi}} \tag{5.21}$$

5.1.4 The Finding of the Maximum Value for L

A function f is now introduced:

$$f = -\log L \tag{5.22}$$

or (see eq. 5.1):

$$f = -\sum_i^n \log(L_i) \tag{5.23}$$

One now searches for the parameters that minimize f (that is equivalent to finding the parameters that maximize L). The fit is done by fixing one of the fit coefficients (to one) and one phase angle (to zero). The minimization of f is done by the CERN package called MINUIT [36]. This is a minimizing routine, that, among several features, finds the minimum of a multi-parameter function.

5.2 Fit Fraction Error Analysis

The fit fraction for a given decay channel k is f_k and is defined as follows:

$$f_k = \frac{c_k}{N_c}$$

where N_c is the normalization constant, $N_c = \int L_{is} d\Omega$. (The efficiency is not included in this integral) [37]. N_c is a function of the fit coefficients and phase angles:

$$N_c = N_c(c_1, c_2, c_3, \theta_1, \theta_2, \theta_3)$$

(One of the three phases angles and one fit coefficient are held constant). The variance for the fit fraction f_k is given by [38]:

$$Var f_k = \sum_{i,j} \frac{\partial f_k}{\partial \beta_i} \frac{\partial f_k}{\partial \beta_j} Var(\beta_i, \beta_j)$$

In the above formula the derivative is taken with respect to the fit coefficients and phase angles, and Var(β_i,β_j) is the covariance error matrix. The correlation matrix is obtained from MINUIT and the covariance error matrix is calculated from the relation:

$$V_{ij} = \rho_{ij} \sqrt{V_{ii} V_{jj}}$$

where ρ_{ij} is an element of the correlation matrix, V_{ij} is an element of the covariance error matrix and V_{ii} is a diagonal term of the error matrix ($\sigma_i^2 = V_{ii}$ and $\sigma_{ij}^2 = V_{ij}$).

5.3 Branching Ratio Error Analysis

The correlation among the fit coefficients is included in determining the error in the branching ratio. For example the branching ratio for the D_s decaying to $\overline{K}^{*0}K$ with respect to D_s decaying to $\phi\pi$ is given by the following relation:

$$\frac{\Gamma(D_s \to \overline{K}^{*0} K)}{\Gamma(D_s \to \phi\pi)} = \frac{f_{\overline{k}^{*0}k}}{f_{\phi\pi}} \frac{BR(\phi \to KK)}{BR(\overline{K}^{*0} \to K\pi)}$$

Since $f_i = \frac{c_i}{N_c}$, the above relation becomes:

$$\frac{\Gamma(D_s \to \overline{K}^{*0} K)}{\Gamma(D_s \to \phi\pi)} = \frac{c_{\overline{k}^{*0}k}}{c_{\phi\pi}} 0.74 = u$$

where 0.74 is the ratio of the ϕ decay probability to K^+K^- to the $\overline{K}^{*0}$ decay probability to $K\pi$. Thus the error for the branching ratio is given by:

$$\sigma_u^2 = (0.74)^2 \sum_{i,j} \frac{\partial u}{\partial c_i} \frac{\partial u}{\partial c_j} Var(c_i, c_j)$$

where c_i are the approppiate fit coefficients, and $Var(c_i,c_j)$ is calculated in a manner similar to that described for the fit fraction error analysis.

CHAPTER 6

DALITZ PLOT FIT RESULTS

6.1 Introduction

In this chapter are presented the results of Dalitz plot fits to the D_s and D^+ samples. Fits to generated data as well as to real data are presented. Branching ratio results for D_s and D^+ are reported and compared with world averages.

The convention for the name of the parameters as used in this chapter which were described in chapter 5 (c_j for the fit coefficients and θ_j for the phase angles) is as follows:

- β_1 represents the $K\overline{K}\pi$ non-resonant fit coefficient;
- β_2 represents the $\overline{K}^{*0}K$ fit coefficient;
- β_3 represents the $\phi\pi$ fit coefficient;
- β_4 represents the $K\overline{K}\pi$ non-resonant phase angle;
- β_5 represents the $\overline{K}^{*0}K$ phase angle;
- β_6 represents the $\phi\pi$ phase angle;
- f_{1bk} represents the $K\overline{K}\pi$ non-resonant background fit fraction;
- f_{2bk} represents the $\overline{K}^{*0}K$ background fit fraction;

- f_{3bk} represents the $\phi\pi$ background fit fraction.

The convention for the fit fractions is as follows:

- f_1 represents the $K\overline{K}\pi$ non-resonant fit fraction;
- f_2 represents the $\overline{K}^{*0}K$ fit fraction;
- f_3 represents the $\phi\pi$ fit fraction;

The correlation and covariance error matrices are 4 X 4 arrays (two of the 6 fit parameters are held fixed in the fits). The term V_{ij} represents an element of the covariance error matrix and the indices "i" and "j" run from β_1 through β_6 respectively. Explicitly the covariance error matrix is written as follows:

$$V = \begin{pmatrix} V_{\beta_1\beta_1} & V_{\beta_3\beta_1} & V_{\beta_4\beta_1} & V_{\beta_6\beta_1} \\ V_{\beta_1\beta_3} & V_{\beta_3\beta_3} & V_{\beta_4\beta_3} & V_{\beta_6\beta_3} \\ V_{\beta_1\beta_4} & V_{\beta_3\beta_4} & V_{\beta_4\beta_4} & V_{\beta_6\beta_4} \\ V_{\beta_1\beta_6} & V_{\beta_3\beta_6} & V_{\beta_4\beta_6} & V_{\beta_6\beta_6} \end{pmatrix} \tag{6.1}$$

6.2 Dalitz Plot Fit to the Background Regions

As mentioned in chapter 4, a Dalitz plot fit was performed to the four background regions. The fit was done with the signal term in the likelihood function set to zero. In Fig. 6.1 is shown the Dalitz plot fit to the background region from 1.70 Gev to 1.77 Gev. From Dalitz plot fits such as this to the background regions, one obtains an estimate of the number of $K\overline{K}\pi$ (n.r.), $\overline{K}^{*0}K$ and $\phi\pi$ background events under the D^+ and D_s signal region. In Fig. 6.2 are shown the numbers of $\overline{K}^{*0}K$ and $\phi\pi$ events per unit mass for the four background regions and the D and D_s signal regions for events with $L/\sigma_L > 7$. From these fits, one obtains an estimate of the background fit fractions that were used in the Dalitz plot fits to the D^+ and D_s. The values used are 0.92 $\pm$ 0.04 for the $K\overline{K}\pi$ (n.r.) background fit fraction, 0.06 $\pm$ 0.04 for the $\overline{K}^{*0}K$

background fit fraction, and 0.02 $\pm$ 0.02 for the $\phi\pi$ background fit fraction. These values were held fixed during the fits to the D^+ and D_s. (These results are consistent with those of section 4.7).

6.3 Fits to Generated Samples

Several samples were generated in order to test the method used for the Dalitz plot fit. The samples were generated using the Acceptance-Rejection Method ([39]), [40]). That is, the same efficiency function used with the data, was used in generating the samples in order to simulate the acceptance of the spectrometer. The samples were generated under several conditions such as: incoherent decays with no background; incoherent decays with background; and coherent decays with and without background. The generated samples were fitted by the same program used to fit the data.

In Table 6.1 and in Fig. 6.3 are shown results of fits to D_s simulated samples. These samples were generated with a coherent mixture of 60% $\phi\pi$ and 40% $K\overline{K}\pi$ (n.r.) decay in the signal and 92% $K\overline{K}\pi$ (n.r.) and 8% $\phi\pi$ for the background respectively. The value of f_s used was 0.5. The parameter under study in these simulated samples was the phase angle for the $\phi\pi$ decay channel (β_6). Given the narrow width of the ϕ (5 MeV) it was important to know if the fitter was able to measure the generated value. The fitted values were consistent with the generated values.

In Table 6.2 are shown the results for D_s simulated samples generated with a coherent mixture of 60% $\overline{K}^{*0}K$ and 40% $K\overline{K}\pi$ (n.r.) modes with no background (f_s = 1). Again the fitted values were consistent with the generated values. Samples with only background events were also generated and fitted. In Fig. 6.4 is shown the fit to a simulated sample of 4000 background events consisting of 60% $K\overline{K}\pi$ (n.r.) 30% $\overline{K}^{*0}K$ and 10% $\phi\pi$. (For this case f_s is equal to 0.0). Note that the bands that correspond to the K^* and ϕ in Fig. 6.4.a do not have the depletions in the center (due

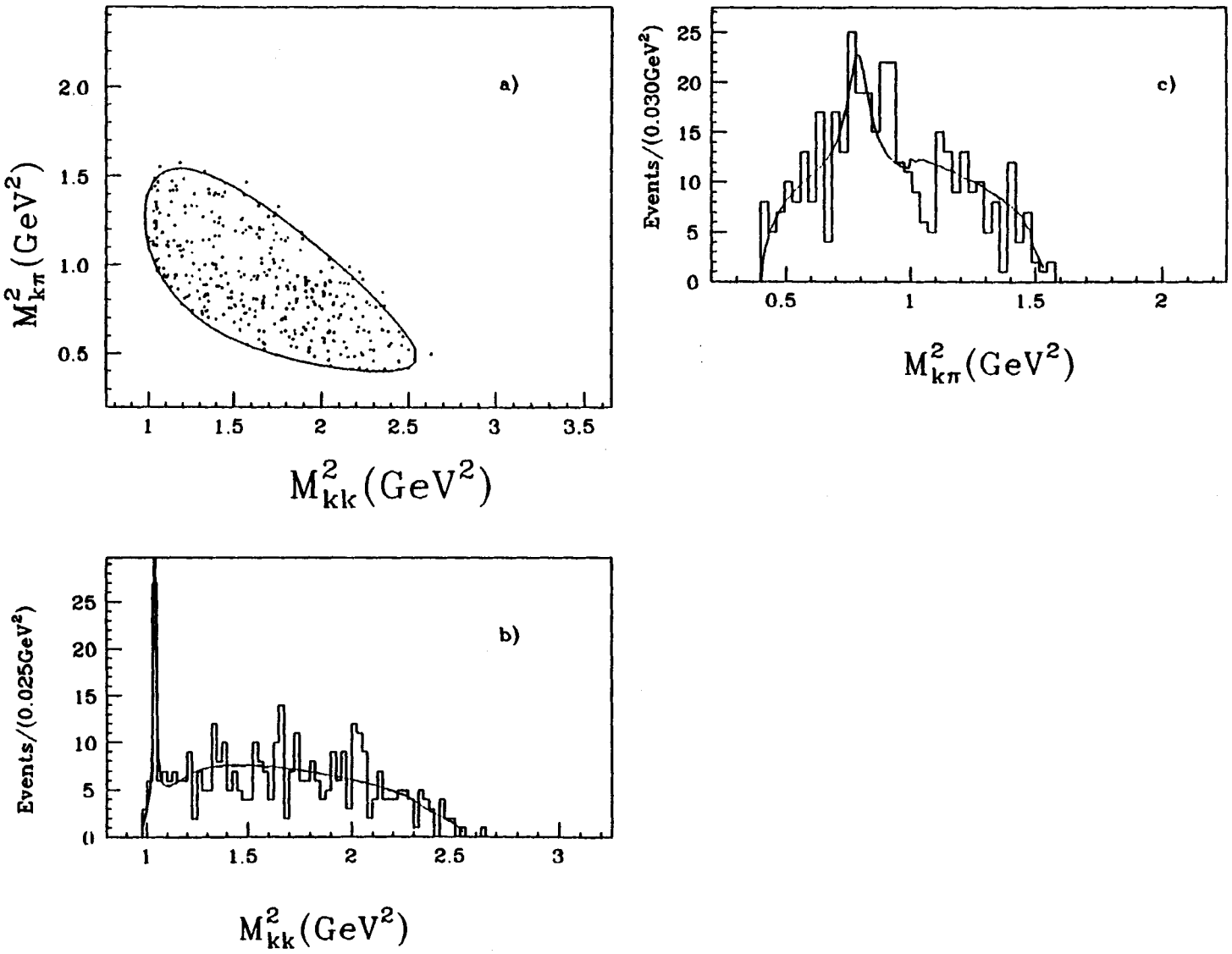

Figure 6.1: Fits to the background region 1.70 GeV - 1.77 GeV. showing the: b) $\phi\pi$ component and c) the $\overline{K}^{*0}K$ component.

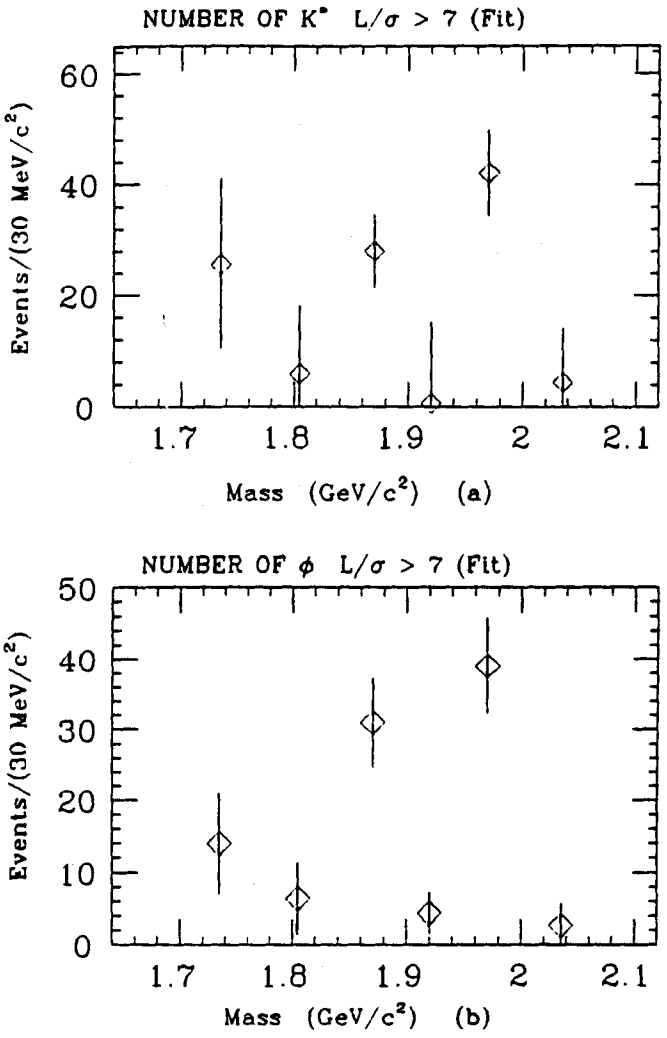

Figure 6.2: Number of $\overline{K}^{*0}K$ per 30 MeV/c^2 for events with $L/\sigma_L > 7$. b) Number of $\phi\pi$ per 30 MeV/c^2 for events with $L/\sigma_L > 7$.

TABLE 6.1
FIT RESULTS TO D_s SIMULATED DATA SAMPLES

SAMPLE	N. OF EVENTS	PAR.	GEN. VALUE	FIT
1	4000	β_4	0.0 rad	(fixed)
1		β_6	1.0 rad	0.97 $\pm$0.12 rad
2	2600	β_4	0.0 rad	(fixed)
2		β_6	1.2 rad	1.21 $\pm$0.08 rad

TABLE 6.2
FIT RESULTS TO D_s SIMULATED DATA SAMPLES ($f_s = 1$)

SAMPLE	N. OF EVENTS	PAR.	GEN. VALUE	FIT
1	1000	β_4	0.0 rad	(fixed)
1		β_5	2.0 rad	2.06 $\pm$0.06 rad
2	1000	β_4	0.0 rad	(fixed)
2		β_5	1.5 rad	1.49 $\pm$0.06 rad

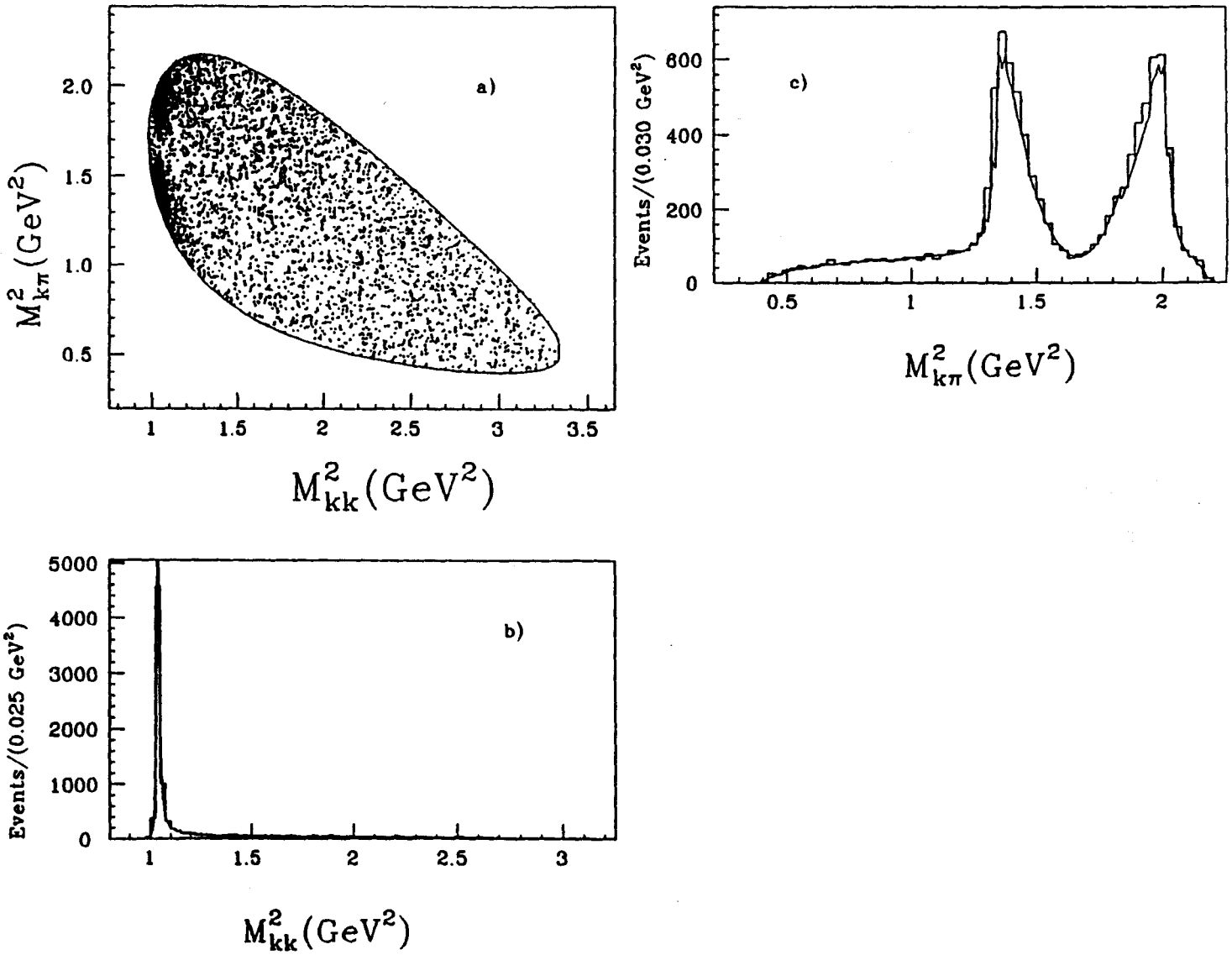

Figure 6.3: Dalitz plot fit for a generated coherent sample of 60% $\phi\pi$ and 40% $K\bar{K}\pi$ (n.r.). b) projection onto the m^2_{kk} axis and c) projection onto the $m^2_{k\pi}$ axis.

TABLE 6.3
FIT RESULTS TO SIMULATED BACKGROUND SAMPLE ($f_s = 0.0$)

PARAMETER	GEN. VALUE	FIT RESULT
f_{1bk}	0.6	0.60 $\pm$0.08
f_{2bk}	0.3	0.30 $\pm$0.05
f_{3bk}	0.1	0.09 $\pm$0.02

TABLE 6.4
FIT RESULTS TO D_s SIMULATED DATA SAMPLE ($f_s = 0.5$)

PARAMETER	GENERATED VALUE	FIT RESULTS
f_1	0.20	(fixed)
f_2	0.52	0.50 $\pm$0.05
f_3	0.31	0.28 $\pm$0.03
β_4	0.0 rad	(fixed)
β_5	2.0 rad	1.99 $\pm$0.02 rad
β_6	1.5 rad	1.51 $\pm$0.04 rad
f_{1bk}	0.90	(fixed)
f_{2bk}	0.06	(fixed)
f_{3bk}	0.04	(fixed)

to the $\cos^2\theta$ decay dependence for the D^+ and D_s decays) which are observed in the signal events. In Table 6.3 are shown the results of the fit.

In Table 6.4 are shown the results of a fit to a D_s simulated sample of 60000 events that was generated with the full set of fit parameters with an f_s value of 0.5. For this case too, the fitted values were consistent with the generated values.

6.4 Resolution Studies

The effect of the error in the invariant masses on the Dalitz plot fit was studied using a ROGUE sample of D_s decaying to $K\overline{K}\pi$(n.r.). The sample of 200000 events

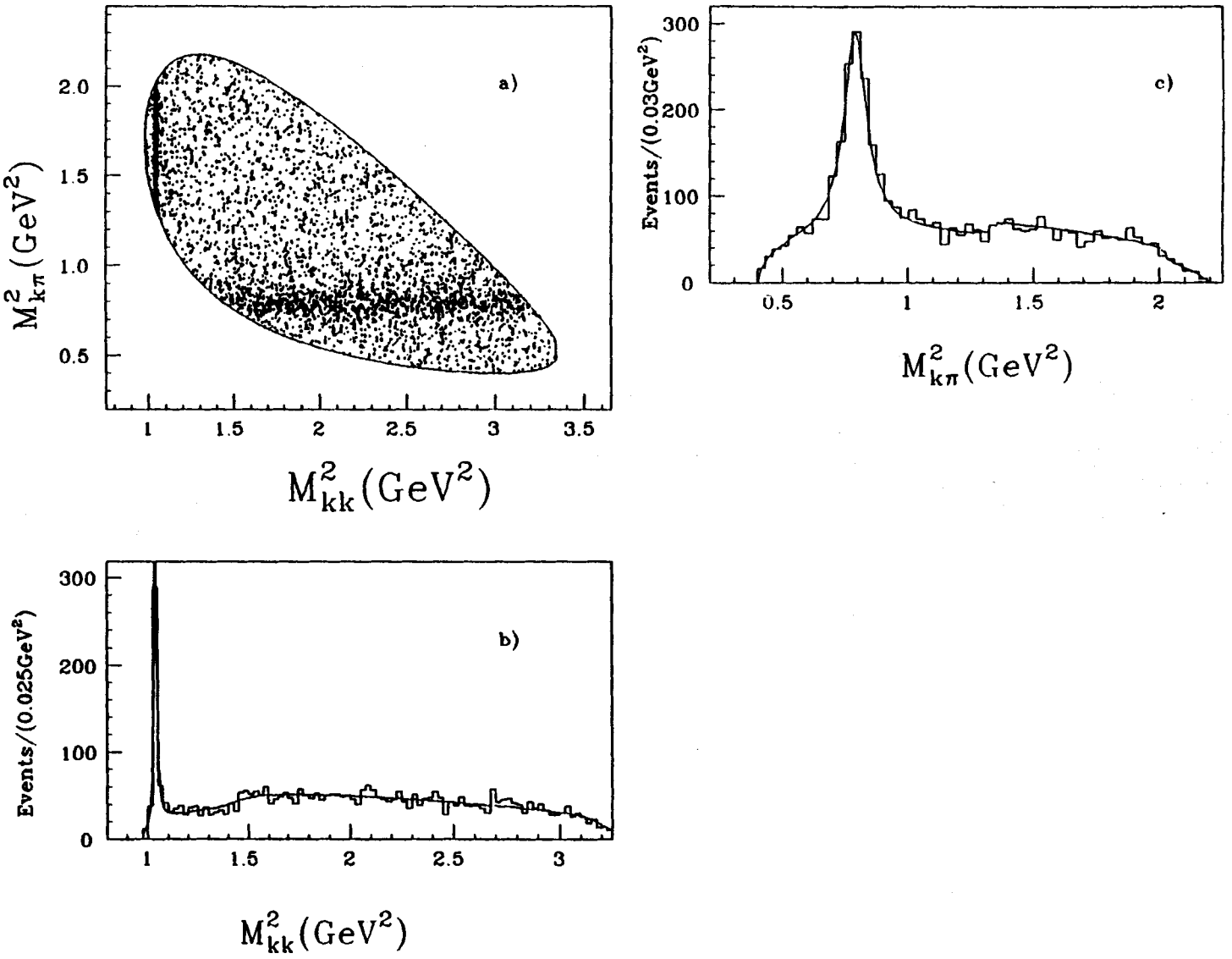

Figure 6.4: Dalitz plot fit for a D, generated background sample of 10% $\phi\pi$, 60% $K\bar{K}\pi$ (n.r.) and 30% $\bar{K}^{*0}K$. b) projection onto the m^2_{kk} axis and c) projection onto the $m^2_{k\pi}$ axis.

TABLE 6.5
RESOLUTION RESULTS FOR THE $M_{k\bar{k}}$ MASS

REGION	σ (MeV)
C1	2.47±0.06
C2	4.10±0.09
C3	5.25±0.10
C4	6.52±0.17
C5	8.02±0.26
C6	9.34±0.63

was passed through the same analysis cuts used on the data. The Dalitz plot was divided into strips of columns and rows (4 rows and 6 columns of size 0.4 GeV^2 by 0.45 GeV^2). For every column and row the difference between the reconstructed masses and the generated masses was histogrammed. In Fig. 6.5 is shown the Dalitz plot with the respective regions (rows and columns) used for the resolution studies. In Fig. 6.6 is shown histograms of the difference between the reconstructed masses and the generated masses for the $K\overline{K}$ combinations for each of the columns used. In Fig. 6.7 is shown histograms of the difference between the reconstructed masses and the generated masses for the $K\pi$ combinations for each of the rows used. The distributions were fitted with Gaussian functions. In Table 6.5 and in Table 6.6 are shown the value of the standard deviations (σ) found from the fits.

The ϕ band falls inside the C1 region, where the resolution is the best. For higher values of $m^2_{k\bar{k}}$ mass the resolution gets broader. The resolution in $m^2_{k\pi}$ changes quite slowly as one goes from the low mass to high mass values.

In order to see how the resolution effects the determination of the fit parameters, several samples were generated with different values for the fit parameters. In the generation of the samples, the generated values of $m^2_{k\bar{k}}$ and $m^2_{k\pi}$ were changed using

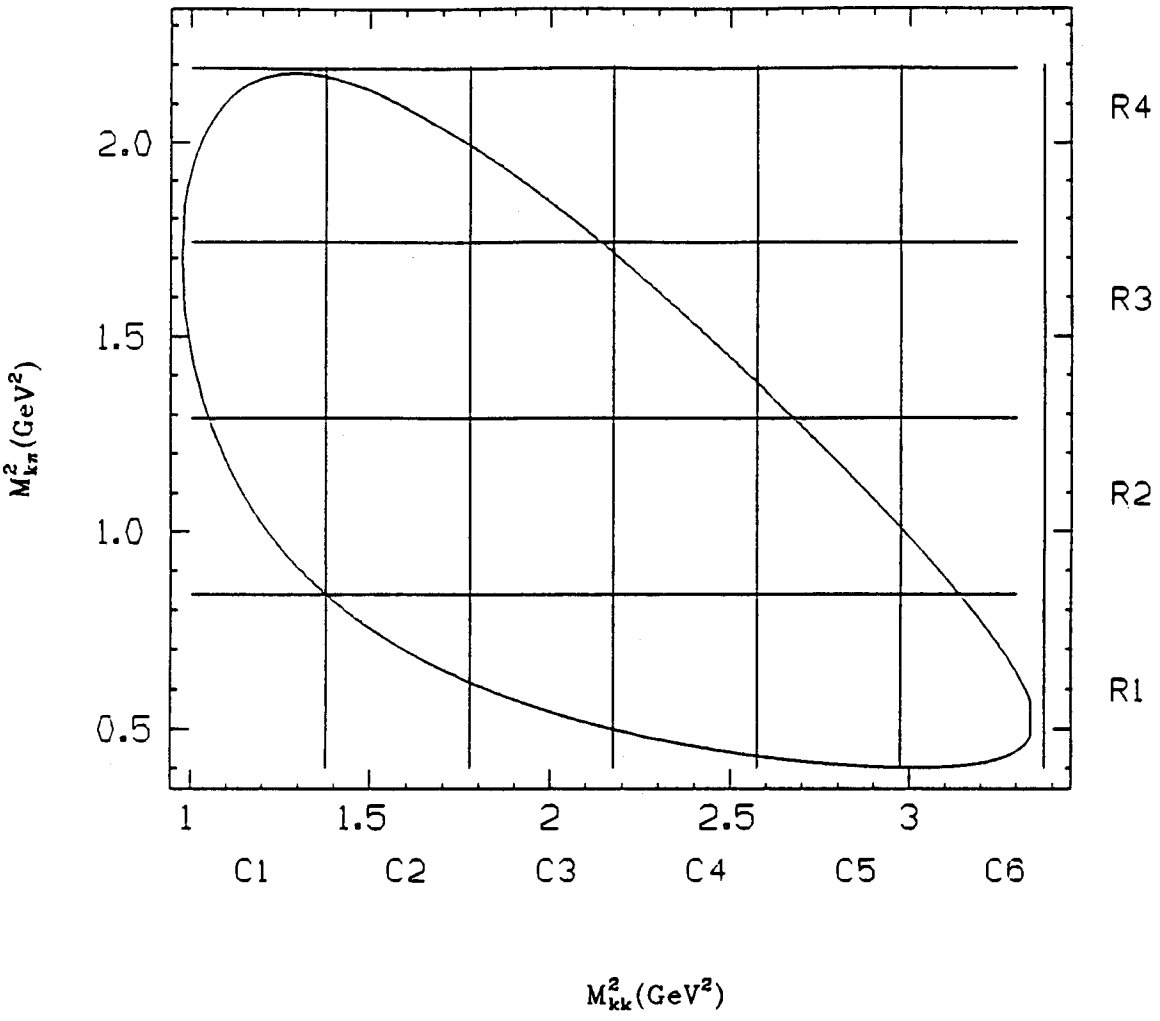

Figure 6.5: D_s Dalitz plot showing the different columns and rows used for the resolution studies.

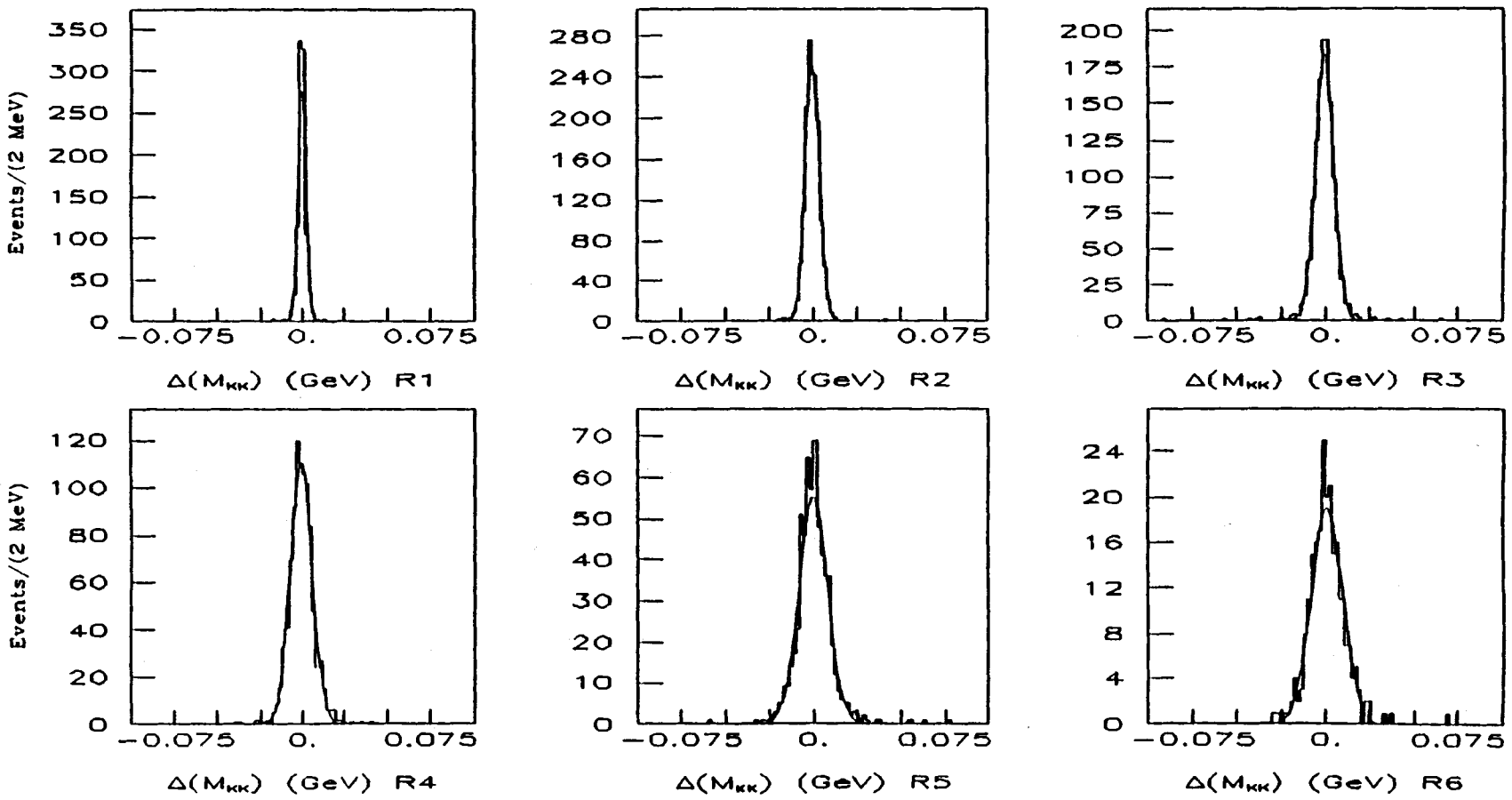

Figure 6.6: Histograms for the difference between the reconstructed and generated masses for the several regions of the $m_{k\bar{k}}$ mass.

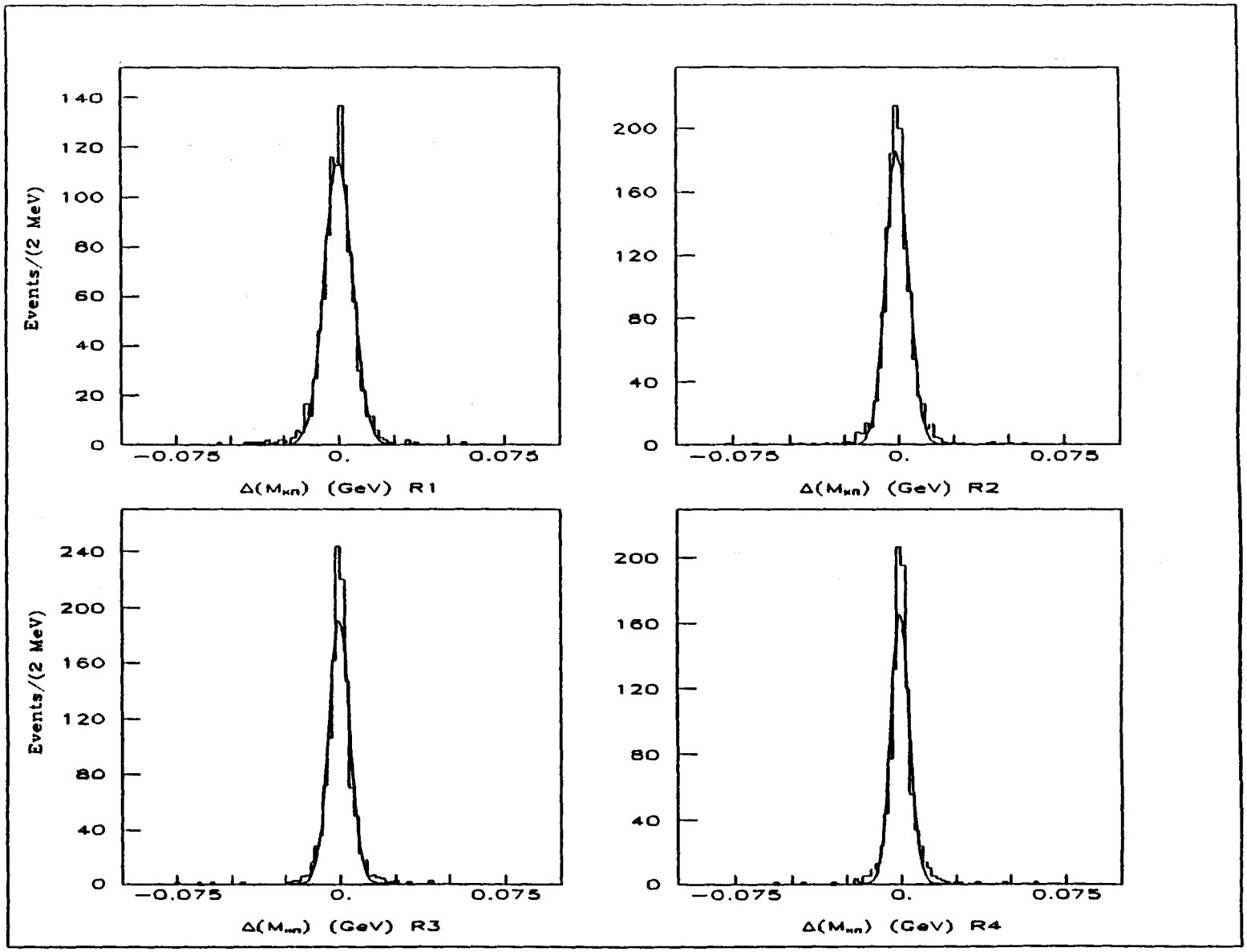

Figure 6.7: Histograms for the difference between the reconstructed and generated masses for the several regions of the $m_{K\pi}$ mass.

TABLE 6.6
RESOLUTION RESULTS FOR THE $M_{k\pi}$ MASS

REGION	σ (MeV)
R1	6.79±0.20
R2	5.64±0.14
R3	4.95±0.14
R4	4.85±0.15

TABLE 6.7
RESOLUTION RESULTS

PARAMETER	GENERATED VALUE	FIT (NO RES.)	FIT (WITH RES.)
f_1	0.20	(fixed)	
f_2	0.52	0.50 ±0.05	0.48 ±0.06
f_3	0.31	0.28 ±0.03	0.32 ±0.03
β_4	0.0 rad	(fixed)	
β_5	2.0 rad	1.99 ±0.02 rad	1.93 ±0.03 rad
β_6	1.5 rad	1.51 ±0.04 rad	1.57 ±0.04 rad
f_{1bk}	0.90	(fixed)	
f_{2bk}	0.06	(fixed)	
f_{3bk}	0.04	(fixed)	

the σ's of Table 6.5 and Table 6.6 to reproduce the Gaussian distributions in the data.

In Table 6.7 are shown the results for a fit to a generated sample of 60000 events. when the resolution effects are take in consideration. In the same table are shown the results for a sample of the same size when the resolution effects are not considered (the value of f_s used was 0.5). The fitted results when resolution effects were included were consistent with the ones without resolution effects.

6.5 D_s Results

The results of the Dalitz plot fit to the D_s data sample for $L/\sigma_L > 7$ are presented in this section. The fit coefficient and the phase angle for the $\overline{K}^{*0}K$ decay channel were held fixed during the fit. The sample has 282 data points, and (from the fit to the invariant mass distribution) the number of signal events is 138 $\pm$18. Consequently the value of f_s used was 0.5. The background fit fractions used were the ones found from the Dalitz plot fits to the background regions. These parameters were also held fixed.

There were two different solutions to the D_s Dalitz plot fit. The two solutions were found while mapping the likelihood (see Fig. 6.9.c). The two minima observed indicate that there are two possible solutions to the Dalitz plot fit. One gives a positive value for the the $\phi\pi$ phase angle (the "positive solution") and the other minimum gives a negative value for the $\phi\pi$ phase (the "negative solution"). The solution found by the fit will depend on the starting value for the $\phi\pi$ phase angle. The negative solution has a deeper minimum and is thus the more likely solution.

6.5.1 Results for the "negative solution"

In Table 6.8 are given the results of the fit for the negative solution. At the bottom of Table 6.8 is shown the value for -log(likelihood) and in Fig. 6.8 is shown the fit.

The correlation matrix for this fit is:

$$\begin{pmatrix} 1.00 & 0.36 & 0.05 & -.004 \\ 0.36 & 1.00 & -.19 & -.25 \\ 0.05 & -.19 & 1.00 & 0.76 \\ -.004 & -.25 & 0.76 & 1.00 \end{pmatrix}$$

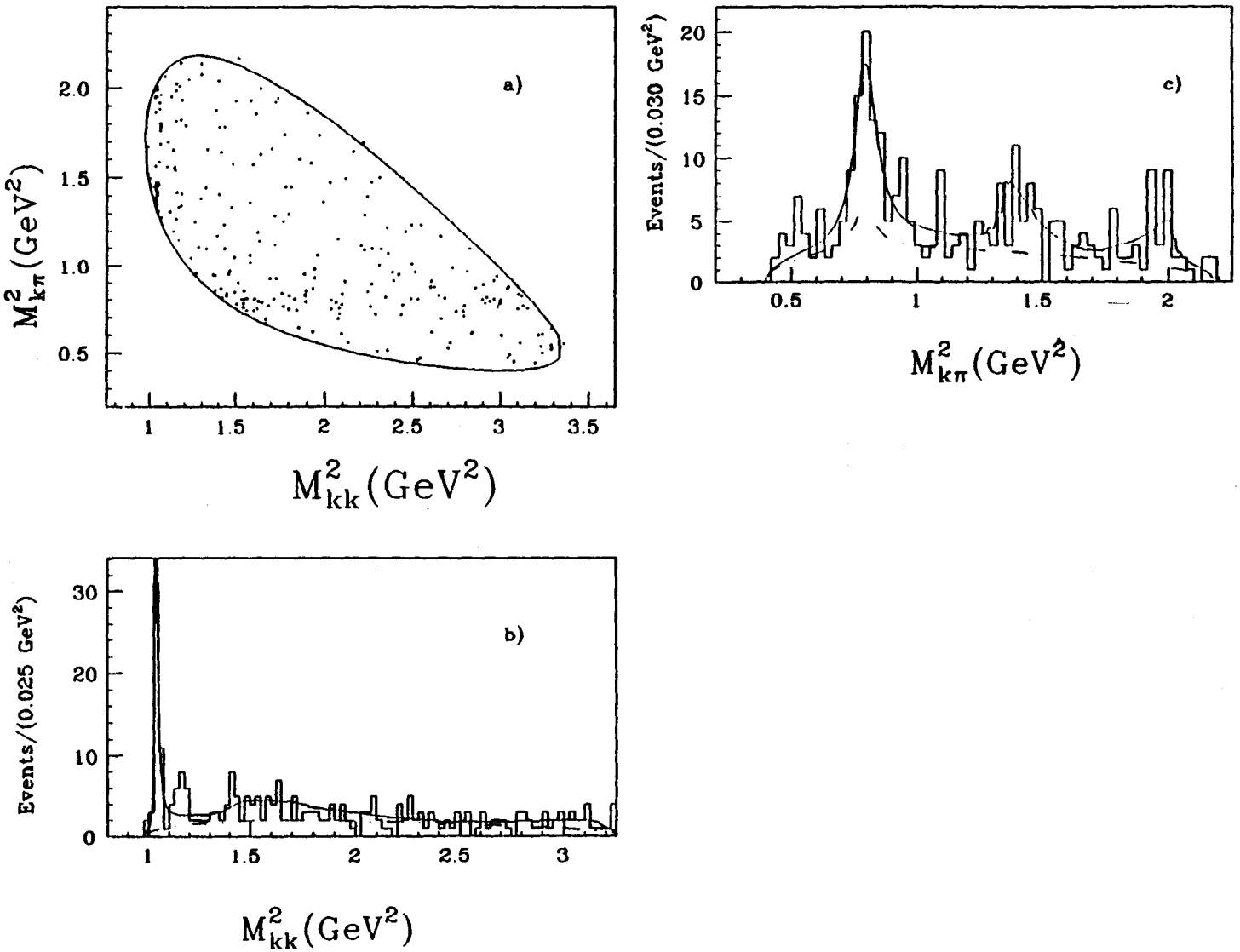

Figure 6.8: Dalitz plot fit for the D_s signal together with the projections and results of the fit. The solid curve shows the combined signal and background. The dot-dashed curves show the background contribution.

TABLE 6.8
FIT RESULTS FOR L/σ_L > 7 AND f_s = 0.5 (NEGATIVE SOLUTION)

Parameter	Output Values
β_1	0.37±0.18
β_2	1.0 (fixed)
β_3	0.53±0.12
β_4	-1.49 ±0.45 rad
β_5	0.0 rad (fixed)
β_6	-2.39 ±0.56 rad
f_{1bk}	0.92(fixed)
f_{2bk}	0.06(fixed)
f_{3bk}	0.02(fixed)
f_1	0.19±0.07
f_2	0.52±0.07
f_3	0.27±0.04
-log(like)	106.0

and the covariance error matrix obtained is:

$$\begin{pmatrix} 0.03 & .008 & .004 & -.0004 \\ .008 & 0.02 & -.01 & -0.02 \\ .004 & -0.01 & 0.20 & 0.19 \\ -.0004 & -0.02 & 0.19 & 0.32 \end{pmatrix}$$

The branching ratio results are:

$$\frac{\Gamma(D_s \to \overline{K}^{*0} K^+)}{\Gamma(D_s \to \phi\pi^+)} = 1.40 \pm 0.33$$

$$\frac{\Gamma(D_s \to K^+K^-\pi^+(n.r.))}{\Gamma(D_s \to \phi\pi^+)} = 0.34 \pm 0.18$$

Variable Background Fit

In order to study the effect of the background parameterization and the systematic uncertainty on the fit fractions and branching ratios, a fit was performed allowing the background fit fractions to vary. The results for this fit are shown in Table 6.9.

TABLE 6.9
FIT RESULTS FOR $L/\sigma_L > 7$ AND $f_s = 0.5$ (NEGATIVE SOLUTION BACKGROUND VARIED)

Parameter	Output Values
β_1	0.36±0.20
β_2	1.0 (fixed)
β_3	0.60±0.14
β_4	-1.81 ±0.29 rad
β_5	0.0 rad (fixed)
β_6	-2.89 ±0.27 rad
f_{1bk}	0.91±0.10
f_{2bk}	0.09±0.10
f_{3bk}	0.00 (fixed)
f_1	0.16±0.07
f_2	0.44±0.06
f_3	0.27±0.04
-log(like)	98.5

The correlation matrix for this fit is:

$$\begin{pmatrix} 1.00 & 0.43 & 0.09 & 0.14 \\ 0.43 & 1.00 & -.07 & -.11 \\ 0.09 & -.07 & 1.00 & 0.45 \\ 0.14 & -.11 & 0.45 & 1.00 \end{pmatrix}$$

and the covariance error matrix obtained is:

$$\begin{pmatrix} 0.04 & 0.01 & .005 & .007 \\ 0.01 & 0.02 & -.003 & -.004 \\ .005 & -.003 & 0.09 & 0.03 \\ .007 & -.004 & 0.03 & 0.07 \end{pmatrix}$$

The branching ratio results are:

$$\frac{\Gamma(D_s \to \overline{K}^{*0} K^+)}{\Gamma(D_s \to \phi\pi^+)} = 1.23 \pm 0.28$$

$$\frac{\Gamma(D_s \to K^+K^-\pi^+(n.r.))}{\Gamma(D_s \to \phi\pi^+)} = 0.29 \pm 0.21$$

The results are within one standard deviation of those for which the background fractions are fixed.

Likelihood Variation for the "negative solution"

In order to observe the behavior of the likelihood near the minimum found by the fit, the log of the likelihood was plotted as a function of the fit parameters. A fit parameter was held fixed at a given value and the other parameters were allowed to vary so that the likelihood is maximized. This procedure was then repeated for various values of the fit parameter.

The parameters studied were the fit coefficient and phase angle for the $K\overline{K}\pi$ (n.r.) decay channel, and the fit coefficient and phase angle for the $\phi\pi$ decay channel. (The fit coefficient and phase angle for the $\overline{K}^{*0}K$ decay channel were held fixed and equal to 1.0 and 0.0 respectively). The background fit fractions were also held fixed. The values were $f_{1bk} = 0.92$, $f_{2bk} = 0.06$ and $f_{3bk} = 0.02$. In Fig. 6.9 are shown the results of mapping the likelihood for the negative solution. From the plots one observes that variation of the fit parameters produces curves with well-defined minima.

6.5.2 Results for the "positive solution"

The results of the Dalitz plot fit for the "positive solution" are presented in Table 6.10.

The correlation matrix for this fit is:

$$\begin{pmatrix} 1.00 & 0.34 & -.29 & -.28 \\ 0.34 & 1.00 & -.04 & 0.06 \\ -.29 & -.04 & 1.00 & 0.75 \\ -.28 & 0.06 & 0.75 & 1.00 \end{pmatrix}$$

and the covariance error matrix obtained is:

$$\begin{pmatrix} 0.04 & 0.01 & -.03 & -.03 \\ 0.01 & 0.02 & -.004 & .005 \\ -.03 & -.004 & 0.36 & 0.24 \\ -.03 & .005 & 0.24 & 0.28 \end{pmatrix}$$

The branching ratio results obtained from this fit are:

$$\frac{\Gamma(D_s \to \overline{K}^{*0}K^+)}{\Gamma(D_s \to \phi\pi^+)} = 1.18 \pm 0.28$$

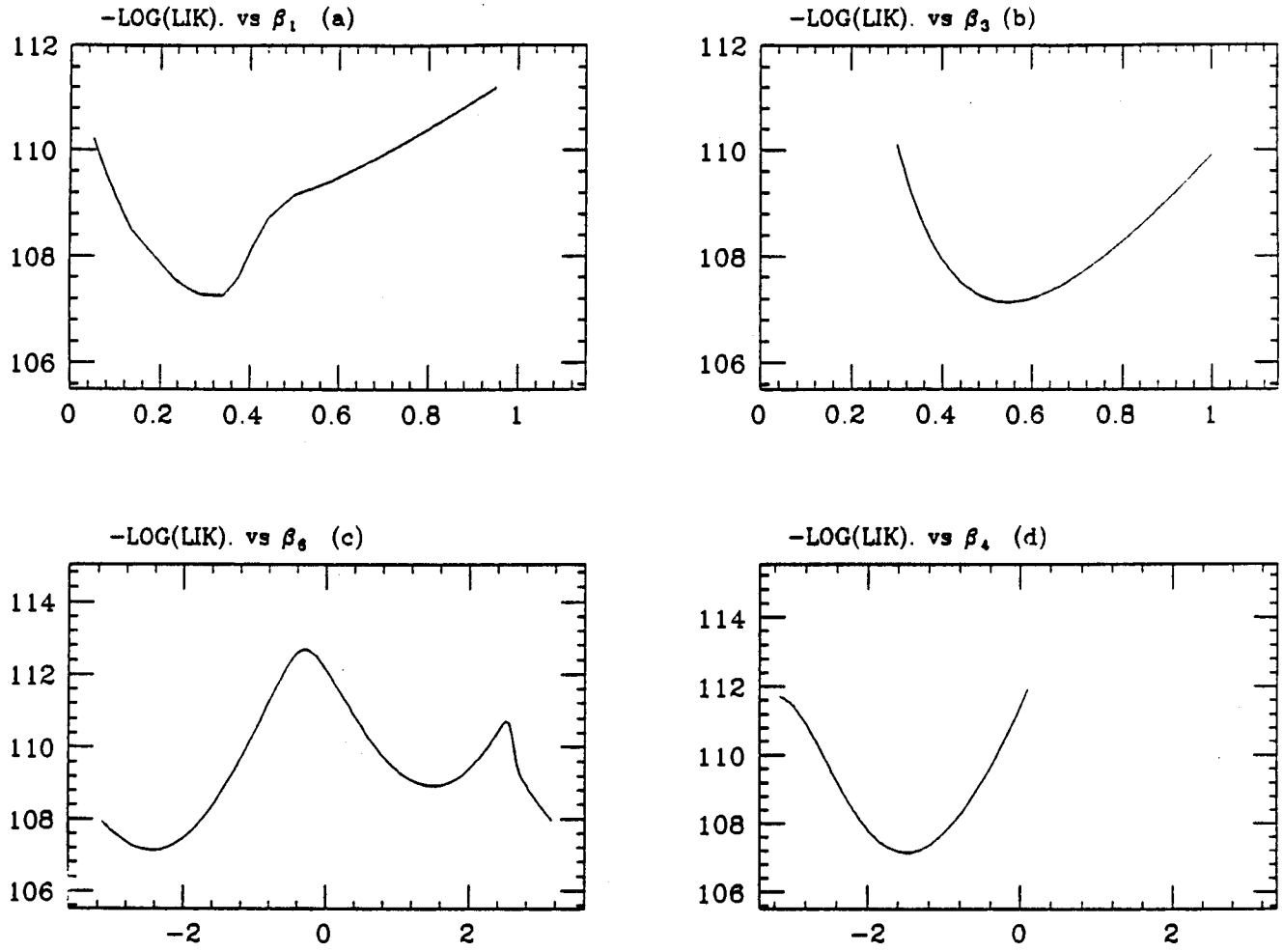

Figure 6.9: D, Mapping of the Likelihood for the "negative solution": a) -log(like) vs β_1, b)-log(like) vs β_3, c) -log(like) vs β_6, and d) -log(like) vs β_4.

TABLE 6.10
FIT RESULTS FOR L/σ_L > 7 AND f_s = 0.5 (POSITIVE SOLUTION)

Parameter	Output Values
β_1	0.33±0.19
β_2	1.0 (fixed)
β_3	0.63±0.15
β_4	-0.30 ±0.60 rad
β_5	0.0 rad (fixed)
β_6	1.35 ±0.53 rad
f_{1bk}	0.92 (fixed)
f_{2bk}	0.06 (fixed)
f_{3bk}	0.02 (fixed)
f_1	0.16±0.08
f_2	0.49±0.07
f_3	0.31±0.05
-log(like)	107.6

$$\frac{\Gamma(D_s \to K^+K^-\pi^+(n.r.))}{\Gamma(D_s \to \phi\pi^+)} = 0.26 \pm 0.20$$

Variable Background Fit

When the background fit parameters are allowed to vary the results obtained for the "positive solution" are presented in Table 6.11. There were no significant changes in the output fit parameters when compared to the fit with fixed fractions. The values obtained are in agreement with the values found from the fit to the background regions. As found previously the background in the D_s signal region is mostly due to $K\overline{K}\pi$ (n.r.) background events, with a small $\overline{K}^{*0}$ contribution.

The correlation matrix for this fit is:

$$\begin{pmatrix} 1.00 & 0.39 & -.53 & -.57 \\ 0.39 & 1.00 & -.38 & -.31 \\ -.53 & -.38 & 1.00 & 0.68 \\ -.57 & -.31 & 0.68 & 1.00 \end{pmatrix}$$

TABLE 6.11
FIT RESULTS FOR L/σ_L > 7 AND f_s = 0.5 (BACKGROUND VARIED)

Parameter	Output Values
β_1	0.35±0.23
β_2	1.0 (fixed)
β_3	0.68±0.15
β_4	-0.29 ±0.52 rad
β_5	0.0 rad (fixed)
β_6	1.36 ±0.46 rad
f_{1bk}	0.91 ±0.21
f_{2bk}	0.09 ±0.03
f_{3bk}	0.00 ±0.006
f_1	0.17±0.09
f_2	0.48±0.07
f_3	0.33±0.05
-log(like)	106.9

and the covariance error matrix obtained is:

$$\begin{pmatrix} 0.05 & 0.01 & -.06 & -.06 \\ 0.01 & 0.02 & -.03 & -.02 \\ -.06 & -.03 & 0.27 & 0.16 \\ -.06 & -.02 & 0.16 & 0.21 \end{pmatrix}$$

The branching ratio results are:

$$\frac{\Gamma(D_s \to \overline{K}^{*0} K^+)}{\Gamma(D_s \to \phi\pi^+)} = 1.08 \pm 0.24$$

$$\frac{\Gamma(D_s \to K^+K^-\pi^+(n.r.))}{\Gamma(D_s \to \phi\pi^+)} = 0.25 \pm 0.22$$

It should be noted that the branching ratios determined from the negative solution differ from those obtained from the positive solution (1.18 ± .28 and 0.26 ± .20 respectively) by less than one standard deviation. (See Table 6.10).

Likelihood Variation for the "positive solution"

In Fig. 6.10 are shown the results of mapping the likelihood for the "positive solution".

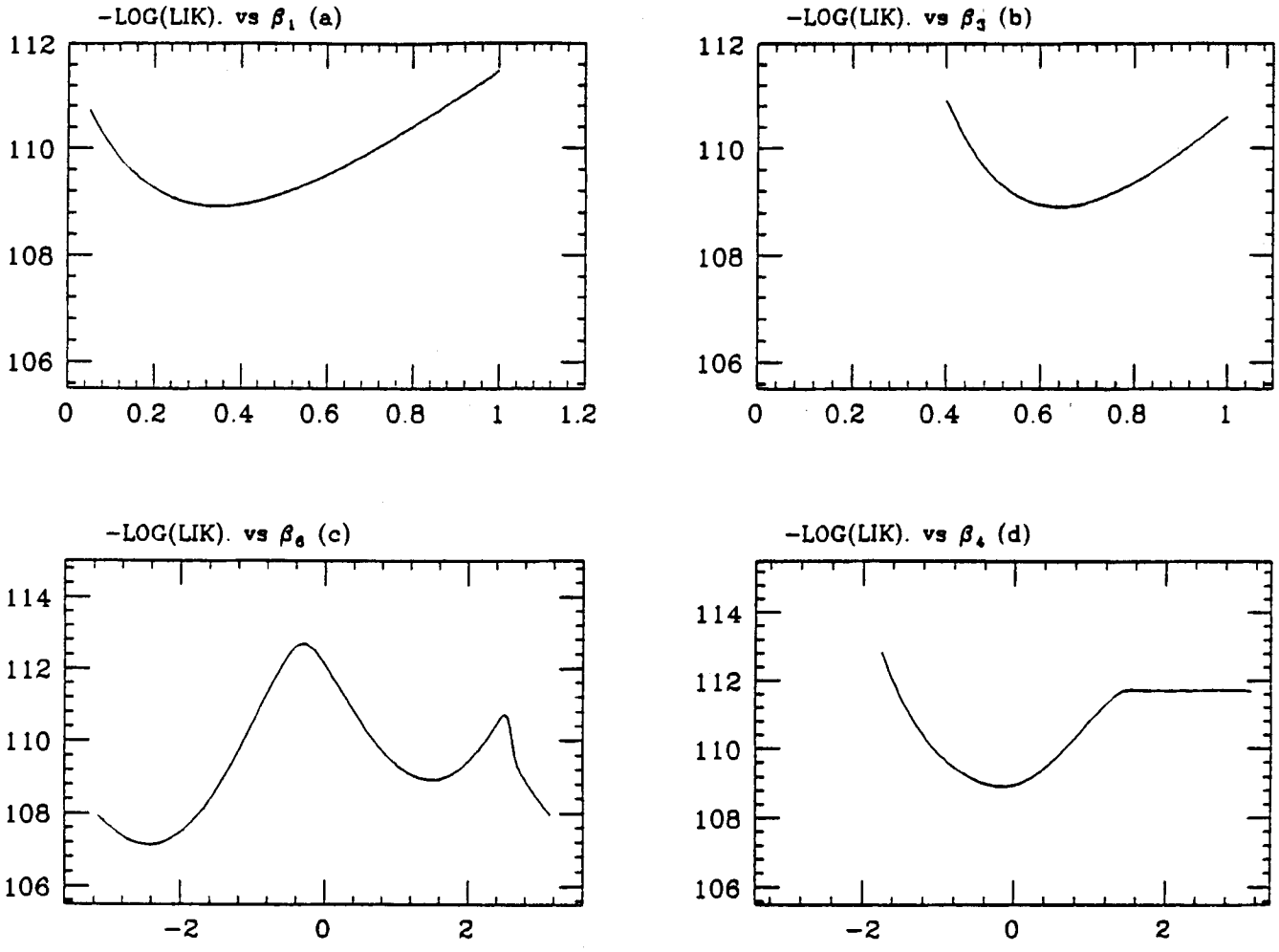

Figure 6.10: D_s Mapping of the Likelihood for the "positive solution": **a)** -log(like) vs β_1, b)-log(like) vs β_3, c) -log(like) vs β_6, and d) -log(like) vs β_4.

TABLE 6.12
FIT RESULTS FOR L/σ_L > 7 AND f_s = 0.5 (INCOHERENT CASE)

Parameter	Output Values
β_1	0.44±0.21
β_2	1.0 (fixed)
β_3	0.58±0.14
f_1	0.22±0.08
f_2	0.49±0.07
f_3	0.29±0.05
-log(like)	108.9

From the plots one observes that variation of the two fit coefficients, and the two phase angles produces parabolic curves with well-defined minima.

6.5.3 Incoherent Fit Results

As described in chapter 4, in the incoherent case the three decay channels do not interfere. The phase angles do not enter in the fit. The number of fitted parameters is reduced from 4 in the coherent case to two for the incoherent case. As usual one of the fit coefficients is set equal to one. The results of the fit are shown in Table 6.12. The background fit coefficients used were the same as in the coherent case and were held fixed during the fit. The branching ratio results obtained are:

$$\frac{\Gamma(D_s \to \overline{K}^{*0} K^+)}{\Gamma(D_s \to \phi\pi^+)} = 1.26 \pm 0.29$$

$$\frac{\Gamma(D_s \to K^+K^-\pi^+(n.r.))}{\Gamma(D_s \to \phi\pi^+)} = 0.37 \pm 0.24$$

6.5.4 Removal of the $K\pi\pi$ Events

In chapter 4 the problem of possible $K\pi\pi$ contamination was discussed. The following procedure removes that contamination: for all the $K\overline{K}\pi$ events that are in the D_s signal region (1.955 GeV - 1.985 GeV), the pion mass is assigned to the kaon with the same sign as the pion. Then the value of the $K\pi\pi$ invariant mass is calculated and if this value is in the D signal region (1.855 Gev - 1.885 GeV) the event is rejected. In this section results of the D_s Dalitz plot fit are presented after this cut. The efficiency function ϵ used in this fit is different than the one presented in chapter 4. This is due to the new cut introduced in order to remove the possible contamination. The fit results are shown in Fig. 6.11. In this sample the number of data points is 199 (83 events were removed) and the number of signal events is 92. $\pm$16. In Fig. 6.11.c one observes that the component most affected by the removal of the $K\pi\pi$ misidentified events is the $\overline{K}^{*0}$, while the ϕ component is reduced by only a small amount. The results of the fit are presented in Table 6.13.

The fit results for this sample are independent of the initial values of the fit parameters.

The correlation matrix for this fit is:

$$\begin{pmatrix} 1.00 & 0.42 & 0.17 & -.07 \\ 0.42 & 1.00 & 0.23 & 0.02 \\ 0.17 & 0.23 & 1.00 & 0.54 \\ -.07 & 0.02 & 0.54 & 1.00 \end{pmatrix}$$

and the covariance error matrix obtained is:

$$\begin{pmatrix} 0.05 & 0.02 & 0.04 & -.02 \\ 0.02 & 0.06 & 0.06 & .005 \\ 0.04 & 0.06 & 1.29 & 0.60 \\ -.02 & .005 & 0.60 & 0.97 \end{pmatrix}$$

The branching ratio results are:

$$\frac{\Gamma(D_s \to \overline{K}^{*0} K^+)}{\Gamma(D_s \to \phi\pi^+)} = 1.02 \pm 0.35$$

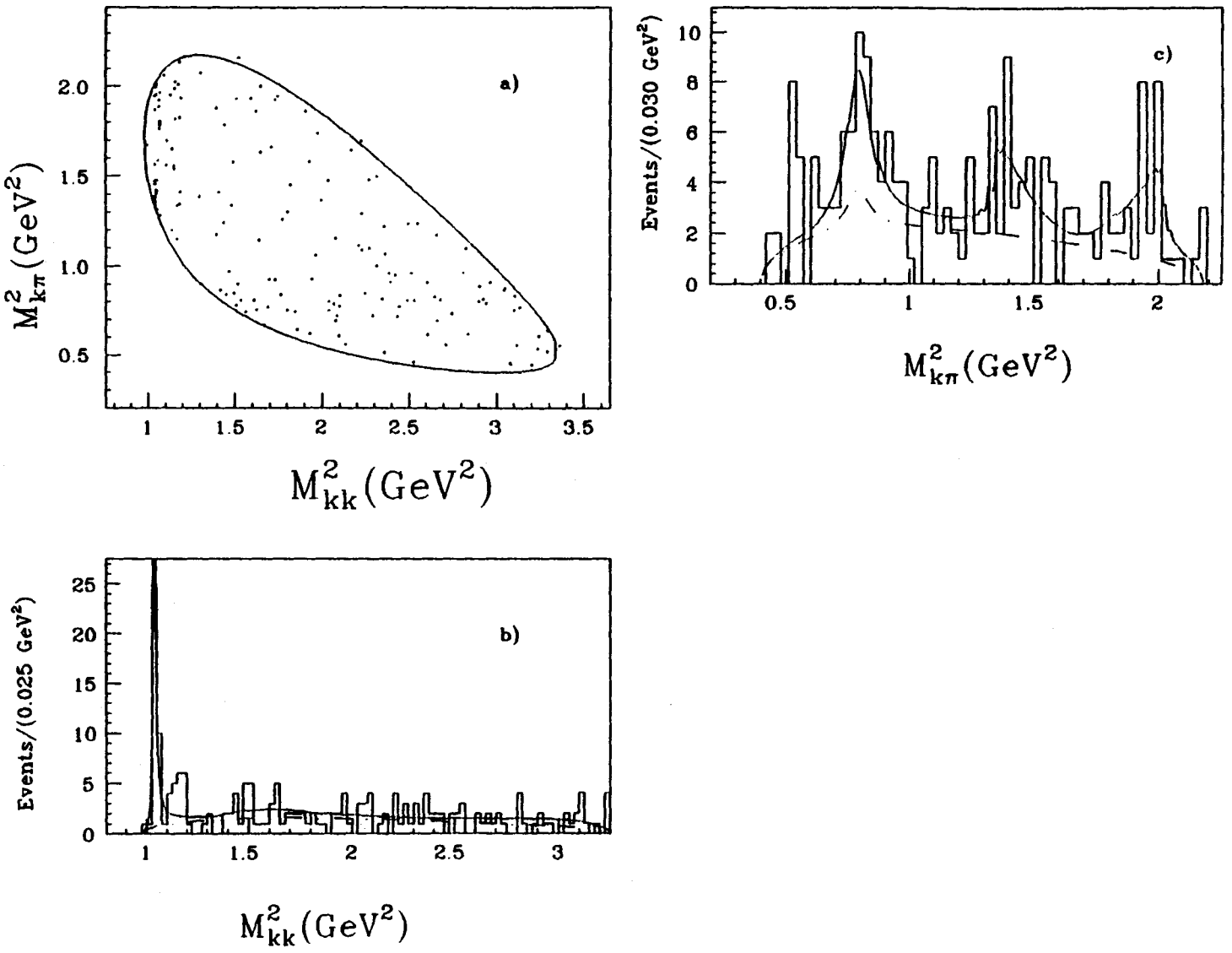

Figure 6.11: Dalitz plot Fit to the D_s signal after the removal of the $K\pi\pi$ events

TABLE 6.13
FIT RESULTS FOR L/σ_L > 7 AND f_s = 0.46

Parameter	Output Values
β_1	0.31±0.22
β_2	1.0 (fixed)
β_3	0.68±0.22
β_4	2.01 ±1.13 rad
β_5	0.0 rad (fixed)
β_6	2.08 ±0.98 rad
f_{1bk}	0.92 (fixed)
f_{2bk}	0.06 (fixed)
f_{3bk}	0.02 (fixed)
f_1	0.14±0.09
f_2	0.47±0.09
f_3	0.34±0.06
-log(like)	94.3

$$\frac{\Gamma(D_s \to K^+K^-\pi^+(n.r.))}{\Gamma(D_s \to \phi\pi^+)} = 0.20 \pm 0.20$$

When the background fit parameters are allowed to vary the results obtained are presented in Table 6.14.

the correlation matrix for this fit is:

$$\begin{pmatrix} 1.00 & 0.61 & 0.24 & -.06 \\ 0.61 & 1.00 & 0.27 & 0.04 \\ 0.24 & 0.27 & 1.00 & 0.53 \\ -.06 & 0.04 & 0.53 & 1.000 \end{pmatrix}$$

and the covariance error matrix obtained is:

$$\begin{pmatrix} 0.09 & 0.06 & 0.09 & -.02 \\ 0.06 & 0.10 & 0.12 & 0.01 \\ 0.09 & 0.12 & 1.84 & 0.71 \\ -.02 & 0.01 & 0.71 & 1.00 \end{pmatrix}$$

The branching ratio results are:

$$\frac{\Gamma(D_s \to \overline{K}^{*0}K^+)}{\Gamma(D_s \to \phi\pi^+)} = 0.88 \pm 0.34$$

TABLE 6.14
FIT RESULTS FOR L/σ_L > 7 AND f_s = 0.46 (BACKGROUND VARIED)

Parameter	Output Values
β_1	0.34±0.30
β_2	1.0 (fixed)
β_3	0.84±0.32
β_4	2.06 ±1.35 rad
β_5	0.0 rad (fixed)
β_6	2.10 ±1.00 rad
f_{1bk}	0.90±0.11
f_{2bk}	0.10±0.11
f_{3bk}	0.00 (fixed)
f_1	0.15±0.10
f_2	0.44±0.11
f_3	0.37±0.07
-log(like)	94.3

$$\frac{\Gamma(D_s \to K^+K^-\pi^+(n.r.))}{\Gamma(D_s \to \phi\pi^+)} = 0.20 \pm 0.20$$

The results are close to those for which the background fractions are fixed.

Incoherent Fit

The incoherent fit results for this sample are shown in Table 6.15. The fit fractions values for the $\overline{K}^{*0}K$ and $\phi\pi$ decay channel do not change much when compared with those from the coherent fit. The branching ratios are:

$$\frac{\Gamma(D_s \to \overline{K}^{*0}K^+)}{\Gamma(D_s \to \phi\pi^+)} = 1.02 \pm 0.34$$

$$\frac{\Gamma(D_s \to K^+K^-\pi^+(n.r.))}{\Gamma(D_s \to \phi\pi^+)} = 0.29 \pm 0.25$$

TABLE 6.15
FIT RESULTS FOR L/σ_L > 7 AND f_s = 0.46 (INCOHERENT CASE)

Parameter	Output Values
β_1	0.44±0.31
β_2	1.0 (fixed)
β_3	0.72±0.24
f_1	0.20±0.10
f_2	0.46±0.10
f_3	0.33±0.06
-log(like)	95.7

6.5.5 Summary of the D_s Branching Ratio Results

The results obtained for the branching ratios are compared in Fig. 6.12. Shown in the plot are the different branching ratios obtained under the conditions discussed in the previous sections.

In Fig. 6.12.a is shown the branching ratio results for the D_s decaying to $\overline{K}^{*0}K$ with respect to the $\phi\pi$ decay channel, and in Fig. 6.12.b the results for the D_s decaying to $K\overline{K}\pi$ (n.r.) with respect to the $\phi\pi$ decay channel. The labels M1, M2, M3, M4, M5, M6, M7 and M8 correspond to the following cases:

- M1: positive solution and fixed background fit coefficients.
- M2: positive solution and variable background fit coefficients.
- M3: negative solution and fixed background fit coefficient.
- M4: negative solution and variable background fit coefficient.
- M5: Incoherent fit and fixed background fit coefficient.
- M6: $K\pi\pi$ misidentified events excluded and fixed background fit coefficients.

- M7: K$\pi\pi$ misidentified events excluded and variable background fit coefficients.
- M8: K$\pi\pi$ misidentified events excluded (incoherent case).

From the plots one observes that there is overall agreement for the branching ratios using the various methods.

The preferred solution correspond to the method "M4". For this case the background fit coefficients were allowed to vary, and the -log(like) has the smallest value.

The results from the different methods were used in order to estimate the systematic error for the "preferred solution". In addition, the uncertainties due to the variation in the L/σ_L cut were estimated. The branching ratio results with statistical plus systematic errors are the following:

$$\frac{\Gamma(D_s \to \overline{K}^{*0} K^+)}{\Gamma(D_s \to \phi\pi^+)} = 1.23^{+0.33}_{-0.27} \pm 0.30$$

$$\frac{\Gamma(D_s \to K^+K^-\pi^+(n.r.))}{\Gamma(D_s \to \phi\pi^+)} = 0.29^{+0.25}_{-0.18} \pm 0.18$$

6.5.6 Likelihood Error Analysis

Subroutine MINOS (part of the MINUIT package) finds the errors on each fitted parameter by examining the minimum of the likelihood function as the parameter is varied. If the model fitted is linear, the MINOS errors will be symmetric and equal to the errors derived from the covariance matrix (so-called "parabolic" errors) [36]. MINOS calculated errors take into account both parameter correlations and non-linearities. The MINOS errors are in general asymmetric [41].

The results shown in Table 6.16 correspond to the fit that was assigned the label "M4" in the previous section (the preferred solution). In Table 6.16 are shown the "parabolic" errors and the confidence intervals given by MINOS.

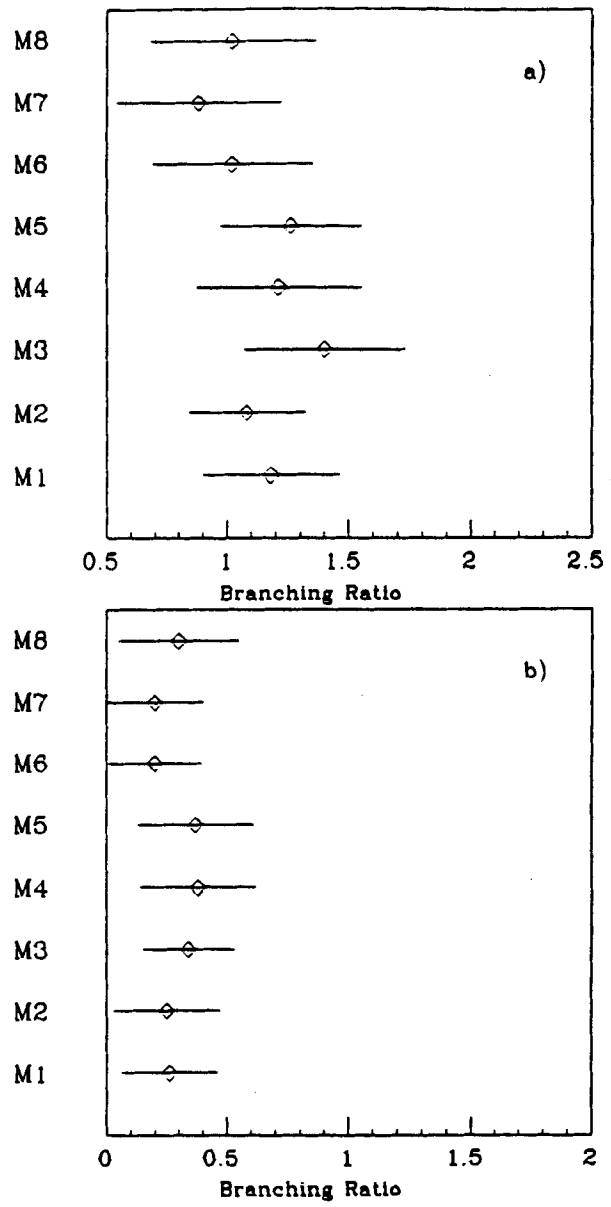

Figure 6.12: Branching ratio results: a) D_s decaying to $\overline{K}^{*0}K$ with respect to the $\phi\pi$ decay channel, b) D_s decaying to $K\overline{K}\pi$ (n.r.) with respect to the $\phi\pi$ decay channel.

TABLE 6.16
MINOS ERROR ANALYSIS

Parameter	Value	Parabolic error	MINOS Errors	
			Positive	Negative
β_1	0.36	0.20	0.24	0.17
β_2	1. (fix)			
β_3	0.60	0.14	0.16	0.13
β_4	-1.81	0.29	0.29	0.30
β_5	0.0 (fix)			
β_6	-2.89	0.27	0.27	0.27

The positive and negative error form what is called the one-sigma likelihood interval. For example for parameter β_1, with a mean value equal to 0.36 the likelihood interval has the following meaning: the probability that the true value of parameter β_1 lies between (0.36 - 0.17) and (0.36 + 0.24) is equal to 68.3% (the probability of a normally-distributed parameter lying within one standard-deviation of its mean [43]). Similar statements can be made for the others parameters.

In order to obtain the probability value of 68.3%, one uses the MINUIT command "SET ERROR DEF" equal to 0.5 (for a more detailed explanation about the interpretation of the likelihood interval see [38], [42]).

In Fig. 6.13 and Fig. 6.14 are shown the plots of -log(likelihood) as a function of the fit parameters. (This procedure was done with the SCAN command of MINUIT). From Fig. 6.14.a and Fig. 6.14.b one can see the parabolic shape of the -log(like) for the parameters β_4 and β_6. As a consequence the MINOS error are symmetric and equal to the parabolic errors.

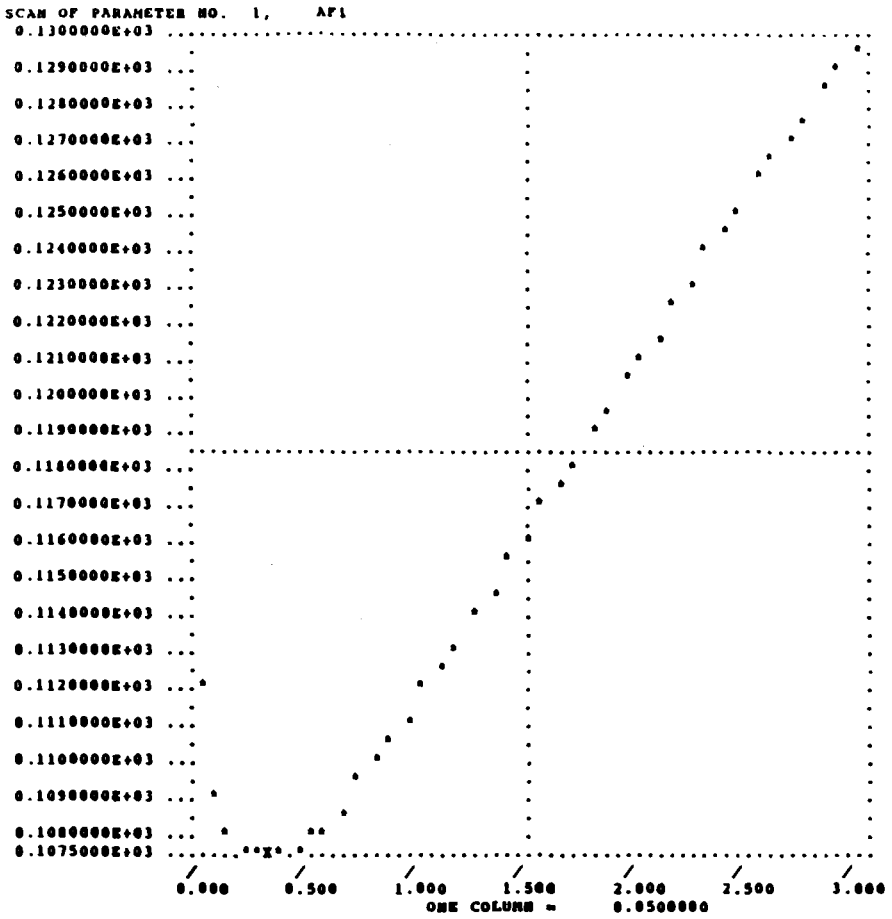

(a) β_1

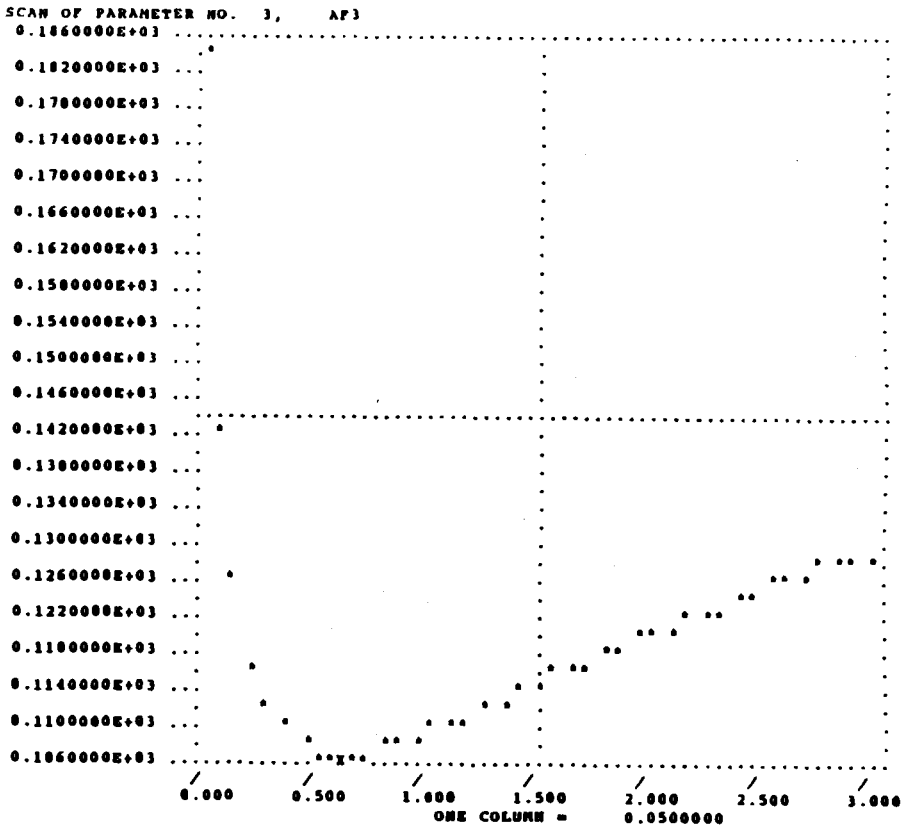

(b) β_3

Figure 6.13: Plot of -log(like) versus fit parameters. a) -log(like) vs. β_1, b)-log(like) vs. β_3

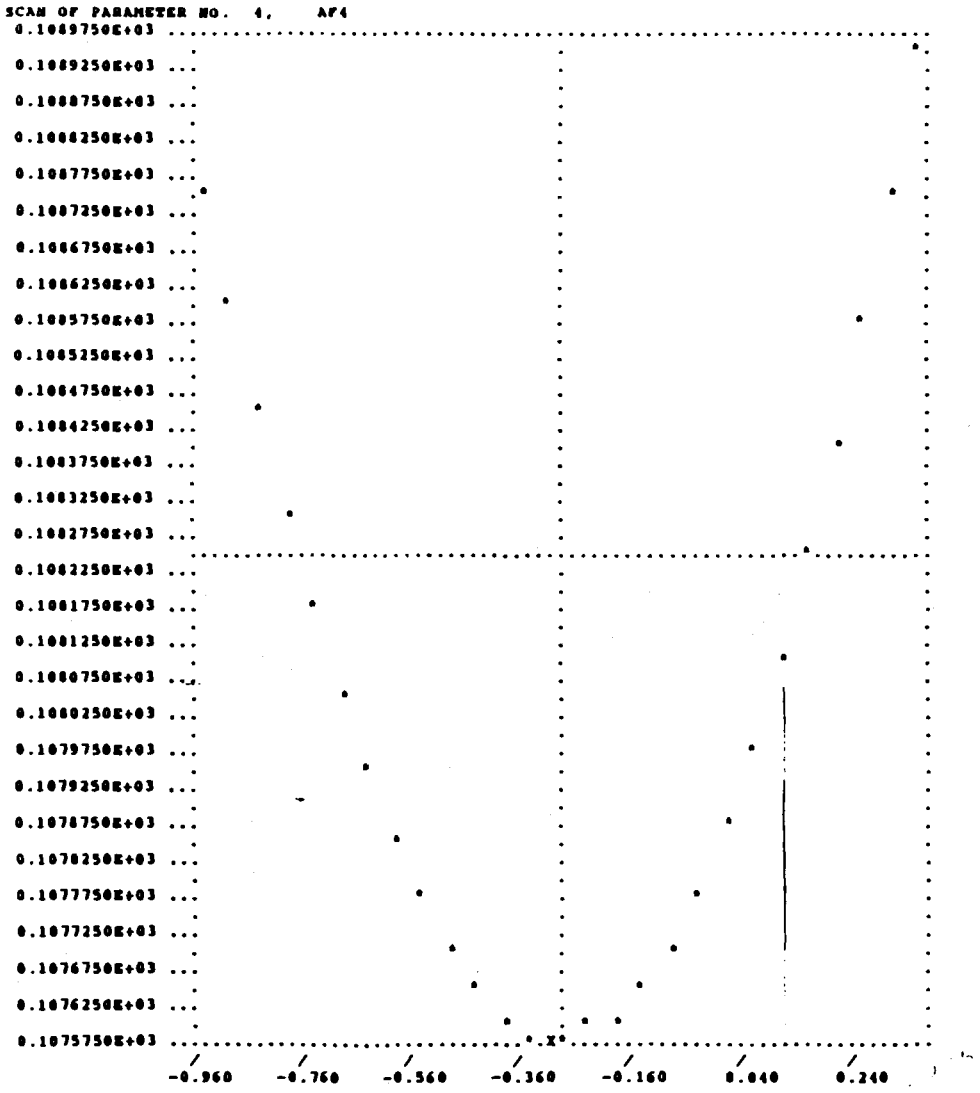

(a) β_4

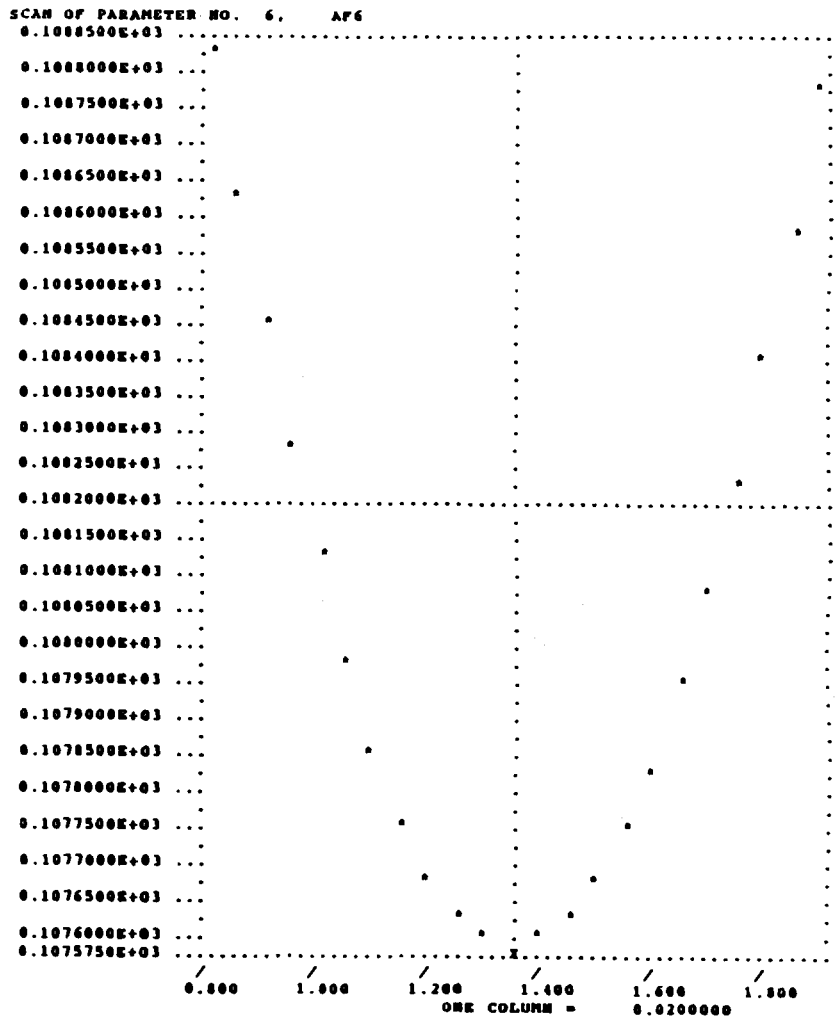

(b) β_6

Figure 6.14: Plot of -log(like) versus fit parameters. a) -log(like) vs. β_4, b)-log(like) vs. β_6

6.5.7 Likelihood Contours

Likelihood contours are curves of constant values of likelihood in a (β_i,β_j) plane. In the vicinity of the maximum likelihood these curves will be a series of smooth contours around the maximum point [38].

In Fig. 6.15 are shown likelihood contours in the (β_1,β_3) plane. The inner curve labeled "o" surrounds the maximum likelihood point. The curves with labels 1,2,3,4,5 correspond to increasing values of -log(like) as indicated in the plot (this plot was done with the MINUIT command: "CONTOUR").

It is interested to note that an asymmetric orientation of the 1σ contour relative to the coordinate axes reflects a non-zero correlation between the variables [38].

6.5.8 D_s Results as a Function of L/σ_L

The D_s Dalitz plot fit was performed using events with $L/\sigma_L > 7$, > 8, and > 9. The case selected was the "negative solution" and variable background fit coefficients. In Fig. 6.16 are shown the results of the fits. (In these fits, the $\overline{K}^{*0}K$ phase angle was fixed at zero radians). In Table 6.17 are shown the branching ratio results and in Fig. 6.17 are shown the plot of the branching ratio results as a function of L/σ_L.

TABLE 6.17
D_s RESULTS AS A FUNCTION OF L/σ_L

L/σ_L	$\frac{\Gamma(D_s\to\overline{K}^{*0}K^+)}{\Gamma(D_s\to\phi\pi^+)}$	$\frac{\Gamma(D_s\to K^+K^-\pi^+(\text{n.r.}))}{\Gamma(D_s\to\phi\pi^+)}$
7	1.23 ±0.28	0.29 ±0.21
8	1.34 ±0.32	0.47 ±0.27
9	1.39 ±0.37	0.54 ±0.30

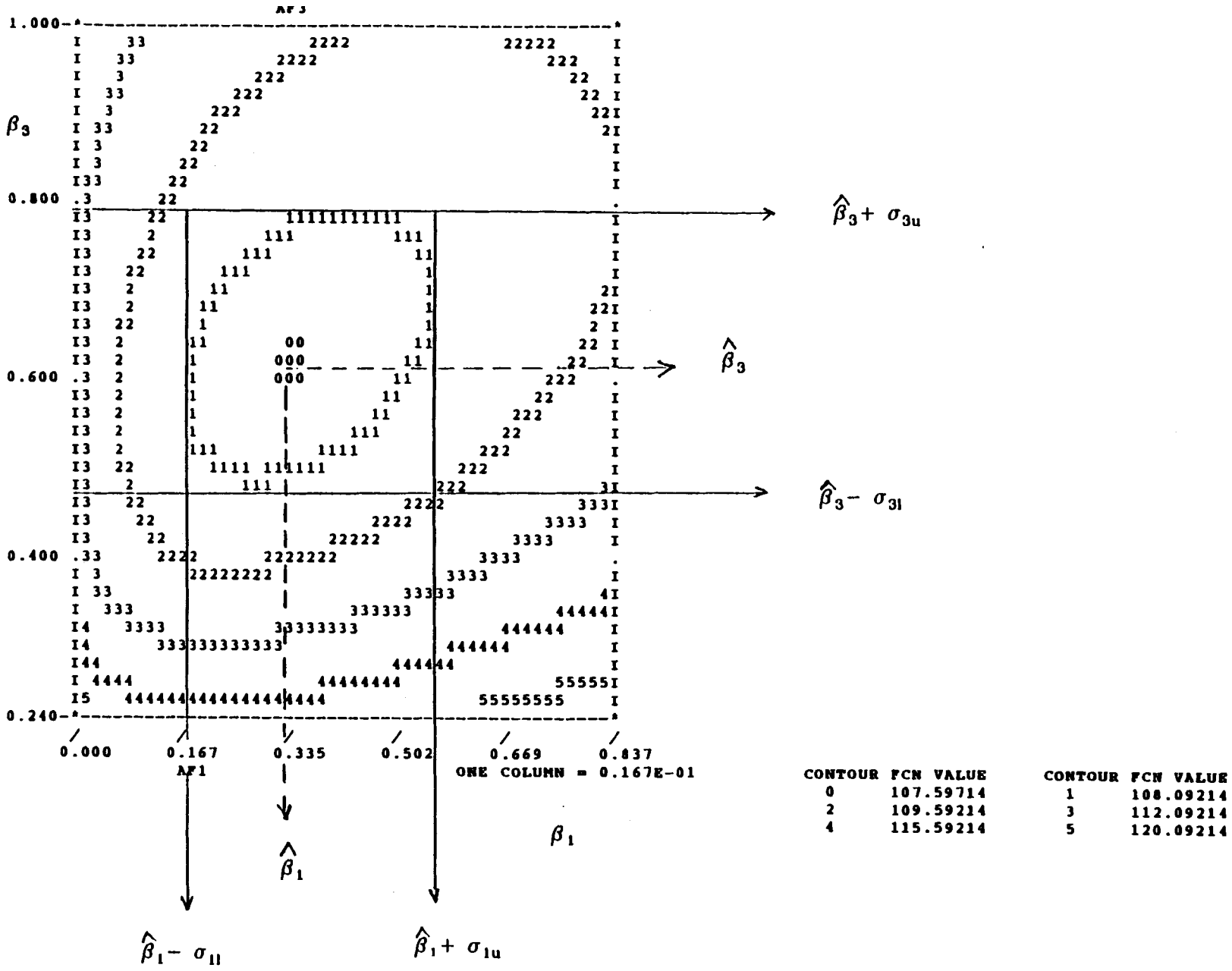

CONTOUR	FCN VALUE	CONTOUR	FCN VALUE
0	107.59714	1	108.09214
2	109.59214	3	112.09214
4	115.59214	5	120.09214

Figure 6.15: Plot of likelihood contour curves in the (β_1, β_3) plane.

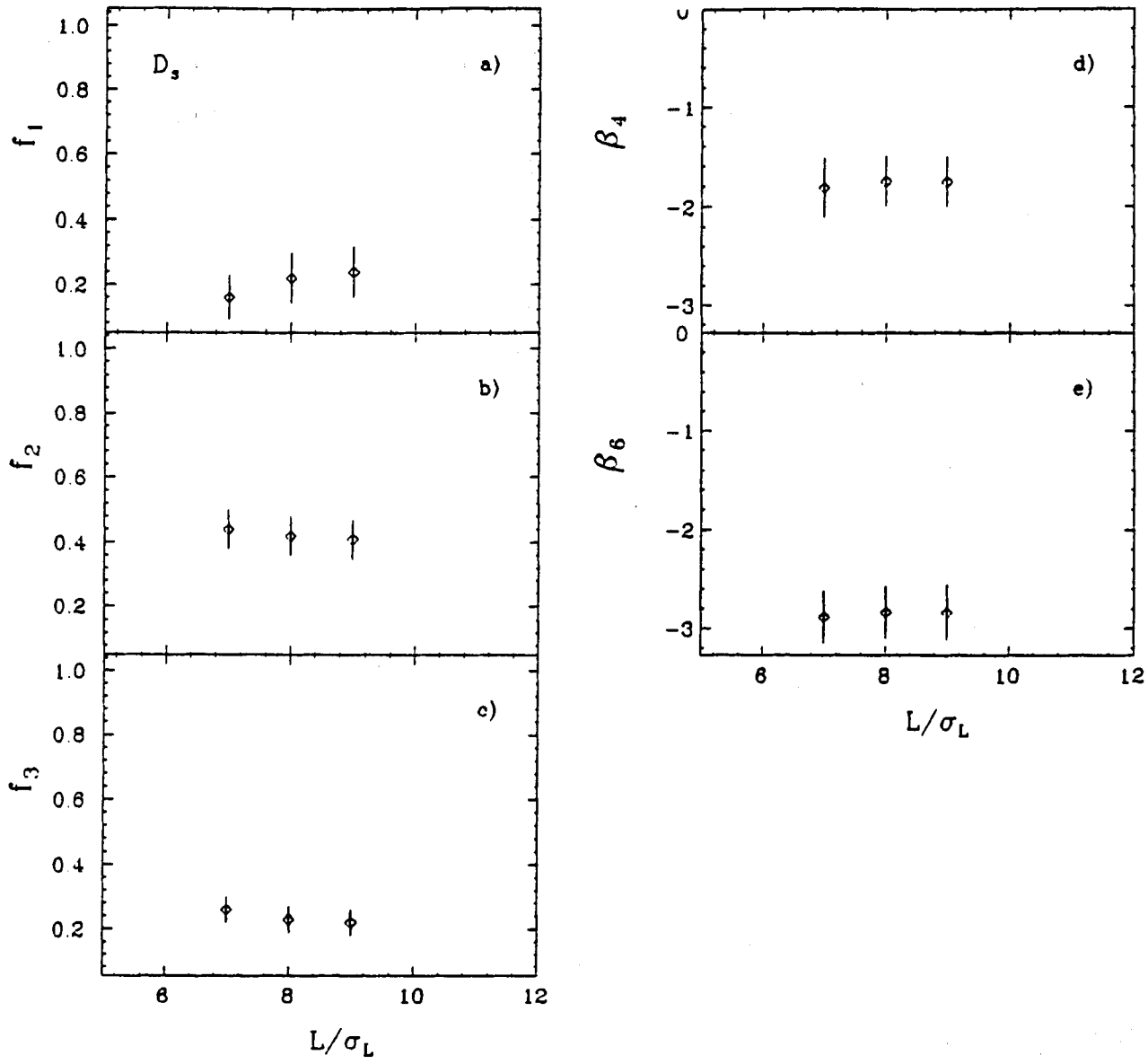

Figure 6.16: D_s Dalitz plot fit results as a function of L/σ_L: a) f_1 is the $K\overline{K}\pi$ n.r. fit fraction, b) f_2 is the $\overline{K}^{*0}K$ fit fraction, c) f_3 is the $\phi\pi$ fit fraction, d) β_4 is the $K\overline{K}\pi$ n.r. phase angle, e) β_6 is the $\phi\pi$ phase angle.

D_s

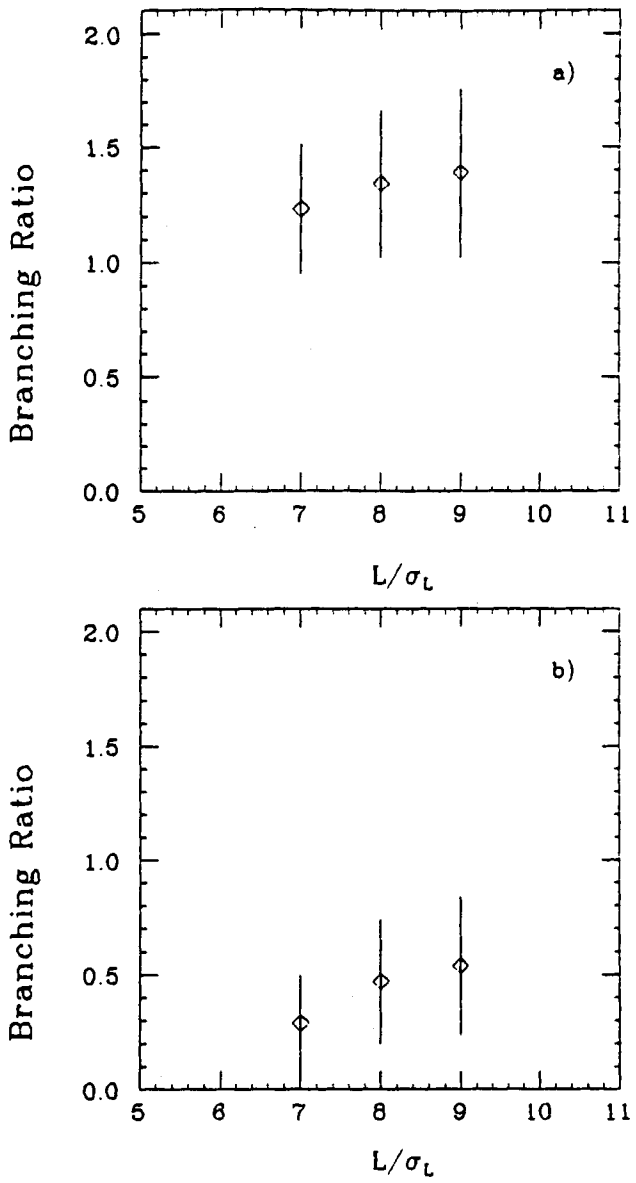

Figure 6.17: D_s Branching ratio results as a function of L/σ_L. : a) D_s decaying to $\overline{K}^{*0}K$ with respect to the $\phi\pi$ decay channel, b) D_s decaying to $K\overline{K}\pi$ (n.r.) with respect to the $\phi\pi$ decay channel.

TABLE 6.18
D^+ FIT RESULTS FOR $L/\sigma_L > 7$ AND $f_s = 0.4$

Parameter	Output Values
β_1	0.92±0.49
β_2	1.0 (fixed)
β_3	1.21±0.44
β_4	3.25 ±0.68 rad
β_5	0.0 rad (fixed)
β_6	3.12 ±1.00 rad
f_{1bk}	0.94 (fixed)
f_{2bk}	0.05 (fixed)
f_{3bk}	0.01 (fixed)
f_1	0.28±0.09
f_2	0.31±0.08
f_3	0.37±0.06
-log(like)	47.1

6.6 D^+ Results

The Dalitz plot fit to the D^+ is similar to the D_s. The same parameterization is used. Fortunately, for the D^+ fit there is no problem of $K\pi\pi$ contamination. In addition, there is only one clear minimum in the likelihood function.

6.6.1 Fixed Background

The results of the Dalitz plot fit for an L/σ_L cut of 7 for the D^+ data sample are presented in Table 6.18 and in Fig. 6.18 is shown the fit. The sample has 240 data points and the number of signal events is 99 ±15 (results from the fit to the $K\overline{K}\pi$ invariant mass distribution). Consequently the value of f_s used was 0.4.

The correlation matrix for this fit is:

$$\begin{pmatrix} 1.00 & 0.59 & 0.10 & -.08 \\ 0.59 & 1.00 & -.19 & -.38 \\ 0.10 & -.19 & 1.00 & 0.82 \\ -.08 & -.38 & 0.82 & 1.00 \end{pmatrix}$$

and the covariance error matrix obtained is:

$$\begin{pmatrix} 0.24 & 0.13 & 0.03 & -.04 \\ 0.13 & 0.20 & -.06 & -0.17 \\ 0.03 & -.06 & 0.46 & 0.56 \\ -.04 & -.17 & 0.56 & 1.00 \end{pmatrix}$$

The branching ratios are:

$$\frac{\Gamma(D^+ \to \overline{K}^{*o} K^+)}{\Gamma(D^+ \to \phi\pi^+)} = 0.61 \pm 0.22$$

$$\frac{\Gamma(D^+ \to K^+K^-\pi^+(n.r.))}{\Gamma(D^+ \to \phi\pi^+)} = 0.37 \pm 0.23$$

6.6.2 Variable Background

When the background fit parameters are allowed to vary the results obtained are presented in Table 6.19. It is interested to note that the fit result for the parameter f_{2bk} is zero (the fitter gives a warning message that the parameter is at its limit). The correlation matrix for this fit is:

$$\begin{pmatrix} 1.00 & 0.43 & 0.24 & 0.09 \\ 0.43 & 1.00 & -.22 & -.37 \\ 0.20 & -.22 & 1.00 & 0.84 \\ 0.09 & -.37 & 0.84 & 1.00 \end{pmatrix}$$

and the covariance error matrix obtained is:

$$\begin{pmatrix} 0.13 & 0.06 & 0.05 & 0.03 \\ 0.06 & 0.13 & -0.06 & -.14 \\ 0.05 & -.06 & 0.52 & 0.64 \\ 0.03 & -.14 & 0.64 & 1.10 \end{pmatrix}$$

The branching ratio results are:

$$\frac{\Gamma(D^+ \to \overline{K}^{*0} K^+)}{\Gamma(D^+ \to \phi\pi^+)} = 0.66 \pm 0.21$$

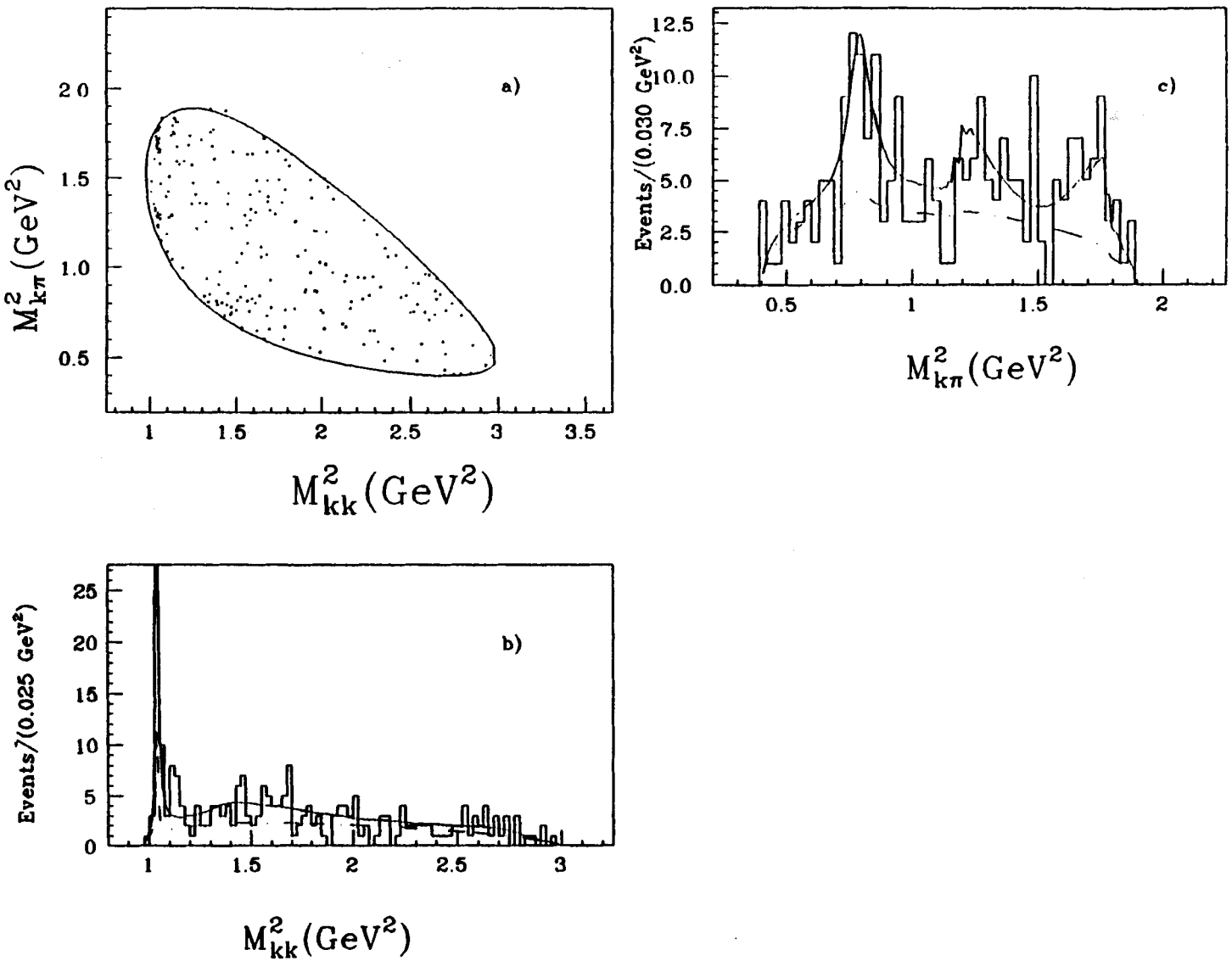

Figure 6.18: Dalitz plot fit for the D^+ signal together with the projections and results of the fit. The solid curve shows the combined signal and background. The dot-dashed curves show the background contribution.

TABLE 6.19
D$^+$ FIT RESULTS FOR L/σ_L > 7 AND f_s = 0.4 (BACKGROUND VARIED)

Parameter	Output Values
β_1	0.71±0.35
β_2	1.0 (fixed)
β_3	1.13±0.36
β_4	3.12 ±0.72 rad
β_5	0.0 rad (fixed)
β_6	2.95 ±1.04 rad
f_{1bk}	1.00±0.33
f_{2bk}	0.00±0.75
f_{3bk}	0.00 (fixed)
f_1	0.26±0.09
f_2	0.36±0.08
f_3	0.41±0.06
-log(like)	49.7

$$\frac{\Gamma(D^+ \to K^+K^-\pi^+(n.r.))}{\Gamma(D^+ \to \phi\pi^+)} = 0.31 \pm 0.18$$

6.6.3 D$^+$ Incoherent Fit

The incoherent fit results for this sample are shown in Table 6.20. The overall value for the fit fractions do not change significantly when compared with the coherent case.

The branching ratios are:

$$\frac{\Gamma(D^+ \to \overline{K}^{*0}K^+)}{\Gamma(D^+ \to \phi\pi^+)} = 0.62 \pm 0.21$$

$$\frac{\Gamma(D^+ \to K^+K^-\pi^+(n.r.))}{\Gamma(D^+ \to \phi\pi^+)} = 0.41 \pm 0.25$$

6.6.4 D$^+$ Results as a Function of L/σ_L

The D$^+$ Dalitz plot fit was performed using events with L/σ_L > 7, > 8, and > 9. 7,8, and 9. The fits were also done with variable background. As already mentioned for

TABLE 6.20
D^+ FIT RESULTS FOR $L/\sigma_L > 7$ AND $f_s = 0.4$ (INCOHERENT CASE)

Parameter	Output Values
β_1	0.98±0.53
β_2	1.0 (fixed)
β_3	1.19±0.40
f_1	0.31±0.10
f_2	0.32±0.08
f_3	0.37±0.06
-log(like)	51.0

the case of $L/\sigma_L > 7$, when the background fit coefficients were allowed to vary, the fitter finds mostly $K\overline{K}\pi$ non-resonant background. The value for -log(like) is smallest when the background fit coefficients were held fixed. In Table 6.21 are presented the results for a fit to events with $L/\sigma_L > 8$. The correlation matrix for this fit is:

$$\begin{pmatrix} 1.00 & 0.57 & 0.07 & -.04 \\ 0.57 & 1.00 & -.10 & -.20 \\ 0.07 & -.10 & 1.00 & 0.54 \\ -.04 & -.20 & 0.54 & 1.00 \end{pmatrix}$$

and the covariance error matrix obtained is:

$$\begin{pmatrix} 0.23 & 0.09 & 0.01 & -.006 \\ 0.09 & 0.11 & -.01 & -.02 \\ 0.01 & -.01 & 0.10 & 0.06 \\ -.006 & -.02 & 0.06 & 0.12 \end{pmatrix}$$

The branching ratios are:

$$\frac{\Gamma(D^+ \to \overline{K}^{*0} K^+)}{\Gamma(D^+ \to \phi\pi^+)} = 0.67 \pm 0.21$$

$$\frac{\Gamma(D^+ \to K^+K^-\pi^+(n.r.))}{\Gamma(D^+ \to \phi\pi^+)} = 0.50 \pm 0.26$$

In Fig. 6.19 is shown the variation of the fitted parameters with the L/σ_L cut. For all these cases the background fit coefficients were held fixed. (In these fits, the $\overline{K}^{*0}K$

TABLE 6.21
D^+ FIT RESULTS FOR $L/\sigma_L > 8$ AND $f_s = 0.47$

Parameter	Output Values
β_1	1.12±0.48
β_2	1.0 (fixed)
β_3	1.10±0.33
β_4	3.98 ±0.31 rad
β_5	0.0 rad (fixed)
β_6	3.50 ±0.34 rad
f_{1bk}	0.94 (fixed)
f_{2bk}	0.05 (fixed)
f_{3bk}	0.01 (fixed)
f_1	0.36±0.08
f_2	0.32±0.08
f_3	0.36±0.06
-log(like)	28.2

phase angle was fixed at zero radians). In Fig. 6.20 are shown the branching ratio results as a function of L/σ.

6.6.5 Mapping the Likelihood for the D^+

The likelihood function was studied as a function of the fit variables as was done for the D_s. The fit coefficient and phase angle for the $\overline{K}^{*0}K$ decay channel were held fixed as were the background fit coefficients. The values used were β_2 =1.0, β_5= 0.0 rad, f_{1bk} = 0.94, f_{2bk} = 0.05 and f_{3bk} = 0.01.

In Fig. 6.21 are shown the results for the case of $L/\sigma_L > 7$. From the plots one observes that the two fit coefficients each have a parabolic dependence on the likelihood. The plot for the $\phi\pi$ phase (β_6) is a continuous function. On the other hand the plot for the $K\overline{K}\pi$(n.r.) phase angle (β_4) has a discontinuity around the value of -2.0 radians. As in the case of the D_s the fitter gives a warning message that the

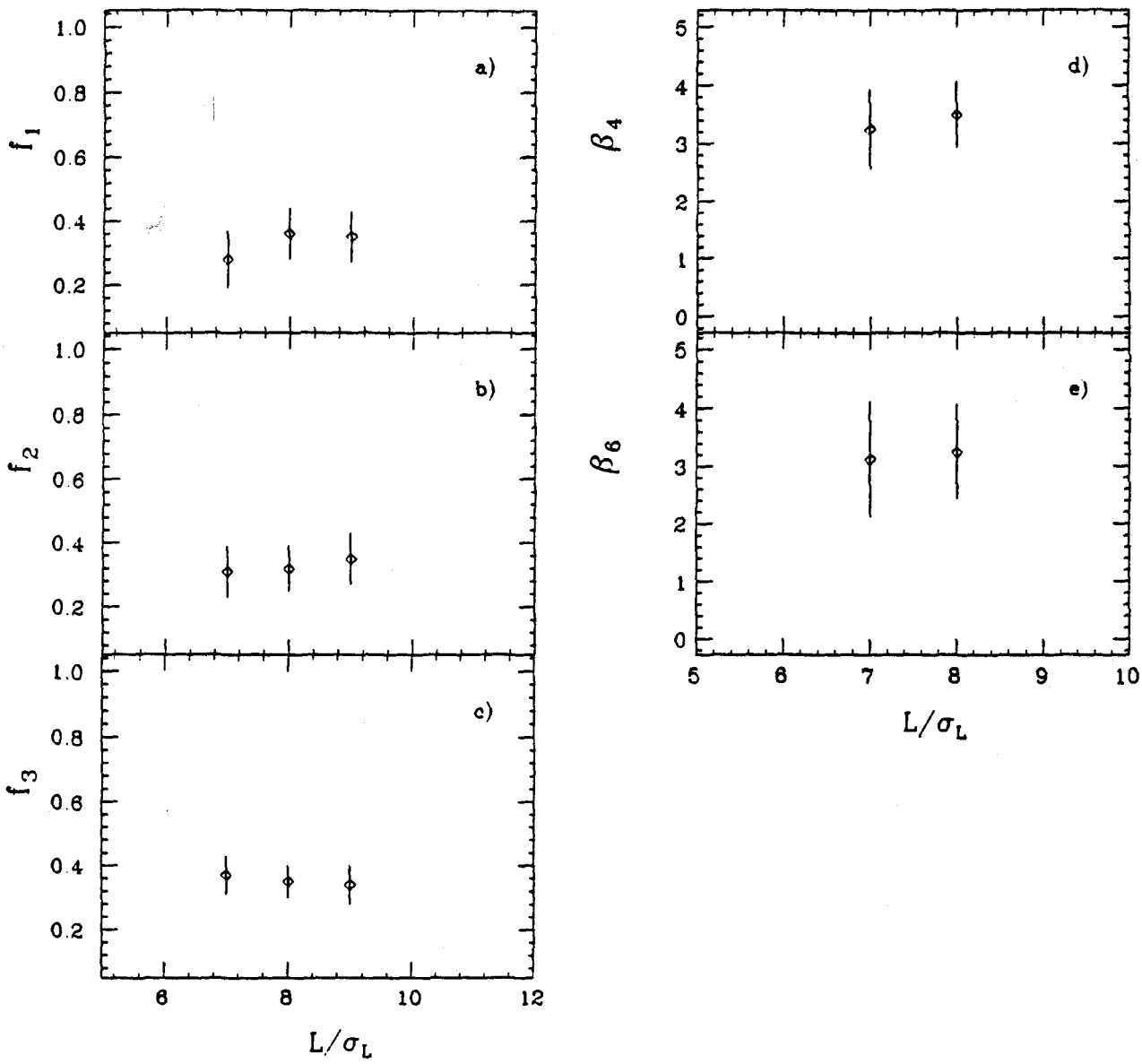

Figure 6.19: D^+ Dalitz plot fit results as a function of L/σ_L: a) f_1 is the $K\overline{K}\pi$ n.r. fit fraction, b) f_2 is the $\overline{K}^{*0}K$ fit fraction, c) f_3 is the $\phi\pi$ fit fraction, d) β_4 is the $K\overline{K}\pi$ n.r. phase angle, e) β_6 is the $\phi\pi$ phase angle.

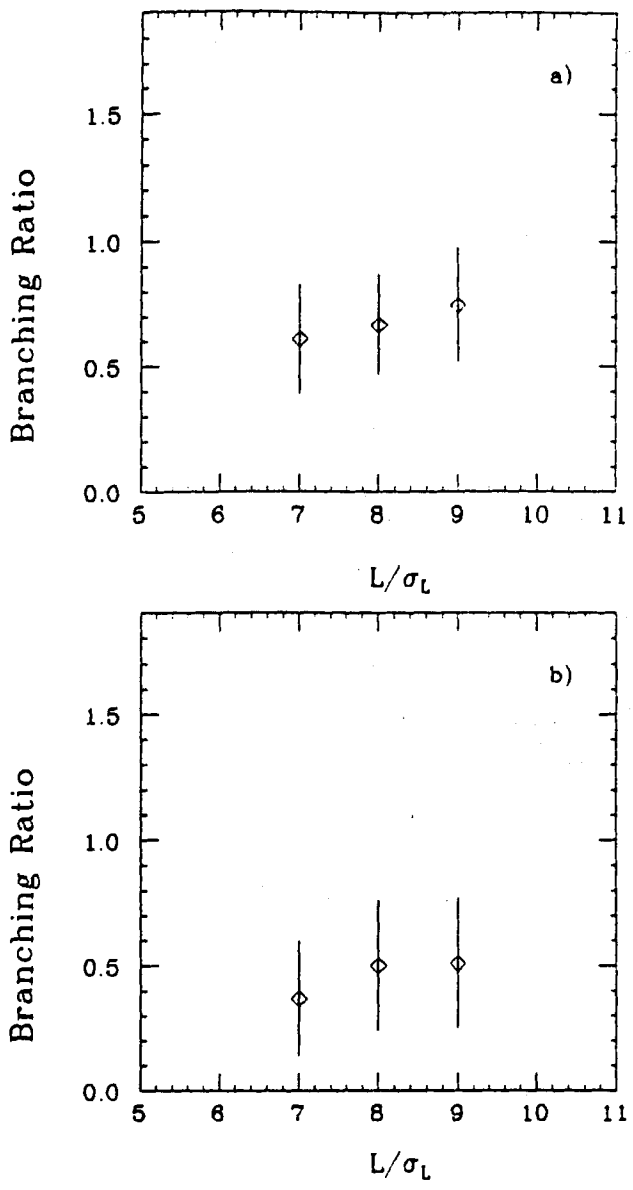

Figure 6.20: D^+ Branching ratio results as a function of L/σ_L. : a) D^+ decaying to $\overline{K}^{*0}K$ with respect to the $\phi\pi$ decay channel, b) D^+ decaying to $K\overline{K}\pi$ (n.r.) with respect to the $\phi\pi$ decay channel.

$K\overline{K}\pi$(n.r.) fit coefficient is at its limit (zero), so one should disregard the results of the fit for the region where the discontinuity occurs.

6.6.6 D^+ Error Analysis

As in the case of the D_s, MINOS errors were determined for the D^+ fit parameters. In Table 6.22 and in Table 6.23 are shown these MINOS errors for L/σ_L greater than 7 and 8 respectively.

TABLE 6.22
D^+ MINOS ERROR ANALYSIS FOR $L/\sigma_L > 7$

Parameter	Value	Parabolic error	MINOS Errors	
			Positive	Negative
β_1	0.92	0.49	0.66	0.40
β_2	1. (fixed)			
β_3	1.22	0.46	0.56	0.36
β_4	3.26	0.72	0.68	0.71
β_5	0.0 (fixed)			
β_6	3.13	1.04	1.09	0.90

TABLE 6.23
D^+ MINOS ERROR ANALYSIS FOR $L/\sigma_L > 8$

Parameter	Value	Parabolic error	MINOS Errors	
			Positive	Negative
β_1	1.13	0.48	0.59	0.39
β_2	1. (fixed)			
β_3	1.10	0.33	0.41	0.29
β_4	3.98	0.31	0.30	0.31
β_5	0.0 (fixed)			
β_6	3.50	0.34	0.34	0.33

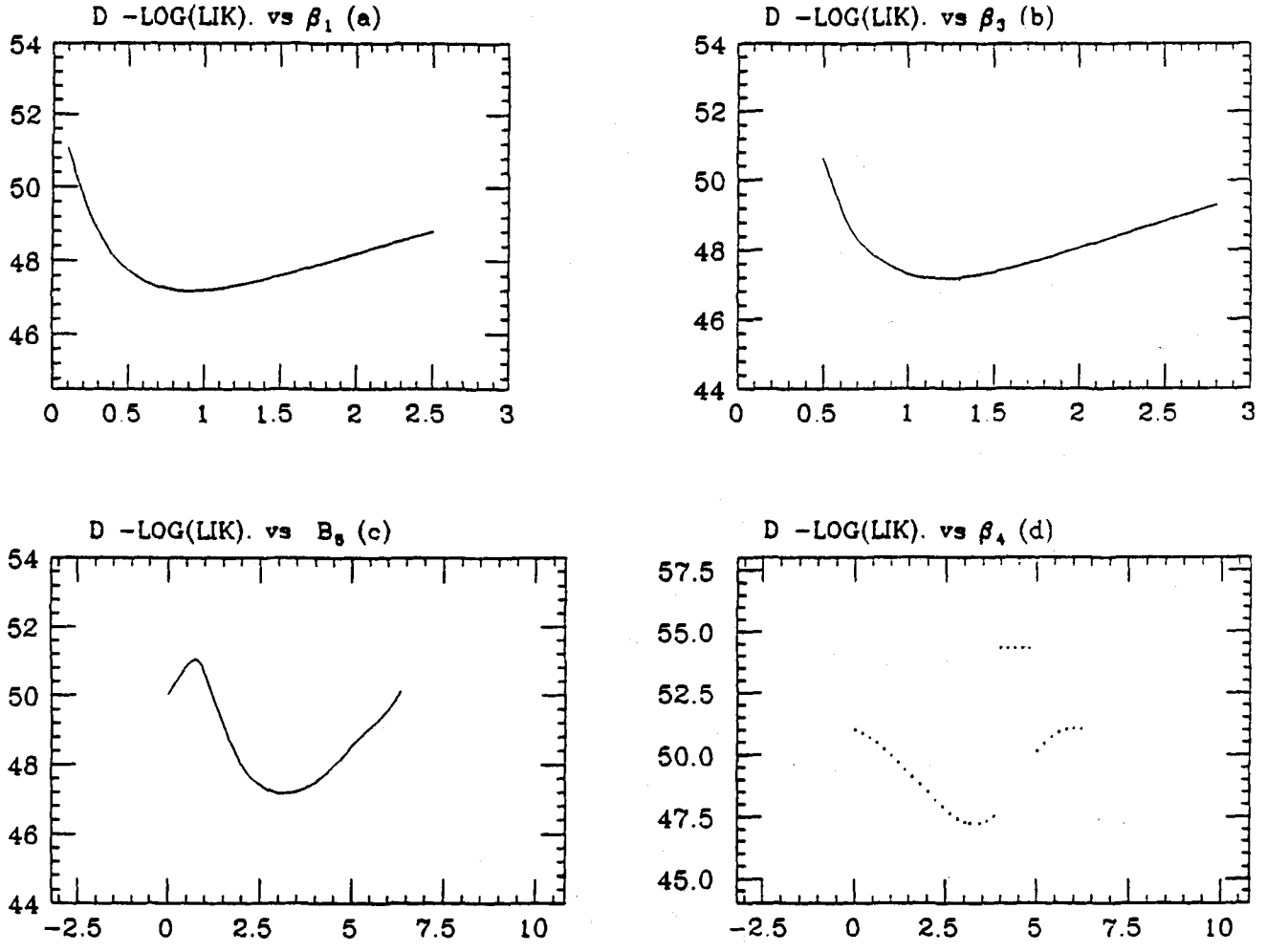

Figure 6.21: D^+ Mapping of the Likelihood: a) -log(like) vs β_1, b)-log(like) vs β_3, c) -log(like) vs β_4, and d) -log(like) vs β_4.

In Fig. 6.22 and Fig. 6.23 are shown the the plot of -log(like) versus the fit parameters for $L/\sigma_L > 8$.

6.6.7 D^+ Likelihood Contours

In Fig. 6.24 are shown the contour lines for the (β_1,β_3) plane for $L/\sigma_L > 8$. The inner curve with label "0" corresponds to the minimum of -log(like) with a value of 28.21. In Fig. 6.25 and Fig. 6.26 are shown the likelihood contour curves for several combinations of the parameters β_i, and β_j.

6.6.8 D^+ Summary Result

The preferred solution for the D^+ is the one for the data sample with a $L/\sigma_L > 8$. Due to the longer lifetime of the D^+, it is possible to use higher values of L/σ_L without losing much of the signal and consequently to improve the signal to background ratio. (See in chapter 4 the different plots of the D^+ signal as a function of L/σ_L).

As in the case of the D_s the results from the different fits were used in order to estimate the systematic error for the "preferred solution". The branching ratio results with statistical plus systematic errors are the following: The branching ratios are:

$$\frac{\Gamma(D^+ \to \overline{K}^{*0} K^+)}{\Gamma(D^+ \to \phi\pi^+)} = 0.67^{+0.25}_{-0.18} \pm 0.10$$

$$\frac{\Gamma(D^+ \to K^+K^-\pi^+(n.r.))}{\Gamma(D^+ \to \phi\pi^+)} = 0.50^{+0.31}_{-0.21} \pm 0.20$$

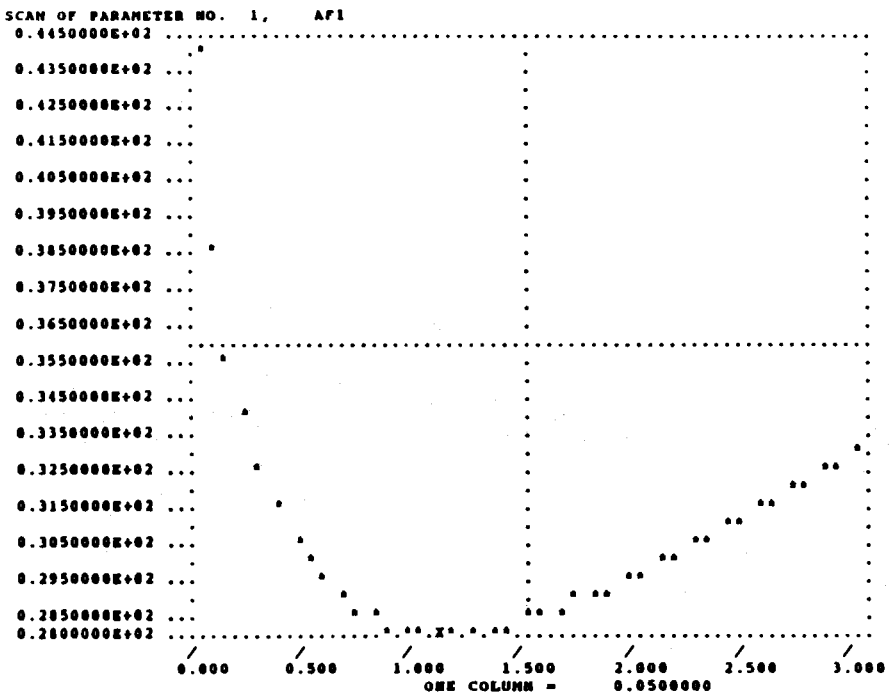

(a) β_1

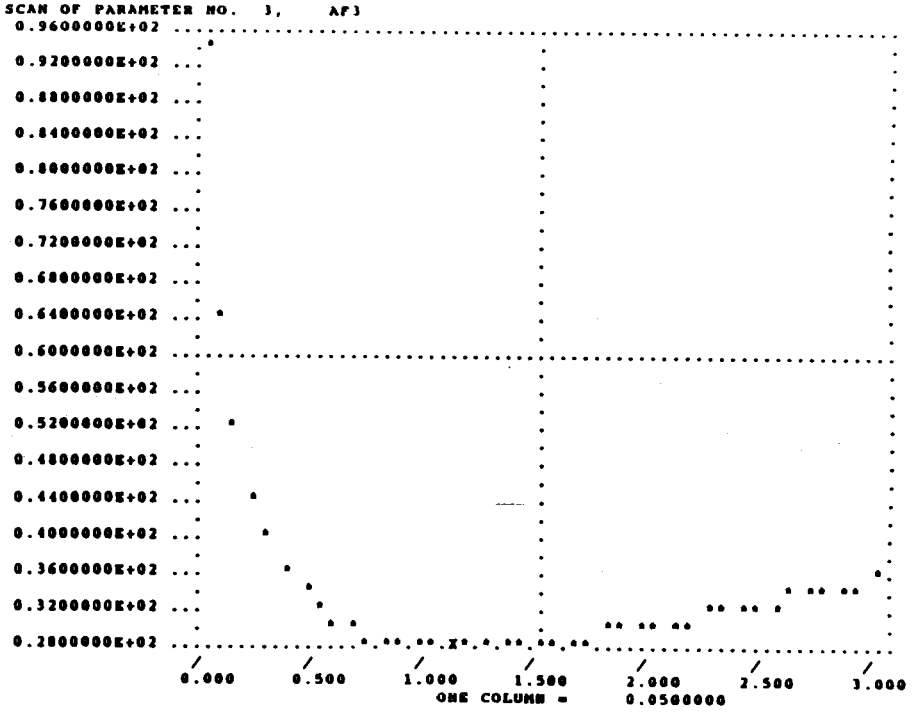

(b) β_3

Figure 6.22: D^+ Plot of -log(like) versus fit parameters for $L/\sigma_L > 8$. a) -log(like) vs. β_1, b)-log(like) vs. β_3

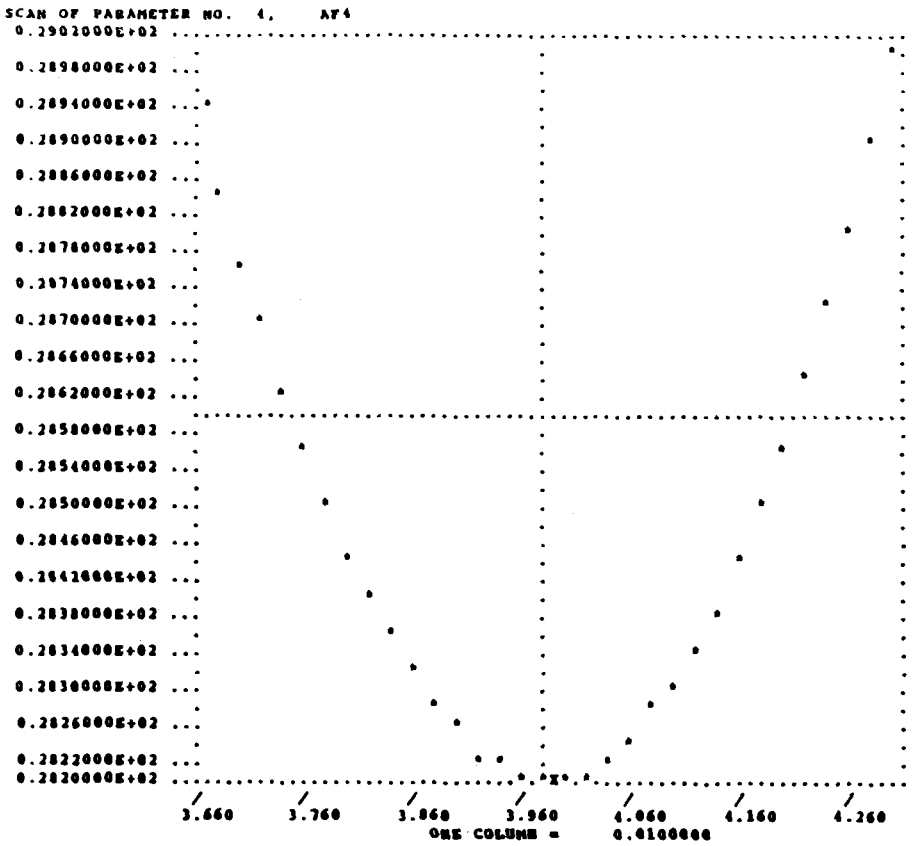

(a) β_4

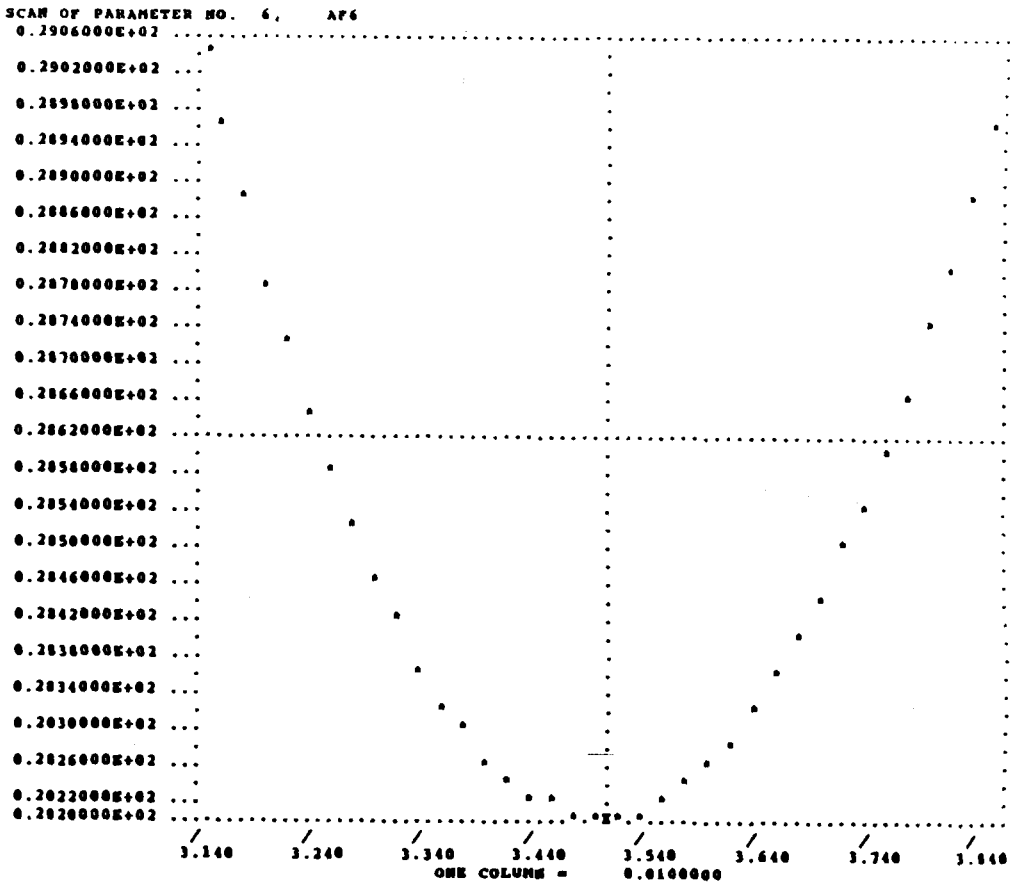

(b) β_6

Figure 6.23: D^+ Plot of -log(like) versus fit parameters for $L/\sigma_L > 8$. a) -log(like) vs. β_1, b)-log(like) vs. β_6

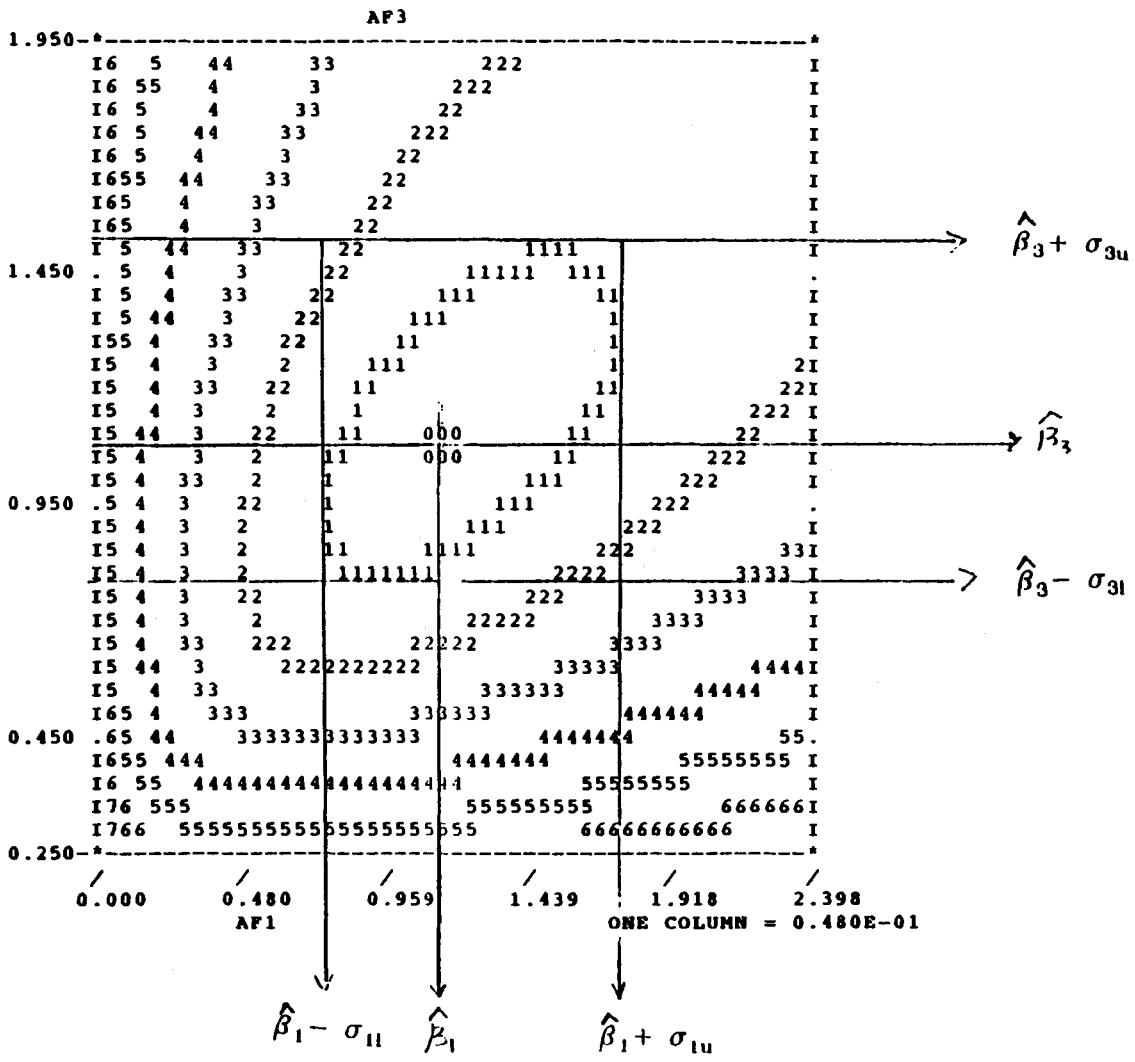

Figure 6.24: D^+ Plot of likelihood contour curves for $L/\sigma_L > 8$ for the (β_1, β_3) plane.

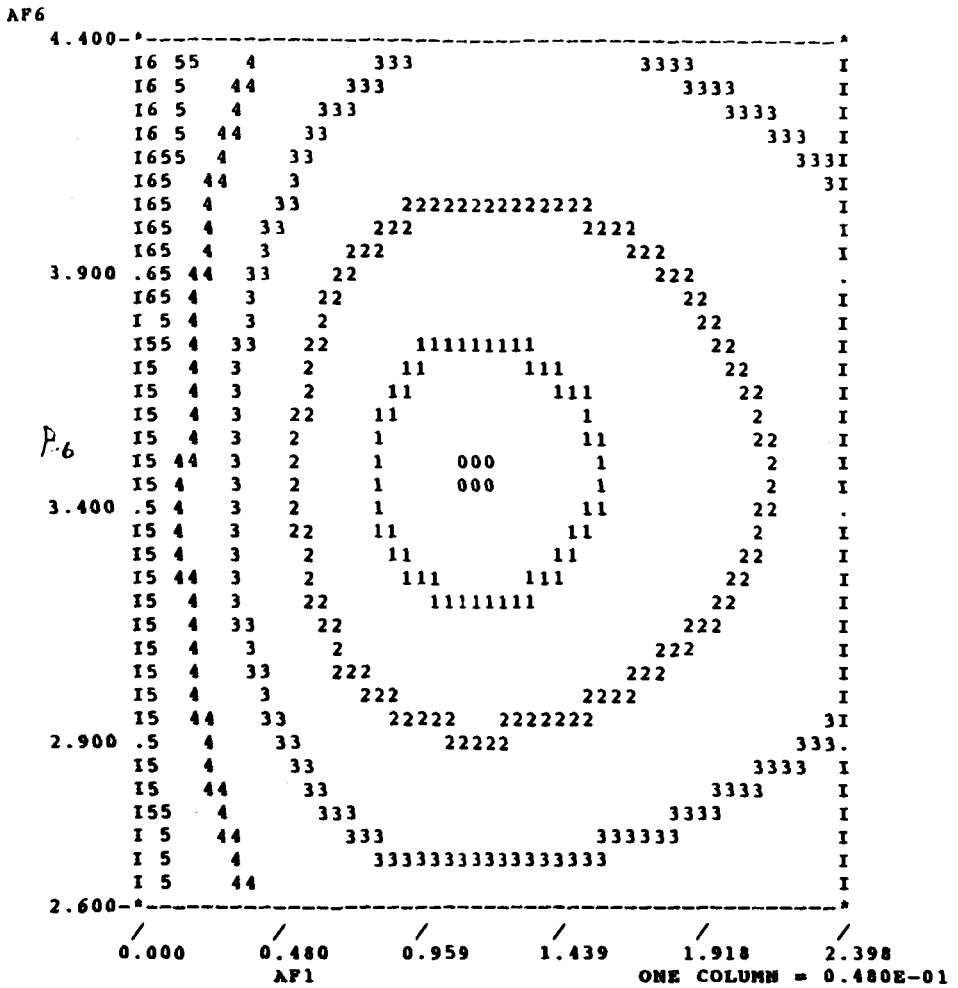

(a) β_1

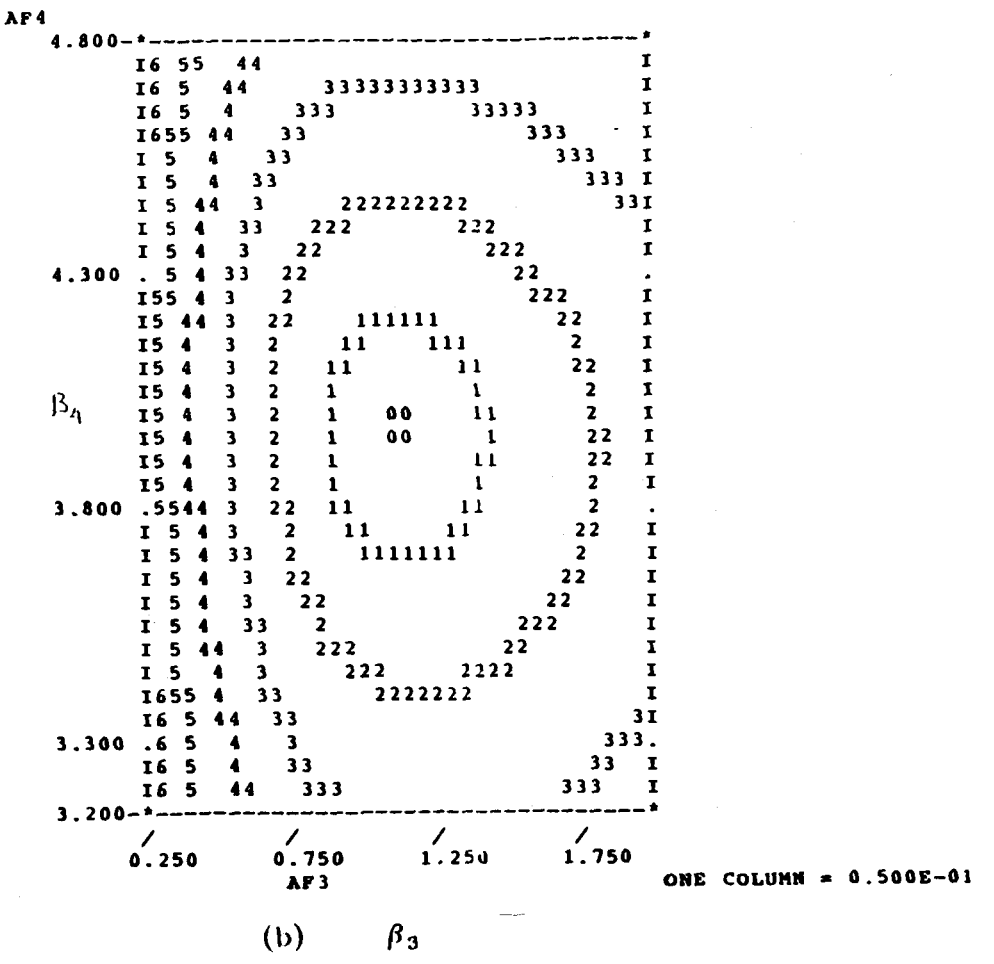

(b) β_3

Figure 6.25: D$^+$ Plot of likelihood contour curves for L/σ_L >8. a) (β_1,β_6) plane, b) (β_3,β_4) plane.

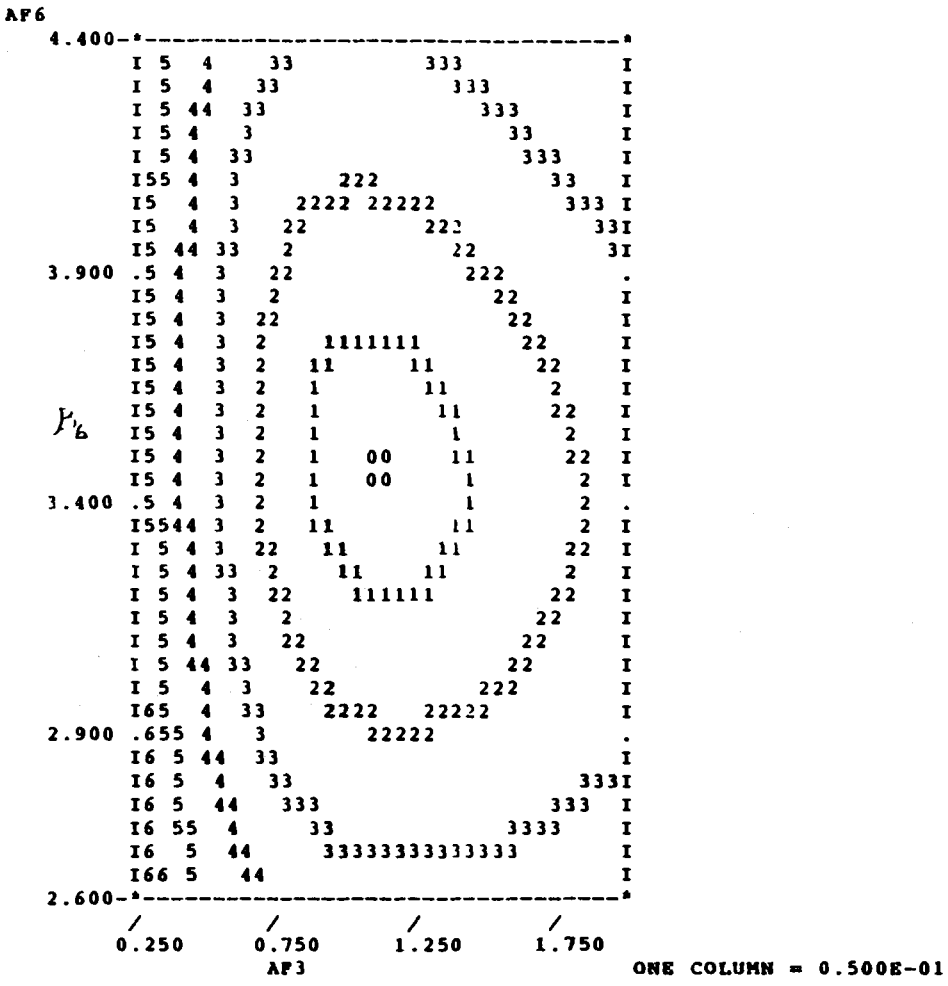

(a) β_3

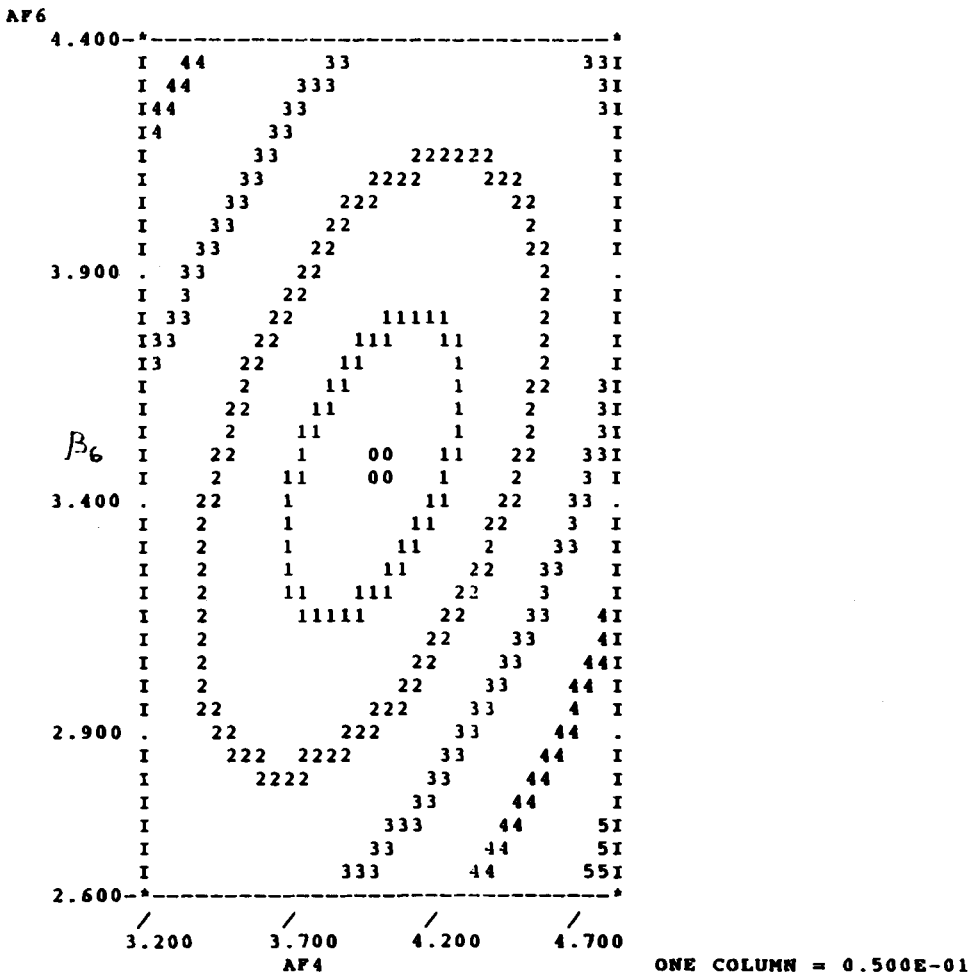

(b) β_4

Figure 6.26: D^+ Plot of likelihood contour curves for $L/\sigma_L > 8$. a) (β_3,β_6) plane, b) (β_4,β_6) plane.

CHAPTER 7

CONCLUSIONS

In this chapter a summary of the results for the D_s and D^+ branching ratios are presented. Results from another experiments are also presented and compared with the results from this work. Finally some remarks are made about the implication of the results obtained in this thesis.

7.1 Summary of D_s Results

The results for the Dalitz plot fit to the D_s sample are summarized in Table 7.1. The branching ratio results are:

$$\frac{\Gamma(D_s \to \overline{K}^{*0} K^+)}{\Gamma(D_s \to \phi\pi^+)} = 1.23^{+0.33}_{-0.27} \pm 0.30$$

and

$$\frac{\Gamma(D_s \to K^+K^-\pi^+(n.r.))}{\Gamma(D_s \to \phi\pi^+)} = 0.29^{+0.25}_{-0.18} \pm 0.24.$$

TABLE 7.1
RESULTS FOR $D_s^+ \to K^+K^-\pi^+$

Decay channel	fit fraction	Phase (radians)
$K^+K^-\pi^+_{nonres}$	0.16±0.07	-1.81 ±0.29
$\overline{K}^{*0}K^+$	0.44±0.06	0.0 (fixed)
$\phi\pi^+$	0.27±0.04	-2.89 ±0.27

TABLE 7.2
BRANCHING RATIOS OF $D_s \rightarrow KK\pi$ RELATIVE TO $D_s \rightarrow \phi\pi$

Decay Mode	Experiment	Result
$D_s^+ \rightarrow K^*(892)^0 K^+$	MARK III	$0.84 \pm 0.30 \pm 0.22$
	CLEO	$1.05 \pm 0.17 \pm 0.12$
	E691	$0.87 \pm 0.13 \pm 0.05$
	ARGUS	1.44 ± 0.37
	NA14/2	$0.85 \pm 0.34 \pm 0.20$
	ACCMOR	0.94 ± 0.35
	E687	$1.23^{+0.33}_{-0.27} \pm 0.30$
	$E687_{Dcut}$	$0.91^{+0.44}_{-0.24} \pm 0.20$
	PDG	0.96 ± 0.11
$D_s^+ \rightarrow (K^+K^-\pi^+)_{nonres}$	E691	$0.25 \pm 0.07 \pm 0.06$
	ACCMOR	0.51 ± 0.20
	E687	$0.29^{+0.25}_{-0.18} \pm 0.24$
	$E687_{Dcut}$	$0.19^{+0.34}_{-0.14} \pm 0.20$

7.2 D_s Comparison with World Averages

Several experiments have reported measurements for the D_s decaying to the $K\overline{K}\pi$ final state. In Table 7.2 are shown those branching ratio results along with those of this experiment. It interested to note that only E691 did maximum-likelihood fits to the D_s and D^+ Dalitz plots. However E691 did not perform a coherent fit [14]. The branching ratio results from all other experiments is based in selecting the individual decay modes by several analysis cuts, and then compute the branching ratio. ([44], [45], [46], [47], [48]). From Table 7.2 one observes that there is an overall good agreement for the D_s branching ratio results obtained in this work when compared with the results from another experiments. In Fig. 7.1 are shown the values listed in Table 7.2. The result with the label $E687_{Dcut}$ corresponds to the case when the $K\pi\pi$ contamination has been removed.

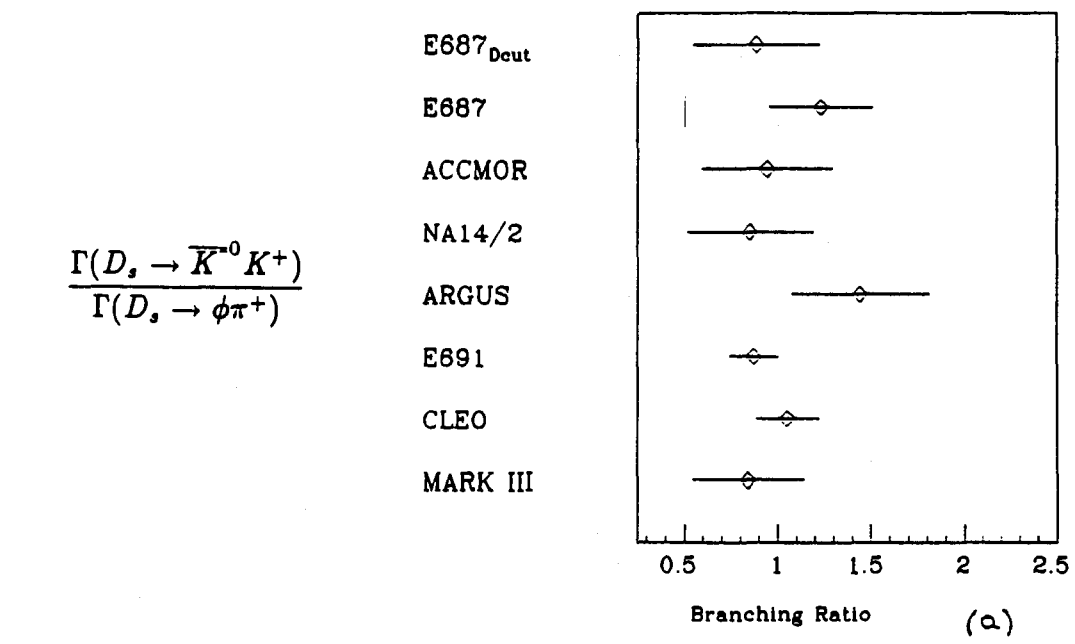

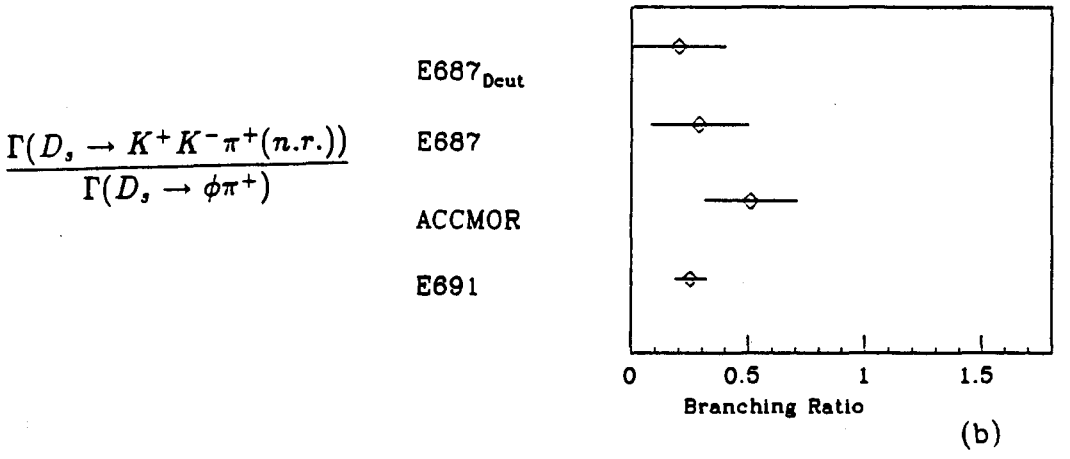

Figure 7.1: D_s Comparison with world averages. Branching ratio results for: a) D_s decaying to $\overline{K}^{*0}K$ with respect to the $\phi\pi$ decay channel, b) D_s decaying to $K\overline{K}\pi$ (n.r.) with respect to the $\phi\pi$ decay channel.

TABLE 7.3
FINAL RESULTS FOR $D^+ \rightarrow K^+K^-\pi^+$

Decay channel	fit fraction	Phase (radians)
$K^+K^-\pi^+_{nonres}$	0.36±0.08	3.98 ±0.31
$\overline{K}^{*0}K^+$	0.32±0.08	0.0 (fixed)
$\phi\pi^+$	0.36±0.06	3.50 ±0.34

7.3 D^+ Summary

In Table 7.3 are shown the results for the D^+.

The branching ratios are:

$$\frac{\Gamma(D^+ \rightarrow \overline{K}^{*0}K^+)}{\Gamma(D^+ \rightarrow \phi\pi^+)} = 0.67^{+0.25}_{-0.18} \pm 0.10$$

$$\frac{\Gamma(D^+ \rightarrow K^+K^-\pi^+(n.r.))}{\Gamma(D^+ \rightarrow \phi\pi^+)} = 0.50^{+0.31}_{-0.21} \pm 0.20$$

7.4 D^+ Comparison with World Averages

The branching ratio results presented in this thesis for the D^+ are relative to the $\phi\pi$ decay channel. The reason for normalizing the branching ratio to the $\phi\pi$ and not to the more abundant decay $K\pi\pi$ is that in the skim process the $K\pi\pi$ decay channel was not included. In Table 7.4 are shown the branching ratio results from another experiments in which the normalization channel is the $K\pi\pi$ mode.

In order to compare with the branching ratio results from the present work, the results presented in Table 7.4 for the decay modes $D^+ \rightarrow \bar{K}^*(892)^0K^+$ and $D^+ \rightarrow (K^+K^-\pi^+)_{nonres}$ are divided by the results of the decay mode $D^+ \rightarrow \phi\pi^+$. The errors are computed from the ones shown in Table 7.4 assuming no correlations. In Table 7.5 are shown the results.

TABLE 7.4
BRANCHING RATIOS OF $D^+ \to K^+K^-\pi^+$ RELATIVE TO $D^+ \to K^-\pi^+\pi^+$

Decay Mode	Experiment	Result
$D^+ \to \phi\pi^+$	MARK III	$0.084 \pm 0.021 \pm 0.011$
	E691	$0.071 \pm 0.008 \pm 0.007$
	ACCMOR	0.083 ± 0.028
	PDG	0.073 ± 0.010
$D+ \to \bar{K}^*(892)^0K^+$	E691	$0.058 \pm 0.009 \pm 0.006$
	MARK III	$0.048 \pm 0.021 \pm 0.011$
	ACCMOR	0.070 ± 0.03
	PDG	0.056 ± 0.01
$D^+ \to (K^+K^-\pi^+)_{nonres}$	E691	$0.049 \pm 0.008 \pm 0.006$
	MARK III	$0.059 \pm 0.026 \pm 0.009$
	ACCMOR	0.067 ± 0.022
	PDG	0.050 ± 0.009

TABLE 7.5
BRANCHING RATIOS OF $D^+ \to K^+K^-\pi^+$ RELATIVE TO $D^+ \to \phi\pi^+$

Decay Mode	Experiment	Result
$D+ \to \bar{K}^*(892)^0K^+$	E691	0.82 ± 0.16
	MARK III	0.57 ± 0.29
	ACCMOR	0.84 ± 0.46
	E687	$0.67^{+0.25}_{-0.18} \pm 0.10$
	PDG	0.76 ± 0.17
$D^+ \to (K^+K^-\pi^+)_{nonres}$	E691	0.69 ± 0.13
	ACCMOR	0.81 ± 0.38
	MARK III	0.70 ± 0.35
	E687	$0.50^{+0.31}_{0.21} \pm 0.20$
	PDG	0.68 ± 0.15

The branching ratio results obtained for the D^+ are in good agreement with the world average results. In Fig. 7.2 are shown the values given in Table 7.5.

To summarize, in this thesis the pseudoscalar-vector (PV) decay sequences for the D_s:

- $D_s \longrightarrow \phi\pi$, $\phi \longrightarrow K^+K^-$
- $D_s \longrightarrow \overline{K}^{*0}K$, $\overline{K}^{*0} \rightarrow \overline{K}\pi$.

have been studied. The evidence for ϕ and $\overline{K}^{*0}$ vector mesons as decay products of the D and D_s has been clearly observed.

As mentioned in chapter one the diagram that contributes to the $D_s \rightarrow \phi\pi$ decay mode is a "spectator-color-allowed" diagram, while the $D_s \rightarrow \overline{K}^{*0}K$ decay mode has a "spectator-color-suppressed" diagram. Since the branching ratio results obtained in this work for the $D_s \rightarrow \overline{K}^{*0}K$ with respect to $D_s \rightarrow \phi\pi$ is close to one, there is evidence that the so-called "color suppression mechanism" contributes to the decay at a level comparable to that of the so-called "color allowed mechanism".

Similarly the Cabibbo-suppressed decays of the D^+ charmed meson:

- $D^+ \longrightarrow \phi\pi^+$, $\phi \longrightarrow K^+K^-$
- $D^+ \longrightarrow \overline{K}^{*0}K^+$, $\overline{K}^{*0} \rightarrow \overline{K^-}\pi^+$.

have been studied. For the case of the D^+ the $\overline{K}^{*0}K^+$ decay mode is a "spectator-color-allowed" decay, while the $\phi\pi^+$ decay mode is a "spectator-color-suppressed" decay. Because of suppression the branching ratio for the D^+ decaying to $\overline{K}^{*0}K^+$ with respect to the $\phi\pi^+$ decay mode should be large. The results obtained for the D^+ in this work show again that the "color-suppression mechanism" is comparable in magnitude to the "color allowed mechanism".

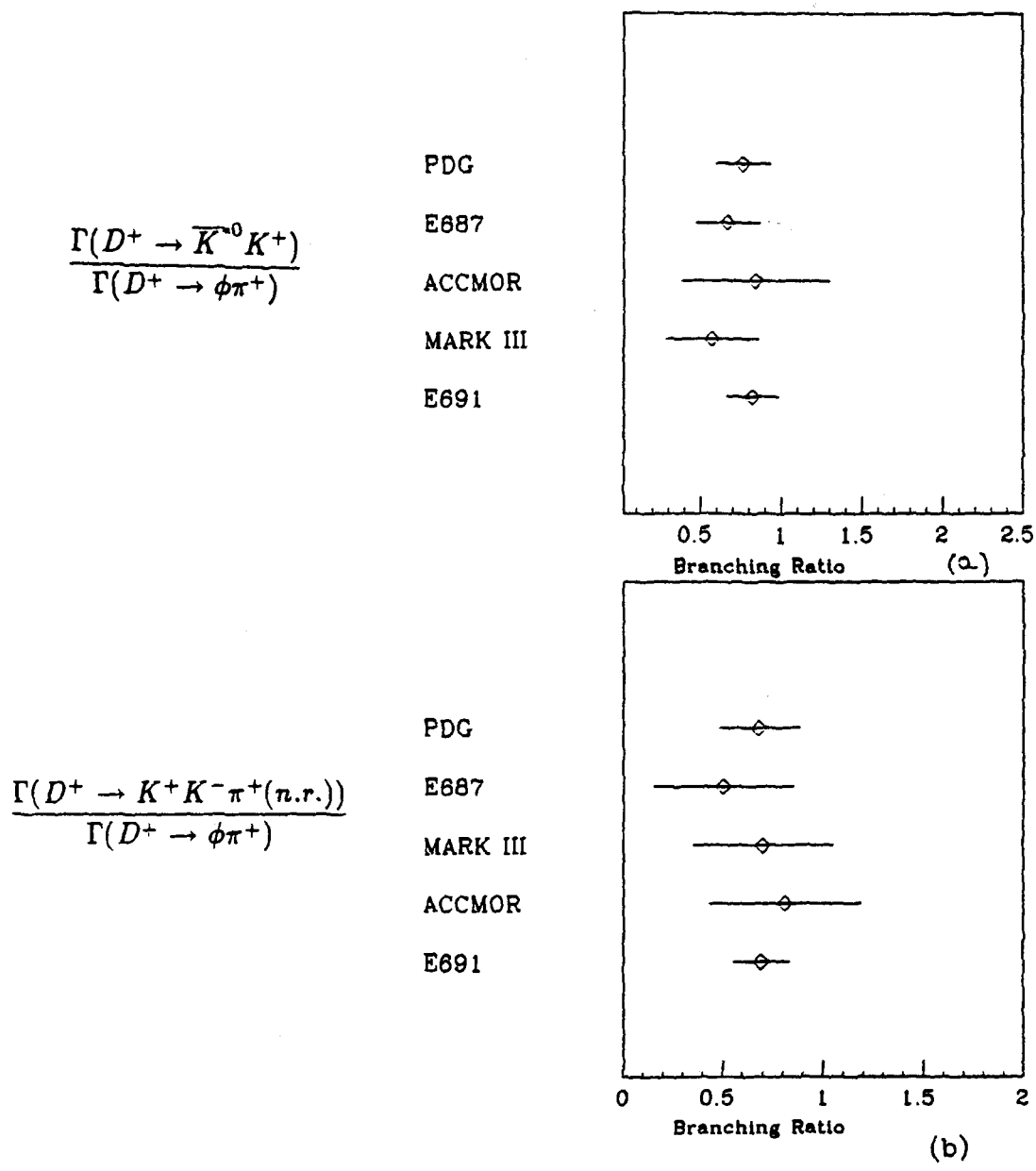

Figure 7.2: D^+ Comparison with world averages. Branching ratio results for: a) D^+ decaying to $\overline{K}^{*0}K$ with respect to the $\phi\pi$ decay channel, b) D^+ decaying to $K\overline{K}\pi$ (n.r.) with respect to the $\phi\pi$ decay channel.

BIBLIOGRAPHY

[1] D.G. Hitlin "Weak Decays of Charmed Quarks an Experimental review" preprint CALT-68-1463. preprint USCB-HEP-89-01 (1989).

[2] D. Griffiths "Introduction to Elementary Particles", Wiley & Sons Publishing Co (1987).

[3] R.J. Morrison and M.S. Witherell, "D-Mesons"

[4] V. Barger, "Collider Physics", Addison-Wesley Publishing Co (1987).

[5] I.I. Bigi "On Our Theoretical Understating of Charm Decays" preprint SLAC-PUB-4607. August (1986).

[6] E. Rojek, Ph.D. thesis, University of Notre Dame (1986). (unpublished).

[7] Particle Data Group, "Review of Particle Properties" Phys. Lett. **B239** (1990).

[8] R.J. Morrison and M.S. Witherell, "D-Mesons" preprint USCB-HEP-89-06 (1989).

[9] M. Bauer, Z Phys. C **34**, 103-115 (1987).

[10] Buras et. al., Nucl. Phys. **B268**, 16 (1986).

[11] J. Donoghue, Phys. Rev. **D33**, 1516 (1986).

[12] Chau et. al., Phys. Rev. **D36**, 132 (1987).

[13] B.R. Kumar "Results on Charm Decays from The Fermilab Tagged Photon Spectrometer" preprint from the talk given at the Lake Louise Winter Institute, Alberta, Canada, February 1987.

[14] J.C. Anjos, et al., Phys. Rev Letters. **60**, 897 (1988).

[15] J. Butler et al., "Design for a New Wide-Band Neutral Beam for the Tevatron." FERMILAB Note TM-963 (1980).

[16] P.L. Frabetti, et al., "Description and Performance of the Fermilab E687 Spectrometer" FERMILAB-PUB-90-258-E (1990). Submitted To *Nucl. Instr. and Meth.*

[17] C.Halliwell, et al., Nuclear Instruments and Methods. **102**, 51-59 (1972).

[18] G. Bellini et al., Nuclear Instruments and Methods. **A252**, 366-372 (1986).

[19] R. Yoshida, Ph.D. thesis, Northwestern University (1990) (unpublished).

[20] S. Park, Ph.D. thesis, Northwestern University (1990) (unpublished).

[21] J. Busenitz et al., Proposed Cerenkov Calibration Scheme for E687, E687 internal memo (1987).

[22] J. Wiss et al., Cerenkov Group Report, E687 internal memo (1988).

[23] L. Moroni and D. Pedrini, "All You Always Wanted To Know About Microrico But Were Afraid To Ask" E687 internal note (1988).

[24] M. Giammarchi, et al., Nucl. Instr. and Meth. **A251**, 40 (1986).

[25] J.E. Wiss, "Calculations Related to Fitting and Linking" E687 internal Memo (1988).

[26] D. Menasce, et al., "The Vertexing Problem in E687" E687 internal memo (1989).

[27] J.E. Wiss and R. Culbertson, "DVERT" E687 internal memo (1989).

[28] J. E. Wiss, "The Logic Cerenkov Algorithm" E687 internal memo (1988).

[29] M.E. Zanabria, et al., "Cerenkov Algorithm" E687 internal memo (1989).

[30] M.E. Zanabria, et al., "Cerenkov Monte Carlo Studies" E687 internal memo (1989).

[31] G. Jaross, et al., "SKIMADEE" E687 internal memo (1990).

[32] K. Lingel, Ph.D. thesis, University of Illinois (1990) (unpublished).

[33] M. Rath, Ph.D. thesis, University of Notre Dame (1988) (unpublished).

[34] C. Zemach, Phys. Rev. **133** 5B, B1201 (1964).

[35] R. Gardner, Ph.D. thesis, University of Notre Dame (1991) (unpublished).

[36] MINUIT, FERMILAB-PUB PM0020, June 1985

[37] D. Jongh, Ph.D. thesis, California Institute of technology (1990) (unpublished).

[38] A. Frodesen, Probability and Statistics in Particle Physics, Universitetsforlaget (1979).

[39] P.D.G., Phys. Rev. **D45**,11-II (1992).

[40] W. H. Press, "Numerical Recipes", Cambridge University Press (1986).

[41] MINUIT, CERN-PUB D506 (1989)

[42] F. James, Computer Phys. Comm. 20 (1980) 29-35

[43] F. James, Proc. of the 1981 CERN School of Computing CERN 81-03 March 1981.

[44] R.M. Baltrusaitis, et al., Phys. Rev Letters. **63**, 1211 (1989).

[45] W-Y Chen, et al., Phys. Lett. B **226** 192 (1989).

[46] M.P. Alvarez, et al., Phys. Lett. B **246** 261 (1990).

[47] H. Albrecht, et al., Phys. Lett. B **179** 398 (1986).

[48] S. Barlag, Z Phys. C **48**, 29-45 (1990).